D I S S E R T A T I O N

# Atomistic Modeling of Si Spin Qubits From First Principles

ausgeführt zum Zwecke der Erlangung des akademischen Grades
eines Doktors der technischen Wissenschaften

unter der Betreuung von

**Univ.Prof. Dr.techn. Tibor Grasser**

und

**Dr. habil. Yann-Michel Niquet**

eingereicht an der Technischen Universität Wien
Fakultät für Elektrotechnik und Informationstechnik
von

**Dipl.-Ing. Lukas Cvitkovich, BSc.**
Matrikelnummer: 1226838

Wien, im Juni 2024 ________________________________

Die approbierte gedruckte Originalversion dieser Dissertation ist an der TU Wien Bibliothek verfügbar.
The approved original version of this doctoral thesis is available in print at TU Wien Bibliothek.
TU WIEN Bibliothek Your knowledge hub

Die approbierte gedruckte Originalversion dieser Dissertation ist an der TU Wien Bibliothek verfügbar.
The approved original version of this doctoral thesis is available in print at TU Wien Bibliothek.
TU WIEN Bibliothek Your knowledge hub

# Abstract

Despite immense research efforts driven by the exciting promises of quantum information processing, the physical realization of a large-scale quantum computer has not yet been successful. The difficulties can be largely attributed to quantum noise, which refers to unwanted disturbances that affect the memory units of a quantum computer, known as qubits. These qubits must interact coherently and maintain their quantum states over time to execute algorithms effectively. Additionally, the qubit devices need to be highly uniform to ensure consistent behavior and minimize errors.

Among the various approaches for qubit implementation, spin qubits, which leverage the quantum mechanical properties of electron (or hole) spins, show extraordinary potential for scalable and efficient quantum computing. Spin qubits consist of a semiconducting host material in which an electron (or hole) spin is confined by barrier materials and electric fields. Split by a magnetic field, this two-level spin system constitutes the qubit. Using silicon (Si) as a host material is a particularly promising approach, because one of the major sources for quantum noise, hyperfine interactions with nuclear spins in the environment, can be mitigated by the removal of $^{29}$Si, the only Si isotope carrying a nuclear spin.

While operational quantum processors have already been demonstrated on this material platform, it has become increasingly evident that meticulous control over material properties down to the atomic level is necessitated by the rigorous requirements on coherence and uniformity. Further improvement of the device performance calls for sophisticated atomistic modeling.

Within the scope of this thesis, density functional theory (DFT), a powerful material modeling method, is employed to investigate the material-related qualities of Si spin qubits, aiming to advance current modeling techniques. In contrast to previous studies that relied on empirically parameterized models, usage of the essentially parameter-free DFT method allows for simulation of a realistic spin qubit environment, including strain, atomic disorder, and electric fields from first principles.

Representing the backbone of our calculations, particular focus is put on the credibility of the utilized atomic model structures. Both relevant types of Si spin qubits are considered: Si in combination with silicon-germanium (Si/SiGe) or with its native oxide $SiO_2$ (Si-MOS). In alignment with experimental setups, various epitaxially grown interface and heterostructure configurations are considered in the case of Si/SiGe. For Si-MOS, *ab-initio* molecular dynamics (AIMD) are used to simulate the thermal oxidation of a Si surface. This novel approach to generating amorphous $Si/SiO_2$ interfaces produces highly realistic model structures, making them well-suited



Die approbierte gedruckte Originalversion dieser Dissertation ist an der TU Wien Bibliothek verfügbar.
The approved original version of this doctoral thesis is available in print at TU Wien Bibliothek.
TU Wien Bibliothek Your knowledge hub

for the intended use in the context of spin qubits. At the same time, the simulations revealed multiple underlying oxidation mechanisms crucial to the full process. Experimentally observed but previously disconnected, these mechanisms are integrated into a comprehensive framework. Motivated by the high computational costs associated with *ab-initio* calculations, a machine learning (ML) model is trained using the previously obtained AIMD data, enabling a significant extension in both system size and simulation time scales.

Based on the thereby achieved atomic structures, a number of properties relevant for qubit applications are extracted from DFT, including valley and spin splittings, hyperfine interactions and decoherence times. A large variability in this data reflects variations in experimental observations and is related to atomistic disorder at the interface. Finally, nuclei in the barrier materials are identified as a significant source of noise and highlight the relevance of hyperfine interactions with non-Si atoms in the barrier materials.

Die approbierte gedruckte Originalversion dieser Dissertation ist an der TU Wien Bibliothek verfügbar.
The approved original version of this doctoral thesis is available in print at TU Wien Bibliothek.
TU WIEN Bibliothek Your knowledge hub

# Kurzfassung

Trotz immenser Fortschritte in der Entwicklung von *Quantum Computing*, ist die physische Realisierung eines für relevante Probleme einsatzfähigen Quantencomputers bisher noch nicht gelungen. Die praktischen Schwierigkeiten können im Wesentlichen auf quantenmechanisches Rauschen zurückgeführt werden: Diese unerwünschte Störungen beeinflussen die Speichereinheiten eines Quantencomputers, sogenannte Qubits, und führen damit zu *Dekohärenz*, also dem Verlust der enthaltenen Information. Darüber hinaus müssen Millionen von Qubits gekoppelt und individuell manipuliert werden können, wodurch die Herstellung von Qubits mit einheitlichen Charakteristiken notwendig ist.

Eine der prominentesten Ansätze zur Implementierung von Qubits, *Spin-Qubits*, nutzen die quantenmechanischen Eigenschaften von Elektronen- (oder Loch-) Spins und versprechen aufgrund der Nähe zur herkömmlichen Transistortechnologie Vorteile in Herstellung und Skalierbarkeit. *Spin-Qubits* bestehen aus einer halbleitenden Nanostruktur, in der ein Elektronen- (oder Loch-) Spin gefangen ist. Die Basiszustände dieses Spins spalten in einem äußeren Magnetfeld auf, wodurch auf natürliche Weise ein Qubit entsteht. Die Verwendung von Silizium (Si) als halbleitendes Material ist dabei ein besonders vielversprechender Ansatz, da eine der Hauptquellen für quantenmechanisches Rauschen, nämlich die unerwünschten Wechselwirkungen mit Kernspins, durch isotopische Aufbereitung stark vermindert werden kann.

Zwar wurden auf Basis dieser Technologie bereits funktionsfähige Quantenprozessoren demonstriert, doch gleichzeitig wird immer deutlicher, dass die strengen Anforderungen an Kohärenz und Einheitlichkeit extreme Kontrolle über die Materialstruktur, bis zur atomaren Ebene, erfordern. Um die Entwicklung von Si-*Spin-Qubits* weiter voranzutreiben, sind daher Simulationen unter Berücksichtigung der atomaren Struktur unerlässlich.

Im Rahmen dieser Dissertation wird die Dichtefunktionaltheorie (DFT) zur Untersuchung der materialbezogenen Eigenschaften von Si-*Spin-Qubits* eingesetzt, mit dem Ziel, die derzeitigen Modellierungstechniken zu verbessern sowie das Verständnis der verwendeten Materialien und ihrer Eigenschaften zu vertiefen. Im Gegensatz zu früheren Studien, die sich auf empirisch parametrisierte Modelle stützen, ermöglicht die Verwendung der im Wesentlichen parameterfreien DFT die Simulation einer realistischen Spin-Qubit-Umgebung, einschließlich Verspannung, atomarer Unordnung und elektrischer Felder auf Basis von Naturkonstanten.

Besonderes Augenmerk liegt auf der Verwendung von realistischen atomaren Modellstrukturen, die das Fundament unserer Berechnungen darstellen. Beide relevanten



Die approbierte gedruckte Originalversion dieser Dissertation ist an der TU Wien Bibliothek verfügbar.
The approved original version of this doctoral thesis is available in print at TU Wien Bibliothek.
TU WIEN Bibliothek Your knowledge hub

Typen von Si-*Spin-Qubits* werden berücksichtigt, nämlich Si in Kombination mit Silizium-Germanium (Si/SiGe) oder mit seinem nativen Oxid $SiO_2$ (Si/$SiO_2$). In Übereinstimmung mit experimentellen Aufbauten werden im Fall von Si/SiGe verschiedene epitaktisch gewachsene Interface- und Heterostrukturkonfigurationen untersucht. Für die Herstellung der Si/$SiO_2$ Strukturen wird *ab-initio* Molekulardynamik (AIMD) verwendet, um die thermische Oxidation einer Si-Oberfläche zu simulieren. Dieser neuartige Ansatz zur Erzeugung amorpher Si/$SiO_2$-Grenzflächen offenbarte mehrere zugrunde liegende Oxidationsmechanismen, die gemeinsam für den gesamten Prozess entscheidend sind. Experimentell beobachtet, aber bisher nicht zusammengeführt, werden diese Mechanismen in ein umfassendes Modell integriert. Angesichts der hohen Rechenkosten der *ab-initio* Methoden, wird ein *Machine Learning* (ML) Modell mit den zuvor erhaltenen AIMD-Daten trainiert, wodurch sowohl die Systemgröße als auch der Simulationszeitraum erheblich vergrößert werden kann.

Auf Grundlage dieser atomaren Strukturen werden eine Reihe von für Qubit-Anwendungen relevante Eigenschaften aus DFT extrahiert, einschließlich *Valley*- und *Spin-Splitting*, Hyperfeinwechselwirkungen und Dekohärenzzeiten. Die große Variabilität dieser Daten spiegelt experimentelle Beobachtungen wider und tritt aufgrund atomarer Unordnung an der Grenzfläche auf. Im Vergleich mit herkömmlichen Modellen werden Vor- und Nachteile der hier verwendeten *ab-initio* Methoden dargestellt. Schließlich werden Kernspins in den Materialbarrieren als bedeutende Störquelle identifiziert und heben die Relevanz von Hyperfeinwechselwirkungen mit Nicht-Si-Atomen hervor.

Die approbierte gedruckte Originalversion dieser Dissertation ist an der TU Wien Bibliothek verfügbar.
The approved original version of this doctoral thesis is available in print at TU Wien Bibliothek.
TU WIEN Bibliothek Your knowledge hub

# Acknowledgement

This thesis is the outcome of a fascinating four year long journey that would not have been possible without the broad support of many people. In the following, I give an incomplete list of people who traveled along, knowing that I can only fail to express what goes beyond words.

First and foremost, I want to thank my supervisor *Tibor Grasser*. As a group leader, he provided a working environment in which I could truly explore my interests and develop my research skills independently. His enthusiasm and candor for opening up new research directions have motivated me to go beyond what I would have thought is possible. On numerous occasions, I have benefited from his tireless efforts to promote collaborations around the world. Thank you, Tibor, for your kind support, your clever advices, and for everything I have learned from you in the past years.

Several research stays have been a crucial factor for my scientific progress. To begin with, I want to express my deepest gratitude to *Yann-Michel Niquet*, who welcomed me with remarkable openness to his group at CEA Grenoble in 2022 and 2023, a collaboration that has essentially determined the topic of this dissertation. Thank you, Yann-Michel, for continuously sharing your incredible knowledge with me, for showing me why one needs whiteboards, a hands-on astrophysics tutorial in the French Alps, and for co-supervising this thesis.

I was lucky enough to work with yet another scientific mastermind. A huge thank you goes to *Peter Stano*, with whom I have collaborated since my research stay in Tokio in 2023. Since then, working with him has been a true pleasure. Despite being separated by a time shift of a working day, Peter provided constant support and countless invaluable insights even after I left. He was a great help in tying up loose ends and developing new ideas. Besides his scientific advice, I especially thank Peter for his unmatched sense of humor and kindness.

Speaking of kind people, my colleague and friend *Christoph Wilhelmer* comes to mind. I cannot imagine the last four years without him. As an office mate, he was my first address for discussions of any sort. Together we did a great job in overcoming the numerous challenges that appear in the course of obtaining a PhD. Thank you, Christoph, for being next to me!

I want to thank *Guido Burkard*, for inspiring discussions, his openness toward my ideas and for numerous insights during a (too) short visit in his group in Konstanz. Specifically, I want to thank Guido for inconspicuous hints that strongly influenced the course of my PhD studies. It is an honor to have him on my examination committee.



Die approbierte gedruckte Originalversion dieser Dissertation ist an der TU Wien Bibliothek verfügbar.
The approved original version of this doctoral thesis is available in print at TU Wien Bibliothek.
TU WIEN Bibliothek Your knowledge hub

On that note, *des remerciements particuliers* go to *Romain Maurand* for assessing my thesis.

There are many other fellow students and postdocs that earned my gratitude. Starting my PhD at the onset of the pandemic, remote support from *Markus Jech* and *Dominic Waldhör* and *Al-Moatassem El-Sayed* helped me to get started with DFT and the computational infrastructure, a certainly not very interesting task that deserves a big thank you. Especially Dominic has always been a point of contact for all kinds of discussions. Other members of my group at TU Vienna were *Diego Milardovich* and *Franz Fehringer*, with whom I have collaborated on several occasions. I wish to thank everybody that was or is a part of the group. It was a pleasure to work with all of you!

In Grenoble, *Esteban Rodríguez-Mena, Boris Brun-Barriere, Prasoon Kumar, Simon Zihlmann, Leo Noirot, Estelle Vincent, Biel Martinez*, and many others made my stay an unforgettable experience. What an amazing group! In Japan, *Maria Spethmann, Kazuki Nakazawa*, and *Juan Rojas-Arias* provided a great working environment and made me feel welcome in their group. Thank you!

I would like to thank *Fabrice and Valerie Beaumont* for their heartwarming hospitality when sharing their apartment in Grenoble with me. We became close friends during these six months and I am extremely grateful for their support in any kind of situation. Thank you so much!

Obviously, my progress relied on a wide network of friends and family without which science is not fun. I would like to thank my parents for their unwavering support and encouragement throughout my life. My deepest thanks go to my friends *Aaron, Dorli, Elias, Felix, Johnny, Lea, Madn, Miri, Sandra, and Suki* for having my back. Finally, thank you, *Freya*, you have been an anchor providing constant support and I can only hope that you know how much that means to me.

Die approbierte gedruckte Originalversion dieser Dissertation ist an der TU Wien Bibliothek verfügbar.
The approved original version of this doctoral thesis is available in print at TU Wien Bibliothek.
TU WIEN Bibliothek Your knowledge hub

# Contents

**Abstract** i

**Kurzfassung** iii

**1 Introduction** 1
1.1 Qubits and Quantum circuits . . . 2
1.2 Decoherence . . . 4
1.3 Motivation and Research Goals . . . 7
1.4 Outline of the Thesis . . . 8

**2 Fundamentals** 11
2.1 Spin qubits in semiconductor quantum dots . . . 11
2.1.1 Quantum dots . . . 11
2.1.2 Materials for semiconductor spin qubits . . . 16
2.1.3 Barrier materials for qubits in silicon . . . 17
2.1.4 Quantum computing with quantum dots . . . 18
2.1.5 Double quantum dots . . . 19
2.2 Physics of Si spin qubits . . . 20
2.2.1 Conduction band valleys . . . 22
2.2.2 Strained Silicon . . . 23
2.2.3 Lifting the conduction band degeneracy . . . 23
2.2.4 Spin-orbit coupling (SOC) . . . 27
2.2.4.1 SOC in quantum dots . . . 29
2.2.4.2 Electric dipole spin resonance . . . 30
2.2.5 Interaction with nuclear spins . . . 31
2.2.5.1 Decoherence in the ergodic limit . . . 33

**3 Computational methods** 35
3.1 Density functional theory . . . 36
3.1.1 Hartree equations . . . 37
3.1.2 Hartree-Fock equations . . . 37
3.1.3 Mapping to the electron density . . . 38
3.1.4 Exchange-Correlation Functionals . . . 39
3.2 DFT setup . . . 40
3.3 Density functional based tight binding . . . 41



Die approbierte gedruckte Originalversion dieser Dissertation ist an der TU Wien Bibliothek verfügbar.
The approved original version of this doctoral thesis is available in print at TU Wien Bibliothek.
TU WIEN Bibliothek Your knowledge hub

3.4 Machine Learning . . . . . . . . . . . . . . . . . . . . . . . . . . . 42
3.4.1 Atomistic Structure Descriptors . . . . . . . . . . . . . . . . . 43
3.4.2 Gaussian Approximation Potential (GAP) Method . . . . . . 44

**4 Structure generation 47**
4.1 Si/SiGe . . . . . . . . . . . . . . . . . . . . . . . . . . . . . . . 48
4.2 $Si/SiO_2$ from first-principles . . . . . . . . . . . . . . . . . . . . . 49
4.2.1 Thermal Oxidation of Si . . . . . . . . . . . . . . . . . . . . 51
4.2.2 State-of-the-art models and experiments . . . . . . . . . . . . 52
4.2.3 Oxidation scheme . . . . . . . . . . . . . . . . . . . . . . . . 53
4.2.4 Initial $O_2$ adsorption and amorphization . . . . . . . . . . . . 55
4.2.5 Molecular precursors and surface saturation . . . . . . . . . . 58
4.2.6 Transition layer at the interface . . . . . . . . . . . . . . . . 62
4.2.7 Oxygen migration . . . . . . . . . . . . . . . . . . . . . . . . 62
4.2.7.1 Migration of adsorbed O atoms . . . . . . . . . . . . 63
4.2.7.2 $O_2$ diffusion through the oxide . . . . . . . . . . . . . 64
4.2.7.3 $O_2$ dissociation at the interface . . . . . . . . . . . . 66
4.2.8 Properties of the $Si/SiO_2$ interface structures . . . . . . . . . 66
4.3 Machine learning force field for the thermal oxidation of silicon . . . . 69
4.3.1 Tools and Methods . . . . . . . . . . . . . . . . . . . . . . . 69
4.3.1.1 Machine Learning Force Field . . . . . . . . . . . . . 69
4.3.1.2 DFT training data . . . . . . . . . . . . . . . . . . . 70
4.3.2 Comparison to DFT . . . . . . . . . . . . . . . . . . . . . . . 71
4.3.3 Structural properties . . . . . . . . . . . . . . . . . . . . . . 72
4.3.4 Growth kinetics . . . . . . . . . . . . . . . . . . . . . . . . . 72
4.3.5 Interface quality . . . . . . . . . . . . . . . . . . . . . . . . . 74
4.3.6 Comparison to classical force field . . . . . . . . . . . . . . . 75
4.3.7 Dangling bond density . . . . . . . . . . . . . . . . . . . . . 76

**5 Valley and spin splitting 79**
5.1 The 2DEG subbands and the valley splitting . . . . . . . . . . . . . . 79
5.1.1 Properties and interpretation of the DFT model . . . . . . . . 79
5.1.2 Comparison to 2-band tight binding model . . . . . . . . . . . 82
5.1.3 Comparison to $sp^3d^4s^*$ tight binding model . . . . . . . . . . . 84
5.1.4 Well designs and comparison to “$2k_0$-theory” . . . . . . . . . . 85
5.1.5 Valley-orbit coupling . . . . . . . . . . . . . . . . . . . . . . 88
5.2 Spin splitting . . . . . . . . . . . . . . . . . . . . . . . . . . . . . 89

**6 Coherence limit due to hyperfine interactions 93**
6.1 Introduction . . . . . . . . . . . . . . . . . . . . . . . . . . . . . 93
6.2 Methodology . . . . . . . . . . . . . . . . . . . . . . . . . . . . . 94
6.2.1 DFT setup . . . . . . . . . . . . . . . . . . . . . . . . . . . . 94
6.2.2 Atomic structure and supercell . . . . . . . . . . . . . . . . . 96
6.2.2.1 Si/SiGe . . . . . . . . . . . . . . . . . . . . . . . . . 97
6.2.2.2 Si-MOS . . . . . . . . . . . . . . . . . . . . . . . . . 97

Die approbierte gedruckte Originalversion dieser Dissertation ist an der TU Wien Bibliothek verfügbar.
The approved original version of this doctoral thesis is available in print at TU Wien Bibliothek.
TU WIEN Bibliothek Your knowledge hub

6.3 The lowest subband of a Si heterostructure 2DEG . . . . . . . . . . . 97
6.4 The magnitudes of the hyperfine couplings . . . . . . . . . . . . . . . 98
6.5 Rescaling the results for gated quantum dots . . . . . . . . . . . . . . 100
6.6 Scaling of the total hyperfine coupling with the dot area . . . . . . . 102
6.7 Discussion . . . . . . . . . . . . . . . . . . . . . . . . . . . . . . . . 105
6.8 Summary . . . . . . . . . . . . . . . . . . . . . . . . . . . . . . . . 108

**7 Conclusions and outlook** **109**
7.1 Future prospects . . . . . . . . . . . . . . . . . . . . . . . . . . . . 110

**Appendices** **112**

**A Machine learning parameters and training dataset** **113**
A.1 Descriptor parameters . . . . . . . . . . . . . . . . . . . . . . . . . . 113
A.2 Generation of the training dataset . . . . . . . . . . . . . . . . . . . 113

**B Electric field from first principles** **115**

**C Permittivity** **117**

**D Validation of the simulation cell setup** **121**
D.1 Convergence of median $E_{\mathrm{VS}}$ with supercell size . . . . . . . . . . . . 121
D.2 Spectra of wiggle wells . . . . . . . . . . . . . . . . . . . . . . . . . 121

**E Estimation of the diffusion coefficient for $^{17}$O atoms** **125**
E.1 Expression for the diffusion constant derived by the method of moments 126
E.2 Numerical values for the diffusion coefficient in various materials . . . 129
E.3 Autocorrelation time of the Overhauser field . . . . . . . . . . . . . . 129
E.4 Power spectral density . . . . . . . . . . . . . . . . . . . . . . . . . . 130

**Own publications** **133**

**Bibliography** **135**

**Curriculum Vitae** **159**

**List of publications and conference contributions** **161**

Die approbierte gedruckte Originalversion dieser Dissertation ist an der TU Wien Bibliothek verfügbar.
The approved original version of this doctoral thesis is available in print at TU Wien Bibliothek.
TU Bibliothek Your knowledge hub WIEN

Die approbierte gedruckte Originalversion dieser Dissertation ist an der TU Wien Bibliothek verfügbar.
The approved original version of this doctoral thesis is available in print at TU Wien Bibliothek.
TU Bibliothek Your knowledge hub WIEN

# Chapter 1

# Introduction

Quantum computation holds the promise of revolutionizing the field of computation as well as science and technology in general. Leveraging the fundamental principles of quantum mechanics, quantum computers offer exponential speed-up for certain computational tasks and even the ability to solve problems that are currently intractable for classical computers. The implications of using quantum mechanical systems for information processing include many mechanisms that have intrigued physicists since the advent of quantum mechanics, most famously quantum superposition and quantum entanglement. Essential contributions to quantum computation came also from other research areas: computer science, information theory, and cryptography. Therefore, quantum computation and quantum information is also an excellent playground for conducting basic research in these fields.

In contrast to a classical bit that can take exactly one of two states, 0 or 1, quantum information is stored in a quantum bit or qubit which is an combined state of both, 0 and 1. Many of these qubits are then arranged in an array so that they can interact and form entangled states. Processing the information that is stored in the qubits, requires control over the individual qubit states. Furthermore, the interactions between the qubits can be arbitrarily turned on and off, in order to run multi-qubit operations or to "isolate" a group of qubits that can then be addressed separately. The result of the computation is obtained upon execution of a quantum algorithm which means that operations on one or more qubits in the array are performed according to a step-by-step protocol.

Ideally, the states can be controlled coherently such that the quantum system can be steered from an initial state to a target state. In real-world systems, the qubit is not a closed system but interacts with its physical environment. As such, it evades the sought-for coherent control, leading to the loss of information in a process called quantum decoherence. From a technological point-of-view, removing these interactions seems extremely difficult, if possible at all, because the qubit is always embedded in some kind of material environment and the origin of the interactions is manifold. In addition, other effects such as faulty quantum gates, faulty state preparation, or faulty measurements come into play. To make matters worse, the exact properties of each individual qubit are often not precisely known. It is thus extremely challenging to realize a quantum computer with thousands or millions of



Die approbierte gedruckte Originalversion dieser Dissertation ist an der TU Wien Bibliothek verfügbar.
The approved original version of this doctoral thesis is available in print at TU Wien Bibliothek.
TU WIEN Bibliothek Your knowledge hub

qubits. These reasons call skeptics into action. “Quantum technologies are, almost by definition, the opposite of robust; they rely on subtle, volatile, transient physical effects. They intend to prevent a macroscopic object from behaving classically”, says Xavier Waintal, a quantum physicist at CEA Grenoble in 2023. And: “I am very skeptical that a quantum computer will ever solve serious problems.” While quantum computation is surely a great topic for scientific discourse, we shall not be discouraged by such (certainly valid) objections and delve right into the subject.

## 1.1 Qubits and Quantum circuits

Essentially, quantum computation utilizes the quantum nature of a given quantum object, that is the ability to describe its state as a superposition of eigenstates, and the possibility to couple several of these systems in order to create entangled states. Each of these objects contains a basic unit of quantum information. In the simplest case, the object exists in a superposition of exactly two states $|0\rangle$ and $|1\rangle$, and is thus described by

$$|\Psi\rangle = \alpha|0\rangle + \beta|1\rangle \tag{1.1}$$

Such a system is called a quantum bit or a *qubit* in analogy to the *bit* in classical computation. This qubit is simultaneously in both states $|0\rangle$ and $|1\rangle$ and if we were to measure the state of the qubit we get either the result 0 with probability $|\alpha|^2$ or 1 with probability $|\beta|^2$. The probabilities need to add up to one, so $|\alpha|^2 + |\beta|^2 = 1$. It is this condition that lets us rewrite Eq. 1.1 in the form

$$|\Psi\rangle = \mathrm{e}^{i\gamma}\Big(\cos\frac{\theta}{2}|0\rangle + \mathrm{e}^{i\phi}\sin\frac{\theta}{2}|1\rangle\Big), \tag{1.2}$$

where $\theta$, $\phi$ and $\gamma$ are real numbers. We can ignore the factor of $\mathrm{e}^{i\gamma}$ because it is a global phase which has no observable effects. Thus, we can write

$$|\Psi\rangle = \cos\frac{\theta}{2}|0\rangle + \mathrm{e}^{i\phi}\sin\frac{\theta}{2}|1\rangle. \tag{1.3}$$

The numbers $\theta$ and $\phi$ can be interpreted as coordinates on a spherical surface with radius 1 called the Bloch sphere, see Fig. 1.1. One mind-boggling consequence of quantum mechanics is that a collection of quantum objects that interact in a closed box will be in all physically realizable states at the same time. Taking a second qubit ($N{=}2$) into consideration, results in a quantum state that is a superposition of all $2^N$ states

$$|\Psi\rangle = \alpha_1|00\rangle + \alpha_2|10\rangle + \alpha_3|01\rangle + \alpha_4|11\rangle \tag{1.4}$$

Such a state is fully described by four variables[1]. The number of variables necessary to describe a quantum state that consists of 300 qubits is $2^{300} \approx 2\times10^{90}$ which is more than the number of atoms in the universe. Nature seems completely untroubled by this complexity which can be leveraged by storing and processing this huge amount of information in quantum computers.

[1] A representation similar to the Bloch sphere picture is not known for multiple qubits.

Die approbierte gedruckte Originalversion dieser Dissertation ist an der TU Wien Bibliothek verfügbar.
The approved original version of this doctoral thesis is available in print at TU Wien Bibliothek.
TU WIEN Bibliothek Your knowledge hub

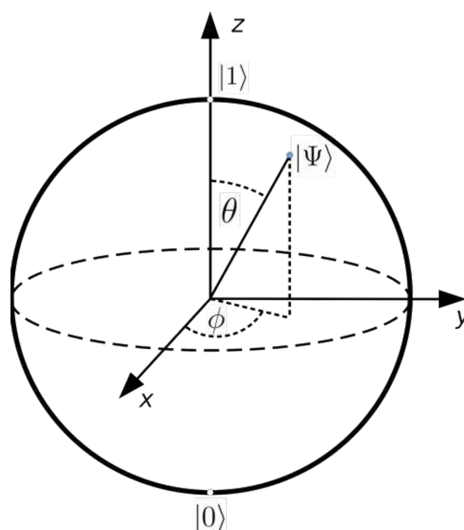


Figure 1.1: Bloch sphere representation of a qubit.

The second unique feature of quantum computation is the simultaneous calculation of all possible input states $|x\rangle$ which is termed quantum parallelism. Applying a function $f$ to $|x\rangle$, the input register with $N$ qubits in superposition, gives the output $f(|x\rangle)$, which is a superposition of all possible outcomes. The state contains all this information as long as it is not observed.

Although this insight paves the way towards a new computation paradigm, it has to be stressed that even though all of this information is present in the output register of the quantum circuit, it is not accessible to us. This is prohibited by a fundamental principle of quantum mechanics which states that the state of the system changes upon measurement. More accurately, it leads to the so-called collapse of the wavefunction, that is a projection to the outcome state, and annihilates the information that was stored in the state prior to the measurement.

An interesting question to ask at this point is: how much information can be represented by the qubit? The question addresses the properties of a superposition state. Let us recall the famous two-slit experiment. Nobody has ever observed a particle travelling through two slits at the same time, yet, the diffraction fringes that are a result of the superposition of the state can be clearly experimentally observed. So the information is somehow there, but also fundamentally not observable. The properties of a quantum mechanical state can even be manipulated in ways that change the measurement outcomes. In this sense, quantum mechanics shows that we have to be very careful when speaking about information. It might be a good idea to not call something information, if it cannot be measured, however, for the time being, it is common ground to accept that the state is a superposition but its composition can not be observed.

Quantum computers are designed to foster quantum superposition and quantum parallelism and execute quantum algorithms which are able to solve certain types of computational problems faster than any algorithm based on the classical concept of computation. A quantum algorithm is a series of qubit manipulations and terminates

Die approbierte gedruckte Originalversion dieser Dissertation ist an der TU Wien Bibliothek verfügbar.
The approved original version of this doctoral thesis is available in print at TU Wien Bibliothek.
TU WIEN Bibliothek Your knowledge hub

with the measurement. Until today, only few quantum algorithms are known that have an advantage over classical algorithms. Most famous are the Shor algorithm that can be used to break classical encryption and Grover's algorithm which establishes a speedup for the widely applicable unstructured search problem. A detailed description of these algorithms is not relevant for the scope of this thesis. However, we shall shortly introduce a basic operation that can act on a single qubit in order to illustrate the functioning of a quantum computation.

Take the quantum NOT gate for example. Analogously to the classical NOT gate, it changes the state from $|0\rangle$ to $|1\rangle$ and vice versa. If the state is a superposition, it exchanges the coefficients. That is, if the quantum NOT gate is applied to $|\Psi\rangle$ from Eq. 1.1, we get

$$|\Psi\rangle = \beta|0\rangle + \alpha|1\rangle. \tag{1.5}$$

Such an operation is achieved with the linear operator $X$, with the matrix representation

$$X = \begin{pmatrix} 0 & 1 \\ 1 & 0 \end{pmatrix} \tag{1.6}$$

This matrix is unitary, so it preserves the normalization condition. Correspondingly, all valid quantum operations are of this form – and this unitarity constraint is in fact the only constraint that is put on quantum gates. Furthermore, it turns out that these operations can be decomposed in a product of rotations

$$\begin{pmatrix} \cos(\theta/2) & -\sin(\theta/2) \\ \sin(\theta/2) & \cos(\theta/2) \end{pmatrix} \tag{1.7}$$

and rotations about the $z$-axis

$$\begin{pmatrix} e^{-i\phi/2} & 0 \\ 0 & e^{-i\phi/2} \end{pmatrix}. \tag{1.8}$$

Deeper insights into such composition have been gained in the 1980s and 1990s. Specifically, it was shown that a universal quantum computer can be realized using only single qubit rotations (so-called single-qubit gates) and one type of two-qubit gate, the controlled-NOT or CNOT gate [1]. Two-qubit gates have two input qubits, the control qubit and the target qubit. The CNOT gate flips the target qubit if and only if the first qubit (the control qubit) is $|1\rangle$. It can also be used to entangle or disentangle Bell states. The circuit representation for the CNOT gate is shown in Fig. 1.2. The development of reliable CNOT gates is extremely important for the implementation of quantum logic, since any arbitrary quantum circuit can be decomposed in a combination of single-qubit gates and CNOT gates [2]. In this sense, the CNOT gate is the quantum analog to the classical NAND gate.

## 1.2 Decoherence

Despite the above mentioned concerns that quantum noise and decoherence renders quantum computation unfeasible, the processing of quantum information is a groundbreaking idea which will be further pursued by humankind. One approach that might

TU Bibliothek Your knowledge hub WIEN
Die approbierte gedruckte Originalversion dieser Dissertation ist an der TU Wien Bibliothek verfügbar.
The approved original version of this doctoral thesis is available in print at TU Wien Bibliothek.

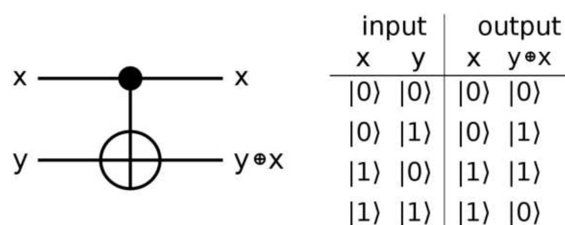


Figure 1.2: Quantum-mechanical version of the CNOT gate.

allow us to circumvent errors without the complete removal of noise is borrowed from classical computation: a certain degree of inaccuracy is accepted and the resulting errors are corrected in a post-processing step. The idea is to reserve some qubits in order to encode the state of the target qubits by adding some redundant information. Based on this redundancy, the true result can be recovered after the determination of the quantum algorithm in the noisy environment. The successful implementation of such error correction codes has been reported in recent years, causing excitement in both the scientific community and the general public. Although the invention of quantum error correction protocols was certainly a big step towards fault-tolerant quantum computing, uniform and noise-resistant qubits are still essential requirements for reliable quantum computation as these protocols can only correct small errors and typically require a state fidelity well above 99%, depending on the type of protocol and proportion of redundant qubits. It has been stated that state-of-the-art error-correction techniques require more than 1,000 physical qubits for each logical qubit [3]. In this scenario, a useful quantum processor needs millions of physical qubits.

In the last decades, several proposals for the physical implementation of qubits have been put forward. Among the most promising platforms are superconducting qubits [4], trapped ions [5], atoms [6], and photons [7]. Currently, the largest quantum computers are based on nuclear spin qubits formed from arrays of optically-trapped neutral atoms (*Atom Computing* were the first to report a 1000 qubit processor) as well as superconducting qubits (*IBM* unveiled a quantum computer with 1121 qubits in late 2023 [3]). However, these approaches require enormous infrastructure which makes up-scaling to useful sizes very difficult. Fortunately, there is another very promising approach for the implementation of quantum computation in a solid-state system, namely spin qubits in semiconductors [8], which will be the focus of this thesis. In semiconductors, the conduction band can be arbitrarily depleted, such that even single electrons can be trapped in a nanostructure. The electron spin can then be used as a qubit, as it provides a natural basis for such a system: There are two basis states (e.g. spin up and down) and the spin can be prepared and controlled via external electric or magnetic fields [9, 10]. This approach is particularly attractive because such quantum devices are very similar to conventional transistors. Therefore, materials and processes can be directly taken over from conventional semiconductor device technology, a platform that has already proven its outstanding scalability.

Within the spectrum of relevant semiconducting materials, silicon is a remarkable candidate because hyperfine interactions between the electron spin and the nuclear

Die approbierte gedruckte Originalversion dieser Dissertation ist an der TU Wien Bibliothek verfügbar.
The approved original version of this doctoral thesis is available in print at TU Wien Bibliothek.
TU Bibliothek WIEN Your knowledge hub

spins can be inhibited by removal of the spin isotopes[2]. This process improves the coherence by several orders of magnitude. A similar procedure is not possible in some other related materials, such as the prototypical semiconductor GaAs, where every stable isotope carries a nuclear spin.

Interactions with nuclear spins are not the only reason for decoherence in semiconductor spin qubits. Decoherence can be induced by various physical mechanisms such as (a) fluctuating defects, spins or electric dipoles in the environment, (b) atomistic disorder leading to non-uniform qubit parameters, and (c) cross-talk with other qubits or states outside the considered two-level qubit system. Some of these issues are addressed within this work.

What do we mean when speaking about decoherence? Quantum decoherence is the decay of a state $|\Psi\rangle$ in time which corresponds to a motion along the Bloch sphere, as depicted in Fig. 1.1 decays in time. One can already anticipate the challenges that this implies, when recalling that a quantum gate is just a rotation around the Bloch sphere. The problem is that the state is distrubed by random processes, therefore, we do not exactly know how the state changes. After some time, the state $|\Psi\rangle$ is effectively lost. There are two mechanisms involved: relaxation and dephasing.

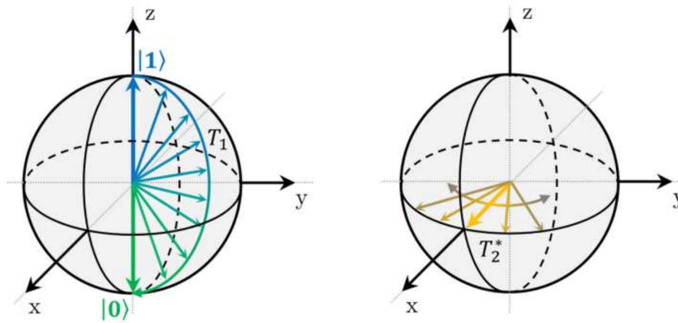


Figure 1.3: Relaxation (left) and dephasing (right) in the Bloch sphere representation. Figure taken from [11].

Relaxation describes the natural decay from an excited state to the ground state, i.e. if we define $|1\rangle$ as the excited state, a decay from $|1\rangle$ to $|0\rangle$. The convention is to call the timescale for this process $T_1$. Dephasing is explained by looking at the time evolution of a spin in an external magnetic field. The spin precesses around the axis of the magnetic field with a frequency proportional to the energy difference between $|0\rangle$ and $|1\rangle$. If this energy difference changes in time due to fluctuations in the environment, then the state precesses with a different frequency and reproducible quantum operations are not possible. The timescale for this process is $T_2^*$. Typically, dephasing is a much bigger issue than relaxation. In Si spin qubits, experimental studies report values for $T_1$ in the range of seconds [12, 13] while $T_2^*$ reaches only a few tens of µs [14, 15, 16].

[2]In other material systems like GaAs (every isotope carries a nuclear spin), hyperfine interactions lead to short coherence times in the range of ns

Die approbierte gedruckte Originalversion dieser Dissertation ist an der TU Wien Bibliothek verfügbar.
The approved original version of this doctoral thesis is available in print at TU Wien Bibliothek.
TU WIEN Bibliothek Your knowledge hub

## 1.3 Motivation and Research Goals

The theoretical foundations for quantum computing have been established in the 1960s and refined in the decades thereafter. Despite extensive research activities with encouraging demonstrations of quantum supremacy [17] and operation with fidelities above the threshold for error correction [18], a large-scale quantum computer has still not been realized. The reasons for that can be summarized in one term, quantum decoherence, that is the loss of quantum information due to interactions with the environment. Nevertheless, there is a lot of progress in understanding the various decoherence phenomena alongside with improvement of fabrication techniques and qubit control. In this respect, spin qubits in semiconducting nanostructures are clearly favored because such structures are miniaturized by default and offer excellent prospects in terms of scalability. With dimensions comparable to those of a modern transistor, they are up to 1 million times smaller than other types of qubits, measuring approximately $50\times50\,\mathrm{nm}^2$. The diminutive size combined with highly optimized fabrication methods hold the promise for efficient scaling. Although other qubit platforms are currently ahead when it comes to the number of qubits on a chip (QuTech in Delft holds the record with 16 qubits [19], Intel' newest chip *Tunnel Falls* has 12), semiconductors are arguably the platform with the greatest potential to deliver scaled-up quantum computing.

This thesis embarks on a journey to investigate various decoherence mechanisms in Si nanostructures from a theoretical perspective. The main goal of this work is to establish an *ab-initio* based modeling approach for semiconductor heterostructures as used in semiconductor spin qubits. A number of atomistic modeling techniques are employed to obtain properties of electronic states at the conduction band minimum and their interactions with the environment, which is modeled as realistically as possible. The backbone of the calculations are realistic interface structures, and the generation of those is the first milestone in this thesis. Subsequently, the electronic properties of the interface structures are calculated within the most sophisticated of the employed techniques, density functional theory (DFT), a highly successful *ab-initio* approach. The use of DFT in the context of spin qubits is a novelty, as the computational costs of the very demanding *ab-initio* calculations put strong restrictions on the system size. Since the simulation of full devices lies completely out of reach, we restrict ourselves to heterostructures which are periodically repeated in the lateral directions. The conduction-band electron forms a two-dimensional electron gas (2DEG) confined to a material interface by an external electric field. Correspondingly, in-plane confinement is not considered. This approximation is justified by the dimensions of a Si quantum dot which is far more delocalized in the direction of the interface plane than in the perpendicular direction. From the spin-resolved DFT calculation, we obtain a detailed picture of the electronic structure by intrinsically including interfacial effects like atomistic disorder. Furthermore, strain and electric fields can be considered within DFT. In this context, an important feature of DFT is the operation without the use of empirically fitted parameter sets as known

Die approbierte gedruckte Originalversion dieser Dissertation ist an der TU Wien Bibliothek verfügbar.
The approved original version of this doctoral thesis is available in print at TU Wien Bibliothek.
TU WIEN Bibliothek Your knowledge hub

from e.g. tight binding (TB)[3]. TB is a widely employed atomistic modeling technique that, together with crystalline or idealized interfaces, has been previously used for spin qubit modeling. The hereby presented DFT approach in combination with the realistic interfaces goes beyond these previously utilized models.

Although the computational costs of DFT do not allow to simulate mesoscopic devices, it serves as a versatile tool to deduct various properties of the 2DEG, like band composition or coherence time. From the splitting of the various (spin) subbands, important properties for reliable qubit operation such as the valley splitting (splitting of otherwise degenerate valley states due to coupling at the interface, see Sec. 2.2.3) and spin splitting (caused by spin-orbit interactions, see Sec. 5.2) can be obtained. DFT is also often used for the analysis of defects. These capabilities can be applied to investigate the impact of localized charge states on the trapped electron. Additionally, the wavefunctions can be calculated under consideration of all electrons (core + valence) so that the spin density at the nuclei can be obtained. This becomes important for determining hyperfine tensors, that are channels for magnetic noise. Because the calculations are conceptually focused on properties of the employed materials, a broader application of the modeling work is possible, for instance in nanoelectronics or spintronics. In the last decades, most of the modeling for spin qubits has been based on effective-mass (EM) or tight-binding approaches. These methods have proven their efficiency and will certainly not be replaced by DFT, but they also have their weaknesses. A further motivation to conduct this DFT study is therefore to provide benchmark values that could be used to improve the assumptions and parameter sets on which EM and TB are based on.

## 1.4 Outline of the Thesis

This thesis explores the abilities of *ab-initio* modeling methods in the context of Si spin qubits. In a summarized manner, the outcomes of this work have been published previously [LC1, LC2, LC3, LC4, LC5], while the thesis contains much more background knowledge and additional data that have been omitted in the publications for the sake of conciseness. The thesis is organized as follows.

**Chapter 2** introduces the reader to the fundamentals of semiconductor spin qubits and to Si spin qubits in particular. It starts with an introduction to quantum dots and shows how they are implemented in various material systems. In a next step, we bridge the gap between material properties and quantum information processing by showing how quantum dots can be employed for quantum computing. Finally, the physical mechanisms and current challenges directly linked to spin qubits in Si are discussed.

[3]Within tight binding, a Hamiltonian is constructed based on parameters which are obtained by fitting to a known material property, typically the band structure. This makes the calculations relatively cheap and even systems with millions of atoms are feasible. However, in some cases these parameters can be nonphysical and external influences like strain and electric fields are often not considered in the fit.

Die approbierte gedruckte Originalversion dieser Dissertation ist an der TU Wien Bibliothek verfügbar.
The approved original version of this doctoral thesis is available in print at TU Wien Bibliothek.
TU WIEN Bibliothek Your knowledge hub

**Chapter 3** outlines concepts of the utilized numerical methods and gives a detailed description of the computational setup that was employed within this work. It gives a rough overview of the theory behind DFT, a short introduction to the closely related density functional based tight binding (DFTB) method, and an outline of the employed machine learning techniques.

**Chapter 4** focuses on the generation of the interface structures. A large part of this chapter is devoted to the generation of amorphous $Si/SiO_2$ interfaces which was facilitated by both *ab-initio* molecular dynamics (AIMD) simulations and by means of a machine learning force field. The properties of this model are carefully investigated and compared to experiments.

**Chapter 5** shows DFT results for the valley splitting and a comparison with tight binding and effective mass approaches. We then investigate spin-orbit coupling effects at the interface and resulting splittings between the individual spin levels.

In **Chapter 6**, we determine hyperfine tensors in order to estimate decoherence due to interactions with nuclear spins. We show that atoms in the barrier layers are a significant source of hyperfine noise limiting the spin coherence time in isotopically purified Si.

Finally, **Chapter 7** concludes the findings of this work and gives ideas for future research directions.

Die approbierte gedruckte Originalversion dieser Dissertation ist an der TU Wien Bibliothek verfügbar.
The approved original version of this doctoral thesis is available in print at TU Wien Bibliothek.
TU WIEN Bibliothek Your knowledge hub

Die approbierte gedruckte Originalversion dieser Dissertation ist an der TU Wien Bibliothek verfügbar.
The approved original version of this doctoral thesis is available in print at TU Wien Bibliothek.

# Chapter 2

# Fundamentals

This chapter provides a summary of the theoretical foundation quantum information processing in semiconductor quantum dots and points out advantages and disadvantages of employing Si as a host material for such applications. The theoretical insights are garnished with some of the most important experimental findings. We start with a general introduction to quantum dots, and review typically employed material systems. Next, we review the current state-of-the-art of spin qubits. This section includes a comparison of employed material systems, approaches to read-out and manipulate spin states in semiconductors, and a description of the theoretical and experimental realization of two-qubit logic. Finally, we discuss the physics of silicon spin qubits with a focus on valley splitting, spin-orbit coupling and hyperfine interactions, since these topics are specifically addressed within this thesis.

## 2.1 Spin qubits in semiconductor quantum dots

Since Loss and DiVincenzo proposed the use of quantum dots for quantum computation in 1998 [8], Si has become a serious contender for hosting quantum devices. The idea is to trap a single electron or hole in a semiconducting nanostructure. Upon application of an external magnetic field, the two spin states “up” and “down” split and can be utilized as qubit basis states. An outline of the Loss/DiVincenzo approach is given in the following.

### 2.1.1 Quantum dots

Quantum dots are material structures in which the charge carriers are confined within a few nanometers in all three spatial directions. The confinement is strong enough to give rise to discrete energy levels, similar to a quantum particle in a box or electrons in single atoms, see Fig. 2.1. Hence, quantum dots are also often referred to as artificial atoms. The reason why quantum dots have recently attracted a lot of attention in nanotechnology and material science is that the optical and electronic properties of such an artificial atom can be tuned by changing the size, shape or electron occupation of the nanostructure. In 2023, Alexei Ekimov, Louis Brus and Moungi Bawendi were



Die approbierte gedruckte Originalversion dieser Dissertation ist an der TU Wien Bibliothek verfügbar.
The approved original version of this doctoral thesis is available in print at TU Wien Bibliothek.
TU WIEN Bibliothek Your knowledge hub

awarded the Nobel prize for chemistry for the discovery and synthesis of quantum dots. Due to their versatile properties, quantum dots are used as photon sources for scientific applications (ranging from biology to all-optical computational systems) and even found commercial application in solar cells, TV screens and other illumination sources. However, and most importantly for the topic of this thesis, quantum dots in semiconductors offer control over the number of electrons in the conduction band (or holes in the valence band) at ultra-low temperatures in order to trap and manipulate single electrons or holes in the dot. The spin of the respective charge carrier is then used as a qubit system [9, 10]. Split by an external magnetic field, the spin levels (Zeeman-split states referred to "up" and "down" or equivalently $|1\rangle$ and $|0\rangle$) naturally define a qubit.[4]

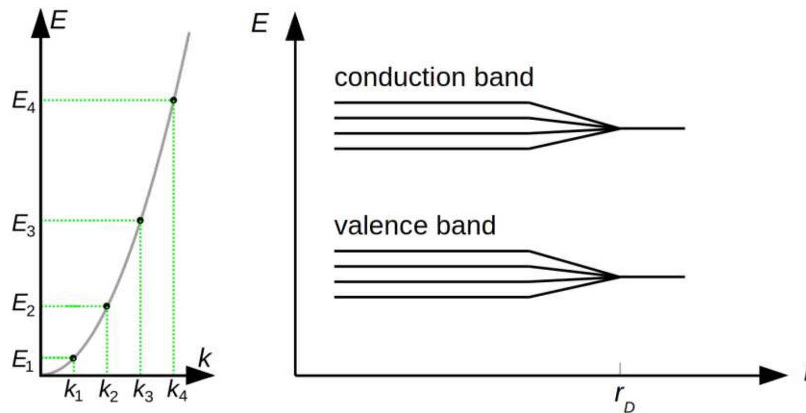


Figure 2.1: A particle in a box (black circles) shows the same dispersion relation as a free particle (gray line). However, the confined particle may only have discrete energy levels. Similarly, in a quantum dot, the valence and conduction band split into discrete energy levels due to the confinement. This splitting becomes significant as the size of a quantum dot (described by variable $r$) becomes smaller than a certain threshold value.

Various types of quantum dots can be fabricated, e.g. in AlGaAs/GaAs [22], Si/SiGe [23], or in Si-metal-oxide-semiconductor (Si-MOS) setups, that is Si in combination with its native oxide $SiO_2$ [24, 25]. Typically, such devices are based on semiconductor heterostructures that are grown either by chemical vapor deposition (CVD) or by molecular beam epitaxy (MBE). To create a quantum dot out of these planar heterostructures, an additional confinement is introduced in the remaining two dimensions. Here, one can distinguish between self-assembled quantum dots, where a random semiconductor growth process provides the two-dimensional confinement, and electrostatically defined quantum dots, where lithographically fabricated metallic gates create the confinement, see Fig. 2.2. As can be seen, the top gates P1 and P2 (called plunger gates) are used to create the confining potential in plane. Moreover, the gate potential is used to load/unload the quantum dot, that is capturing/emit-

[4]There are also other types of spin qubits. For instance, one can trap two electrons and use the singlet and triplet state as the qubit basis states [20, 21].

Die approbierte gedruckte Originalversion dieser Dissertation ist an der TU Wien Bibliothek verfügbar.
The approved original version of this doctoral thesis is available in print at TU Wien Bibliothek.
TU WIEN Bibliothek Your knowledge hub

ting of a charge carrier. At low temperatures < 1 K, the conduction band can be completely depleted. If the potential well that arises from the gate is deep enough, single particles can either "fall" into the well from adjacent materials or get injected by an external current.

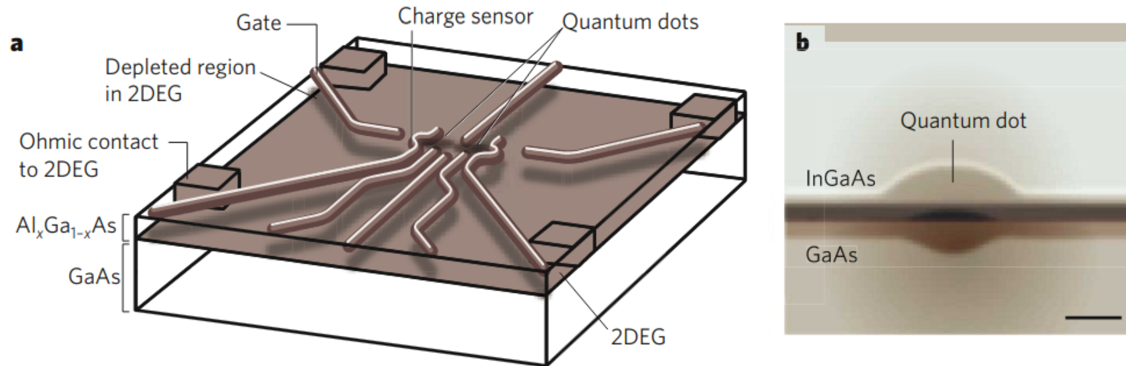


Figure 2.2: Gate setup on top of a planar GaAs/AlGaAs heterostructure to form a electrostatically defined quantum dot. The gates confine the particle in the planar direction. Taken from [26].

Electrostatically confined quantum dots have a number of advantages over self-assembled dots [27]. First, the growth of well-defined heterostructures gives better uniformity than a randomized growth process. Second, the confinement of the dots, as well as loading and measuring of electrons in the dot can be controlled via the gates which allows for convenient operation. Third, the gates also allow to manipulate the state of the trapped particle coherently by application of AC fields that drive oscillations between the ground and excited states mediated via spin-orbit coupling. As a result, $\alpha$ and $\beta$ of Eq. (1.1) depend on the duration of the external driving field. The state of a qubit can be manipulated using this effect. This feature is called electric dipole spin resonance (EDSR, see Sec. 2.2.4.2) and becomes essential when building larger arrays of dots that have to be controlled individually. State transitions in self-assembled quantum dots on the other hand are usually driven optically which makes individual control of thousands of qubits extremly difficult. All these reasons combined led to the use of gate-confined dots for modern qubit applications.

A quantum dot can also contain multiple charge carriers. Such a state is created by further increasing the voltage of the plunger gate. When the voltage of the plunger gate is swept, periodic peaks in the conductance of a quantum dot appear. These peaks occur when a discrete energy level of the quantum dot aligns with the Fermi energy of the charge reservoir. At the conductance peak, the dot is equally stable in both charge states and thus occupied half of the time. When the plunger gate shifts the energy levels of the dots further down/up, the quantum dot captures/emits a charge. The conductance reaches a minimum if the Fermi energy of the reservoir falls exactly halfway between the quantum dot energy levels. In order to determine the charge state of the quantum dot, a quantum point-contact (QPC), a narrow, ballistic constriction, can be placed close to the QD [28]. The conductance of such a device is

Die approbierte gedruckte Originalversion dieser Dissertation ist an der TU Wien Bibliothek verfügbar.
The approved original version of this doctoral thesis is available in print at TU Wien Bibliothek.
TU WIEN Bibliothek Your knowledge hub

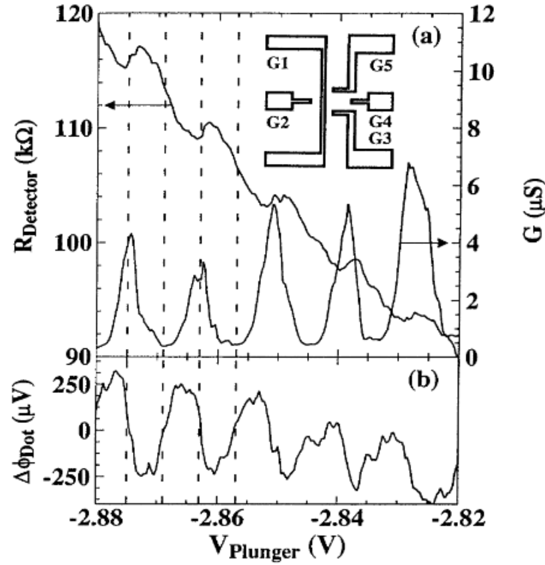


Figure 2.3: Charge sensing via a quantum point contact (QPC) taken from [28]. The gate setup depicted as an inset is deposited on a GaAs/AlGaAs heterostructure. The gates are labelled G1 to G5. The QPC is established between G1 and G2, the quantum dot is on the right, where G4 acts as a plunger gate. The resistance in the charge sensor modulates periodically above a rising background. The oscillations correlate directly with the Coulomb peaks in the conductivity of the dot. The measured detector resisitivity can be used to measure the occupation number in the dot.

very sensitive to changes in the electrostatic potential. Different charge occupation states of the QD can thus be directly distinguished by measuring the current through the QPC.

The techniques outlined above allow the measurement of the occupation of a quantum dot. This principle was further evolved in order to measure also the spin of the charge carrier by a electrical single-shot readout [29]. Assuming the spin-up state is the excited state, corresponding to the energies $E_{\mathrm{up}} > E_{\mathrm{down}}$. Now, the idea is to align two Zeeman split spin states of a trapped particle in such a way with the reservoir that the spin-up state lies above and the spin-down state below its Fermi level, see Fig. 2.4. If the charge state of the dot changes within a certain time window $\tau$ (the inverse of the tunnel rate between dot and reservoir), it is evident that the charge carrier was in the up state. The energy of a spin-down electron would have been too low in order to leave the dot and tunnel back to the reservoir.

The occupation of a quantum dot can be measured by the read-out procedure described above. This measurement protocol is often referred to as Elzermann readout. Let us now consider transport through the quantum dot, as sketched in Fig. 2.5. The depicted setup constitutes a single-electron transistor (SET). Electrical current can only flow if the quantum dot has an available level in the bias window between source and gate. The levels of the quantum dot are spaced by $\Delta E_{\mathrm{QD}} = E_{\mathrm{C}} + \Delta E$, where $\Delta E$ is the spacing due to the quantum confinement and $E_{\mathrm{C}} = \mathrm{e}^2/2C$ is the charging

Die approbierte gedruckte Originalversion dieser Dissertation ist an der TU Wien Bibliothek verfügbar.
The approved original version of this doctoral thesis is available in print at TU Wien Bibliothek.
TU WIEN Bibliothek Your knowledge hub

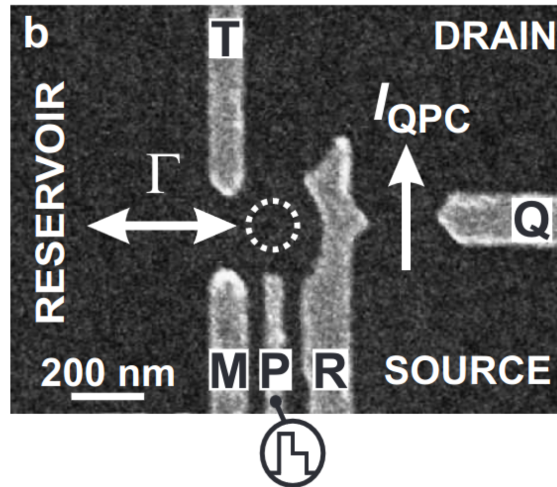


Figure 2.4: SEM image of a device used for single-shot spin read-out. By measuring the current through the QPC channel (denoted in the figure as $I_{QPC}$), the change in the charge of the quantum dot that results from tunneling of charge carriers between reservoir and quantum dot can be recorded. A spin state can then be associated to the dot by the outcome of the single-shot current measurement. Figure taken from [29].

energy needed to add the unit charge e to a system with capacity $C$. The ladder of states in the dot can be shifted by means of an external gate. Whenever a free state in the dot alignes with the electrochemical potential of source and drain, current can flow. Since the quantum dot states are equally spaced in energy, a periodic signal in the conductance of the channel from source to drain $\mathrm{d}I/\mathrm{d}V_{\mathrm{SD}}$ can be observed. These are the so-called Coulomb peaks. With no available states, there is no current flow-

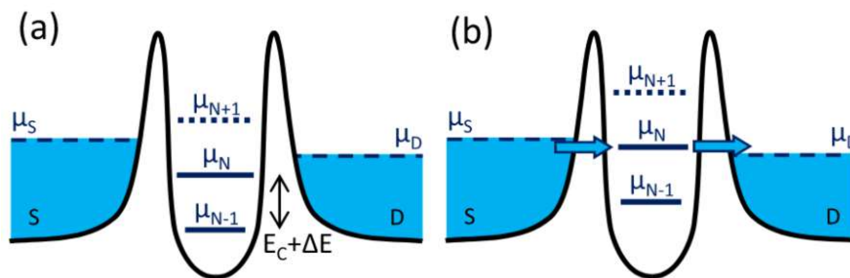


Figure 2.5: Electrochemical potential of a single-electron transistor consisting of a quantum dot coupled on both sides to charge reservoirs (source and drain) (a) with no states available for charge transport (Coulomb blockade) and (b) with transport enabled by a state that is aligned between the electrochemical potentials of source and drain. In (b), the number of electrons in the dot alternates between N and N-1 and thus generates a single-electron tunneling current. Taken from [9].

ing. Mapping the conductance of the channel from source to drain $\mathrm{d}I/\mathrm{d}V_{\mathrm{SD}}$ reveals a periodic pattern (diamond pattern) that allows to determine the occupation of the dot for the respective gate voltages, see Fig. 2.6.

Die approbierte gedruckte Originalversion dieser Dissertation ist an der TU Wien Bibliothek verfügbar.
The approved original version of this doctoral thesis is available in print at TU Wien Bibliothek.
TU WIEN Bibliothek Your knowledge hub

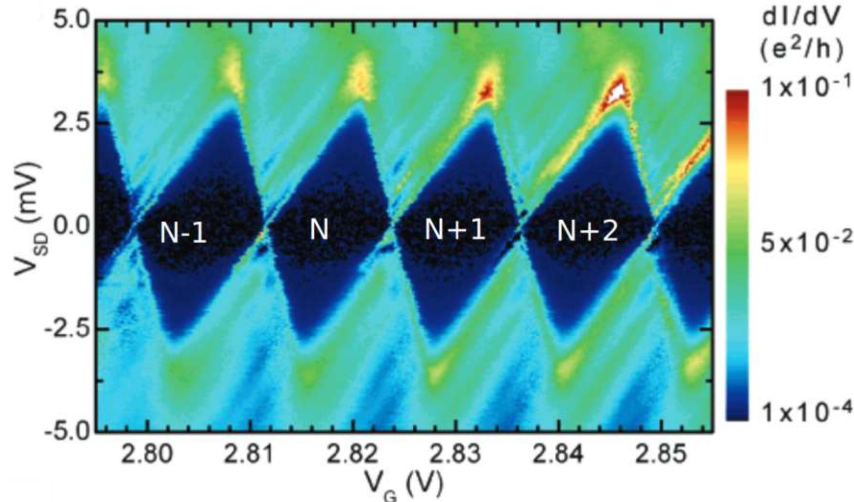


Figure 2.6: Diamond pattern observed in the conductance as a function of voltage between source and drain ($V_{\mathrm{SD}}$) and plunger gate ($V_{\mathrm{G}}$) through a single-electron transistor. The occupation number is constant in each dark diamonds, while the edges of the diamonds mark the Coulomb peaks. Figure adapted from [30].

### 2.1.2 Materials for semiconductor spin qubits

The performance of solid-state qubit platforms critically depends on the quality of the host material. Disorder and other material properties ultimately impact important qubit metrics such as coherence time and operation speed. Currently fabricated qubit devices suffer from significant decoherence caused by a variety of material imperfections including point defects, grain boundaries, and interfacial disorder [31] leading to strong variabilities between individual devices [32, 11] [LC3]. Having the QD implemented in a solid-state material means that the spin is surrounded by noise sources. If the environment contains nuclear spins, magnetic noise due to hyperfine interactions between the central spin and the nuclear spins leads to quick decoherence [33]. Similar to the improvement of classical transistor technology that is driving modern computation until today, solving the challenges imposed by the host material might be key for reliable quantum computation.

Until today, two-qubit logic has been demonstrated in three host materials: GaAs, Si, and Ge, see Fig. 2.7. Despite early achievements such as spin injection, control and read-out accomplished in GaAs-based devices, it has soon been realized that hyperfine interactions in this material system impose strong restrictions on the coherence time of such devices [34, 35]. Based on this insight, silicon has moved to the center of attention, because it offers the possibility of removing the isotope $^{29}$Si, being the only isotope carrying nuclear spin with about 5% natural abundance. Other reasons are high availability, low charge-noise susceptibility and well known fabrication techniques. These are all good arguments for using electron spins in Si, although

Die approbierte gedruckte Originalversion dieser Dissertation ist an der TU Wien Bibliothek verfügbar.
The approved original version of this doctoral thesis is available in print at TU Wien Bibliothek.
TU WIEN Bibliothek Your knowledge hub

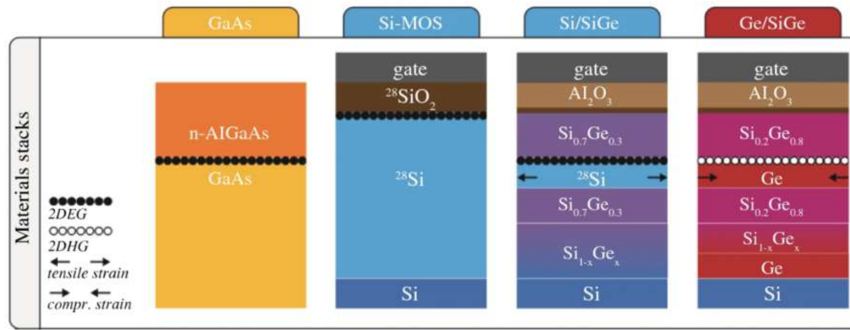


Figure 2.7: Overview of material stacks that have demonstrated two-qubit logic until today. Figure taken from [31].

there are a few drawbacks. Among those is the intrinsically low spin-orbit coupling[5]of conduction-band electrons in silicon which leads to slow spin operations when using EDSR to manipulate the electron spin state, as shown in Sec. 2.2.4.2. There are novel approaches to overcome this problem, namely the use of hole spins in Si [36] or Ge [37] which are new candidates showing strong potential [38]. A hole qubit can be manipulated faster due to the strong spin-orbit interaction, but is also more prone to charge noise, a problem that could be addressed by properly chosen structural geometries and magnetic field orientations [39, 40]. However, it is still an open question which material system is best suited to host spin qubit devices. Currently, research activities examine all possible directions.

### 2.1.3 Barrier materials for qubits in silicon

Within the realm of Si qubits, there are two materials that can be combined with Si to realize the confinement, both naturally coming with distinct advantages and disadvantages. One approach is to interface Si with SiGe (the Ge content is typically between 25 and 30%), the second is adapted from the Si metal-oxide-semiconductor (Si-MOS) technology and combines Si with its native oxide $SiO_2$.

Before going into more details, let us discuss the requirements that we put on a suitable arrangement of materials. First, the conduction band of the barrier material needs a positive band offset with respect to the Si conduction band edge to ensure confinement. Larger band offsets yield large valley splittings and are therefore favored. Second, the resulting interface should be uniform. Any source of disorder should be minimized in order to reduce variabilities of the qubit device parameters. Third, low defect densities are desired because defects can act as fluctuating charges or dipoles and thus generate charge noise. Furthermore, as will be shown in this thesis, also the barrier should be free from isotopes with nuclear spin as these nuclei impose a limit on the coherence of the electron spin.

We can now discuss the advantages and disadvantages of both barrier materials. As depicted in Fig. 2.8, the Si/SiGe interface is pseudomorphic, that is, the atoms

[5]The intrinsically low spin-orbit coupling is also an advantage because it reduces the influence of charge noise.

Die approbierte gedruckte Originalversion dieser Dissertation ist an der TU Wien Bibliothek verfügbar.
The approved original version of this doctoral thesis is available in print at TU Wien Bibliothek.
TU WIEN Bibliothek Your knowledge hub

are arranged on the same lattice. In comparison to the Si/$SiO_2$ interface, the degree of disorder in Si/SiGe is in principle much lower and mobilities are rather high ($\approx 10^5\,cm^2/Vs$ vs. $\approx 10^4\,cm^2/Vs$) [41]. On the other hand, the Si/oxide interface has a band offset that is one order of magnitude larger than the Si/SiGe interface. Due to the large band offset, the valley splitting (cf. 2.2.3) in Si-MOS is large enough to provide a clean two-state spin system, making operation at 1 K feasible.

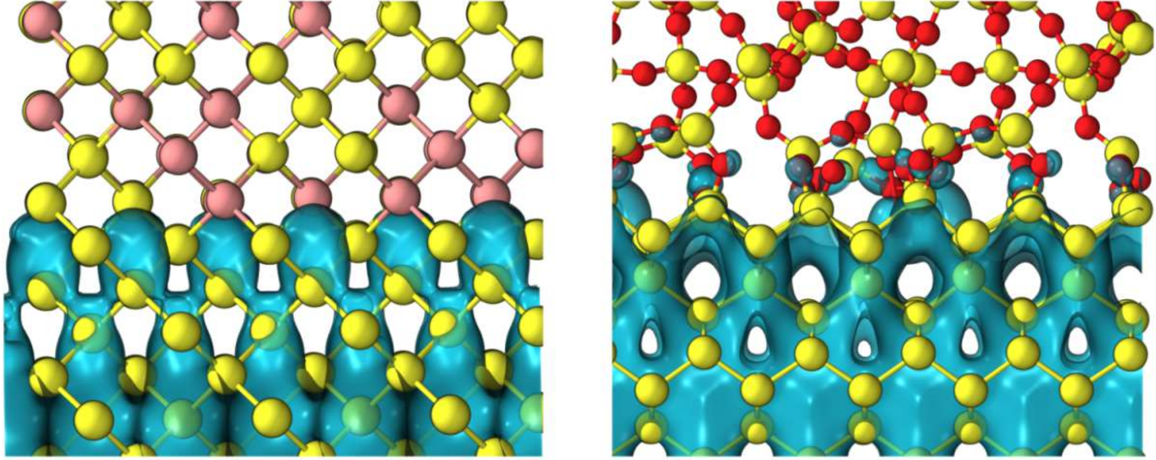

Figure 2.8: Interfaces between Si/SiGe and Si/$SiO_2$ as obtained within this work (Si in yellow, Ge in rose, and O in red). The blue isosurface represents a wavefunction confined to the interface.

### 2.1.4 Quantum computing with quantum dots

We have seen in Sec. 1.1, that any arbitrary quantum circuit can be build up from a combination of single qubit gates and the CNOT gate. In the Loss-DiVincenzo quantum computer, a quantum computer based on confined spins in quantum dots, the controlled NOT gate is further decomposed in SWAP[6] operations and local spin manipulations [8]. The latter is a single-qubit operation and can be performed by local magnetic fields, while the former is a two-qubit gate that requires application of a pulsed inter-dot gate voltage. This voltage is applied on a gate that controls the coupling between the two qubits. If the gate voltage increases the barrier potential between the two qubits, tunneling is forbidden and the qubit states are stable with no evolution in time. If the barrier is low, the total two-qubit system is described by the Heisenberg Hamiltonian

$$H_s(t) = J(t)\mathbf{S}_1\mathbf{S}_2 \tag{2.1}$$

where $J(t) = 4t_0(t)/u$ is the time-dependent exchange constant produced by turning the tunneling matrix element $t_0(t)$ on and off in time. We then obtain the time evolution operator

$$U_s(t) = \mathcal{T}\exp\{-i\int_0^t dt' H_s(t')\} \tag{2.2}$$

[6]The SWAP gate swaps two qubits.

Die approbierte gedruckte Originalversion dieser Dissertation ist an der TU Wien Bibliothek verfügbar.
The approved original version of this doctoral thesis is available in print at TU Wien Bibliothek.
TU WIEN Bibliothek Your knowledge hub

$\mathcal{T}$ is the time-ordering operator and ensures correct ordering. Assuming a specific pulse duration $\tau_S$ such that the time integral of $J(t)$ gives $J_0\tau_S = \pi$ (modulo $2\pi$). In this case, $U_S$ turns into the SWAP operator $U_{SW}$, that is $U_{SW} = U_S(J_0\tau_S = \pi)$. Furthermore, the square root of the SWAP gate $U_{SW}^{1/2}$ is obtained when taking half the pulse width $U_{SW}^{1/2} = U_S(J_0\tau_S = \pi/2)$. Other gates can be built by combining $U_{SW}^{1/2}$ with individual spin rotations. For example, the XOR gate can be decomposed to

$$U_{XOR} = e^{i\frac{\pi}{2}S_L^z} e^{-i\frac{\pi}{2}S_R^z} U_{SW}^{1/2} e^{i\pi S_L^z} U_{SW}^{1/2}, \tag{2.3}$$

where $S_L$ and $S_R$ refer to the spins. A CNOT gate is directly obtained from the XOR gate by surrounding the target qubit with Hadamard gates [8].

The essence of the seminal work of Loss and DiVincenzo is that universal quantum gates can be constructed from relatively simple building blocks. By taking a set of double quantum dots in which the coupling between the qubits can be controlled, SWAP operations and therefore CNOT operations become feasible. This was truly exciting news and started the increasingly active research on semiconductor spin qubits.

### 2.1.5 Double quantum dots

In the previous section, we have discussed the need for two-qubit gates to build arbitrary quantum gates. A prototypical setup, as shown in Fig. 2.9 consist of two gate defined quantum dots that are coupled via exchange interaction. The device in Fig. 2.9 depicts a Si/SiGe quantum well. The coupling can be controlled by the middle barrier gate. For single qubit operations, the barrier to the other qubit is established by gate M before manipulating the qubit state, either by a magnetic field or (more practically) by electrical fields, see Sec. 2.2.4. Subsequently, the barrier can be removed so that the coupling to other qubits is restored.

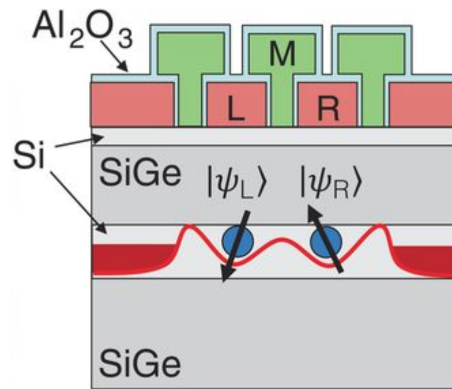


Figure 2.9: Two-qubit device in Si/SiGe from [42]. Depicted are the two gates $L$ and $R$ defining the quantum dots in a Si/SiGe heterostructure. The coupling is controlled via gate M. This device was used to demonstrate a CNOT operation in ≈ 200 ns.

The first demonstration of a two-qubit logic gate in silicon was presented in 2015 [43]. The device used in this work was based on isotopically purified Si (with

Die approbierte gedruckte Originalversion dieser Dissertation ist an der TU Wien Bibliothek verfügbar.
The approved original version of this doctoral thesis is available in print at TU Wien Bibliothek.
TU WIEN Bibliothek Your knowledge hub

800 ppm $^{29}$Si) in combination with $SiO_2$ as a barrier material, see Fig. 2.10a. It was operated at a temperature of $\approx 50\,\text{mK}$.

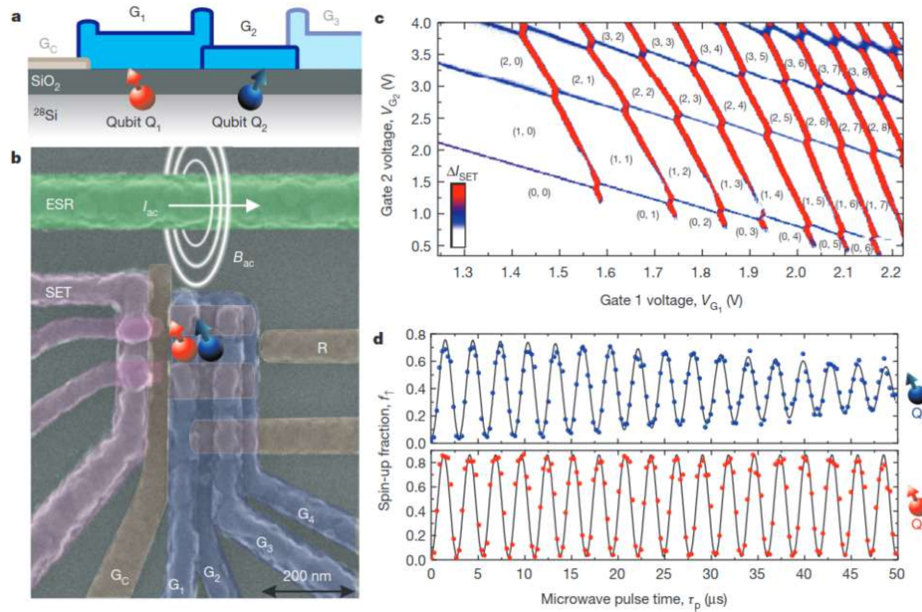


Figure 2.10: Two-qubit device in Si-MOS from [43]. (a) Schematic and (b) scanning electron microscope image of the device. The electrons are confined by gate $G_C$ and the occupation of the dots is controlled by gates $G_1$ and $G_2$, respectively. (c) Coloumb diamonds in the conductance of the close by SET with occupation numbers given in brackets. (d) Rabi oscillations of qubit 1 and 2.

Furthermore depicted in Fig. 2.10c is the charge stability diagram of a double quantum dot. The occupation of the two dots is indicated in brackets for left and right quantum dot respectively. Similar to the Coulomb diamonds of Fig. 2.6 in single qubits, measuring the current through a close by SET as a function of the gate voltages that define the dots reveals a diamond-like pattern reflecting regions of constant QD occupation.

Figure 2.10d shows Rabi oscillations in the two qubits, both can be controlled individually. Here, qubit manipulation was achieved by an ac current through a nearby placed wire, generating an ac magnetic field driving the Rabi oscillations. A more convenient mechanism to drive spin transitions, namely by oscillating electric fields, is presented in Sec. 2.2.4. Another point is worthwhile to mention: This device showed an extremely long dephasing time of $T_2^* = 120\,\mu\text{s}$ [14], a record that has not been beaten until today even though this experiment was conducted 10 years ago.

## 2.2 Physics of Si spin qubits

Silicon has been at the center of the most groundbreaking technological achievements of the last century: the semiconducting material proved to be extremely well suited

Die approbierte gedruckte Originalversion dieser Dissertation ist an der TU Wien Bibliothek verfügbar.
The approved original version of this doctoral thesis is available in print at TU Wien Bibliothek.
TU WIEN Bibliothek Your knowledge hub

for the implementation of transistors. One reason for that is that semiconductor-insulator interfaces with extraordinary low defect densities can be formed between Si and its native oxide $SiO_2$. This led to the successful integration of billions of micro- and nanoscale devices on a single chip. The most important representative device in which the material system $Si/SiO_2$ is employed is the metal-oxide-semiconductor field-effect transistors (MOSFETs), the most fabricated device in human history.

As discussed in Sec. 2.1.2, the implementation of logic gates in gate-confined quantum dots has been demonstrated in several host material systems. Typically, a combination between a semiconductor and a barrier material (which could be semiconducting too, but should then show an adequate band-alignment) with similar lattice parameters has to be found. Material systems in which quantum dots for qubit applications have been fabricated include GaAs/AlGaAs [44], Si/SiGe [42], Ge/SiGe [38], and $Si/SiO_2$ (Si-MOS) [14].

Each of these material systems come with advantages and disadvantages and the most suitable platform is yet to be found. Numerous experimental and theoretical research in the last decades, allowed to identify limiting factors for reliable qubit operation. Some of which can be resolved by adequate engineering solutions, e.g. by replacing magnetic fields by electric fields in order to conveniently drive spin-rotations, see Sec. 2.2.4, or by design measures that can minimize charge and hyperfine noise [45]. Other problems are directly linked to the material system. For example, all stable isotopes in GaAs have nuclear spin which means that the coherence of an electron or hole spin in this material is strongly affected by hyperfine interactions. These interactions can be minimized in silicon or germanium by enrichment of isotopes that are nuclear-spin free, as is the silicon isotope $^{28}$Si. On the other hand, the degenerate valley structure of Si introduces detrimental loss channels for the quantum information contained in the spin state. This was one of the main reasons why Si qubits attract a lot of interest in the quantum device community [46]. Furthermore, the vast advancements of Si technology over the last 70 years can be directly applied to quantum devices. This includes highly advanced fabrication processes such as the MOS technology [30] and the theoretical and practical knowledge of other commonly used materials like SiGe. Given the high compatibility between classical MOSFET and state-of-the-art quantum devices, the potential in terms of scalability is obvious.

The research effort put into Si qubits pays off. Operating on Si-MOS structures, encouraging achievements such as the experimental realization of two-qubit gates [43], which has been elaborated to carry out high-fidelity two-qubit operations [16], have been reported. Using SiGe as a barrier material, recent achievement of fidelities exceeding the threshold for quantum error correction in one and two-qubit gates impressively demonstrates the practicality of this material platform [47, 18]. Although the important step of demonstrating single and two-qubit logic has been taken, Si spin qubits are still facing a number of issues, including limited coherence time and operation speed. Currently, many research activities focus on mitigating such adverse effects to establish reliable platforms for spin qubit applications [48, 32]. Within the scope of this thesis, the physical mechanisms connected to the host material Si are specifically investigated, either in combination with the semiconducting SiGe or with its native oxide $SiO_2$.

TU Wien Bibliothek Your knowledge hub
Die approbierte gedruckte Originalversion dieser Dissertation ist an der TU Wien Bibliothek verfügbar.
The approved original version of this doctoral thesis is available in print at TU Wien Bibliothek.

### 2.2.1 Conduction band valleys

To ensure self-containment for later discussions in this thesis, a concise overview of established analytical band structure approximations is provided. For comprehensive details, readers may refer to fundamental texts on solid-state physics focused on semiconductors [49, 50]. We start from the Schrödinger equation for mobile electrons in a periodic lattice

$$\frac{-\hbar^2}{2m}\frac{d^2\Psi(\mathbf{r})}{d\mathbf{r}^2} + V_\mathrm{C}(\mathbf{r})\Psi(\mathbf{r}) = E\Psi(\mathbf{r}) \tag{2.4}$$

for which the Bloch theorem tells us that the solutions will have the form

$$\Psi(\mathbf{r}) = u_\mathbf{k}(\mathbf{r})\exp(i\mathbf{kr}) \tag{2.5}$$

where $u_\mathbf{k}(\mathbf{r}+\mathbf{R}) = u_\mathbf{k}(\mathbf{r})$ is a cell-periodic function (Bloch function) which is also periodic in reciprocal space. By inserting Eq. (2.5) into Eq. (2.4) we get

$$\left[\frac{1}{2m_0}\left(\frac{\hbar}{i}\frac{\partial}{\partial z} + \hbar k\right)^2 + U_C(\mathbf{r})\right] u_\mathbf{k} = E(k)u_\mathbf{k} \tag{2.6}$$

We can now solve this equation for $u_\mathbf{k}$ for any $k$ we select. Since this equation has an infinite number of eigenfunctions, we will label the solutions as $E_n(\mathbf{k})$. Repeating this procedure for all $\mathbf{k}$ results in the disperion relation $E_n(\mathbf{k})$ of band $i$. One important result is that $E(\mathbf{k})$ can often be approximized by a parabola near a band minimum or maximum, e.g. for the conduction band

$$E \approx E_\mathrm{C} + \frac{\hbar^2 k^2}{2m^*}. \tag{2.7}$$

The value that determines the curvature of the parabola is called the effective mass $m^*$[7]. The parabolic relation means that (close to the band minimum) the electron in the crystal behaves like a free electron but with a different mass. For many semiconductors the conduction band minimum is at $\mathbf{k} = 0$ (usually referred to as the $\Gamma$ point) for example in GaAs. Thus, the constant energy surface in $\mathbf{k}$-space is a sphere. However, for Si, the situation is more complex. The effective masses become non-isotropic and the minimum of the conduction band is not at $\Gamma$ but close to the edge of the Brillouin zone near the X point, see Fig. 2.11. The silicon conduction band at these points can be well described by the effective mass expression

$$E(\mathbf{k}) = \frac{\hbar^2 k_x^2}{2m_\mathrm{t}} + \frac{\hbar^2 k_y^2}{2m_\mathrm{t}} + \frac{\hbar^2 k_z^2}{2m_\mathrm{l}}, \tag{2.8}$$

where $m_\mathrm{l} = 0.98$ and $m_\mathrm{t} = 0.19$ are the longitudinal and transversal effective masses, respectively [50]. As a consequence of Eq. (2.8), there are six energy degenerate conduction band minimas that form ellipsoids lying on the axis of reciprocal space, for instance at $\mathbf{k} = [0,\ 0,\ 0.85\frac{2\pi}{a}]$ in [001] direction.

[7] In anisotropic materials, the effective mass is a tensor

Die approbierte gedruckte Originalversion dieser Dissertation ist an der TU Wien Bibliothek verfügbar.
The approved original version of this doctoral thesis is available in print at TU Wien Bibliothek.
TU WIEN Bibliothek Your knowledge hub

Ideally, a qubit should be comprised of exactly two energy levels. In a spin qubit, these two levels arise by application of an external magnetic field which splits each spin-degenerate valley state by the Zeeman effect. For Si spin qubits, the valley degeneracy is detrimental because it introduces additional states in the energy range of the qubit states (from other valleys) that can act as a decoherence channel. Fortunately, the degeneracy can be lifted as shown below and in Sec. 2.2.3.

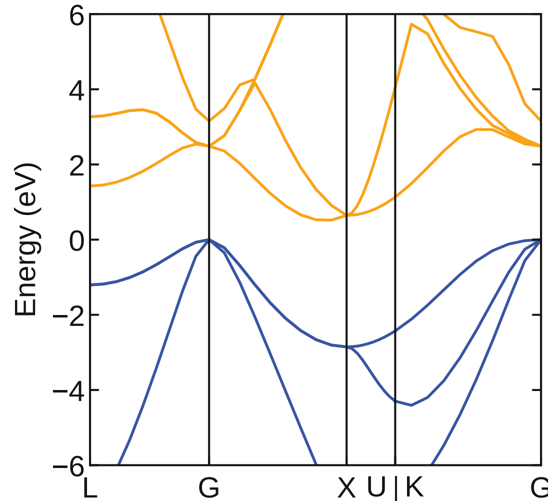


Figure 2.11: Electronic bandstructure of silicon obtained from DFT. The conduction band edge has a minimum close to the X point of the Brillouin zone which is referred to as conduction band valley or simply valley.

### 2.2.2 Strained Silicon

The band structure of Si and thus particularly its valley degeneracy can be influenced by straining the material. A detailed mathematical description including strain can be found in the literature [51, 52]. Let us directly discuss the results of a numerical calculation of biaxially strained bulk Si, as presented in Fig. 2.12. Tensile strain of 1 % is applied in the $x/y$-plane. As a result, the four in-plane valleys are lifted far above the remaining $z$-valleys. The separation of the energy levels is on the order of 100 meV and therefore large enough for qubit applications.

The easiest way to strain the crystal in plane is to deposit Si on a layer with comparable but slightly larger lattice constant, for example a relaxed layer of SiGe [53]. Fortunately, the fabrication of quantum dots in Si/SiGe requires to do exactly that.

### 2.2.3 Lifting the conduction band degeneracy

As pointed out in Sec. 2.2.1, the conduction band minimum of silicon is six-fold degenerate. The degeneracy of these so-called valley states can be partly lifted by the application of strain (let us assume in the $x/y$-plane), so that two of these states

Die approbierte gedruckte Originalversion dieser Dissertation ist an der TU Wien Bibliothek verfügbar.
The approved original version of this doctoral thesis is available in print at TU Wien Bibliothek.
TU WIEN Bibliothek Your knowledge hub

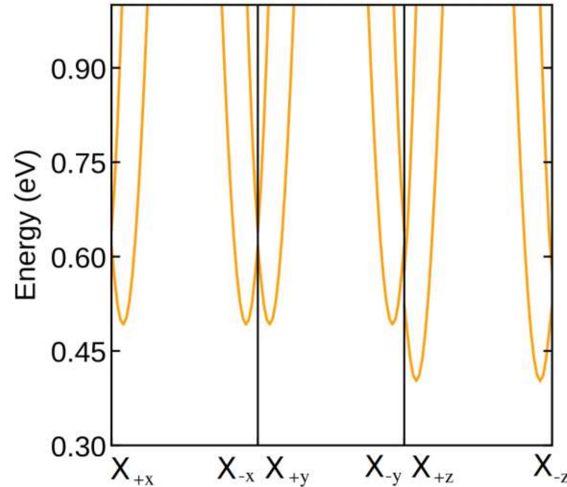


Figure 2.12: Lifting the valley degeneracy by strain. The shown band structure is obtained from DFT by straining the unit cell of Si by 1 % in $x$ and $y$ directions. The plot shows the band structure in the energy range of the conduction band minimum, so that all six valleys can be seen. The graph consists of three panels, each panel shows the results for $k$-points along direction $i$ ($i = \{x, y, z\}$) across the first Brillouin zone (from $X_i$ to $X_{-i}$). The two $z$ valleys lie approximately 100 meV below the four-fold degenerate $x$- and $y$ valleys.

($+z$ and $-z$ valley) remain [9]. During the past two decades, another aspect has been established in the literature: inter-valley coupling mediated by the interface [54, 55]. This mechanism enables splitting of the two $z$-valleys by scattering between the $+z$ and the $-z$ valley, see Fig. 2.13. The energy separating the two valley states is the valley splitting $E_{\mathrm{VS}}$. The scattering potential is the quantum well potential and is thus essentially the energy barrier at the interface. Note that this barrier arises due to the conduction band offset between Si and the barrier material.

Ideally, a spin qubit consists of only two levels (spin up/down, singlet/triplet, etc.). In a real system, any other states have to be separated from the two states that comprise the qubit. Thus, in a Si spin qubit, large valley splittings are needed, so that the two spin states of the lowest valley do not interact with any of the higher states. Fulfilling this requirement becomes even more challenging since current Si/SiGe devices suffer from a large variability in the valley splittings in the range between 20 and 300 µeV [56, 57, 58, 59]. Wide distributions can even be observed on devices that have been fabricated on the same wafer. Recent experimental evidence consolidates theoretical presumptions that these variations can be traced back to atomic fluctuations at the interface [60, 48]. It was also shown that the valley splitting varies strongly when a quantum dot is moved along a Si/SiGe interface by adjusting the gate biases [61]. These results underpin the importance of details of the interface.

Since fabricating very sharp interfaces, possibly with monolayer precision and a very low amount of alloy disorder, is currently extremely challenging, theorists have been searching for other ways to enhance valley splitting. Several proposals for enhancing $E_{\mathrm{VS}}$ by constructive measures in the well, such as Ge spikes [62] and

Die approbierte gedruckte Originalversion dieser Dissertation ist an der TU Wien Bibliothek verfügbar.
The approved original version of this doctoral thesis is available in print at TU Wien Bibliothek.
TU Bibliothek WIEN Your knowledge hub

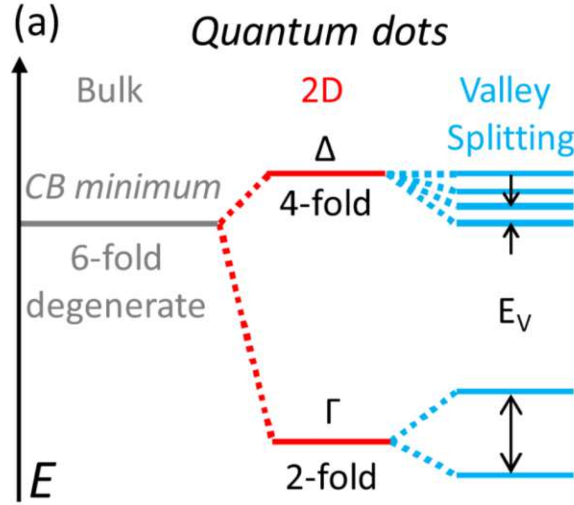


Figure 2.13: Valley splitting in a Si/SiGe quantum well. The sixfold valley degeneracy of bulk Si is broken by large in-plane tensile strains emerging due to the lattice mismatch between Si and SiGe. The strain splits the six levels in sets of two (marked by Γ) and four (marked by Δ) levels, respectively. The remaining twofold degeneracy is broken by the confinement (symmetry reduction) and the splitting is even further enhanced by external electric fields pushing the electron against a quantum well interface.

oscillating Ge concentrations [63, 64] have been put forward. The idea is to build wells that guarantee large valley splittings independent of atomic-scale fluctuations. It turned out that wells with oscillating Ge content (so-called wiggle wells) can give extremely large valley splittings.

The principle mechanism can be described by an effective-mass approach (EMA). The unperturbed valley wavefunctions are

$$\Psi_{\pm}(\mathbf{r}) = \Phi(z)\mathrm{e}^{\pm ik_0 z}\sum_{\mathbf{K}} c_{\pm}(\mathbf{K})\mathrm{e}^{i\mathbf{K}\cdot\mathbf{r}}, \tag{2.9}$$

where $\Phi(z)$ is the envelope function, $\mathbf{K}$ are the reciprocal lattice vectors, and the sum is a Fourier expansion of the cell-periodic part of the Bloch function. These coefficients can be found in [65]. In the next step, we separate the full scattering potential $V_{\mathrm{scat}} = V_{\mathrm{osc}} + V_{\mathrm{if}} + V_{\mathrm{lat}}$ in three parts: contributions from the oscillating Ge concentration, from the interface, and from the lattice. In the following, we consider only the oscillating potential, assuming that the growth process can be engineered to produce suitable wells. The valley splitting $E_{\mathrm{VS}}$ induced by the added Ge in the well is then [66, 63, 64]

$$E_{\mathrm{VS}} = 2|\langle\Psi_+|V_{\mathrm{osc}}(z)|\Psi_-\rangle| = 2|\sum_{\mathbf{K},\mathbf{K}'} c_+^*(\mathbf{K})c_-^*(\mathbf{K}')\delta_{K_x,K_x'}\delta_{K_y,K_y'}I(K_z - K_z')| \tag{2.10}$$

where the last term represents the integral

$$I(K_z - K_z') = \int |\Phi(z)|\mathrm{e}^{iQz}V_0\cos(qz)\mathrm{d}z, \tag{2.11}$$

Die approbierte gedruckte Originalversion dieser Dissertation ist an der TU Wien Bibliothek verfügbar.
The approved original version of this doctoral thesis is available in print at TU Wien Bibliothek.
TU Bibliothek WIEN Your knowledge hub

in which we use $Q = K_z - K'_z - 2k_0$ and assume a harmonically oscillating potential $V_{\text{osc}} = V_0 \cos(qz)$. The integral $I$ peaks strongly when the condition

$$q = \pm Q \tag{2.12}$$

is fulfilled (Because $|\Phi(z)|^2$ is a smooth function with exactly one peak, its Fourier transform has a single peak at zero). Therefore, the valley splitting will also show a peak if this condition is fulfilled. Because $|K_z - K'_z|$ is an integer multiple of $4\pi/a$, Eq. 2.12 has multiple solutions and thus, multiple peaks are found for $E_{\text{VS}}(q)$. Indeed, $E_{\text{VS}}(q)$ has three peaks at $q \approx 3.5\text{nm}^{-1}, 10\text{nm}^{-1}$, and $2k_0 \approx 20\text{nm}^{-1}$, see Fig. 2.14. The strong peak at $q = 2k_0$ ($|K_z - K'_z| = 0$) corresponds to an oscillating quantum well potential with $\lambda = 2\pi/(2k_0) \approx 0.3\,\text{nm}$. This means that the matrix element of Eq. 2.10 reaches a maximum if the potential oscillates with a wavevector that corresponds to the distance between the valleys in $k$-space. In other words, $q = 2k_0$ is the resonance condition for the coupling between $\psi_+$ and $\psi_-$. A smaller peak appears at $q = 2k_0/2$ which is identified as a harmonic of the first peak [64]. Another peak at $q \approx 3.5\,\text{nm}^{-1}$ ($|K_z - K'_z| = 4\pi/a$) becomes rather small because the various combinations of $\mathbf{K}$ and $\mathbf{K}'$ cancel out due to symmetries in the crystal lattice. Nevertheless, a peak appears due to the reduced symmetry due to alloy disorder.

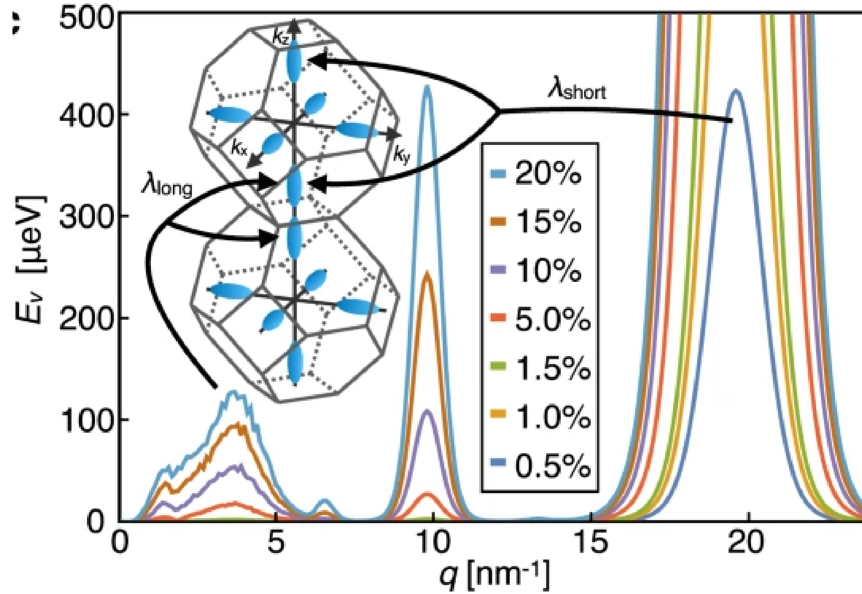


Figure 2.14: Valley splitting due to scattering between $-z$ and $+z$ valley as proposed in [64]. The scattering potential is the oscillating part of the quantum well potential due to Ge concentration oscillations in the quantum well, for Ge peak values shown in the inset box. The left inset shows two neighboring Brillouin zones, with the valleys depicted as constant energy isosurfaces in blue. The peaks at $q \approx 3.5\,\text{nm}^{-1}$ stems from Umklapp coupling between the $z$ valleys across two Brillouin zones, and the peaks at $q \approx 20\,\text{nm}^{-1}$ arise from coupling between $z$ valleys within one zone.

Based on simple yet effective perturbative arguments, Losert *et al.* suggested a universally applicable theory according to which $E_{\text{VS}}$ is proportional to the $2k_0$ Fourier

Die approbierte gedruckte Originalversion dieser Dissertation ist an der TU Wien Bibliothek verfügbar.
The approved original version of this doctoral thesis is available in print at TU Wien Bibliothek.
TU WIEN Bibliothek Your knowledge hub

component of the quantum well potential $V_{\mathrm{qw}}(z)$ [67]. This becomes apparent when evaluating the intervalley-coupling matrix element with simplified valley wavefunctions $\Psi_{\pm} \approx \mathrm{e}^{\pm k_0 z}\Phi(z)$

$$E_{\mathrm{VS}} = |\langle\Psi_{+}|V_{\mathrm{qw}}(z)|\Psi_{-}\rangle| = \int \mathrm{e}^{-2ik_0 z} V_{\mathrm{qw}}(r)|\Phi(r)|^2 \mathrm{d}r^3 \tag{2.13}$$

This effective-mass approach provides an idea on how the valley splitting can be conceptually understood and also provides a recipe for enhancing the valley splitting drastically: Incorporation of an oscillating Ge content with wavevector $q \approx 20\,\mathrm{nm}^{-1}$. However, these insights are only partially applicable to real devices because it completely neglects the atomic lattice. A wavevector $q \approx 20\,\mathrm{nm}^{-1}$ is associated with a wavelength of $\lambda = 0.3\,\mathrm{nm}$. So the wavelength is even shorter than the spacing between two Si layers, which makes the fabrication of such structures virtually impossible. Realistically speaking, out of the three peaks that are predicted by the EMA, wiggle wells with $q \approx 3.5\,\mathrm{nm}^{-1}$ seem the only feasible solution in the near future. Other approaches to enhance the valley splitting are qualitatively explained by this model as well. Ge spikes, for example, enhance the valley splitting because the Fourier transform of the scattering potential (which is a rather sharp peak in real space) gives a very broad spectrum so that the scattering amplitude is also enhanced at $q \approx 20\,\mathrm{nm}^{-1}$.

With current growth/deposition techniques, the fabrication of oscillating Ge concentrations with a wavelength of $\lambda = 2\pi/q = 2\pi/20\,\mathrm{nm}^{-1} \approx 0.3\,\mathrm{nm}$ – which is close to the distance between two atomic layers – is far out of reach, see Fig. 2.15. Devices with $q = 4\,\mathrm{nm}^{-1}$ on the other hand, could be realized in the foreseeable future.

A different approach to quantify the valley splitting in Si is given by TB [54, 68, 55, 67]. It is quite remarkable that a good description can already be obtained by simple two-band models with one atom of two orbitals per unit cell [54]. Losert *et. al* recently reported an agreement between the effective mass solution of Eq. (2.13) and a more advanced $sp^3d^4s^*$ TB model [67].

### 2.2.4 Spin-orbit coupling (SOC)

Spin-orbit coupling (SOC) arises through the relativistic motion of a charged particle in a potential gradient [69]. For isolated atoms, SOC leads to splittings of electronic energy levels called fine structure. In solid state materials, the potential is generated by the ionic environment of the electron. Thereby, the atomic structure is imprinted into the electronic wavefunction. Roughly speaking, the spin becomes coupled to its orbital motion.

Take Si as an example. At the valence band maximum (with $p$-like character), the heavy and light-hole band are separated from the so-called split-off band due to SOC [70]. On the other hand, SOC is relatively weak for conduction band electrons due to the stronger $s$-like character [71]. In electron spin qubits, the low SOC implies weak coupling to charge noise and thereby enhances qubit lifetimes. The downside is that strong SOC facilitates fast and easy qubit manipulations as such techniques require a physical mechanism suitable to drive transitions between the qubit states.

TU Bibliothek WIEN Your knowledge hub
Die approbierte gedruckte Originalversion dieser Dissertation ist an der TU Wien Bibliothek verfügbar.
The approved original version of this doctoral thesis is available in print at TU Wien Bibliothek.

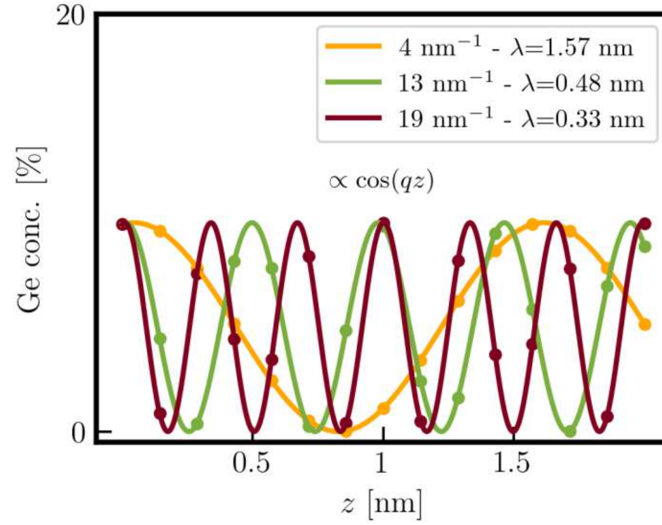


Figure 2.15: Ge oscillation profiles of the three peaks proposed based on the effective mass approach from [64]. The dots mark the positions of the monolayers. The quickly oscillating profile with $q \approx 20\,\mathrm{nm}^{-1}$ requires extremely fine control of the Ge content in each monolayer. Furthermore, such profiles would need to withstand Ge diffusion in order to maintain their shape. Slower oscillations with $q \approx 4\,\mathrm{nm}^{-1}$ are more practical to fabricate.

Constructive measures, such as placing a micromagnet in the vicinity of the qubit, can be used to artifically enhance SOC. The magnets generate a magnetic field gradient which strongly enhances the SOC, see Fig. 2.16. By doing so, it was shown that the Rabi frequency can be increased by one order of magnitude [57]. By means of this method, high-fidelity qubit operations have been demonstrated [72, 73, 74].

Rather than simply fast operation, reliable quantum computation requires high-fidelity qubit operations. The upper bound of the qubit fidelity is given by the Rabi oscillation quality factor [72]

$$Q^{\mathrm{Rabi}} = T_2^{\mathrm{Rabi}}/T_\pi \tag{2.14}$$

where $T_2^{\mathrm{Rabi}}$ is the decay time during Rabi oscillations and $T_\pi$ is the time needed for a $\pi$ rotation. A straightforward approach to obtain a qubit fidelity higher than the quantum error correction threshold for fault-tolerant quantum computing would either be to prolong the qubit decay time $T_2^{\mathrm{Rabi}}$ or shorten the $\pi$ rotation time $T_\pi$ [72]. Therefore, faster rotations yield higher fidelity.

The realization of a SOC-based spin-driving mechanism is difficult given the small intrinsic SOC strength in Si. Previously, it was believed that SOC would be practically negligible for electrons in Si. However, it turned out that SOC is strongly enhanced in 2D electron/hole gases as found in quantum dots. This enhancement is facilitated by inversion asymmetry of the crystal at the barrier interface [75, 76, 77, 78]. The physics behind this mechanism will be discussed below.

Die approbierte gedruckte Originalversion dieser Dissertation ist an der TU Wien Bibliothek verfügbar.
The approved original version of this doctoral thesis is available in print at TU Wien Bibliothek.
TU Bibliothek WIEN Your knowledge hub

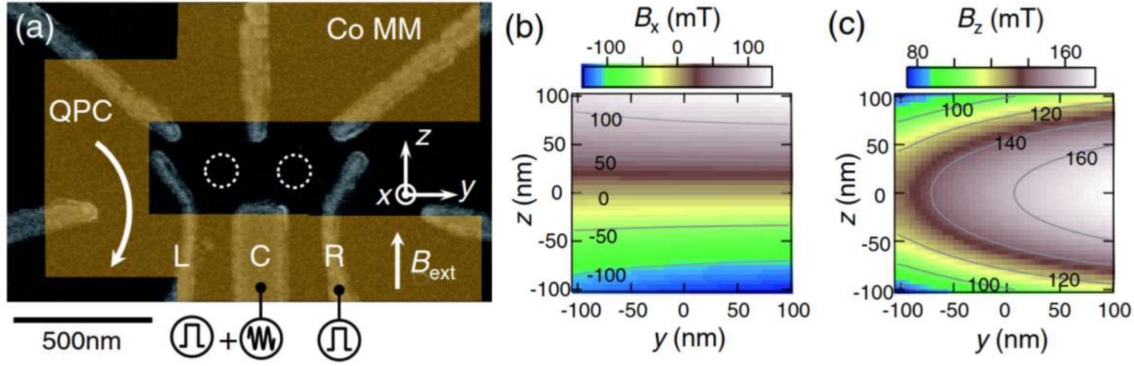


Figure 2.16: (a) Scanning electron micrograph of a Si two-qubit device with a micromagnet. The 250 nm thick Co magnet is depicted in orange (additionally labeled "Co MM"). In order to drive the transitions, AC pulses are applied to gates C and R. (b) Numerically simulated distribution of the stray field in the $x$ direction. The origin of the plot is at the center of the two QDs. (c) Numerically simulated distribution of the stray field in the $z$ direction. Figure from [73].

#### 2.2.4.1 SOC in quantum dots

Given the weak SOC in bulk silicon, the discoveries of Dresselhaus [79], Rashba [80] and Golub *et al.* [76, 77] have opened an exciting gateway to manipulate electron spins in Si. These works commonly show enhanced SOC by additional terms that arise due to a symmetry reduction with respect to the bulk crystal. As inversion symmetry is broken by the interface barrier (the confining potential is asymmetric), the additional SOC terms cause a splitting of the energy bands that is large enough to drive transitions between the spin states by ac electric fields.

First, Dresselhaus showed that in materials with bulk inversion symmetry (BIA), such as ZnSe or wurtzite crystals, SOC terms appear that are odd in momentum.

$$H_{\mathrm{D}} = \alpha_{\mathrm{D}}(\sigma_x k_x - \sigma_y k_y), \tag{2.15}$$

where $\alpha_{\mathrm{D}}$ is the Dresselhaus coefficient, $\sigma_i$ are the Pauli matrices and $k_i$ denotes the momentum in direction $i$. Because silicon is inversion symmetric, this term is absent. It is, however, strong in III-V materials.

About thirty years later, Vas'ko, Bychkov, and Rashba applied this idea to two-dimensional systems and predicted a coupling of the form

$$H_{\mathrm{R}} = \alpha_{\mathrm{R}}(\sigma_x k_y - \sigma_y k_x), \tag{2.16}$$

with the material-dependent Rashba SOC coefficient $\alpha_{\mathrm{R}}$. This term is based on structural inversion asymmetry (SIA), namely the asymmetry of the heteropotential that arises due to the presence of the interface.

In 2004, Golub *et. al* showed that another contribution to SOC can arise in quantum-well heterostructures [76, 77], which depends on the symmetry of the complete heterostructure and is based on interface inversion asymmetry (IIA). Assuming perfectly planar interfaces, this term can only appear if there is a odd number of

Die approbierte gedruckte Originalversion dieser Dissertation ist an der TU Wien Bibliothek verfügbar.
The approved original version of this doctoral thesis is available in print at TU Wien Bibliothek.
TU WIEN Bibliothek Your knowledge hub

layers in the quantum well, and vanishes if the number of layers is even. The term has the same representation in the Hamiltonian as the Dresselhaus term in Eq. (5.4) and is therefore often simply referred to as the Dresselhaus term (which would be absent otherwise in Si).

#### 2.2.4.2 Electric dipole spin resonance

The most promising spin-driving method that harnesses SOC is called electric dipole spin resonance (EDSR) and is specifically convenient because it allows to use the top gates to control the spin [81]. Fig. 2.17 depicts an efficient scheme for high-speed and high-fidelity qubit operation using EDSR, a technique that is employed to electrically control the spin of a single qubit by shifting the quantum dot position periodically by modulating the gate voltage. The movement in the gradient generates an oscillating magnetic field in the motion frame of the electron. This field is used to drive transitions between the spin states. One advantage of this technique is that the dots can be addressed independently by local electric fields which simplifies operation compared to using magnetic fields that typically have a large stray field. Zajac *et. al* were the first to demonstrate EDSR on their Si/SiGe double-dot device [42].

Without EDSR, the infrastructure supporting the qubit operations is more complex, as additional on-chip coplanar striplines [14, 43] have to be added to the architecture. Such striplines have a number of disadvantages. For example, they are not suitable to generate large magnetic fields. Furthermore, in an array of qubits, avoiding cross-talk between the magnetic AC fields would be challenging and inhibits scalability.

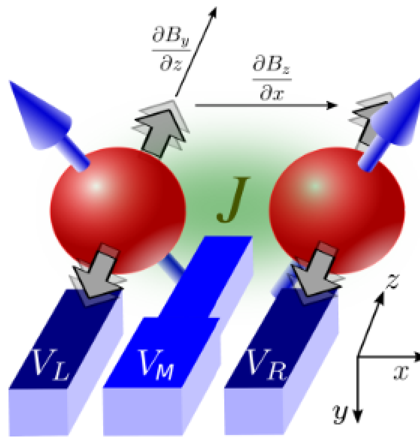


Figure 2.17: Two-qubit device from [81]. Depicted are the two gates $V_L$ and $V_R$ defining the quantum dots. The dots are occupied with one electron each. The degeneracy of the two respective spin levels is lifted by a large homogeneous magnetic field. In addition, there is an inhomogeneous field creating a field gradient $\frac{\partial B_z}{\partial x}$ along the double-dot axis. This gradient shifts the spin resonance frequencies relatively to each other.

Die approbierte gedruckte Originalversion dieser Dissertation ist an der TU Wien Bibliothek verfügbar.
The approved original version of this doctoral thesis is available in print at TU Wien Bibliothek.
TU WIEN Bibliothek Your knowledge hub

### 2.2.5 Interaction with nuclear spins

One of the main requirements for quantum computation is coherent control of the spin during the execution of quantum gates and operations. Interactions with the environment impede coherence and allow the quantum information to "escape". The interplay between various coherence mechanisms is still under debate [82, 83], however, hyperfine interaction between the electron spin and nuclear spins in the host material is indisputably one major source of spin decoherence in quantum dots. While hyperfine interactions have been known for many decades [84], the theoretical works of Burkard *et al.* [85], Coish *et al.* [86, 87], Merkulov *et al.* [88], and Khaetskii *et al.* [89] published around the turn of the millennium provide an analysis of this phenomenon in quantum dots.

With regard to hyperfine interaction, Si is an outstanding candidate platform to implement spin qubits due to the naturally low abundance of $^{29}$Si, the only stable Si isotope carrying nuclear spin. Natural silicon contains about 4.7% of $^{29}$Si. The nuclear spin of all other isotopes, including the naturally most abundant isotope $^{28}$Si, is zero and does not contribute to hyperfine noise. It was shown experimentally that the coherence of an electron spin can be highly enhanced when removing $^{29}$Si isotopes from the Si substrate. Tyryshkin *et al.* reported coherence times up to seconds enabled by means of such isotopic purification [90].

What is the principle mechanism of hyperfine interaction and how does it lead to spin decoherence? Assume an electron spin in a constant magnetic field so that the two spin levels are split by the Zeeman effect and therefore constitute a two-level quantum system. Because the electron resides in a crystal, it is exposed to a spin bath composed of nuclear spins. The nuclear spins combined generate an effective magnetic field, the so-called Overhauser field, which in turn interacts with the electron spin. Decoherence can be illustrated by an additional Zeeman splitting due to the Overhauser field. If the Overhauser field fluctuates, caused by fluctuations of the spin bath, the energy splitting changes. Because driving the spin requires accurate knowledge of the splitting (for determining the excitation frequency), coherent control is inhibited and the spin state is quickly lost. This is a highly illustrative description of the phenomenon. Let us be more rigorous in the following.

In the following, we give a quick overview of the theory of hyperfine interactions. More information can be found in the classic book of Abragam [84] or in the excellent review of Schliemann [91]. The Hamiltonian describing hyperfine interaction by means of a hyperfine tensor $\mathbf{A}$ was derived by Fermi in 1930 [92] and can be simply denoted as

$$H = \vec{I}\mathbf{A}\vec{S} \tag{2.17}$$

where $\vec{I}$ is the nuclear spin operator and $\vec{S}$ is the operator of the electron spin. The hyperfine tensor is typically notated as the sum of isotropic and anisotropic contributions [93].

$$\mathbf{A} = A_{\mathrm{iso}}\mathbf{I} + \mathbf{A}_{\mathrm{ani}} \tag{2.18}$$

where $\mathbf{I}$ is the identity matrix. The anisotropic part results from dipole-dipole interactions and is typically negligible for electrons in an $s$-type band, such as the silicon

Die approbierte gedruckte Originalversion dieser Dissertation ist an der TU Wien Bibliothek verfügbar.
The approved original version of this doctoral thesis is available in print at TU Wien Bibliothek.
TU Bibliothek WIEN Your knowledge hub

conduction band [94]. Resulting from the Fermi contact interaction, the isotropic part is proportional to the electron density $|\Psi(\mathbf{r})|^2$ at the atomic core positioned at $\mathbf{r}$.

$$A_{\rm iso} = \frac{4\mu_0}{3} g_{\rm e}\mu_{\rm B} g_{\rm N}\mu_{\rm N} |\Psi(\mathbf{r})|^2, \tag{2.19}$$

with the prefactor given by the vacuum permeability $\mu_0$, the Bohr and nuclear magneton $\mu_{\rm B}$ and $\mu_{\rm N}$, and the electron and nuclear $g$-factor in vacuum $g_{\rm e}$ and $g_{\rm N}$. Equation (2.19) is the non-relativistic limit, in which the Fermi contact interaction takes the form of a delta function. In its relativistic form $A_{\rm iso}$ is defined as

$$A^r_{\rm iso} = \frac{4\mu_0}{3} g_{\rm e}\mu_{\rm B} g_{\rm N}\mu_{\rm N} \int {\rm d}\mathbf{r} |\Psi(\mathbf{r})|^2 \delta(\mathbf{r}), \tag{2.20}$$

The delta function is smeared to a finite size by relativistic effects and its exact shape is determined by the atomic number of the nucleus. This smearing is important to remove spurious divergencies and is adopted in the DFT code CP2K. The implementation in the code was done by Declerck and all information regarding the calculation can be found in [95, 96]. The difference observed between the relativistic and the non-relativistic approach within the utilized simulation framework is significant but typically below 10%. However, in this text, we restrict ourselves to the non-relativistic limit for simplicity.

For energies within a crystal band, the electron density depends on the wavefunction envelope $\Phi$ and the Bloch part $u$ [91],

$$|\Psi(\mathbf{r})|^2 = |\Phi(\mathbf{r})|^2 |u(\mathbf{r})|^2. \tag{2.21}$$

With the Bloch part normalized to one over the crystal unit cell, the latter factor is dimensionless. It is usually denoted as $\eta \equiv |u(\mathbf{r})|^2$. It quantifies how much the electron is pulled towards the atomic core compared to the rest of the unit cell. Quoted values for the silicon conduction band are within $\eta \approx 160$–$190$ [91, 97]. For germanium, the authors of Ref. [98] "have made an experimental estimate based on observed nuclear spin relaxation times which indicates $\eta_{\rm Ge}$ is an order of magnitude larger than $\eta_{\rm Si}$." The authors of Ref. [99] say "We arrive at a value of 570 by an informal fit to our aggregated data across multiple devices with multiple quantum wells, and assume this value throughout, although we acknowledge that the present data leave this number about 30% uncertain." An important difference between this work and Ref. [100] is that our DFT calculation delivers wave functions estimates reliable also near atomic cores. In Ref. [100], the value of $\eta$ is an input that supplements the tight-binding method and the authors adopted the value from Ref. [98].

Earlier computational studies have quantified hyperfine interactions from DFT calculations in bulk materials [94, 93], utilized tight-binding methods [100], or combined DFT and $k \cdot p$ calculations [101]. The novelty of the approach presented in this thesis (and in [LC1, LC3]) is the application of DFT on heterostructures. The interactions between a 2DEG and all other atoms can then be translated into an effective interaction strength, that is used to calculate decoherence times in the ergodic limit. While the latter is discussed in the following, actual results of the study are presented separately in Chapter 6.

TU Bibliothek Your knowledge hub WIEN
Die approbierte gedruckte Originalversion dieser Dissertation ist an der TU Wien Bibliothek verfügbar.
The approved original version of this doctoral thesis is available in print at TU Wien Bibliothek.

#### 2.2.5.1 Decoherence in the ergodic limit

Ergodicity is a term that expresses the capability of a dynamic system to go in all possible states driven by random (thermal) fluctuations in a finite time. The time scale that is of interest for us is the data acquisition time $\Delta t$ of an experiment, that is the time needed to collect data e.g. for determining the dephasing time $T_2^*$ by means of Ramsey spectroscopy [102]. In typical experiments, the acquisition time consists of hundreds of measurement cycles and therefore, exceeds the dephasing time by orders of magnitude. During data collection, the spin bath evolves as a result of thermal fluctuations and nuclear spin-spin couplings.

The ergodic limit in this example describes the situation where the values of the fluctuating Overhauser field prior to $B_{\mathrm{N}}(t)$ and after the experiment $B_{\mathrm{N}}(t+\Delta t)$ are completely uncorrelated. Under these conditions, a measurement of the dephasing time $T_2^*$ yields always the same result. If, however, the data collection time is much shorter, ergodicity does not apply, and $T_2^*$ is prolonged [102]. The reason for that is that the spin bath fluctuations are still correlated on the shorter time scale of $\Delta t$.

Starting from Eq. (2.17) and under the assumption of unpolarized and thermally fluctuating nuclear spins, a standard derivation[8] [103] gives the hyperfine-induced variance of the electron spin energy as

$$\langle \delta E^2 \rangle = \sum_{i \in \text{isotopes}} p_i \frac{I_i(I_i+1)}{3} \sum_{n \in \text{isotope}\, i} |\mathbf{m} \cdot \mathbf{A}_{i,n}|^2. \tag{2.22}$$

Here the index $i \in \{^{73}\mathrm{Ge}, ^{29}\mathrm{Si}\}$ or $i \in \{^{17}\mathrm{O}, ^{29}\mathrm{Si}\}$ runs over spinful isotopes and $n$ runs over atoms of a given isotope. The isotope and atom indices apply for the hyperfine tensor in Eqs. (2.17)-(2.19). For example, we could reinstate these indices on the right-hand side of Eq. (2.19) by recognizing the isotope-dependence of $g_N \to g_{N,i}$ and the atom-dependence by $\mathbf{r} \to \mathbf{r}_{i,n}$. We have omitted indices in Eq. (2.17)-(2.19) to simplify the notation. All atoms of a given isotope have the same nuclear spin magnitude $I_i$, being $9/2$ for $^{73}$Ge, $5/2$ for $^{17}$O, and $1/2$ for $^{29}$Si, and the isotopic concentration $p_i$, being 7.8% for $^{73}$Ge, 377 ppm for $^{17}$O and 4.7% for $^{29}$Si in natural silicon and 50–800 ppm in isotopically purified one. Finally, $\mathbf{m}$ is the unit vector along the direction of the magnetic field and $|\cdot|$ is the Euclidean norm of a vector. We take $\mathbf{m}$ along the $z$ axis but expect no relevant directional dependence of the dephasing since the hyperfine tensors are dominated by the isotropic part. Concerning the dephasing from the oxygen atoms in Si-MOS, we expect that any anisotropy of the hyperfine tensor would be averaged out by the random orientation of the atomic bonds in the amorphous oxide.

Eq. (2.22) estimates the energy fluctuations of the two-level qubit system. The dephasing time $T_2^*$ can be evaluated in the ergodic limit by the textbook formula [84, 10]

$$T_2^* = \hbar \frac{\sqrt{2}}{\sqrt{\langle \delta E^2 \rangle}}. \tag{2.23}$$

[8] The derivation averages over the nuclei states in a semi-classical approach, assuming that the nuclear spins are continuous vectors pointing in all possible spherical directions.

Die approbierte gedruckte Originalversion dieser Dissertation ist an der TU Wien Bibliothek verfügbar.
The approved original version of this doctoral thesis is available in print at TU Wien Bibliothek.
TU Bibliothek WIEN Your knowledge hub

Let us stress again, that the assumption of ergodicity is valid in experiments where the total time for the data collection (data acquisition time) is much larger than the auto-correlation time of the nuclear spin bath. The latter depends on the diffusion constant of the nuclear spins, which is estimated for the relevant atomic nuclei in App. E.

Die approbierte gedruckte Originalversion dieser Dissertation ist an der TU Wien Bibliothek verfügbar.
The approved original version of this doctoral thesis is available in print at TU Wien Bibliothek.
TU WIEN Bibliothek Your knowledge hub

# Chapter 3

# Computational methods

The goal of this thesis is to establish an *ab-initio* based description of material properties that affect the performance of Si spin qubits. We employ density function theory (DFT) calculations in order to determine the electronic structure at the conduction band minimum of quantum confined electrons in Si. The outstanding feature of DFT calculations with respect to other numerical methods for such applications is that it provides a description of the electronic configuration without any specifically designed parameters. As implied by its name, *ab-initio* methods derive material properties from first principles, i.e. natural constants. There are, however, some subtleties that are worth discussing. As we will see in the following section, DFT uses some approximations necessary to make the calculations feasible. Although it has been known since the 1930s that determinantal functions (so-called Slater determinants) can be constructed from molecular orbitals and provide arbitrarily good approximations to the full wave function, such methods are extremely challenging to implement numerically for larger systems. The approximations that are being made in DFT concern the computation of exchange and correlation effects. The Slater determinant ensures that the wavefunction is antisymmetric with respect to exchange of two particles, as stated by the Pauli principle [104]. As such, it is an eigenstate of the interaction-free many-body Hamiltonian. Correlation effects, meaning spatial correlations in the motion of electrons, result from the fact that electrons interact with each other through Coulomb interactions – they repel each other as they carry negative charge.

The extreme computational requirements resulting from treating exchange by this approach can be easily exemplified. Taking all electrons of a single Au atom (atomic number 79) results in a determinant with $79! = 8.95 \times 10^{116}$ terms (again, a number that is larger than the number of atoms in the universe). A single Slater determinant corresponds to only one of all possible configurations (for example the singlet state of a two-electron system). Thereby, it is assumed that the motion of electrons is independent. Treating correlation is enabled by taking linear combinations of Slater determinants, a method called configuration interaction (CI). Despite the incredible advances in computational power since the 1930s, Dirac was right when claiming, that this procedure can not be implemented in practice, so that approximations are essential.



Die approbierte gedruckte Originalversion dieser Dissertation ist an der TU Wien Bibliothek verfügbar.
The approved original version of this doctoral thesis is available in print at TU Wien Bibliothek.
TU WIEN Bibliothek Your knowledge hub

That is why the ideas of Hohenberg, Kohn, Sham, and others that led to the development of density functional theory were so successful. DFT is one of the most accurate methods to determine the electronic structure of a given atomic configuration that has proven its capabilities over the last decades [105]. Its rise truly began with the formulation of efficient functionals that approximate exchange and correlation with satisfying accuracy. While the vast possibilities and applications of DFT speak for themselves, steady improvement of computational infrastructure is an additional driving force for using this method.

Although the foundations of DFT can be considered "textbook knowledge", a rough overview is given in the following. Excellent literature on this topic includes the detailed books of Parr and Weitao [106] as well as Szabo and Ostlund [107], the less rigorous book of Dreizler [108], and the rather recent review of Jones from 2015 [105].

## 3.1 Density functional theory

DFT is a quantum mechanical modeling technique that is widely used to investigate the electronic structure of many-body systems. It is an *ab-initio* method meaning that its predictions and calculations are solely based on quantum mechnical considerations and natural constants. There are no empirically fitted parameters[9] present that would be tuned for a specific application in order to reproduce experimental results. Such parametrizations are required in other atomistic modeling techniques like tight-binding, in which the hopping parameters and on-site energies are adjusted to reproduce the band structure of the respective material.

A usual approximation in many-body electronic structure calculations is that the nuclei of the system are assumed to be fixed. This assumption is called Born-Oppenheimer approximation and is justified by the difference in the mass of electrons and nuclei: Since the electrons are much lighter, the corresponding time-scale of their motion is much shorter. Following this argument, we are allowed to separate the full Hamiltonian into electronic and nuclear terms. We consider a stationary electronic state with $N$ particles as $\Psi(\mathbf{r}_1, \ldots, \mathbf{r}_\mathrm{N})$ in a static external potential $V$. Interactions in the system are described by the electronic Hamiltonian

$$\hat{H}\Psi = \left[\hat{T} + \hat{V} + \hat{U}\right]\Psi = \left[\sum_{i=1}^{N}\left(-\frac{\hbar^2}{2m_i}\nabla_i^2\right) + \sum_{i=1}^{N} V(\mathbf{r}_i) + \sum_{i<j}^{N} U(\mathbf{r}_i, \mathbf{r}_j)\right]\Psi = E\Psi, \tag{3.1}$$

where $\hat{T}, \hat{V}$ and $\hat{U}$ are the kinetic energy, the potential energy and the electron-electron interaction energy, respectively. The operators $\hat{T}$ and $\hat{U}$ are universal for any given system, while the external potential $\hat{V}$ is system-dependent. This equation is not further separable because of the e-e interaction term $\hat{U}$ which makes solving Eq. 3.1 a very challenging task.

[9] Hybrid functionals are an exception as they use a free factor that controls the mixing between Hartree-Fock and LDA exchange, see Sec. 3.1.4.

Die approbierte gedruckte Originalversion dieser Dissertation ist an der TU Wien Bibliothek verfügbar.
The approved original version of this doctoral thesis is available in print at TU Wien Bibliothek.
TU WIEN Bibliothek Your knowledge hub

### 3.1.1 Hartree equations

In order to overcome this practical limitations, physicists employed further approximations. Historically, one of the first approaches to obtain approximate solutions was the Hartree method. It uses the simplest way to approximate the wave function of a many-body system, that is a simple product of wave functions of individual particles $\chi_i(\mathbf{r}_i)$, so

$$\Psi(\mathbf{r}_1, \ldots, \mathbf{r}_N) = \chi_1(\mathbf{r}_1) \cdots \chi_N(\mathbf{r}_N). \tag{3.2}$$

This expression is called the Hartree product. Douglas Hartree developed an iterative method to solve Eq. (3.1), the so-called self-consistent field method [109]. This method first assumes that the wave functions of each electron are independent (non interacting), so that Eq. (3.2) is valid. The total charge density at position $\mathbf{r}$ due to all electrons except $i$ is

$$\rho(\mathbf{r}) = -\mathrm{e} \sum_{j \neq i} |\chi_j(\mathbf{r})|^2. \tag{3.3}$$

As can be seen, the interactions between the electrons are replaced by a interaction of the electron $i$ with an average field and is thus a mean-field theory. This charge distribution creates a mean field potential $\nabla^2 V_{\mathrm{MF}}(\mathbf{r}) = -\rho(\mathbf{r})/\epsilon_0$, with $\epsilon_0$ the vacuum permittivity. This is the Poisson equation which can be solved using a Green's function

$$V_{\mathrm{MF}}(\mathbf{r}) = -\frac{\mathrm{e}}{4\pi\epsilon_0} \int \mathrm{d}^3\mathbf{r}' \frac{|\chi_j(\mathbf{r}')|^2}{\mathbf{r} - \mathbf{r}'} \tag{3.4}$$

We can then use this potential to write down a Schrödinger equation for electron $i$ which results in a set of coupled differential equations for the full system

$$\left[ -\frac{\hbar^2}{2m} \nabla^2 - \mathrm{e}V_{\mathrm{lat}}(\mathbf{r}) - \mathrm{e}V_{\mathrm{MF}}(\mathbf{r}) \right] \chi_i = E_i \chi_i \tag{3.5}$$

These equations are called the Hartree equations. The Hartree potential $V_{\mathrm{H}}$ is the potential from the lattice $V_{\mathrm{lat}}$ and mean field electronic potential $V_{\mathrm{MF}}$ combined.

This set of equations can be solve iteratively, by means of a variational method. The basic idea is that the energy of a system $\hat{H}$ calculated with a trial wavefunction is always larger than the ground state energy: $E_{\mathrm{T}} > E_0$. We start from known eigenfunctions $\chi_i(\mathbf{r})$, e.g. the orbitals of the hydrogen atom, and calculate the mean-field potential. Then, we can solve the Hartree equations with $V_{\mathrm{MF}}$ which yields a total energy $E_{\mathrm{T}}$ and a new set of $\chi_i(\mathbf{r})$. We can obtain a new $V_{\mathrm{MF}}$, plug it into the Hartree equations, get again new eigenfunctions, and so on. An estimate for the ground state energy is found, when the difference in $E_{\mathrm{T}}$ between two consecutive iterations is smaller than a certain threshold, i.e. the solution has converged to a set of eigenfunctions representing the electronic ground state. As the mean-field potential contains informations about all electrons $j$, the solution is called self consistent.

### 3.1.2 Hartree-Fock equations

The description of a fermionic system by means of a Hartree product is not suitable because the wave function in Eq. (3.2) is not antisymmetric under exchange of

Die approbierte gedruckte Originalversion dieser Dissertation ist an der TU Wien Bibliothek verfügbar.
The approved original version of this doctoral thesis is available in print at TU Wien Bibliothek.
TU Bibliothek WIEN Your knowledge hub

two particles as demanded by the Pauli principle (which was not fully understood when Hartree formulated his equations). The antisymmetry was incoorporated three years later by Fock and Slater independently. They built the wavefunction out of determinants, the so-called Slater determinants. Writing a two-particle state as

$$\Psi(\mathbf{r}_1, \mathbf{r}_2) = \frac{1}{\sqrt{2}} [\chi_1(\mathbf{r}_1)\chi_2(\mathbf{r}_2) - \chi_1(\mathbf{r}_2)\chi_2(\mathbf{r}_1)] \quad (3.6)$$

satisfies $\Psi(\mathbf{r}_1, \mathbf{r}_2) = -\Psi(\mathbf{r}_1, \mathbf{r}_2)$ and can also be extended to the general case with $N$ particles $\Psi(\mathbf{r}_1, \ldots, \mathbf{r}_N)$. Consider the case of two particles in the same orbital $\chi(\mathbf{r})$. Exchanging the particles leaves the system unchanged. The only way to satisfy the antisymmetry requirement while still having an unchanged wavefunction is that the function is zero everywhere. This corresponds to the characteristic property of fermions, that is that two particles can not occupy the same orbital. Using a slater determinant for the operators $\hat{T}$ and $\hat{V}$ in Eq. (3.1) gives the same result as the Hartree product in Eq. (3.2). However, operators that couple the particles, like $\hat{U}$ above, yield an additional "exchange term". Take, for example, a Coulomb interaction $\hat{U} = \mathrm{e}^2/r_{12}$ with $r_{12} = |\mathbf{r}_1 - \mathbf{r}_2|$. Then we get

$$\langle\Psi|\hat{U}|\Psi\rangle = \frac{1}{2}\sum_{ij}\left[\langle\chi_i\chi_j|\frac{\mathrm{e}^2}{r_{ij}}|\chi_i\chi_j\rangle - \langle\chi_i\chi_j|\frac{\mathrm{e}^2}{r_{ij}}|\chi_j\chi_i\rangle\right], \quad (3.7)$$

where $|\chi_i\chi_j\rangle$ denotes a Hartree product state. These terms are referred to as the Coulomb term and the exchange term, respectively. Employing slater determinants in the self-consistent scheme, is called the Hartree-Fock method. Hartree-Fock assumes that the $N$-body wave function can be approximated by a single Slater determinant. There are more accurate theories, often referred to as post-Hartree-Fock methods, like configuration interaction (CI) or multi-configurational self-consistent field (MC-SCF) which use linear combinations of Slater determinants. However, the problem of these (post-)Hartree-Fock calculations is the tremendous computational effort that is needed for larger systems.

### 3.1.3 Mapping to the electron density

DFT offers a practical alternative to solving the Hartree-Fock equations that can be applied to atoms, molecules and periodic bulk structures alike. The trick in DFT is to express all properties of the system by the electron density. The electron density is a function of the spatial directions, and thus its properties are expressed as a functional, that is, roughly speaking, a function of a function. First, let us consider the electron density

$$n(\mathbf{r}) = N\int \mathrm{d}^3\mathbf{r}_2 \cdots \int \mathrm{d}^3\mathbf{r}_N\, \Psi^*(\mathbf{r}, \mathbf{r}_2, \ldots, \mathbf{r}_N)\Psi(\mathbf{r}, \mathbf{r}_2, \ldots, \mathbf{r}_N). \quad (3.8)$$

It can be shown that the ground-state density $n_0$ is directly connected to the ground-state wavefunction $\Psi_0$, in fact $\Psi_0$ is a unique functional of $n_0$ [110]. Based on this, we can also express other measurable quantities that are expectation values of observables, as functionals of $n_0$. Specifically, the ground-state energy can be expressed

Die approbierte gedruckte Originalversion dieser Dissertation ist an der TU Wien Bibliothek verfügbar.
The approved original version of this doctoral thesis is available in print at TU Wien Bibliothek.
TU WIEN Bibliothek Your knowledge hub

as

$$E_0 = E[n_0] = \langle \Psi[n_0] | \hat{T} + \hat{V} + \hat{U} | \Psi[n_0] \rangle \tag{3.9}$$

More generally, the same can be done for electron densities which are not the ground-state density. Assuming we have suitable expressions for $T[n]$ and $U[n]$ (these are universal functionals) and for a given system-specific $\hat{V}$ we can write down a energy functional

$$E[n] = T[n] + U[n] + \int \mathrm{d}\mathbf{r} V(\mathbf{r}) n(\mathbf{r}) \tag{3.10}$$

which has to be minimized with respect to $n$.

In one of the most successful DFT procedures called Kohn-Sham DFT, the kinetic energy is computed by assuming that the density corresponds to a wavefunction consisting of a single Slater determinant ("non-interacting limit" analogous to Hartree-Fock) as shown in Eq. (3.5)

$$T_s[n] = \sum \langle \chi_i | - \frac{\hbar}{2m} \nabla^2 | \chi_i \rangle \quad \text{and} \quad n(\mathbf{r}) = \sum_{i=1}^{N} |\chi_i(\mathbf{r})|^2 \tag{3.11}$$

The electron-nuclei interactions (expressed by $\hat{V}$, last term in Eq. (3.10) can be computed exactly, and so can the Coloumb part of the electron-electron interactions $J[n]$ (a part of $\hat{U}$) by

$$V[n] = \sum_{\mathrm{A}} \int \mathrm{d}\mathbf{r} \frac{Z_{\mathrm{A}} n(\mathbf{r})}{|\mathbf{R}_{\mathrm{A}} - \mathbf{r}|} \quad \text{and} \quad J[n] = \frac{1}{2} \int \int \mathrm{d}\mathbf{r}\mathrm{d}\mathbf{r}' \frac{\rho(\mathbf{r})\rho(\mathbf{r}')}{|\mathbf{r} - \mathbf{r}'|}. \tag{3.12}$$

These expressions contain errors, first, because $J[n]$ is not the full electron-electron term. We have seen in Eq. (3.7) that there should appear exchange terms. Furthermore, the single-particle expressions for the kinetic energy is only an approximation. This errors are usually collected in the so-called exchange-correlation term $E_{\mathrm{XC}}$. In condensed matter physics, "correlation" denotes the interaction between electrons in a quantum system and "exchange" describes the terms that appear due to the anti-symmetry of the wavefunction with respect to exchange of the particles. $E_{\mathrm{XC}}$ is unknown but crucial for accurate results. The challenge here is to find an expression which gives good results with acceptable computational costs.

### 3.1.4 Exchange-Correlation Functionals

Many functionals have been developed, with quite different approaches to estimate the exchange and correlation parts which ultimately determine accuracy and computational costs. We can arrange these approaches in a hierarchy of DFT exchange-correlation functionals from lowest to highest accuracy, which corresponds directly to the scaling of the computational costs.

- Local density approximation (LDA): The functional depends only on the density at a given point. Example: S-VWN

Die approbierte gedruckte Originalversion dieser Dissertation ist an der TU Wien Bibliothek verfügbar.
The approved original version of this doctoral thesis is available in print at TU Wien Bibliothek.
TU WIEN Bibliothek Your knowledge hub

- Generalized Gradient Approximation (GGA): The functional depends on local density and its gradient. Examples are PBE, PW91, LYP, B88
- Meta-GGA: Functional depends on density, its gradient, and its second derivative. Example: M06-L
- Hybrid DFT: Mixes in Hartree-Fock exchange. Examples: PBE0, B3LYP (hybrid GGA)

LDA or LSDA (local spin density approximation) if spin orbitals are employed, is a simple way to estimate exchange and correlation based on results for a uniform electron gas (slowly varying electron density). It served as a starting point for the first DFT calculations used by Kohn and Sham in 1965 [111]. However, the electron density in real molecules can vary rapidly over a small region in space. GGA improves over LDA by also taking changes of the electron density into account. Satisfying results can be achieved by GGA specifically for solids. A drawback that remains is that GGA can not capture the $-1/r$ asymptotic behavior of the exchange potential [112].

Hybrid functionals were introduced by Becke in 1993 [113] and marked the onset of an extreme rise of the popularity of DFT calculations. Becke utilized Hartree-Fock theory which treats exchange exactly at a cost that scales well with the size of the system but still gives unacceptable results without further corrections for correlation. Post-Hartree-Fock approaches like CI on the other hand capture correlation but do not scale well with system size. As we have seen before, local density-functional correlation approximation can be evaluated easily (by numerical integration of functionals that depend only on the electron density). So the idea in hybrid functionals is to mix Hartree-Fock theory and L(S)DA, which turned out to give much better results with reasonable computational costs. The mixing is controlled via a free parameter that can be adapted by the user.

## 3.2 DFT setup

We conduct most of our DFT calculations within the CP2K package [114]. This code provides a general Kohn-Sham DFT framework to obtain the electronic structure of molecules or bulk materials as well as for geometry optimizations, molecular dynamics or transition state optimization using the nudged elastic band (NEB) method. In every DFT approach, the wavefunctions are expanded in terms of a basis

$$\chi_i(\mathbf{r}) = \sum_\alpha c_{\alpha i}\phi_\alpha(\mathbf{r}). \tag{3.13}$$

Common choices for basis functions are Gaussian-type orbitals (GTO) and plane waves (PW). A PW set has the advantage that the orbitals are orthogonal and it is thus computationally simple. For instance, derivatives are straight-forward to perform. However, representing orbitals requires a large PW basis set which furthermore scales with the simulation cell. Localized basis sets like GTO are typically more compact (it is sufficient to have a few basis functions per atom) and allow to model various

Die approbierte gedruckte Originalversion dieser Dissertation ist an der TU Wien Bibliothek verfügbar.
The approved original version of this doctoral thesis is available in print at TU Wien Bibliothek.
TU WIEN Bibliothek Your knowledge hub

regions of the cell with different accuracy. On the other hand, they are non-orthogonal and often computationally more demanding.

CP2K employs both Gaussian-type orbitals (GTO) and plane waves (PW). The basis sets are mixed in order to combine benefits of both methods. This approach is called gaussian and plane wave (GPW) approach. In our usual framework, the core electrons are not explicitly considered but replaced with so-called pseudopotentials so that the bare Coulomb potential is replaced by a screened Coulomb potential. The calculation of hyperfine interactions is a specific use case which demands knowledge of the spin density at the nucleus and therefore requires explicit treatment of the core electrons. Such all-electron calculations are done within the gaussian augmented plane wave (GAPW) approach which uses an augmented basis set and separates domains of hard and soft densities for increased performance [115].

As we are dealing with rather large structures containing up to 2500 atoms, we employ various correlation and exchange functionals depending on the use case. The structure is first optimized using the semi-local GGA functional PBE [116], and, in the next step, the electronic structure is determined by means of the hybrid functional PBE0 [117] which gives accurate results in semiconductors [118]. In the case of valley splitting calculations in SiGe, presented in Cha. 5, the cell is additionally relaxed using PBE0 [117] which improves the band offsets (and therefore also the valley splittings) with respect to experimental values.

For calculating hyperfine interactions, the orbitals are expanded in correlation-consistent polarized double-$\zeta$ basis sets[10] for valence and core electrons [119, 120, 121]. Since the same basis sets are not available for Ge, we used the 6-31G double-$\zeta$ Pople basis sets [122], which were previously reported to provide accurate hyperfine couplings [123, 124]. The combination of PBE0 and all-electron basis sets for the calculation of hyperfine interactions is currently not feasible, therefore these calculations were performed using PBE. The orbitals are expanded in double-$\zeta$ basis sets [125] and the core electrons are approximated by Goedecker-Teter-Hutter (GTH) pseudopotentials [126]. In all calculations, homogeneous electric fields are applied within the formalism presented in [127]. Calculating spin splittings requires the consideration of spin-orbit coupling which is unfortunately not implemented in CP2K. For those cases we employed the Vienna Ab-initio Simulation Package (VASP) [128] with its projector-augmented-wave method [129, 130].

## 3.3 Density functional based tight binding

The Density Functional Based Tight Binding method is an approximate version of density functional theory which reduces the Kohn-Sham equations to a tight binding Hamiltonian [131]. As such, the approximation gives accurate results for many bonding situations but fails if a delicate charge balance is required between different atom types. This basic description, can be significantly improved by considering a second-order expansion of the Kohn-Sham energy [132, 133]. In fact, this gives

[10] The valence orbitals are often represented by multiple basis functions. Basis sets with two (or three) basis functions per valence orbital are called double (or triple) $\zeta$ basis sets.

Die approbierte gedruckte Originalversion dieser Dissertation ist an der TU Wien Bibliothek verfügbar.
The approved original version of this doctoral thesis is available in print at TU Wien Bibliothek.
TU Bibliothek WIEN Your knowledge hub

rise to a self-consistent treatment of the (Mulliken) charge in the system [134]. The self-consistent charge (SCC) scheme combined with the computational approach of tight-binding (TB) allows a good approximation to the DFT results while reducing the computational effort drastically.

The standard TB method [104] expands the eigenstates of a given Hamiltonian in an orthogonal basis of atomic-like orbitals. Then, the many-body Hamiltonian is represented as a Hamiltonian matrix in this basis. The matrix elements would be overlap integrals of the atomic orbitals responsible for tunneling of particles between neighboring orbitals. However, these integrals are replaced by "hopping" parameters, which are chosen in such a way that the Hamiltonian reproduces the bandstructure of a reference system. DFTB starts from the Kohn-Sham energy functional Eq. (3.10) with Eq. (3.11) and substitutes the electron density with a superposition of a reference density and a small fluctuation $n \rightarrow n_{\text{ref}} + \delta n$. Upon expansion around the reference density, terms linear in $\delta n$ cancel out, and the obtained functional is correct to second order in the density fluctuations. Furthermore, some correction appear that are necessary for a TB total energy when charge fluctuations are considered. The complete derivation of the DFTB Hamiltonian can be found in [134].

We employed DFTB as implemented in the DFTB+ code [135] for generating realistic $Si/SiO_2$ interfaces. We modeled the full thermal oxidation of Si as elaborated in Sec. 4.2. This process required simulations on long time scales and large system sizes well outside the scope of feasibility of DFT. DFTB provides a suitable alternative for conducting simulations on such scales. In order to justify the use of DFTB, we compared the results of a DFT based *ab-initio* MD with data from DFTB. A typical reaction that occurs during the thermal oxidation of Si was chosen as a test case: The adsorption and subsequent dissociation of an $O_2$ molecule at the clean Si surface. The details of this process are described in the next section, however, the qualitative and quantitative agreement between the approaches is evident. As shown in Fig. 3.1, the charge transfer during the reaction marks the dissociation of the $O_2$ molecule. As can be seen, the transfer of one elementary charge is captured by both methods and the dissociation happens on a similar time scale. The spontaneous character of the adsorption process is indicated by a barrierless energy profile along the reaction trajectory.

## 3.4 Machine Learning

Machine learning (ML) has attracted a lot of attention in recent years. The extreme rise in its popularity is connected to the potential applicability in almost every area of science and technology. With respect to material science, ML has had specifically strong impact when it comes to large-scale calculations of molecular dynamics (MD) simulation [136, 137]. The idea is to train a ML model on atomistic structures and their corresponding DFT energies and forces. Assuming a well chosen data set, the machine learning force field (MLFF) should then be able to predict the energies and forces of arbitrary yet related structures solely based on geometric informations of the atomistic structure, that is without any knowledge of the electronic structure. This

Die approbierte gedruckte Originalversion dieser Dissertation ist an der TU Wien Bibliothek verfügbar.
The approved original version of this doctoral thesis is available in print at TU Wien Bibliothek.
TU Bibliothek Your knowledge hub WIEN

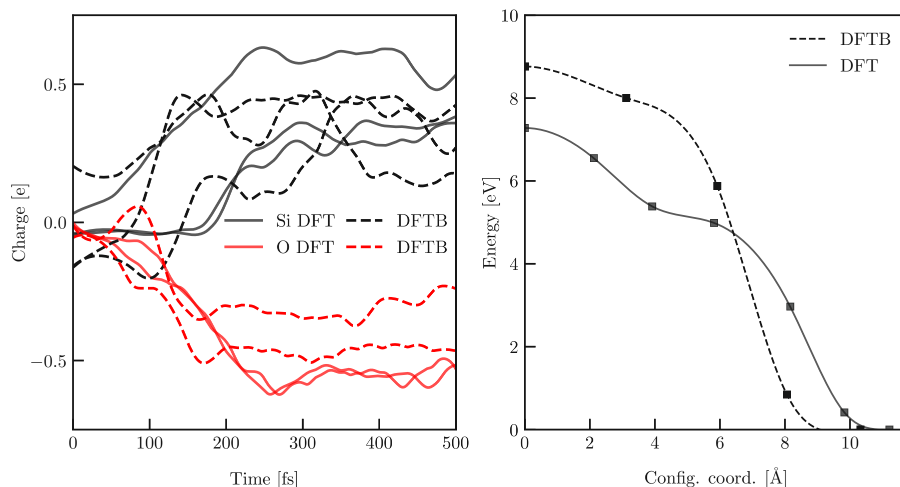


Figure 3.1: The results of dynamic molecular dynamics simulations calcuated with DFT and DFTB, respectively (left panel). The charge transfer reaction proceeds at comparable time scales. Recalculating some frames of the MD run indicates barrierless reactions in both cases with a similar energy gain (right) of around 8 eV.

can then be put to use for dynamic simulations. Instead of calculating the electronic structure at every time step $t$ of the MD run – a computationally very expensive procedure, especially for larger systems – the MLFF is used to predict the forces which are used to determine the atomic positions at $t + \Delta t$. Ideally, the predictions of the MLFF yield the same results as a DFT calculation, however, with strongly reduced computational costs. As presented in the next chapter, Ch. 4, the growth of $SiO_2$ on a Si substrate can be simulated via *ab-initio* calculations. However, the system size is limited to a few hundred atoms. We trained a ML model on the DFT data generated during the thermal oxidation process. The resulting machine learning force field (MLFF) allows to extend the system size as well as the time scales of our approach. In the following, we will briefly describe the methodology as well as the utilized tools for this process.

### 3.4.1 Atomistic Structure Descriptors

The potential energy of a given atomistic structure is an inherent property that does not change when the structure is rotated or translated in space. One example for a description that contains an artificial offset is the typical representation in cartesian coordinates, as it is based on an arbitrarily chosen origin. However, the usage of unbiased metrics is essential for the training data of a ML model. For this purpose, so-called descriptors are used to generate more abstract representations of the input structures. A descriptor maps the atomistic structure to a mathematical object like a vector that is invariant to rotation, translation, or the permutation of identical atoms. This approach allows to reduce the size of the training data-set drastically by only providing the essential information to the ML model without any artificially

Die approbierte gedruckte Originalversion dieser Dissertation ist an der TU Wien Bibliothek verfügbar.
The approved original version of this doctoral thesis is available in print at TU Wien Bibliothek.
TU WIEN Bibliothek Your knowledge hub

introduced offset. In other words, the descriptor processes the structural data in order to provide the ML model with an optimized representation.

Within the scope of this work, we employed the often used smooth overlap of atomic positions (SOAP) descriptor [138]. SOAP builds a local description of the structure using gaussian smeared "orbitals" based on spherical harmonics and radial basis functions. The accuracy is controlled by the user who can set parameters corresponding to quantum numbers in atomic orbitals. It generates a vector of real numbers (the number of entries depends on the settings) which will be passed on to the ML model either for training or for evaluation.

### 3.4.2 Gaussian Approximation Potential (GAP) Method

The Gaussian Approximation Potential (GAP) is one of the most successful ML models for interatomic potentials [139]. For our purposes, we use QUIP, the software implementation of GAP. Interatomic potentials can be separated in short and long range contributions. Long range interactions are typically electrostatic effects like polarizability or van der Waals forces. GAP builds on the hypothesis that the long range interactions are negligible when computing the total energy of a system. Of course, this is an *ad hoc* assumption and its validity has to be verified by numeric experiments. However, within the scope of this assumption, the total energy of a system can be taken as a sum of local contributions. Each of these contributions depend on the local atomistic environment (neighboring atoms, bond lengths, etc. We now employ the SOAP descriptor to generate a representation of the local environment, defined by a cut-off radius $r_c$. This data will be compared to other contributions in the training data-set that was generated in an analogous procedure. The comparison is represented by a function $K(d_i, d_t)$, with the SOAP vectors $d_i$ and $d_t$ from the given structure and training data, respectively. The total energy $E$ is then evaluated as a sum of the local contributions $\epsilon_j$

$$E = \sum_j \epsilon_j \quad \text{with} \quad \epsilon_j = \sum_i \alpha_i K(d_i, d_t) \tag{3.14}$$

as schematically shown in Fig. 3.2. The weights $\alpha$ are learned during the training. As can be seen, GAP estimates the potential energy surface without any previous knowledge about its functional form. Efficient training is enabled due to the linear relation between $\epsilon_j$ and $K$ [140].

Die approbierte gedruckte Originalversion dieser Dissertation ist an der TU Wien Bibliothek verfügbar.
The approved original version of this doctoral thesis is available in print at TU Wien Bibliothek.
TU WIEN Bibliothek Your knowledge hub

Figure 3.2: Schematic of the GAP potential. The total energy $\epsilon$ is obtained by comparison (using the kernel function $K$) of the input structure (red) with structures from the training dataset (blue). The weights $\alpha_\mathrm{n}$ are obtained from training the ML model.

Die approbierte gedruckte Originalversion dieser Dissertation ist an der TU Wien Bibliothek verfügbar.
The approved original version of this doctoral thesis is available in print at TU Wien Bibliothek.
TU WIEN Bibliothek Your knowledge hub

Die approbierte gedruckte Originalversion dieser Dissertation ist an der TU Wien Bibliothek verfügbar.
The approved original version of this doctoral thesis is available in print at TU Wien Bibliothek.
TU WIEN Bibliothek Your knowledge hub

# Chapter 4

# Structure generation

Die approbierte gedruckte Originalversion dieser Dissertation ist an der TU Wien Bibliothek verfügbar.
The approved original version of this doctoral thesis is available in print at TU Wien Bibliothek.
TU Bibliothek WIEN Your knowledge hub

Within the scope of this thesis, we present modeling approaches for two types of Si heterostructures in which the confining material is either SiGe or $SiO_2$. The principle set-up of the simulation cell, as depicted in Fig. 4.1, is valid for both. However, the interfaces are qualitatively very different, see Fig. 2.8. The alloy $Si_{1-x}Ge_x$ crystallizes in a diamond lattice just like Si. The Ge atoms simply occupy Si lattice sites leading to a lattice mismatch of up to 4% for $x = 1$ [141]. The oxide $SiO_2$, on the other hand, is an amorphous material which implies a more complex atomic configuration especially at the interface between the crystalline Si and the amorphous $SiO_2$.

The drawback of DFT, as of any *ab-initio* method, is certainly the high computational costs which limit the size of our model system to a few thousand atoms. The modeling of a complete quantum device is currently completely out of reach and even a quantum dot of realistic size alone is far out of reach. Therefore, we have to neglect planar confinement and consider cells that repeat after a few nm in the in-plane directions. The resulting heterostructure represents a quantum well, and the electrons are confined in $z$ direction within the well.

Realistic atomistic interface structures are the backbone of our calculations and set this work apart from previous computational studies. The rigorous generation of the interfaces is an essential condition for modeling the subtle effects that arise in spatially confined Si structures. In order to obtain realistic atomistic interfaces, we relied on several computational methods such as *ab-initio* molecular dynamics (AIMD) or density functional based tight binding (DFTB) and employed a machine learning (ML) model to generate larger structures with less computational costs. Especially the production of realistic $Si/SiO_2$ interfaces is a challenging task. Here, we present a novel approach for the generation of such crystalline/amorphous interfaces [LC4] which can be potentially extended to other material systems as well.

The two types of heterostructures that will be investigated require distinct approaches for the generation of the interfaces. Si/SiGe interfaces are straight-forward to construct and can be directly used as credible model structures after optimizing their cell and geometry. For $Si/SiO_2$ interfaces, we model the thermal oxidation of a Si surface within a framework of dynamic simulations. A detailed description of the applied procedures is given in the following for both material systems, respectively. The section on $Si/SiO_2$ (Sec. 4.2) additionally contains a number of insights that

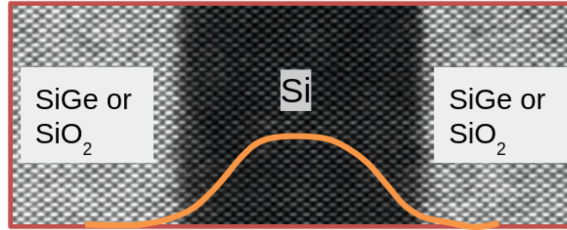


Figure 4.1: Schematic of the heterostructure model employed in the DFT calculations. The electron envelope $\Phi(z)$ is sketched in orange.

have been gained from the dynamic growth model. This includes a comprehensive oxidation scheme that explains the growth kinetics of thermal oxidation of silicon.

## 4.1 Si/SiGe

As explained above, SiGe and Si share the same lattice type with different lattice constants, $a_{Si}$ and $a_{SiGe}$. When forming a periodic heterostructure the resulting lattice constant of a cell optimization will be somewhere in between $a_{Si}$ and $a_{SiGe}$. However, in typical qubit designs, there is only a thin layer of Si (around 10 nm or 70 monolayers) that is sandwiched between thick $Si_{1-x}Ge_x$ layers. Thus, the Si layer gets strained as it adapts to the $Si_{1-x}Ge_x$ substrate. A Ge concentration of 30 % is typically used in experimental prototypes [9] and also employed as the confining material in our models. We furthermore adapt the in-plane lattice to the pristine $Si_{0.7}Ge_{0.3}$ lattice constant $a_{SiGe} = b_{SiGe} = 0.555$ nm from a cell optimization within our DFT framework. For the pure Si cell we find $a_0 = 0.545$ nm. The Si layer experiences a tensile, biaxial strain of 1.8 % in our simulation cell. In plane, we use a three-by-three superlattice which adds up to 1.665 nm in plane, see Fig. 4.2. The thickness of the Si layer is up to 10 nm which means that we reach the actual dimension of Si heterostructures utilized for spin qubits [48]. The cell vector of the full simulation cell in $z$-direction is optimized for every structure individually to account for different average Ge concentrations that occur due to disorder or as a result of the various Ge profile that we consider in our simulations, see Fig 4.2. Ge atoms are randomly distributed at the lattice sites of each monolayer in such a way that the cross-section averaged Ge concentration reproduces a predefined Ge profile. This way, we include atomistic disorder but avoid unrealistically strong fluctuations in the Ge concentration that would be averaged out in both larger models or real devices. Here, one drawback of DFT that can not yet be overcome is the limited size of the cell which limits consideration of long-range disorder. Each monolayer in our supercell consists of 18 atoms. Therefore, we obtain a step-like distribution of Ge atoms in the cell, as one Ge atom per monolayer in the [001] oriented simulation cell represents a Ge concentration of $1/18 \approx 5.5\%$, Fig 4.2a. As a result, we can not model arbitrary Ge profiles. After distributing the Ge atoms on the lattice as described above, the resulting SiGe/Si/SiGe heterostructure is relaxed within a cell optimization based on

Die approbierte gedruckte Originalversion dieser Dissertation ist an der TU Wien Bibliothek verfügbar.
The approved original version of this doctoral thesis is available in print at TU Wien Bibliothek.
TU WIEN Bibliothek Your knowledge hub

DFT calculations with the hybrid PBE0_TC_LRC functional [117]. Residual atomic forces are below $3\times10^{-4}$ H/$a_0$.

As elaborated in Sec.2.2.3, spin qubits in Si/SiGe often show detrimentally low valley splitting. Recently, there have been various propositions on how to overcome this problem, namely by engineering the properties of the quantum well by means of Ge spikes or oscillating Ge concentrations in the well [67]. Our *ab-initio* approach allows to incoorporate such designs to some extend. We have seen in Sec. 2.2.3 that the valley splitting can be understood as a coupling of the valley states via the quantum well potential. Evaluating the matrix element within the framework of an effective mass approach leads to the insight that the valley splitting is proportional to the Fourier transform of the (envelope weighted) quantum well potential evaluated at $2k_0 \approx 20\,\mathrm{nm}$, see Eq. (2.13). The step-like Ge distribution corresponds to sharp features in the quantum well potential which in turn corresponds to a broad Fourier spectrum. Thereby, the Fourier component at $2k_0$ is lifted, resulting in artificially large valley splittings. This error would become smaller with increasing cell size. In order to circumvent these problems, we restrict ourselves to a subset of well designs, namely Ge profiles in which the Ge content varies within each monolayer in steps of 5.5%. Obviously, such profiles can be built in large simulation cells containing thousands or millions of atoms, but they are also naturally reproduced when filling our simulation cell with Ge. Thus, comparison with other modeling techniques becomes possible.

## 4.2 Si/$SiO_2$ from first-principles

*The results presented in this section have been published in [LC4]. Text and figures are adapted from there.*

The construction of credible Si/a-$SiO_2$ interfaces is a more complex process as we are dealing with a crystalline/amorphous interface and can not simply optimize a lattice structure as in the case of Si/SiGe. Such a calculation would simply converge into a local energy minimum of two adjacent crystalline materials. The production of amorphous materials has a long history in material modeling [142, 143]. A commonly used method is the so-called melt-and-quench procedure in which a crystalline structure containing the correct atomic composition is the starting point. This structure is melted within a molecular dynamics run using a classical inter-atomic force-field by ramping up the temperature above its melting point at several thousand K. Subsequently, the temperature is quenched (i.e. reduced to 0 K within a few ps) which "traps" the structure in an amorphous phase. For this purpose, classical force-fields are used because of the relatively long simulation time of µs. Although the melt-and-quench procedure is commonly used to generate amorphous atomistic structures that agree reasonably well with the experimental values of geometry parameters such as density or bond lengths, the approach involves several constraints that become particularly important when constructing interface structures to crystalline materials. First, the atoms of the crystalline material (in our case the Si layer) are fixed

Die approbierte gedruckte Originalversion dieser Dissertation ist an der TU Wien Bibliothek verfügbar.
The approved original version of this doctoral thesis is available in print at TU Wien Bibliothek.
TU Bibliothek WIEN Your knowledge hub

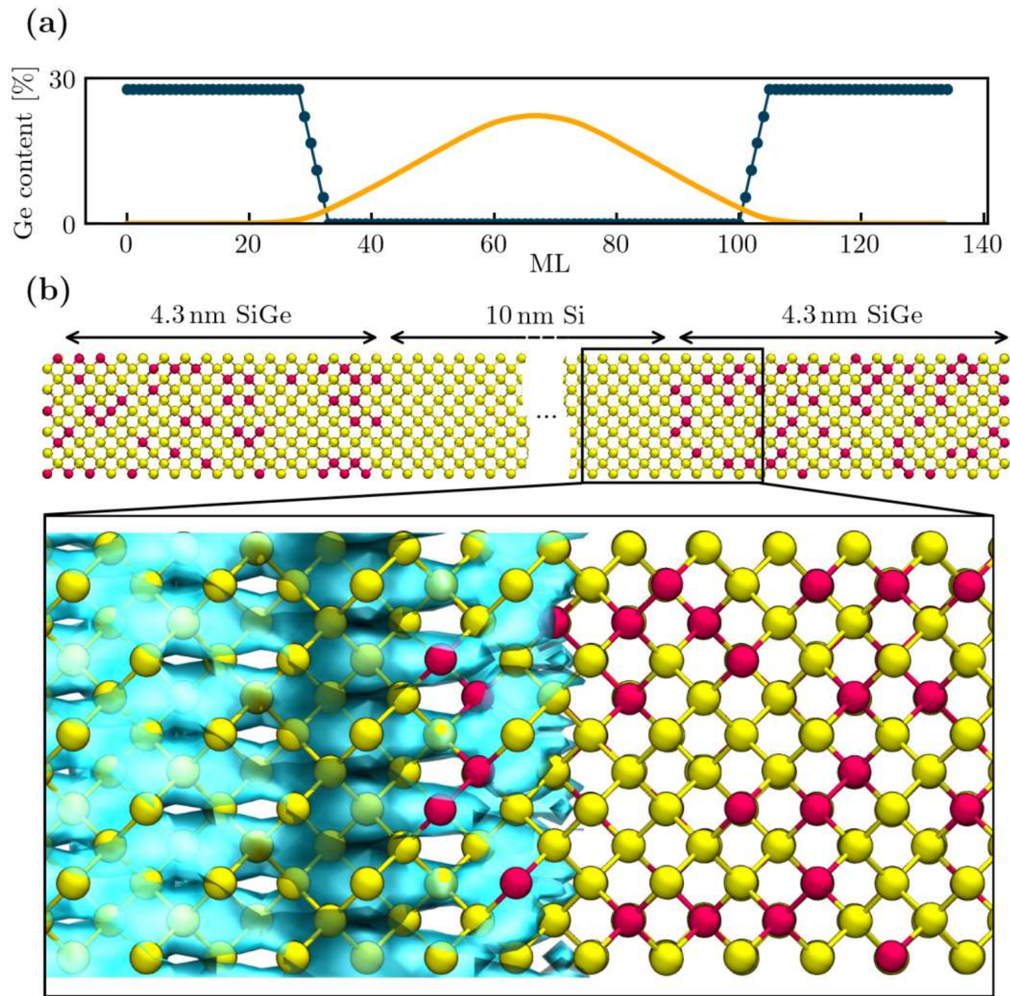


Figure 4.2: Si/SiGe heterostructures. (a) The limited size of the simulation cell leads to a step-like distribution of Ge atoms in the respective layers. The Ge atoms randomly replace Si atoms in each monolayer in such a way that the cross-section averaged Ge content corresponds to the desired well profile. (b) The heterostructure consists of a 10 nm thick Si layer with 4.3 nm SiGe barriers on both sides. A region around the Si/SiGe interface is depicted in the lower panel. Represented by a blue isosurface is the wavefunction of a conduction band electron as obtained from DFT.

during the MD to retain their crystalline structure. Thus, an extremely unrealistic temperature gradient between the melt (several thousand K) and the crystal (0 K) is considered in the simulation cell. Second, atoms from the melt tend to diffuse to the crystalline part due to their high kinetic energy. The migration of these atoms is usually avoided by introducing artificial potentials (acting as reflective "walls") at the interface. Third, the classical force fields are used for their low computational costs, however, also imply lower accuracy. All these effects combined, might artificially influence qualities of the structures like interface roughness, strains, and thickness of the transition layer.

TU Bibliothek, WIEN Your knowledge hub
Die approbierte gedruckte Originalversion dieser Dissertation ist an der TU Wien Bibliothek verfügbar.
The approved original version of this doctoral thesis is available in print at TU Wien Bibliothek.

To overcome the limitations of the melt-and-quench procedure, we modeled the thermal oxidation of an initially clean and reconstructed Si surface that is exposed to gaseous $O_2$. We employ *ab-initio* molecular dynamics (AIMD) simulations based on DFT as well as density functional based tight-binding (DFTB) simulations to grow an ultra-thin layer of amorphous $SiO_2$ on the Si surface at a temperature of 1000 K. In addition to obtaining more realistic interface structures, this approach offered new insights concerning the thermal oxidation process itself, as many details such as the onset of amorphization and $O_2$ diffusion are still under debate in the literature. Furthermore, the interface structures have been used to train a machine learning force field (MLFF) that allows to conduct simulations on a larger scale due to lower computational costs while keeping the accuracy of DFT.

In this subsection, we provide details about the oxidation scheme as based on our AIMD/DFTB results and a detailed geometric analysis of the atomic configuration. We furthermore compare to the state-of-the-art melt-and-quench procedure, which shows that more realistic interfaces can be obtained by the proposed gradual surface oxidation. Finally, we show larger models of oxidized surfaces that have been generated with the machine learned potential.

### 4.2.1 Thermal Oxidation of Si

While we use the interface structures within the context of qubit applications, $Si/SiO_2$ is still an integral part of many electronic devices. In fact, silicon has played a major role in semiconductor technology since the 1950s. The insights into the thermal oxidation process from the *ab-initio* perspective is therefore not only relevant within the scope of this thesis but might find a broad range of applications spanning from modern transistors to single-electron devices [144] and up to spintronics [145] or quantum devices [9].

One of the most important reasons for the extensive use is the interplay with its native oxide $SiO_2$ which allows to construct semiconductor/insulator interfaces of exceptional quality [146]. Massively produced devices like MOSFETs benefit from low defect densities at the interface and convenient growth of the oxide directly onto a Si substrate by thermal oxidation [147]. Although pure $SiO_2$ is being gradually substituted as a gate dielectric by other materials possessing significantly higher dielectric constants [148, 149], commonly referred to high-$k$ dielectrics, the inclusion of an ultra-thin $SiO_2$ passivation layer on the Si substrate prior to the application of the high-$k$ film remains crucial. This $SiO_2$ passivation layer greatly enhances device performance, making it an essential component also in modern devices [150, 151, 152]. Contemporary trends in fabrication and down-scaling of device dimensions have redirected research focus towards low-temperature chemical-based bottom-up fabrication methods [153, 154, 155]. Among these methods, the creation of ultra-thin $SiO_2$ layers holds paramount significance.

Typically, thin layers of $SiO_2$ are generated through the thermal oxidation of silicon. The underlying mechanisms of this process have been examined extensively over decades, both through experimental and theoretical means [156, 157, 158, 159, 160, 161, 162, 163, 164]. In modern technologies, a-$SiO_2$ layers have thicknesses on

Die approbierte gedruckte Originalversion dieser Dissertation ist an der TU Wien Bibliothek verfügbar.
The approved original version of this doctoral thesis is available in print at TU Wien Bibliothek.
TU Bibliothek WIEN Your knowledge hub

the order of a few nm. Consequently, the intricacies of the initial oxidation phase have gained heightened significance in recent times. Nevertheless, issues such as the onset of amorphization and the intricate interplay of various oxidation mechanisms are still unresolved.

Here, we provide a comprehensive bottom-up approach focused on the atomistic details during the full thermal oxidation process and the intricacies associated with the various oxidation mechanisms. For the first time, the complete growth of an ultra-thin $SiO_2$ layer was realistically modeled within dynamic simulations in full agreement with all experimental and theoretical knowledge that has been gained on this subject until now. The results have been published in [LC4] with a preliminary version in [LC5].

### 4.2.2 State-of-the-art models and experiments

Among the various theoretical assessments of thermal oxidation, the seminal model developed by Deal and Grove accurately describes the later stages of the silicon oxidation process [156]. The model is based on the well-established concept for Si oxidation that $O_2$ molecules enter the $SiO_2$ surface layers and diffuse to the $Si/SiO_2$ interface where they dissociate and individually relax into their respective lattice sites [157, 158, 159, 160, 161, 162, 163, 164]. However, these assumptions seem to be only valid for a well-progressed oxididation stage (oxide thickness > 30 Å) as the model predictions strongly underestimate the growth rates for thin oxide films [165, 166], see Fig. 4.3.

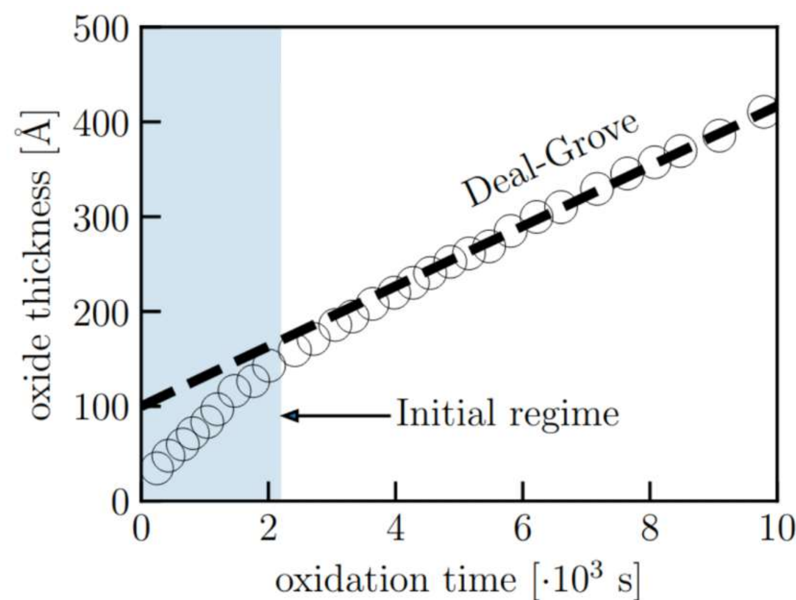


Figure 4.3: The prediction of the Deal-Grove model (dashed line) fails in the initial oxidation stage, the oxidation rate is strongly underestimated which can be explained by spontaneous surface reactions. The experimental data at 850°C (black circles) is taken from [165].

Die approbierte gedruckte Originalversion dieser Dissertation ist an der TU Wien Bibliothek verfügbar.
The approved original version of this doctoral thesis is available in print at TU Wien Bibliothek.
TU WIEN Bibliothek Your knowledge hub

Previous *ab-initio* calculations showed that the initial oxidation of a clean and reconstructed Si surface is based on chemisorption events resulting in the dissociation of the adsorbing $O_2$ molecule directly at the surface [167, 168, 169]. This was confirmed experimentally in recent electron microscopy and photoemission studies [170, 171, 172]. In addition, metastable molecular surface states were observed by means of scanning electron microscopy and electron spectroscopy techniques on thin oxide layers [173, 174, 172, 175, 176]. At low temperatures, these states precede dissociation events, however, vanish upon annealing. Hence, they are merely intermediate states toward the dissociative surface reaction. Both adsorption types, direct and molecular precursor mediated, were observed in molecular beam experiments [177]. According to this study, incident $O_2$ molecules of high kinetic energy ($> 1\,\mathrm{eV}$) tend to dissociate directly, whereas the molecular precursor states originate from trapping-mediated adsorption of $O_2$ with low kinetic energy ($< 0.2\,\mathrm{eV}$). Upon dissociation, the O atoms moved into backbonds of Si surface atoms, as correctly predicted by the above mentioned theoretical studies [167, 168, 169].

Combing these results, two major kinetic mechanisms seem to be at work: surface reactions dominate the initial stage, while the diffusion of $O_2$ becomes more important as the oxidation continues. Based on this concept, a theoretical growth model that considers dissociative chemisorption at the surface has been formulated [178] and reported to give good agreement with experimental data. Further experiments indeed support the concept of two distinguishable oxidation stages. As reported in a photoelectron spectroscopy study [179], the initial stage at low $O_2$ exposure of up to 10 L (1 L: $10^{-6}$ Torr s) featured relatively rapid oxidation. Maintaining the supply of $O_2$, the oxygen surface coverage saturated and the oxidation rate was reduced as the system gradually transitioned into the Deal-Grove regime. According to transmission electron microscopy (TEM) experiments on Si nanoparticles, diffusion of $O_2$ molecules becomes important after formation of a 5 Å thick oxide layer [170].

Besides establishing the fundamental processes of oxidation, the origin of amorphization is still a controversial issue in literature. Although some studies predicted the initial growth of a crystalline Si oxide monolayers [180, 181], an increase in the surface roughness during the initial oxidation was observed by atomic force microscope measurements [166] indicating an amorphous oxide growth. More recent TEM measurements support this idea and reported evidence that amorphous oxides were obtained by rapid thermal oxidation (RTO) [182, 170]. These experiments only studied oxide surfaces with more than five monolayers (ML) of $SiO_2$ (from crystalline $SiO_2$: 1 ML: $6.78 \times 10^{14}\,\mathrm{atoms/cm^2}$ [179]). In contrast, our simulations go beyond these measurements and offer detailed insight into the oxidation process from the onset of oxidation.

### 4.2.3 Oxidation scheme

The thermal oxidation was modeled by the subsequent adsorption of $O_2$ molecules within *ab-initio* molecular dynamics (AIMD) simulations in conjunction with density functional theory (DFT). Energy barriers for the migration of oxygen in the oxide layers were obtained by nudged elastic band (NEB) calculations. The initial oxidation

Die approbierte gedruckte Originalversion dieser Dissertation ist an der TU Wien Bibliothek verfügbar.
The approved original version of this doctoral thesis is available in print at TU Wien Bibliothek.
TU Wien Bibliothek Your knowledge hub

process featured the highest oxidation rate enabled by spontaneous surface reactions. An immediate amorphization was indicated by arbitrarily incorporated oxygen along many possible adsorption trajectories. The oxidation led to the spontaneous formation of $SiO_4$ tetrahedrons, the characteristic structural elements of a-$SiO_2$. With increasing O coverage, we observed that O-coordinated Si atoms were less susceptible for $O_2$ chemisorptions. Hence, repulsion of the incident $O_2$ became more probable and the oxidation rate decreased gradually as the surface was oxidized. In this stage, direct dissociation ($< 0.5$ ps) was only possible for $O_2$ molecules of high kinetic energy while the molecular precursor states were typically observed for low energy molecules leading to a further decrease in the oxidation rate. The subsequent transition to the diffusion limited regime and the associated migration of $O_2$ was investigated on a 20 Å thick surface layer of a-$SiO_2$. $O_2$ diffusion became the dominate mechanism as soon as a sufficiently thick surface layer was saturated with O. The saturation was consistent with the formation of a-$SiO_2$ and indicated the transition into the Deal-Grove regime. A spontaneous dissociation, similar to the surface reaction, was then observed at the Si/$SiO_2$ interface. An overview of the mechanisms and their onset during the oxidation process is given in Fig. 4.4.

Our calculations were mainly conducted at the *ab-initio* level utilizing density functional theory (DFT). In order to study oxidation mechanisms beyond the initial steps of O adsorption and dissociation, further investigations inevitably had to be carried out on larger model systems. Especially for DFT calculations, the computationally feasible simulation time was limited to a few ps and could be even lower for structures with an increased density of crystallographic defects. To be able to further extend our data set, we additionally used density functional based tight binding (DFTB) in conjunction with a Slater-Koster parameter set designed for Si surfaces and interfaces with $SiO_2$ [183, 184]. Initial benchmarks showed that both methods yield comparable results. The details of the utilized methods and their applications within this work (cf. Fig. 4.4) are summarized in Sec. 3.

The starting point of our investigations was a $4 \times 4 \times 12$ reconstructed Si surface structure. A cleaved Si surface leads to undercoordinated Si atoms at the surface that reconstruct by forming alternating rows of tilted dimers to minimize its energy. This reconstruction reduces the number of dangling bonds on the surface via electron transfer from the lower Si dimer atom to the upper one [185]. In the present structure eight dimer pairs formed within the simulation cell. The dimers were aligned in rows that build terraces on the surface separated by cavities, the so-called channels. The dangling bonds at the bottom of the structure were passivated with hydrogen. The bottom Si layer and the passivating H atoms were fixed in AIMD runs to resemble a bulk like structure. After reconstruction of the surface, optimizing the cell including the ionic cores in the lateral directions within DFT resulted in cell dimensions of $a = b = 15.523$ Å. The cell size in the $c$-direction was set to $c = 37.22$ Å leaving a vacuum of 20 Å above the slab. The thermal oxidation of Si was studied on this model by means of AIMD until 1.6 ML of O were adsorbed. Thereafter, we employed DFTB to model the thermal oxidation up to an oxide thickness of 8.5 Å.

Die approbierte gedruckte Originalversion dieser Dissertation ist an der TU Wien Bibliothek verfügbar.
The approved original version of this doctoral thesis is available in print at TU Wien Bibliothek.
TU WIEN Bibliothek Your knowledge hub

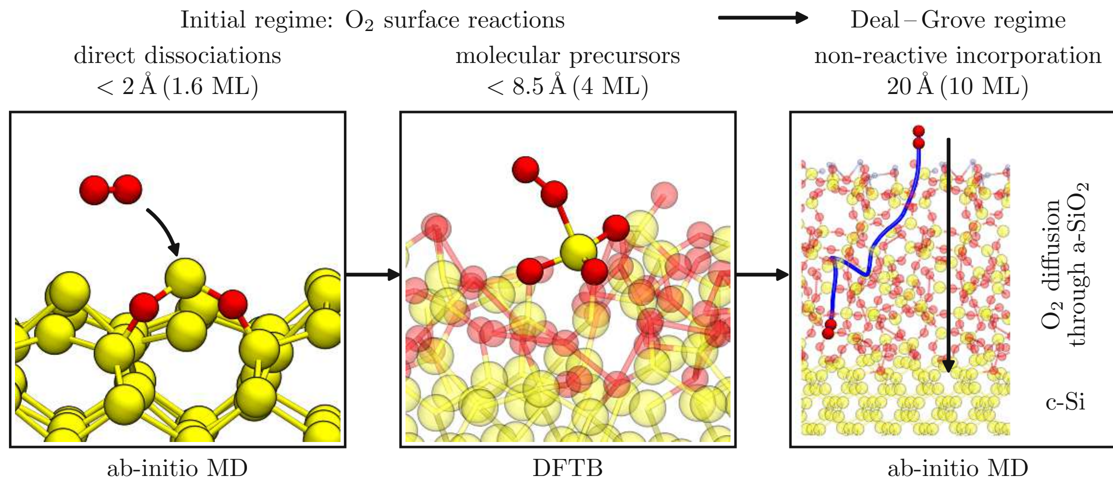


Figure 4.4: Oxidation scheme: In the initial stage, spontaneous and dissociative adsorptions of $O_2$ molecules are observed in DFT-based *ab-initio* MD (AIMD) calculations. These surface reactions are responsible for the increased growth rate compared to the Deal-Grove regime and lead to an immediate amorphization of the surface oxide. After oxidation of the first layer (oxygen coverage of 1 ML), an adsorption barrier forms and requires imposing initial velocities onto the $O_2$ molecules. As soon as the oxygen coverage reached 1.6 ML, the predominant adsorption mechanism changed to a slower process exhibiting molecular $O_2$ precursors that dissociated after a few ps. In order to cope with the longer simulation times needed, we employed DFTB for the further oxidation of the Si slab until a 8.5 Å oxide layer formed which showed structural characteristics of bulk a-$SiO_2$. Eventually, the saturated surface became inert to any surface reactions and $O_2$ diffusion to the Si/$SiO_2$ interface – the fingerprint of Deal-Grove oxidation – set in as observed on a 20 Å thick oxide.

### 4.2.4 Initial $O_2$ adsorption and amorphization

Our investigations started with a single $O_2$ molecule that was placed 2.5 Å above the reconstructed Si(100) surface. An ensemble of randomly generated and Maxwell-Boltzmann (MB) distributed velocities, scaled to match the specified temperature $T = 1000\,\mathrm{K}$, was assigned to all atoms and a spin-restricted ($S = 0$) AIMD simulation with a simulation time of 3 ps and a step size of 0.5 fs was performed. Subsequently, the structure was relaxed within DFT. In this vein, several simulations with various starting configurations yielded consistent results as discussed in the following. Fig. 4.5 shows snapshots of one representative $O_2$ adsorption and dissociation event together with the associated charges obtained by a Mulliken charge analysis. The $O_2$ molecule spontaneously moved toward an upper Si dimer atom that was charged positively as the $O_2$ molecule approached. After 170 fs the molecule was centered above the Si dimer atom and started to dissociate. Within the next 80 fs, the dissociation process was completed and the charges remained constant for the rest of the simulation. The two oxygen atoms relaxed into the backbonds of the upper Si dimer. In total, a

TU Bibliothek Your knowledge hub WIEN
Die approbierte gedruckte Originalversion dieser Dissertation ist an der TU Wien Bibliothek verfügbar.
The approved original version of this doctoral thesis is available in print at TU Wien Bibliothek.

charge of roughly $-e$ was transferred from the surrounding Si surface atoms to the $O_2$ molecule. In a simple molecular orbital picture, the donated electron occupied the antibonding $\pi^*$ orbital of the $O_2$ molecule, triggering its dissociation. Note that the gradual increase of charge depicted in Fig. 4.5 resulted from the adiabatic representation within DFT. In reality, the charge would be transferred much faster in a non-adiabatic process. Regardless, a spontaneous dissociative surface reaction was indicated by the very rapid reaction with the Si surface that was found to be independent from the starting configuration. This result was further supported by a series of static calculations. Placing $O_2$ molecules at random positions above the clean and reconfigurated Si(100) surface and relaxing the structure within DFT led to the dissociation of the molecule. Furthermore, a barrierless dissociative oxidation was also reported in [168]. Compared to the pre-adsorbed state, the intact $O_2$ molecule above the pristine Si slab, the dissociated and geometry optimized structure was 7.28 eV lower in energy. As shown in the last snapshot in Fig. 4.5, the Si atom on top was still undercoordinated resulting in a surface dangling bond. This exact configuration was already observed experimentally by STM images of a sparsely oxidized Si surface [172].

Crystalline oxide structures on Si surfaces have been investigated thoroughly within theoretical studies [180, 181]. However, the fact that thermally grown $SiO_2$ is amorphous was established decades ago and more recent studies reported evidence that this is also true for thin films of 10 Å to 50 Å obtained by RTO, as reported by various TEM studies [182, 170]. However, it is still unclear if the very first oxide layer is already amorphous. Within our dynamic simulations, strong evidence for immediate amorphization was found as presented in the following.

We modeled the thermal oxidation process by a series of AIMD simulations at 1000 K in which $O_2$ molecules were consecutively introduced above the reconfigurated Si(100) surface as shown in Fig. 4.5. The individual initial position was assigned randomly within a distance of 2 Å to 3 Å above the top Si atom. As for the adsorption in Fig. 4.5, the velocity was chosen randomly from a MB distribution at $T = 1000$ K. The axis of the $O_2$ molecule was aligned with the surface in order to allow for effective interaction due to larger spatial overlap between the surface dangling bonds and the oxygen $\pi^*$ orbital. The simulation time for each adsorption event was set to 1 ps. After this time, another $O_2$ molecule was introduced similarly to the previous one, while all other atoms continued to move according to their current velocity. A Mulliken charge analysis showed that the fundamental oxidation mechanism – a dissociative chemisorption via a charge transfer similar to the reaction shown in Fig. 4.5 – underlay every single adsorption during the initial surface oxidation. However, adsorption became less probable as the oxidation progressed. Only the first six adsorptions, corresponding to an oxygen coverage of 0.7 ML in our structures, happened spontaneously. After that, the $O_2$ molecules were occasionally repelled from already oxidized Si atoms. In this case, the run was discarded. After 9 successful adsorptions (or 1.1 ML), a spontaneous adsorption could not be observed within 10 runs. We interpreted the decrease in adsorption probability as the emergence and subsequent increase of an adsorption barrier with proceeding oxidation. In order to overcome the formed adsorption barrier and to study further oxidation within a reasonable

TU WIEN Bibliothek Your knowledge hub
Die approbierte gedruckte Originalversion dieser Dissertation ist an der TU Wien Bibliothek verfügbar.
The approved original version of this doctoral thesis is available in print at TU Wien Bibliothek.

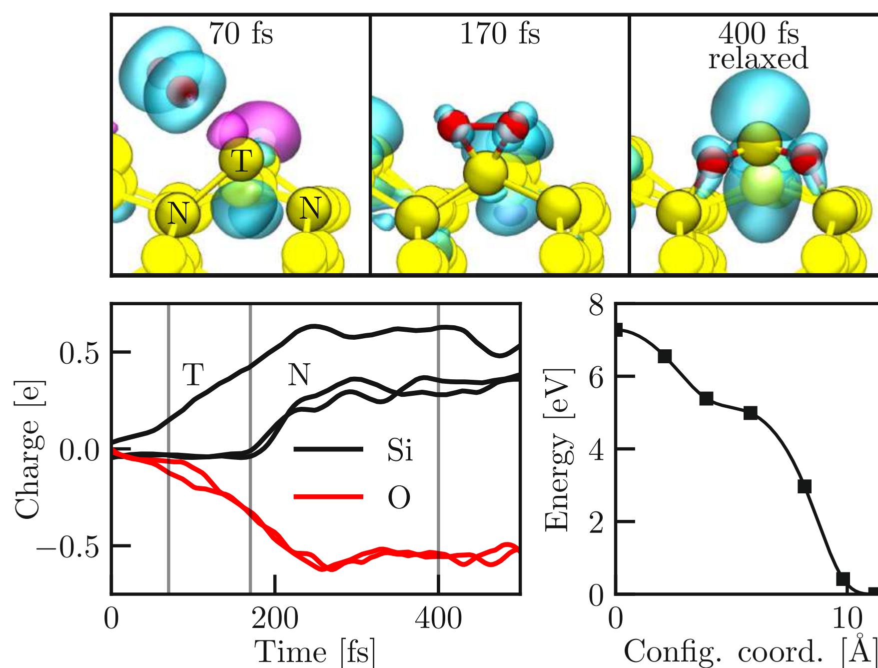


Figure 4.5: The dissociative chemisorption of $O_2$ (red atoms) onto a clean and reconstructed Si(100) surface (yellow atoms). Snapshots of the AIMD simulation are given in the upper panel. The top right panel shows the geometry optimized structure after dissociation. The spin density for values $\pm 0.002\,\mathrm{e}/a_0{}^3$ is depicted by cyan and magenta isosurfaces, respectively. The Mulliken charges of the oxygen atoms, the top dimer Si atom (T), and the neighboring Si atoms (N) during the first 500 fs of the chemisorption are shown in the lower left panel. A barrierless adsorption and dissociation is indicated by a NEB calculation along the adsorption trajectory in the lower right panel.

Die approbierte gedruckte Originalversion dieser Dissertation ist an der TU Wien Bibliothek verfügbar.
The approved original version of this doctoral thesis is available in print at TU Wien Bibliothek.
TU Bibliothek WIEN Your knowledge hub

time frame, we imposed an initial velocity of 1000 m/s toward the surface for the $O_2$ molecule from this point onward. This value roughly complies with the average velocity of $\overline{v} = 810$ m/s according to the MB distribution of non interacting $O_2$ molecules at $T = 1000$ K. Adsorption of $O_2$ – a process that happened spontaneously onto the clean surface within static and dynamic calculations – was inhibited by the oxide formation on the surface. This behavior qualitatively explained the decrease of the oxidation rate measured in the initial stage of oxidation [179] and gave rise to the non-reactive $O_2$ diffusion process later on [156].

The immediate amorphization of the oxide layer is enabled by a stochastic adsorption process in which the adsorption trajectory of each $O_2$ molecule depends strongly on its initial position and velocity and even on fluctuations of the surface lattice due to thermal vibrations. The stochastic character of the oxidation process is indicated by many different adsorption trajectories featuring comparable energy gains and strongly varying final configurations.

The adsorption trajectories were very sensitive to changes of the environment as investigated by two comparative AIMD runs. As shown in Fig. 4.6, the adsorption of an $O_2$ molecule was sampled for two different velocity distributions (taken from a MB distribution as described above) of the surface lattice. The initial position and velocity of the $O_2$ molecule was identical for both runs. The resulting trajectories are completely different although the energy gain of around 6.5 eV is very similar. This implies that even weak perturbations alter the resulting structure substantially. The intrinsic high degree of randomness during the oxidation provides strong evidence for the immediate amorphization of the oxide layer.

### 4.2.5 Molecular precursors and surface saturation

Sampling slower surface reactions and more spontaneous adsorptions in which the adsorption barrier was overcome, requires a longer simulation time together with an increased number of calculations. Furthermore, extending our investigations in the direction of the formation of a-$SiO_2$ required a larger amount of oxygen. Hence, we conducted these calculations within DFTB. The molecules were placed about 2 to 3 Å above a surface Si atom before MD simulations of 10 ps with a step size of 0.5 fs were conducted. The first simulation started with random initial velocities (MB distribution at $T = 1000$ K) for all surface atoms that were passed on to the subsequent run. The $O_2$ velocities were sampled from the same distribution though restricted to the negative $z$-direction. If a molecule was repelled from the surface, it was removed from the simulation cell at the end of the run.

After the first Si layer was oxidized, spontaneous dissociative adsorptions could hardly be observed. Instead, the $O_2$ molecules adsorbed via a metastable molecular precursor state. Dissociation events of these molecules could be sampled within the time-extended DFTB simulations, as shown in Fig. 4.7. Again, the dissociation was induced by a charge transfer. The surface was subjected to a considerable reconfiguration, mainly associated with the breakage of multiple Si-O bonds which adjust for the dissociation and incorporation in a $SiO_4$ tetrahedron. Such precursor states block further adsorption of oxygen molecules and thus effectively lower the rate of oxida-

Die approbierte gedruckte Originalversion dieser Dissertation ist an der TU Wien Bibliothek verfügbar.
The approved original version of this doctoral thesis is available in print at TU Wien Bibliothek.
TU WIEN Bibliothek Your knowledge hub

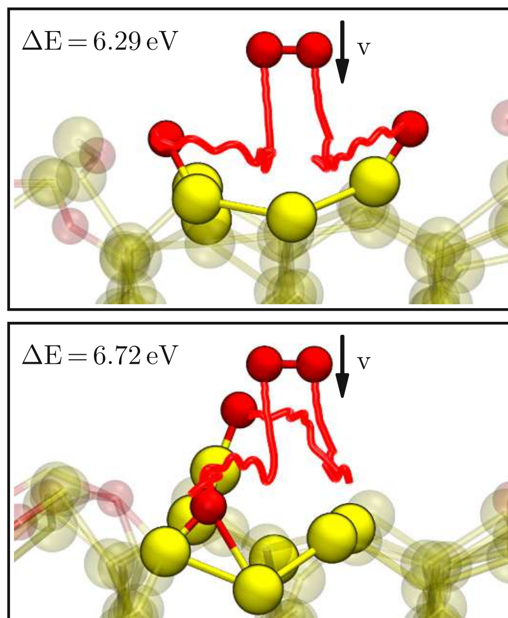


Figure 4.6: Two examples of $O_2$ adsorption trajectories of $O_2$ adsorptions with the same initial position and velocity of the $O_2$ molecule but different velocities for the surface atoms. The snapshots show the final positions after a simulation time of 450 fs superimposed with the starting configuration. Also shown are the trajectories of the adsorbing O atoms (red lines). The energy gains ΔE were calculated for geometry optimized structures.

tion. As mentioned above, we also observed the direct adsorption and dissociation mechanism, provided the $O_2$ molecules possess a sufficiently high kinetic energy, see the supplemental material. However, this process required $O_2$ velocities from the top one percent of the MB distribution and was thus ranked negligible in the framework of this work. However, both mechanisms involve the breaking of bonds between already dissociated O atoms and neighboring Si which is only feasible if the O atoms find new positions, i.e. can bind to Si atoms below not fully oxidized ones. Thus, the rate for direct dissociative oxidation gradually decreases as the oxidation advances and eventually can be considered negligible once a few layers of Si are oxidized. The precursor-mediated process with a reduced oxidation rate is dominant in this regime.

The oxide layer reached a total thickness of 8.5 Å after the adsorption of 32 $O_2$ molecules or 4 ML. As presented in the following section, the oxide could be subdivided into a 3.5 Å thick layer of a-$SiO_2$ on top of a 5 Å transition region. In this stage, all Si atoms on the surface were fully O coordinated and incorporated in a spontaneously formed $SiO_4$ tetrahedron, see Fig. 4.7 and 4.8. As a result, the surface structure was highly unordered. A spontaneous adsorption of $O_2$ molecules onto this surface could not be observed, as an additional molecule was repelled from 25 random positions. The chemical composition of the a-$SiO_2$ surface layer was $SiO_{1.95}$. A structural analysis of this layer showed that the bond lengths and angles are already

Die approbierte gedruckte Originalversion dieser Dissertation ist an der TU Wien Bibliothek verfügbar.
The approved original version of this doctoral thesis is available in print at TU Wien Bibliothek.
TU WIEN Bibliothek Your knowledge hub

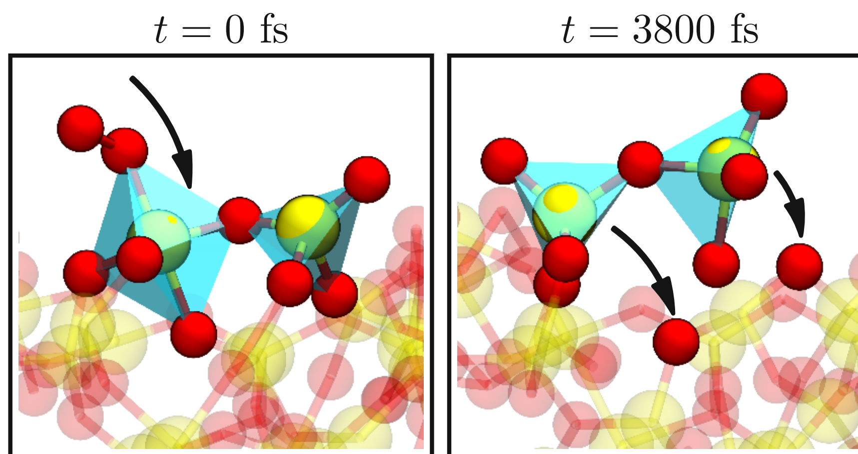


Figure 4.7: Molecular precursor mediated adsorption. The $O_2$ molecule adsorbs to a already fully oxidized Si atom (the $SiO_4$ tetrahedron is indicated by blue planes) and stays in the vicinity of this atom for around 4 ps within our simulations until it finally dissociates. Two O atoms migrate to lower Si atoms which adjust their position to the incorporation of the dissociated O atoms, as indicated by the black arrows.

comparable to the experimentally obtained values for bulk a-$SiO_2$ [186, 187]: the average Si–O distance was 1.66 Å and the binding angles showed an average of 108° for O–Si–O and 132.5° for Si–O–Si, see Fig 4.8. The slightly larger bond lengths (compared to 1.62 Å of bulk $SiO_2$) could be assigned to surface effects. The O–Si–O angles matched the perfect tetrahedral bond angle of 109.47°. The Si–O–Si angle averaged at 132.5°, which agreed well with the conclusions reached in Ref. [188], that the angle is reduced to 135° in thin films compared to 148° in bulk structures. Furthermore, the Si–O–Si angles were broadly distributed between 100° to 160° which indicated a vitreous (amorphous) form of silica. The density of the $SiO_2$ layer was roughly 2.33 g/cm$^3$ in agreement with measured values [186]. The density of the transition layer directly at the Si/$SiO_2$ interface was slightly increased to values up to 2.7 g/cm$^3$ which agrees with an intrinsic compressive stress as reported in [189, 190]. A Mulliken charge analysis allowed us to infer the oxidation state of each Si. Due to the strong electronegativity of O, a Si-O bond is represented by an increase of the Si's associated Mulliken charge. As determined by a reference calculation in defect-free a-$SiO_2$, the fully oxidized state $Si^{4+}$ corresponded to an increase of roughly $1e$ in our DFT setup, yielding $\sim 0.25e$ of excess charge on the Si ion per Si-O bond. The prevalence of different Si oxidation states as determined by this relation during the thermal oxidation is shown in the middle panel in Fig. 4.8. For a sparsely oxidized surface, the O was distributed evenly on the Si atoms as shown by the large number of $Si^{+}$. In later stages however, most Si were fully O coordinated with only a few partially O-coordinated Si atoms that were located at the interface to the Si substrate. $Si^{4+}$ atoms were fully coordinated by O and incorporated in a $SiO_4$ tetrahedron. We observed that the transition into the $O_2$ diffusion regime (Deal-Grove regime) happened

Die approbierte gedruckte Originalversion dieser Dissertation ist an der TU Wien Bibliothek verfügbar.
The approved original version of this doctoral thesis is available in print at TU Wien Bibliothek.
TU WIEN Bibliothek Your knowledge hub

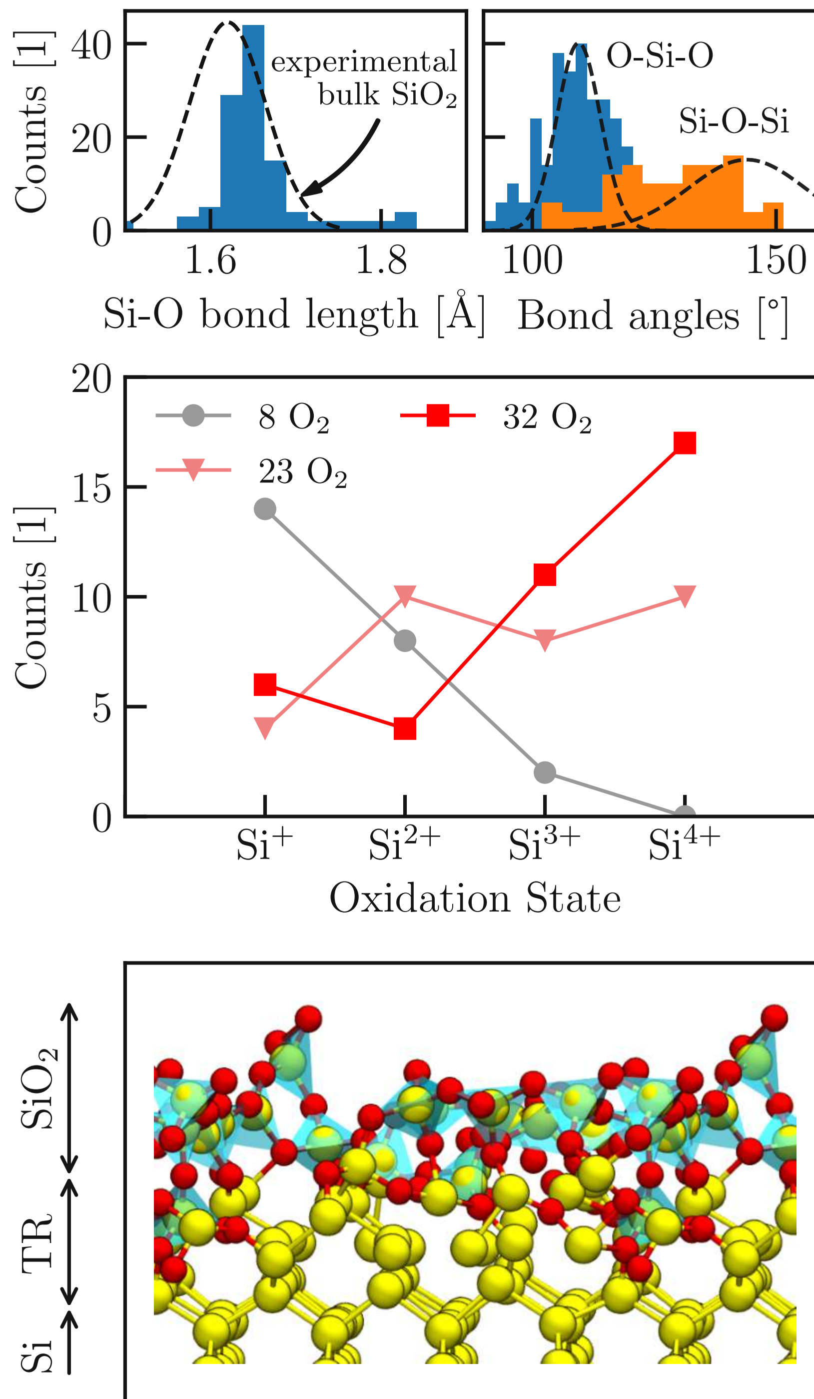


Figure 4.8: Characteristics of the $SiO_2$ growth obtained by dynamic simulations within DFTB. Distributions of the bond lengths and angles and the comparison to experimental values of bulk $SiO_2$ [186, 187] (dashed lines) are shown in the top panel. The prevalence of different Si oxidation states as obtained by a Mulliken charge analysis is shown in the middle panel. As oxidation continues, the amount of $Si^{4+}$ (fully oxidized Si atoms that are incorporated in $SiO_4$ tetrahedrons) increases whereas the amount of $Si^+$ converges to a lower value that represents states in the transition region (TR) between the oxide and the crystalline Si substrate. The final and geometry optimized structure is shown in the lower panel. $SiO_4$ tetrahedrons on the immediate surface are indicated by blue planes.

Die approbierte gedruckte Originalversion dieser Dissertation ist an der TU Wien Bibliothek verfügbar.
The approved original version of this doctoral thesis is available in print at TU Wien Bibliothek.
TU Bibliothek WIEN Your knowledge hub

as soon as a sufficiently thick surface layer was fully oxidized. During this stage, the $O_2$ could not chemically react with the surface anymore and thus diffusion of $O_2$ through the oxide set in.

### 4.2.6 Transition layer at the interface

Within computational material modeling, the construction of credible interface structures between amorphous oxides and crystalline substrates is a challenging task [191, 192]. Typically, computationally modeled Si/$SiO_2$ interfaces are created using a melt and quench procedure [193, 194, 142, 143]. In this approach, atomistic structures are melted at temperatures of up to 7000 K within simulation times of tens of picoseconds while ensuring that the silicon maintains its crystalline structure and the oxygen is confined to a certain region. In contrast, by consecutively adsorbing $O_2$ molecules onto the Si surface in dynamic simulations, we naturally obtained a credible interface between the amorphous oxide and the crystalline Si substrate. In order to investigate oxidation states at the interface, we plotted the Mulliken charges of the Si atoms vs. the corresponding $z$-position, as shown in Fig. 4.9. Note that the oxidation state +1 that is associated with one Si-O bond corresponded to a charge transfer of $0.25e$ in the Mulliken charge analysis. In addition to our observations, previous studies reported an intrinsic stress around the interface [189, 190]. This stress gave rise to lattice distortions that blurred the Mulliken charge analysis. Hence, only a rough assignment of oxidation states in the transition region was attainable. The decrease of the charge of some Si atoms in the transition region was considered to be an artifact of lattice distortions, as these atoms were situated in a layer below the oxidation front and correctly coordinated to other Si atoms. However, binding lengths to upper Si atoms were stretched by about 4 % or 0.1 Å which directly affects the Mulliken charge. In the following section, we show that these weakened interface bonds represented preferred places for the dissociation of $O_2$ molecules. All Si atoms in the surface $SiO_2$ layer were fully oxidized and their associated Mulliken charge was increased by $e$. The transition region was about 5 Å thick and could be identified via intermediate charge states of the silicon atoms. The linear transition of associated charges in the transition region was also found in structures obtained by the melt and quench method [193]. Furthermore, interface regions between crystalline Si and the amorphous oxide of 5 Å to 7 Å were indicated by TEM images [186] and electron-energy-loss spectroscopy [195] (EELS) measurements.

### 4.2.7 Oxygen migration

Another important aspect of the surface oxidation process is the migration of incorporated oxygen. Here it is important to differentiate between diffusion of single O atoms – atoms that are bound in the oxide and migrate while forming and breaking bonds to neighboring Si atoms – and the migration of $O_2$ molecules – molecules that enter the oxide without chemically reacting to the environment. First, we examined the possibilities of thermal diffusion of already adsorbed single O atoms by calculating energy barriers for the migration in Si bulk and from the surface oxide into

Die approbierte gedruckte Originalversion dieser Dissertation ist an der TU Wien Bibliothek verfügbar.
The approved original version of this doctoral thesis is available in print at TU Wien Bibliothek.
TU WIEN Bibliothek Your knowledge hub

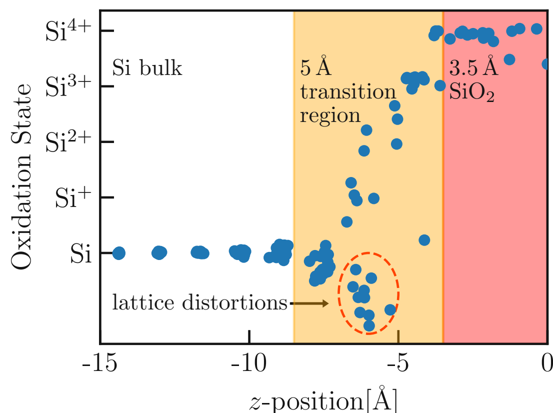


Figure 4.9: Oxidation states as obtained by a Mulliken charge analysis of Si atoms vs. their respective $z$-position at an oxygen coverage of 4 ML. Amorphous $SiO_2$ is indicated by fully oxidized Si atoms (oxidation state +4). The oxidation states in the roughly 5 Å thick transition region can only be assigned approximately and are blurred by lattice distortions.

deeper layers of the Si surface. Large diffusion barriers suggest that this mechanism is not important for the oxide growth. In contrary, in later stages of the oxidation process, i.e. after a layer of about 5 to 10 Å of a-$SiO_2$ formed on the surface, oxygen is incorporated by diffusion of $O_2$ molecules through the amorphous oxide, as assumed within the Deal-Grove model. We investigated this mechanism by AIMD simulations and confirmed the assumptions of Deal and Grove, namely, that oxygen molecules enter the oxide non-reactively and dissociate spontaneously when reaching the Si/$SiO_2$ interface. Larger oxide models were used for these simulations since the interface of our DFTB obtained structure (see Fig. 4.8) is still close to the surface and thus allows for the dissociative incorporation of molecular precursors as described above.

#### 4.2.7.1 Migration of adsorbed O atoms

To obtain diffusion barriers for single O atom migration in a bulk Si system we first calculated the energy barrier for the migration of one single O atom in a Si bulk material. As verified within geometry optimizations, the energetically favored positions of an O atom incorporated in a Si crystal are the Si bond center sites [196]. Utilizing NEB calculations, we obtained the minimum energy path between two neighboring bond center sites. The energy barrier of 1.72 eV in our pristine Si crystal agrees with other theoretical studies of O migration in Si [197, 198, 199]. With this result the experimentally derived energy barrier of 2.5 eV [200] can be obtained by considering a coupled-barrier diffusion [201]. In order to derive an estimate for the rate of the process at $T = 1000\,\mathrm{K}$ we employed the Arrhenius equation with an attempt frequency of $6 \times 10^{12}\,\mathrm{s}^{-1}$ [202] and the 1.72 eV barrier yielding $9 \times 10^{4}\,\mathrm{s}^{-1}$. Enlarged barriers were found for O migration from the surface oxide structures obtained by our AIMD simulations, see Fig. 4.10. We specifically investigated diffusion in the

Die approbierte gedruckte Originalversion dieser Dissertation ist an der TU Wien Bibliothek verfügbar.
The approved original version of this doctoral thesis is available in print at TU Wien Bibliothek.
TU Bibliothek WIEN Your knowledge hub

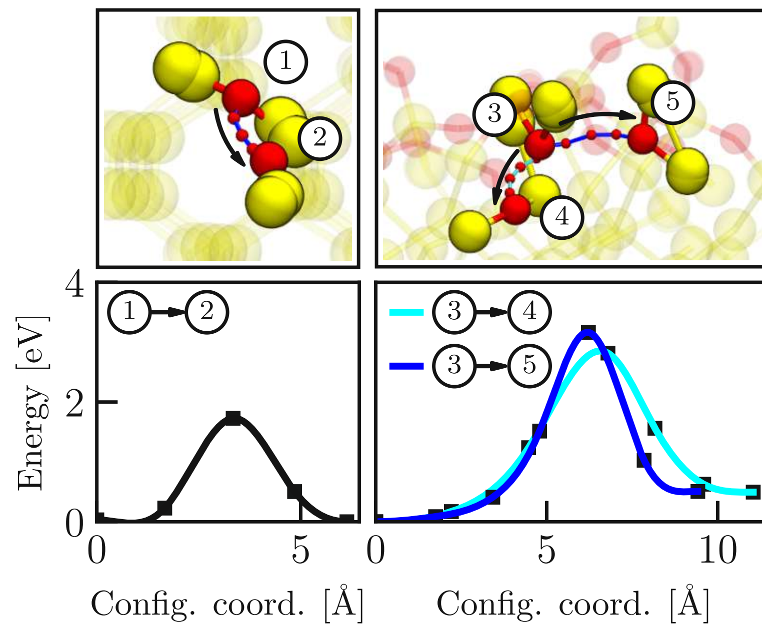


Figure 4.10: Energy barriers for thermal diffusion of O in Si bulk (left) and from a surface oxide layer (right) as obtained by NEB calculations. The trajectories of the diffusion are indicated by solid blue and cyan lines in the top panels and the resulting energy barriers are shown in the respective lower panels. Intermediate configurations along the trajectories are depicted as smaller O atoms. The results show that thermal diffusion of O from the oxidized surface layers is strongly inhibited compared to the diffusion in bulk Si and would only contribute marginally to the overall oxidation process that is almost exclusively driven by $O_2$ diffusion through the oxide.

transition region between the crystalline and amorphous structures since it offered alternative positions for O atoms. Two examples of possible diffusion paths for one O atom were calculated and yielded energy barriers of at least 2.8 eV, or a reaction rate of $4 \times 10^{-4}\,s^{-1}$. Keeping the experimental oxidation growth rate of about 1 Å/s [203] for the initial stage of thermal oxidation of Si in mind, only a small contribution to the overall growth rate by thermal migration of single O atoms is expected. However, migration of O atoms is required for the dissociation of molecular precursors and thus still plays an important role in the oxidation process. The observation of slow oxygen migration in the amorphous surface layers together with an increased adsorption barrier explains the decrease of oxidation rate as the oxidation proceeds. In this manner, the oxide growth rate decreases gradually as the dominant oxidation mechanism transitions from spontaneous surface reactions to precursor reactions and finally into the non-reactive $O_2$ diffusion regime.

#### 4.2.7.2 $O_2$ diffusion through the oxide

Diffusion of $O_2$ through thicker oxide layers during thermal oxidation as proposed by [156] was thoroughly investigated in other studies [157, 158, 159, 160, 161, 162, 163,

Die approbierte gedruckte Originalversion dieser Dissertation ist an der TU Wien Bibliothek verfügbar.
The approved original version of this doctoral thesis is available in print at TU Wien Bibliothek.
TU WIEN Bibliothek Your knowledge hub

164, 204, 205, 206]. The diffusion barrier was found to be extremely sensitive to the local structural topology which is reflected by a wide spread of DFT calculated values from 0.5 eV to 2.8 eV [159, 204]. Experimentally, values between 0.7 and 1.6 eV [206] were found for oxide films produced in various ways. Our own NEB calculations of $O_2$ diffusion processes agree nicely with previous theoretical and experimental results and yielded barriers between 0.7 and 2 eV. Hence, molecular stability as well as sufficient diffusibility of $O_2$ in silicon dioxide can be safely assumed also within the framework of our calculations.

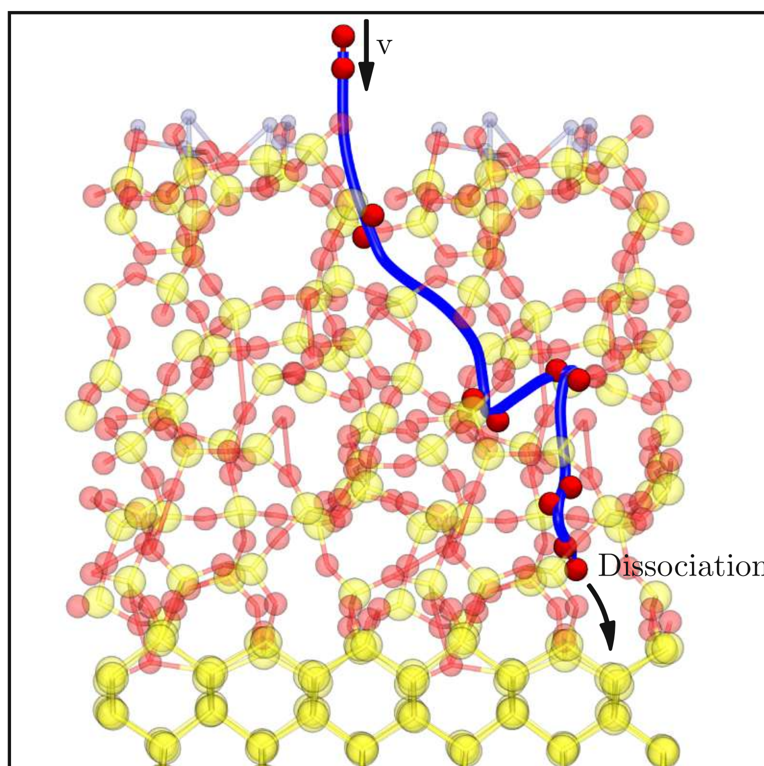


Figure 4.11: Diffusion of $O_2$ in a-$SiO_2$ is easily possible for thicker oxide layers. The non-reactive incorporation and migration through the oxide layer is shown by the results of an AIMD simulation with a simulation time of 3 ps. An initial velocity of 800 m/s was assigned to the $O_2$ molecule. The trajectory of the center of mass of the molecule is depicted by a solid blue line. The molecule eventually reaches the Si/$SiO_2$ interface and dissociates, see Fig. 4.12.

We observed the non-reactive incorporation of $O_2$ molecules on a 20 Å thick oxide layer that was obtained by a melt and quench procedure [193]. As shown in Fig. 4.11, a seamless migration through the oxide could be sampled in an AIMD simulation with a simulation time of 1 ps. Again, the molecules' initial velocity was set to 1000 m/s. Without interaction, the $O_2$ entered the oxidized surface and migrated along a random path determined by deflections at the $SiO_2$ structure. These results show that the molecular state of $O_2$ represents a stable configuration in ultra-thin layers of a-$SiO_2$.

Die approbierte gedruckte Originalversion dieser Dissertation ist an der TU Wien Bibliothek verfügbar.
The approved original version of this doctoral thesis is available in print at TU Wien Bibliothek.
TU WIEN Bibliothek Your knowledge hub

As assumed within the Deal-Grove model [156], the oxidation rate is now governed by the $O_2$ diffusion rate.

#### 4.2.7.3 $O_2$ dissociation at the interface

In the $O_2$ diffusion regime, further oxidation of the Si substrate happens at the $Si/SiO_2$ interface upon dissociation of the $O_2$ molecule [156] as could be confirmed within our simulations by another set of AIMD calculations.

An $O_2$ molecule was placed in the transition region between the amorphous oxide and its crystalline substrate. Due to lattice distortions, some Si atoms in the transition region possess strained bonds or even dangling bonds[11], cf. Fig. 4.9. These dangling bonds are known to affect the reliability of semiconductor devices and are therefore usually passivated with H after the oxidation [193, 207]. However, the simulations showed that these atoms were the preferred dissociation spots. The initial velocity of the $O_2$ molecule was set to zero in order to verify the feasibility of a spontaneous reaction. As shown in Fig. 4.12, the $O_2$ molecule spontaneously dissociates via essentially the same charge transfer process as in the dissociative chemisorption at the Si surface, cf. Fig. 4.5. In addition, further evidence for a barrierless dissociation was obtained by another NEB calculation. Here, $O_2$ was placed above the transition region in order to include a short diffusion path of 4 Å preceding the actual dissociation. The migration toward the strained bond was governed by a comparably low diffusion barrier of 0.2 eV. In Fig. 4.12, the beginning of the dissociative process is indicated by a strong decrease of the potential energy surface. The large energy gain of 9.4 eV could be justified by a complex reconfiguration at the interface in which multiple bonds with considerable binding energies break (O-O: 2.1 eV; Si-Si: 4.9 eV) and form (Si-O: 6.5 eV). Additionally, the molecular configuration contained the incorporation energy of the oxygen molecule in the oxide layer which was evaluated to be 0.4 eV in bulk $SiO_2$ by DFT calculations [208]. During this stage, the oxide growth rate is not limited by the supply of oxygen to the surface anymore but by the $O_2$ diffusion rate through the oxide and is thus certainly much slower compared to the initial oxidation, as assumed within the Deal-Grove model [156].

### 4.2.8 Properties of the $Si/SiO_2$ interface structures

A comparison between the stepwise oxidation and the melt-and-quench technique is shown in Fig. 4.13. Due to the implicit constrains of the melt-and-quench technique, the resulting interfaces are more ordered, meaning, the bond lenghts are distributed more uniformly and the surface is less rough. The stepwise generated interface is characterized by elongated bonds, large interfacial strains and a large number of O-coordinated Si atoms. The formation of a 0.5 nm thick transition region is common for both techniques. Furthermore, we compare our results to crystalline interfaces which have been used in many earlier studies [209, 169, 180]. As can be seen, the transition region of crystalline interfaces is much smaller, and, obviously, there is no surface roughness at all.

[11]The calculation here is done on a structure without dangling bonds.

Die approbierte gedruckte Originalversion dieser Dissertation ist an der TU Wien Bibliothek verfügbar.
The approved original version of this doctoral thesis is available in print at TU Wien Bibliothek.
TU WIEN Bibliothek Your knowledge hub

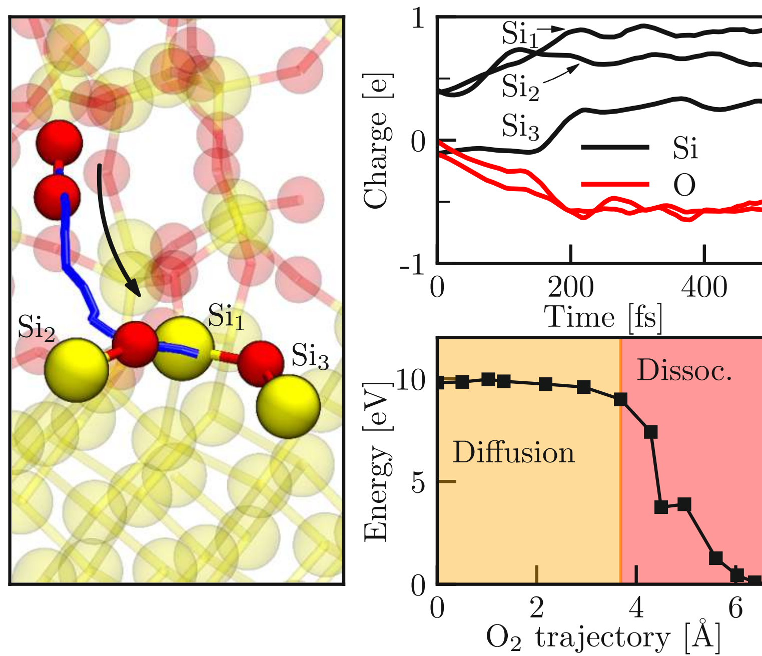


Figure 4.12: $O_2$ dissociation at the $Si/SiO_2$ interface. The left panel shows the trajectory of the center of mass of the $O_2$ molecule (solid blue line) together with the initial (molecular) and final (dissociated) configurations of the NEB calculation. The Mulliken charges for the spontaneous dissociation as captured within an AIMD simulation are depicted in the top right panel. The Mulliken analysis reveals another charge transfer of $-e$ that strongly resembles the dissociative reactions at the surface during the initial stage of oxidation, cf. Fig. 4.5. The associated charges of the $Si_1$ and $Si_2$ atoms show an offset due to the implications of the interface, cf. Fig. 4.9. The potential energy surface of this process is displayed in the lower right panel and indicates diffusion along a 4 Å long trajectory that is only inhibited by a low barrier of 0.2 eV. In addition to the AIMD results, the NEB calculation provides evidence for a spontaneous dissociation as soon as the molecule reached the dissociation spot.

To summarize, the interfacial structures that are obtained from our novel oxidation approach are more realistic than previous modeling attempts. We find streched Si-O bonds that are increased by up to 12%, which also indicates a larger probability to find defects and/or dangling bonds at the interface. The interfaces are rougher, less ordered and strongly strained, while still in line with structural data from experiments (cf. Fig. 4.8)

Die approbierte gedruckte Originalversion dieser Dissertation ist an der TU Wien Bibliothek verfügbar.
The approved original version of this doctoral thesis is available in print at TU Wien Bibliothek.
TU Bibliothek WIEN Your knowledge hub

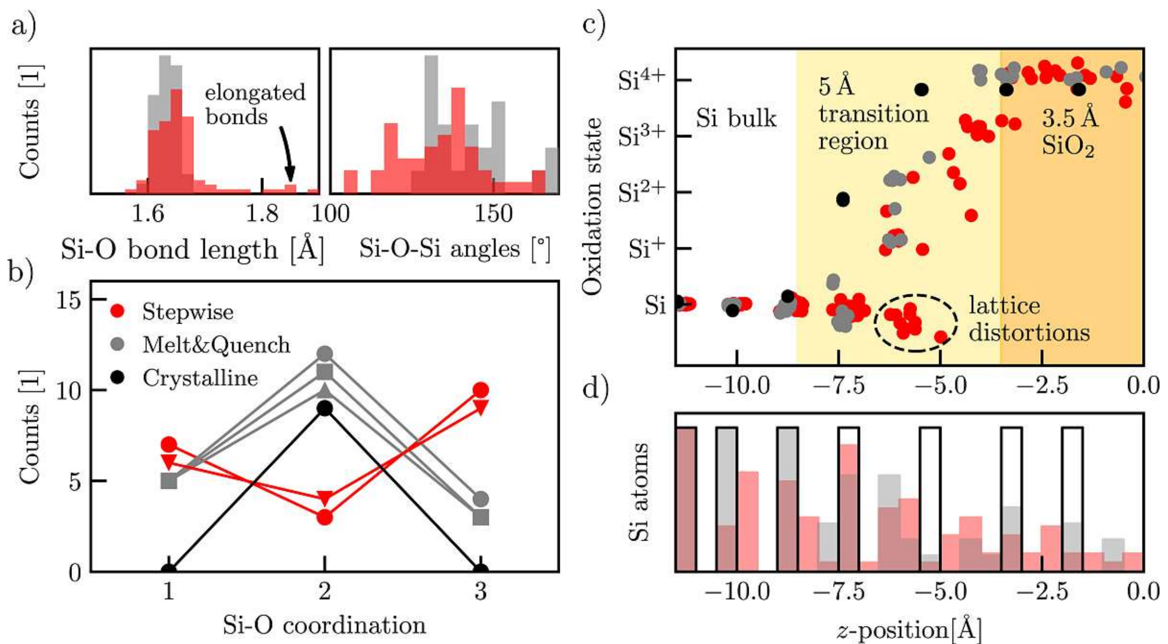


Figure 4.13: Comparison between interfaces obtained via various modeling techniques: the stepwise oxidation approach from this work (red) is compared to the melt and quench method [193] and to ad-hoc crystalline Si-quartz interfaces (black). (a) Distribution of bond lengths and angles around the interface. The stepwise generated interface shows bonds that are elongated by up to 12% and strongly distorted Si–O–Si angles that indicate large strain. (b) O-coordination of Si atoms near the interface. The melt and quench method produced mostly two-fold O-coordinated Si reminiscent of crystalline interfaces. In contrast, the stepwise approach yields higher coordinated Si atoms. (c) Oxidation states as obtained by a Mulliken charge analysis of Si atoms vs. their respective $z$-position. Amorphous $SiO_2$ is indicated by fully oxidized Si atoms (oxidation state +4). The oxidation states in the roughly 5 Å thick transition region can only be assigned approximately. The stepwise oxidation method shows negative oxidation states that are indicative of strong lattice distortions. (d) Distribution of Si atoms vs. their respective $z$-position. The stepwise approach inherently yields a broader distribution indicating a larger degree of disorder compared to the melt and quench approach in which non-oxidized Si atoms are artificially fixed during the MD calculation. A number of interfaces were compared, however, for the sake of simplicity only one representative configuration is shown in (a), (c) and (d) as the results were very similar for each method.

Die approbierte gedruckte Originalversion dieser Dissertation ist an der TU Wien Bibliothek verfügbar.
The approved original version of this doctoral thesis is available in print at TU Wien Bibliothek.
TU WIEN Bibliothek Your knowledge hub

## 4.3 Machine learning force field for the thermal oxidation of silicon

*The results presented in this section have been published in [LC2]. Text and figures are adapted from there.*

We have seen above that AIMD is an excellent tool for the generation of credible Si/$SiO_2$ interface structures. The downside are the extremely high computational costs. Given recent advances in machine learning (ML) that, among many other applications, led to the development of ML-based interatomic potentials, we decided to explore the possibilities of machine learning force fields (MLFF) for our purpose.

From the methodological perspective, the process of thermal oxidation offers an interesting use case for machine learned interatomic potentials, as our MLFF is universally suitable for gaseous oxygen, crystalline Si, and amorphous $SiO_2$. Machine learning techniques enable overcoming the strong limitations on cell sizes and simulation times, the typical drawbacks of *ab-initio* calculations, while keeping the accuracy of the results practically unchanged [137, 210]. The ability to enlarge the system size and for simulating on larger time scales allows for the investigation of the growth kinetics of the oxidation process and for the generation of even more realistic models of Si/$SiO_2$ interfaces, including long-range disorder and interface roughness. Furthermore, we extend our investigations from flat Si surfaces to more complex surface structures such as cylindrical Si nanowires. As shown in Fig. 4.14, our ML approach allows modeling of the thermal oxidation process within dynamic simulations starting from entirely oxygen-free silicon surface structures. Within the MD simulation, these structures are exposed to an $O_2$ gas which reacts with the surface and forms a coating layer of amorphous $SiO_2$.

### 4.3.1 Tools and Methods

Training of an MLFF typically requires the combined use of descriptors [138], machine learning algorithms [139], and high-accuracy training data. Methods and computational techniques employed in this work are described in the following.

#### 4.3.1.1 Machine Learning Force Field

Our MLFF is implemented within the Gaussian approximation potential (GAP) method [139]. Similar to other ML models employed in the context of interatomic potentials, GAP completely neglects the electronic structure of a given system and assumes that the potential energy can be determined solely from the atomic configuration. GAP represents the total potential energy as the sum of local energy contributions from each atom. These local contributions are obtained by comparing a given local atomic environment to the local atomic environments of the atomic configurations available in the training dataset. The training dataset contains a number of atomic systems along with the corresponding energies and forces taken from any

Die approbierte gedruckte Originalversion dieser Dissertation ist an der TU Wien Bibliothek verfügbar.
The approved original version of this doctoral thesis is available in print at TU Wien Bibliothek.
TU WIEN Bibliothek Your knowledge hub

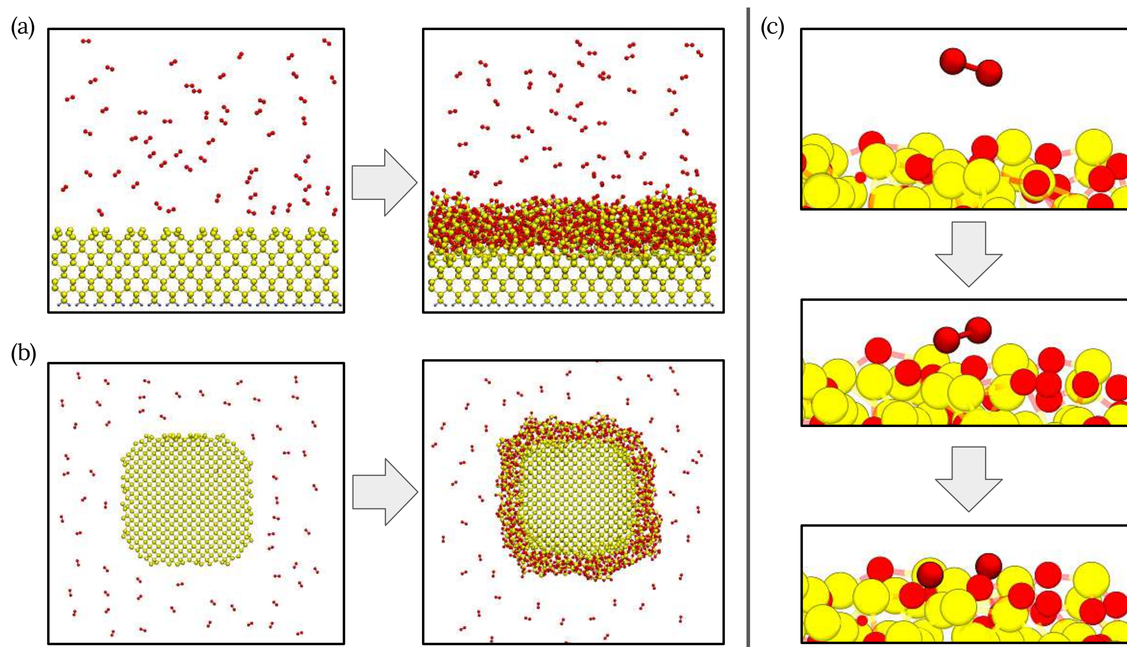


Figure 4.14: Overview of the simulation procedure. **(a)** Reconfigured Si(100) surfaces or **(b)** Si nanowires are exposed to gaseous oxygen within molecular dynamics calculations. **(c)** The $O_2$ molecules spontaneously react with the surface and dissociate to form an oxide coating around the surface. After every 10.000 steps ($\Delta t = 1\,\mathrm{fs}$), the structure is optimized to avoid heating (each dissociation event releases energy), and $O_2$ molecules in the gas phase are refilled to maintain the pressure according to an ideal gas law.

other computational method that can be used to calculate the potential energy of an atomic system. GAP learns to estimate the energy of local atomic environments in the training process based on this data. Analogous to this procedure, GAP can also learn and estimate forces which further reduces the amount of necessary structures in the training dataset.

The usage of unbiased metrics is essential for the training data of a ML model and necessitates the usage of descriptors, see Sec. 3.4. The user-defined parameters used in this work are given in App. A.1.

#### 4.3.1.2 DFT training data

Our MLFF is trained on data from more than 900 density functional theory (DFT) calculations. Underlying structures include single atoms, dimers, bulk structures of Si and $SiO_2$, as well as oxidized Si surfaces and nanowires with various oxygen coverage. Data for the initial training set is obtained by the stepwise oxidation process as presented in [LC4]. In this approach, the starting points are oxygen-free Si surface structures which become gradually oxidized within AIMD calculations. Oxygen is provided by placing $O_2$ molecules in the vicinity of the Si surface. A comprehensive

Die approbierte gedruckte Originalversion dieser Dissertation ist an der TU Wien Bibliothek verfügbar.
The approved original version of this doctoral thesis is available in print at TU Wien Bibliothek.
TU Bibliothek WIEN Your knowledge hub

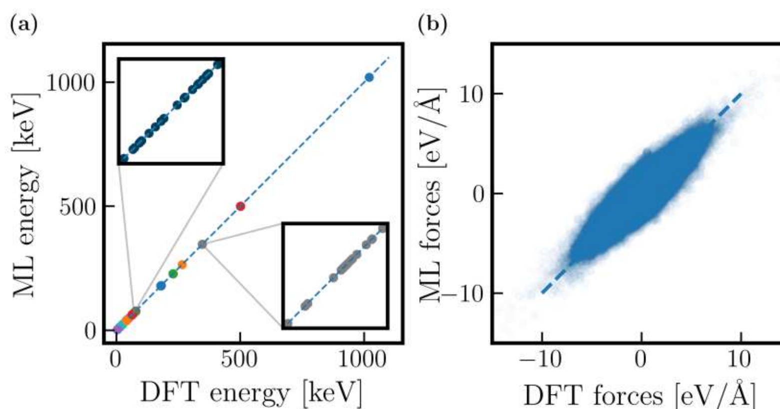


Figure 4.15: Comparison between DFT and the ML model for 400 Si/oxide structures. **(a)** The values of the energies show excellent correlation over the full range of structures as indicated by dashed blue lines with slope 1. Blue and grey points shown in the insets correspond to oxidized Si(100) surfaces and oxidized nanowires, respectively. The MAE is below 10 meV/atom. **(b)** Good agreement between the two methods is also obtained for the inter-atomic forces with an MAE below 0.16 eV/Å .

overview of the structures contained in the training dataset together with a detailed description of their generation can be found in App. A.2.

All density functional theory calculations are carried out using the CP2K package [211], a code that uses the mixed Gaussian and plane waves approach (GPW). We use double-$\zeta$ Gaussian basis set for all atom types and the well-established Goedecker-Teter-Hutter (GTH) pseudopotentials to represent closed-shell electrons [212, 213]. The electron density is expanded using a plane-wave basis with a cutoff of 650 Ry. The exchange-correlation energy is obtained by means of the semilocal generalized gradient approximation (GGA) functional PBE. Atomic relaxations were carried out with a force convergence criterion of 15 meV/Å. Within the AIMD simulations, the total energy was conserved (microcanonical or NVE ensemble) and the total spin was restricted to 0.

### 4.3.2 Comparison to DFT

Validation of the ML model is done on a set of structures which are similar to the training dataset, i.e. structures of oxidized surfaces and nanowires. We compare the energies and forces predicted by DFT with the values from the ML model, see Fig. 4.15. The deviations are estimated by the mean absolute error (MAE) between both methods. The MAE in energy is below 10 meV/atom, and the forces are predicted with an accuracy of 0.16 eV/Å. The clear linear correlation for systems with 200 to 5000 atoms indicates a very good agreement between DFT and the MLFF and allows to rule out systematic errors between the two.

Die approbierte gedruckte Originalversion dieser Dissertation ist an der TU Wien Bibliothek verfügbar.
The approved original version of this doctoral thesis is available in print at TU Wien Bibliothek.
TU Bibliothek WIEN Your knowledge hub

### 4.3.3 Structural properties

The ML model can be further validated by the structural qualities of the resulting structures, as shown in Fig. 4.16. The results refer to an oxidized Si surface which measures $6\times6\,\text{nm}^2$ in plane and exhibits an oxide thickness of around 1 nm. While the mean Si–O bond length of 1.63 Å is in line with experimental values of bulk $SiO_2$ [186, 187], there are a number of strained bonds with a length of more than 1.8 Å. These bonds are exclusively found at the interface indicating a considerable strain in this region.

An important result is the formation of $SiO_4$ tetrahedrons, the building blocks of $SiO_2$, indicating that even ultra-thin oxide layers already exhibit the structural properties of bulk $SiO_2$ [LC4]. The mean O–Si–O bond angle (Fig. 4.16b) matches the ideal tetrahedral bond angle of 109.47° which means that the tetrahedrons are rigid and form already in an early stage of oxidation. The tendency to find enlarged O–Si–O bond angles (the angles between two tetrahedrons) at the interface (up to 140°) agrees with the previous observations of such interface structures [188] [LC4]. Further evidence for the formation of $SiO_2$ is provided by a coordination number analysis, see Fig. 4.16c and Fig. 4.16d. Most of the Si atoms in the oxide are fourfold coordinated by oxygen. Lower O-coordination can only be found at Si atoms close to the Si/oxide interface. The interface is not sharp, but represented by a transition region of 0.5 nm thickness. Within this region, the amount of oxygen increases steadily such that the O-coordination of the Si atoms increases from 0 to 4 in growth direction. Above the transition region, all Si atoms are four-fold O coordinated and integrated in a $SiO_4$ tetrahedron. These results are not only in line with the AIMD simulations from [LC4], they also agree with transmission electron microscope (TEM) images [186, 214], electron-energy-loss spectroscopy (EELS) [195, 215], and photoemission studies [186, 216].

### 4.3.4 Growth kinetics

As found experimentally [165] and confirmed theoretically by means of AIMD calculations [LC4], the oxidation rate decreases strongly as soon as an oxide layer has formed on the initially clean Si surface. As long as the Si surface is only sparsely oxidized, that is, the surface still shows unoxidized Si dimers, $O_2$ molecules can spontaneously adsorb and dissociate at the surface. During this phase, the oxidation rate is limited only by the amount of oxygen available to the surface.

At a later stage, in which the surface is fully covered by an oxide film, the oxidation rate decreases as the limiting factor is now the diffusion of O into deeper layers of Si. The diffusion is necessary in order to make room for further dissociative surface reactions. This behavior is also captured by the MLFF. We evaluate the position of the $Si/SiO_2$ interface $z_\mathrm{i}$ and oxide surface $z_\mathrm{s}$ by averaging the $z$-position of the five lowest and the five highest oxygen atoms, respectively. The oxide thickness $t$ is then the difference between surface and interface $t = z_\mathrm{i} - z_\mathrm{s}$. Evaluating the thickness of the oxide layer by this procedure in an MD run that simulates the thermal oxidation starting from a clean Si surface allows to estimate $t$ as a function

Die approbierte gedruckte Originalversion dieser Dissertation ist an der TU Wien Bibliothek verfügbar.
The approved original version of this doctoral thesis is available in print at TU Wien Bibliothek.
TU WIEN Bibliothek Your knowledge hub

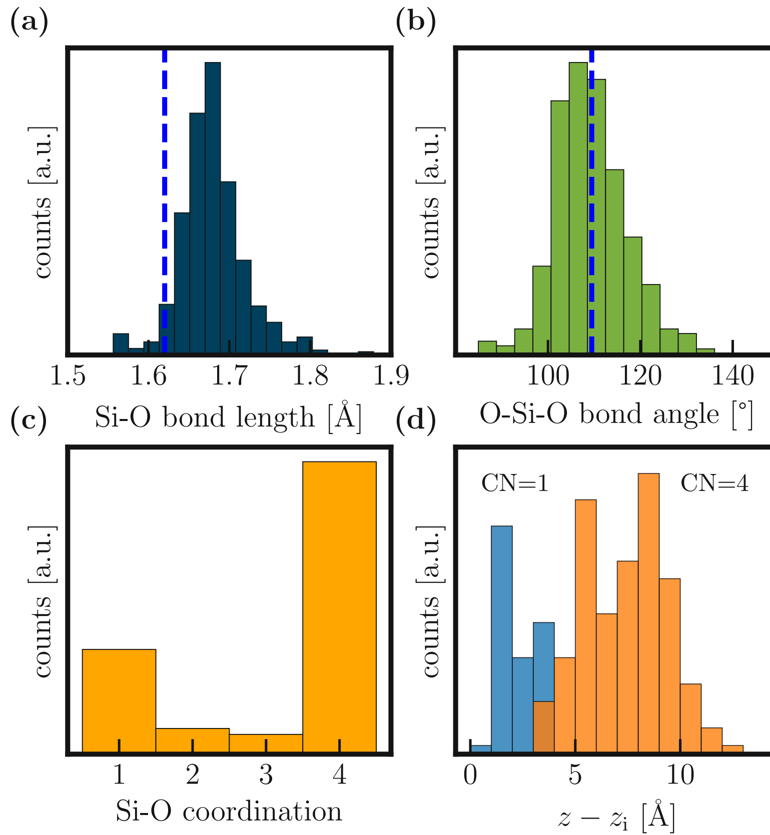


Figure 4.16: Geometric measures indicating the quality of the Si/$SiO_2$ structures. The results are shown for a representative interface structure with an effective oxide thickness of 1 nm. **(a)** The Si-O bond lengths (average 1.65 ) agree reasonably well with experimental values (dashed line) of 1.62 of bulk $SiO_2$ [187, 186]. **(b)** Similar agreement is found for the O–Si–O bond angles which match the optimal tetrahedral bond angle of 109.47° (dashed line). **(c)** The O-coordination for Si atoms ranges from 1 to 4, as expected for interfacial structures. **(d)** Position of Si atoms with one O neighbor (CN=1) and four O neighbors (CN=4). Fourfold O-coordinated Si are found in $SiO_4$ tetrahedrons in the oxide while lower coordinations correspond to Si atoms close to the interface.

of time as shown in Fig. 4.17.[12] The oxidation rate has a maximum at the beginning and decreases significantly as soon as the surface is saturated with oxygen. At this point, $O_2$ molecules can not dissociate spontaneously anymore but adsorb onto the surface where they eventually dissociate after a few ps. This behavior explains the experimentally observed decrease in oxidation rate [165] and is in line with previous observations from [170, 217, 218] [LC4].

[12] We artificially enhance the growth rate by exposing the Si surface to a large number of $O_2$ molecules, corresponding to a pressure in the $O_2$ gas of $p = 50\,\text{bar}$. This is necessary as the actual oxidation time (in the range of seconds) is still well outside the scope of feasible calculations even when using the MLFF.

Die approbierte gedruckte Originalversion dieser Dissertation ist an der TU Wien Bibliothek verfügbar.
The approved original version of this doctoral thesis is available in print at TU Wien Bibliothek.
TU WIEN Bibliothek Your knowledge hub

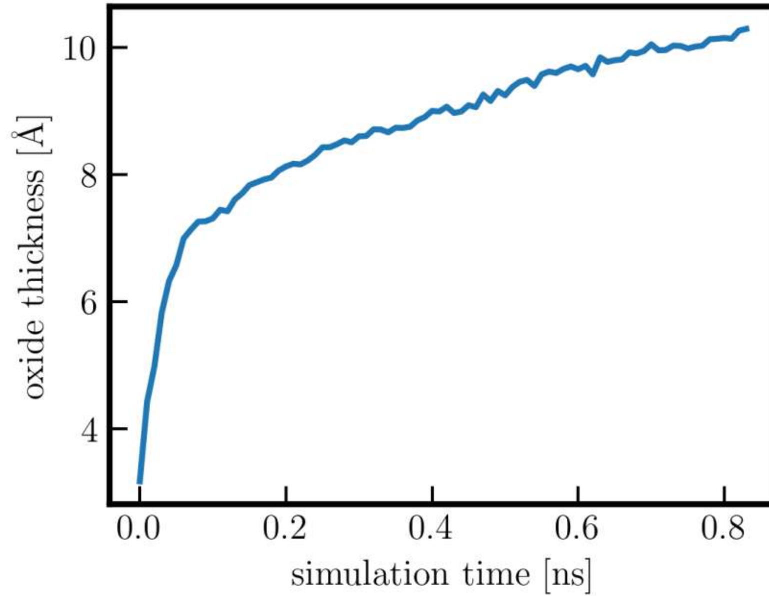


Figure 4.17: Oxide thickness during dynamic oxidation of Si as a function of simulation time. Initially, fast oxidation is enabled by spontaneous surface reactions. After the surface is saturated with O, the dominant reaction mechanism changes to molecular precursor mediated dissociation, a process associated with slower oxidation rates [170].

### 4.3.5 Interface quality

Numerous experiments have shown that the growth of $SiO_2$ on a Si substrate results in a significant interface and surface roughness [219, 220]. In the initial oxidation regime, the roughness increases with the oxide thickness but saturates after the oxide layer exceeds 10 nm. At this point, the oxidation rate becomes constant and the process is governed by $O_2$ diffusion [220], as assumed within the Deal-Grove model [156], instead of $O_2$ surface reactions which enable a faster oxidation in the early oxidation stages [LC4].

In order to investigate the interface roughness, we oxidize a $6{\times}6\,\text{nm}^2$ Si surface by means of the MLFF and depict the roughness of one representative $Si/SiO_2$ interface resolved in the in-plane directions in Fig. 4.18. For this analysis, we take the $z$-position of the lowest oxygen atom in each lateral 2D bin and connect their coordinates. The interface deviates from the average interface position $\bar{z}_\text{i}$ by up to 2.5 Å with an average deviation of $R_a$=0.57 Å. Typically, the interface roughness is characterized by the root mean square deviations for which we find $R_q = 0.79$ in reasonable agreement with the measured values of $\approx 0.5$ Å reported in [220].

Furthermore, we find a mass density of around 2.5 g/cm$^3$ in the oxide layer which slightly overestimates experimental values of ultra-thin a-$SiO_2$ reported in the range of 2.24 to 2.36 g/cm$^{-3}$ [186]. On the other hand, the mass density in the interface region complies with the experimental values from [186].

Die approbierte gedruckte Originalversion dieser Dissertation ist an der TU Wien Bibliothek verfügbar.
The approved original version of this doctoral thesis is available in print at TU Wien Bibliothek.
TU WIEN Bibliothek Your knowledge hub

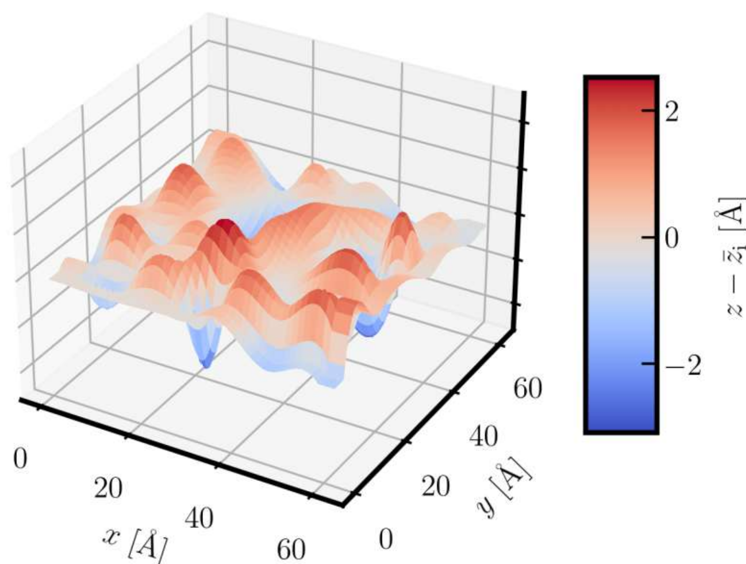


Figure 4.18: Interface roughness as resulting due to the dynamic oxidation process governed by random adsorption trajectories. The RMS roughness of the interface is found to be $R_\mathrm{q} = 0.79$.

### 4.3.6 Comparison to classical force field

In order to further validate our ML force-field, we compare it to one of the most commonly used classical force fields, namely the reactive force field (reaxFF) from Ref. [221]. A comparative data set is generated by dynamically oxidizing a $3 \times 3\,\mathrm{nm}^2$ Si surface with the same initial parameters of position and velocity from identical starting configurations. The simulation time is set to 1.4 ns integrated over 1.4 million time steps. As before, after every $10^4$ steps, new oxygen molecules are added to the vacuum above the surface, to keep the pressure at 50 bar.

Analyzing a number of geometric properties gives results summarized in Tab. 4.1. In terms of two- and three-body geometric measures, our MLFF performs slightly better than the reaxFF potential. While the mean O–Si–O bond angles are close to the ideal tetrahedral angle, the reactive force field gives mean Si–O bond lengths of 1.55 Å (compared to the MLFF value of 1.68 Å and the experimental value of 1.62 Å [186, 187]). Furthermore, we compare the volumetric mass density in the interface region $\rho_\mathrm{IF}$ and in the oxide layer $\rho_\mathrm{OX}$. As mentioned before, our MLFF slightly overestimates the density in the oxide layer but reproduces the density in the interfacial transition region. ReaxFF on the other hand, gives densities about 10% larger than experimental values [186], in line with implications from shortened bond lengths, in both the interface and the oxide regions of the interface structure.

The growth kinetics, however, differ substantially between the two force fields. The number of oxygen molecules that dissolved at the surface is 15 % lower when using reaxFF. On the other hand, reaxxFF overestimates the diffusion of oxygen which leads to a low-density distribution of O atoms among the Si atoms in the crystal.

Die approbierte gedruckte Originalversion dieser Dissertation ist an der TU Wien Bibliothek verfügbar.
The approved original version of this doctoral thesis is available in print at TU Wien Bibliothek.
TU WIEN Bibliothek Your knowledge hub

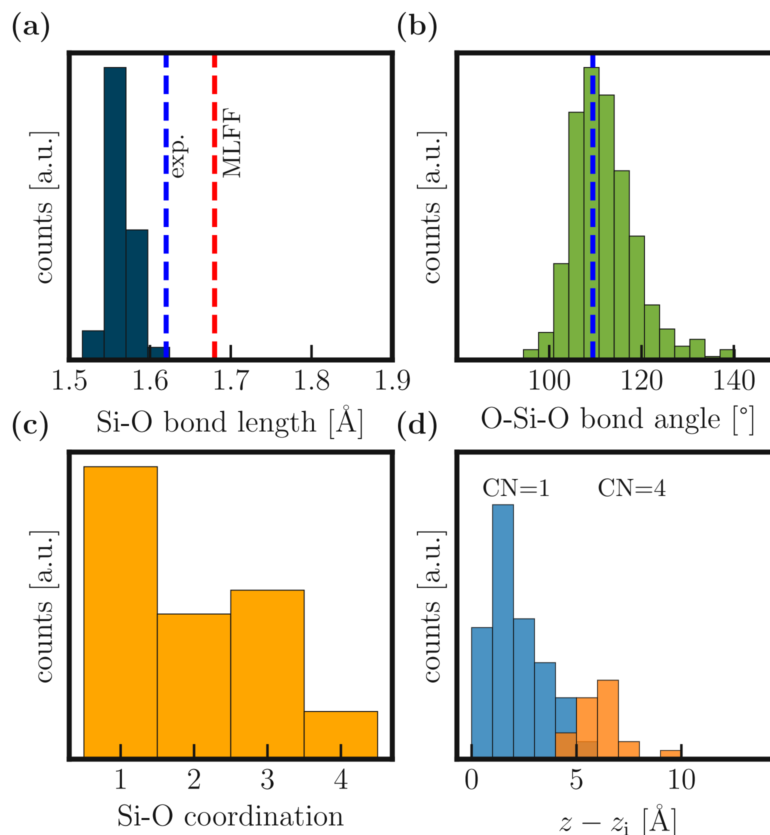


Figure 4.19: Structural properties of a $Si/SiO_2$ interface generated by the reactive force field from Ref. [221]. The plot is analogous to Fig. 4.16. For comparison, the experimental and averaged MLFF values for the bond lengths and the tetrahedral angles are shown as blue and red dashed lines, respectively. With respect to the MLFF and experiments [186], reaxFF slightly underestimates bond lengths while the tetrahedral angles are well captured. The properties of the interface, however, do not match experimental expectations, as O diffusion is overestimated by reaxFF. The number of four-fold O-coordinated Si is very low; on the other hand, there are many Si atoms with only one O neighbor. This results in a thicker interface and a thin oxide layer.

The result is a very large interface (the transition region $d_{\mathrm{IF}}$ measures about 1 nm and the oxide thickness $d_{\mathrm{OX}}$ is only 4 Å), with lower than expected Si–O coordination, as shown in Fig. 4.19. To summarize, the structures obtained by reaxFF are in strong contrast to the experimental findings of [186, 214, 195, 215, 216], while the MLFF – similar to AIMD – reproduces much more realistic interface structures.

### 4.3.7 Dangling bond density

Finally, the last test we subject our model to is the determination of the dangling bond density resulting from the oxidation process. In the most simple definition, a

Die approbierte gedruckte Originalversion dieser Dissertation ist an der TU Wien Bibliothek verfügbar.
The approved original version of this doctoral thesis is available in print at TU Wien Bibliothek.
TU WIEN Bibliothek Your knowledge hub

Table 4.1: Comparison between a classical reactive force field [221], AIMD simulations, the herein presented MLFF, and (if available) experimental values. Basic two- and three-body measures like Si–O bond lengths and O–Si–O angles are relatively well captured by all approaches, with slightly deviating values from reaxFF. In terms of volumetric mass density, we compare the density in the interface region $\rho_{IF}$ and in the oxide layer $\rho_{OX}$. Clear differences in the interface properties are indicated by the thickness of the interface $d_{IF}$ and oxide thickness $d_{OX}$ obtained after 1.4 ns of dynamic oxidation at 1000 K and 50 bar.

| | reaxFF | AIMD [LC4] | MLFF | experiment [186, 214, 195] |
|---|---|---|---|---|
| Si–O length [Å] | 1.57 | 1.66 | 1.68 | 1.62 |
| O–Si–O angle [°] | 112.28 | 109 | 109.45 | 109.47 |
| $\rho_{IF}$ [g/cm$^3$] | 2.45 | 2.34 | 2.37 | 2.36–2.41 |
| $\rho_{OX}$ [g/cm$^3$] | 2.65 | 2.5 | 2.5 | 2.24–2.36 |
| $d_{IF}$ [nm] | 1 | 0.5 | 0.5 | 0.5 |
| $d_{OX}$ [nm] | 0.4 | - | 1 | - |

dangling bond corresponds to a missing neighbor, that is every Si atom with less than 4 and every O atom with less than two neighboring atoms is identified as a dangling bond.

By means of this simple analysis, we detect at least one dangling bond in 96 % of the obtained interface structures. Typically, these dangling bonds do not vanish if the structure is relaxed within a subsequent DFT optimization, as this requires the breaking of other bonds which is unlikely to happen. On average, we find 2.9 dangling bonds in structures grown on a $1.5\times1.5\text{nm}^2$ Si surface area, corresponding to a dangling bond density of $1.3/\text{nm}^2$ ($130 \times 10^{12}\text{cm}^{-2}$).

Compared to the experimentally determined defect density of $0.05/\text{nm}^2$ ($5 \times 10^{12}\text{cm}^{-2}$) [222], our MLFF seems to overestimate the number of defects by almost two orders of magnitude. However, only electric spin resonance (ESR) active defects (depending on the applied bias and the location of the defect in the band gap) appear in the ESR measurement of [222]. Another important difference between simulation and experiment is the presence of hydrogen, which is unavoidable in reality, however, completely absent in our structures. Since atomic hydrogen passivates dangling bonds [223], and therefore reduces the dangling bond density, a significant impact on the experimentally obtained value can not be ruled out. Furthermore, we suspect that the density of dangling bonds in the simulated structures could be reduced by equilibrating the structure at elevated temperatures for some µs. Given these uncertainties, we conclude that our MLFF produces structures with significantly increased

TU Bibliothek, WIEN Your knowledge hub
Die approbierte gedruckte Originalversion dieser Dissertation ist an der TU Wien Bibliothek verfügbar.
The approved original version of this doctoral thesis is available in print at TU Wien Bibliothek.

dangling bond density, although a direct comparison to values inferred from ESR measurements is not valid.

A detailed analysis of the dangling bonds in the simulated structures that goes beyond the simple coordination analysis above requires thorough investigations by means of DFT. Within DFT, one can determine trap levels and relaxation energies [224] and thereby investigate whether the defects are ESR-active. We leave such extensions for the future.

TU WIEN Bibliothek Your knowledge hub
Die approbierte gedruckte Originalversion dieser Dissertation ist an der TU Wien Bibliothek verfügbar.
The approved original version of this doctoral thesis is available in print at TU Wien Bibliothek.

# Chapter 5

# Valley and spin splitting

*Parts of the results presented in this section have been published in [LC3]. Text and figures are adapted from there.*

After dealing with the fundamentals of Si spin qubits in Chapter 1 and explaining our approach to computation and structure generation in Chapters 3 and 4, we are ready to investigate properties of conduction band electrons in the Si heterostructures by means of DFT. First, in the following section, the splitting between the (spin-degenerate) valley states mediated by a coupling at the interface is evaluated. Subsequently, the wavevector-dependent splitting of the spin states (spin splitting) is examined in Sec. 5.2.

## 5.1 The 2DEG subbands and the valley splitting

It was shown in Sec. 2.2.3 that the remaining valley degeneracy of the Si conduction band can be lifted due to coupling mediated by the confinement potential. For spin qubit applications, the resulting valley splitting should be as large as possible (but at least above 200 µeV) in order to provide a clean two-level system comprised of the two spin states in the lowest valley [9]. The concepts of analytical theories to understand the bandstructure of crystalline materials, such as effective-mass theory (EM), have been successfully employed to obtain an intuitive understanding of valley splitting [55, 67]. Although many ideas of EM theory are transferable to interpret DFT calculations, the language of the modeling techniques is not fully compatible. In order to bridge this gap, we now review the properties of our *ab-initio* model and the interpretation of its results, while contrasting the concepts of EM theory and DFT.

### 5.1.1 Properties and interpretation of the DFT model

As demonstrated (see Sec. 2.2.3 for details), the valley splitting is expressed within the effective mass approach as

$$\Delta = \langle \Psi_+ | V_{\mathrm{qw}} | \Psi_- \rangle, \tag{5.1}$$



Die approbierte gedruckte Originalversion dieser Dissertation ist an der TU Wien Bibliothek verfügbar.
The approved original version of this doctoral thesis is available in print at TU Wien Bibliothek.
TU Bibliothek WIEN Your knowledge hub

describing coupling between the $+z$ and $-z$ valleys via the quantum well potential in a perturbative picture. In contrast, the DFT outcome does not allow for a rigorous assignment of these quantities. Within DFT, we do not have access to the pure valley states, but only to the resulting coupled states. Furthermore, there is no well-defined distinction between the Bloch part and envelope, and the extraction of $\Phi(z)$ is therefore always accompanied by some uncertainties.

In an ideal well without electric field, the DFT wavefunctions correspond to the symmetric and anti-symmetric solutions of the lowest orbital [9]. However, in a real gated Si quantum device, the electron resides in an electrostatically defined quantum dot. Therefore, the 2DEG is confined to one interface by the external electrostatic potential. We apply an external electric field of $\mathbf{F} = F_z \mathbf{e}_z = 10\,\mathrm{mV/nm}$ in the direction perpendicular to the interfaces. This ensures realistic modeling conditions and allows to investigate the impact of interface qualities like roughness and disorder. The two lowest conduction band wavefunctions are shown in Fig. 5.1a. Since the properties of a periodic heterostructure (without lateral confinement) can be described by the planar average of its quantities, we consider cross-section averaged well potentials and wavefunctions for our analysis. As expected, the coupled valley wavefunctions oscillate with $k_0 = 2\pi/a_0$ and are phase shifted with respect to each other. Furthermore, we obtain a reasonable estimate for $\Phi(z)$ from the wavefunction by convoluting the DFT probability densities with a Gaussian ($\sigma = 3.4$nm). This is essentially a low-pass filter which removes atomic-scale oscillations and returns the slowly varying envelope.

The Si/SiGe quantum well potential in Fig. 5.1a (and similarly for Si-MOS in Fig. 5.3a), is represented by the Hartree potential $V_\mathrm{H}$, that is the electrostatic potential of ions and electrons combined which is naturally obtained within the *ab-initio* framework. One characteristic of the Hartree potential is that it does not contain any information about exchange and correlation. The DFT calculation builds these interactions by means of hybrid functionals containing exact exchange from Hartree-Fock theory. Thus, there is no *local* representation of the full potential. Due to the non-locality of the DFT potentials, $V_\mathrm{H}$ is still the closest representation available from DFT to the 'classical' well potential. Besides averaging over the lateral extend of the cell, $V_\mathrm{H}(z)$ is low-pass filtered by convolution with a Gaussian, analogous to the procedure for the envelope $\Phi(z)$. However, a good estimate of the height for the potential barrier can be determined from the local density of states (LDOS) in Fig. 5.1b, and corresponds to the valence band offset (VBO) of 200 meV between Si and $\mathrm{Si}_{0.7}\mathrm{Ge}_{0.3}$, overestimating the experimental value of 170 meV [258].

Furthermore, the LDOS provides a comprehensive picture of the full electronic structure in the quantum well, including higher orbital states. The orbital states can be distinguished by the number of nodes $n = 0, 1, \ldots$ and are split by a few tens of meV. Not visible on the energy scale in Fig. 5.1b is that each peak in the LDOS is composed of two valley states which are split again by about 0.1 meV. The spin degree of freedom is not considered for the calculation of the valley splitting.

Using representative Si/SiGe and Si-MOS structures (see Sec. 4), in Fig. 5.2 we compare the local density of states at the conduction band minimum resolved in $z$ direction. The low lying states come in pairs, each pair corresponding to a subband

Die approbierte gedruckte Originalversion dieser Dissertation ist an der TU Wien Bibliothek verfügbar.
The approved original version of this doctoral thesis is available in print at TU Wien Bibliothek.
TU WIEN Bibliothek Your knowledge hub

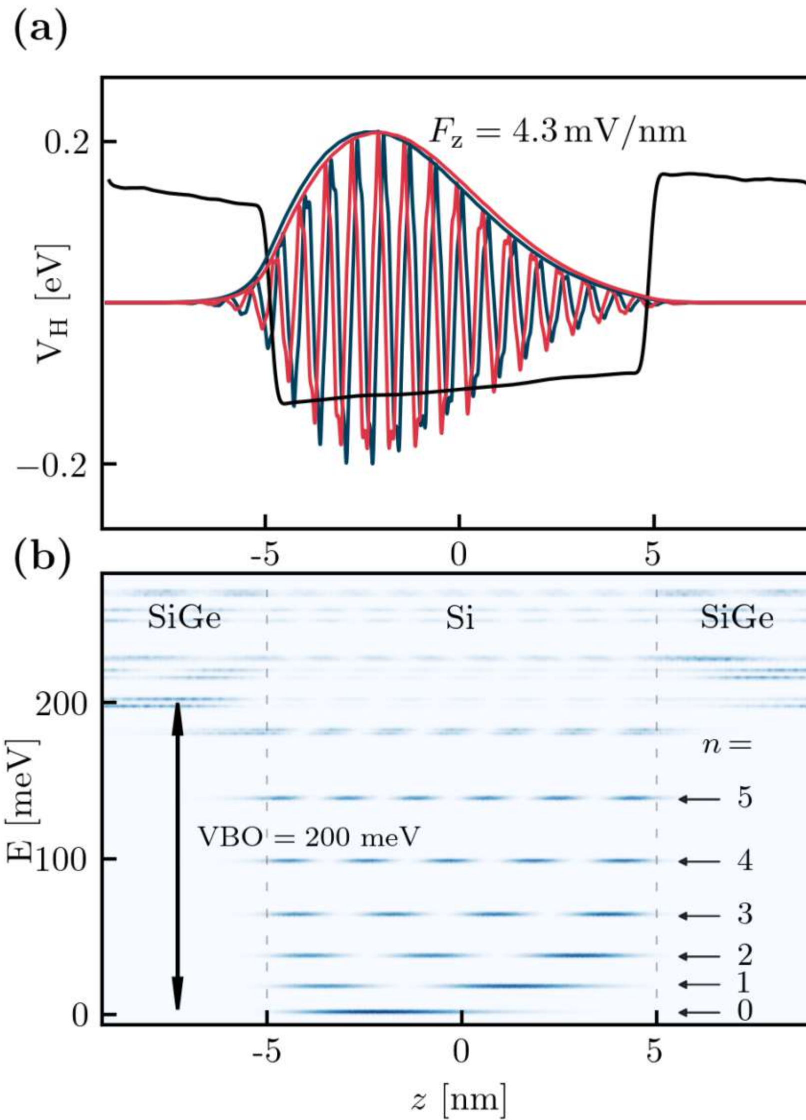


Figure 5.1: **(a)** Cross-section averaged valley wavefunctions $\Psi_{\pm}(z)$ confined in the quantum well represented by the Hartree potential $V_{\mathrm{H}}(z)$. The wavefunctions are phase shifted with respect to each other and have slightly different envelopes $\Phi_{\pm}(z)$. The wavefunction is pushed towards the interface at $z = -5\,\mathrm{nm}$ by an external electric field $F_{\mathrm{z}} = 4.3\,\mathrm{mV/nm}$. **(b)** The local density of states (LDOS) shows the full electronic structure of the conduction band ($F_{\mathrm{z}} = 0$). The orbital states with $n = 0, 1, \ldots$ nodes can be identified within the Si layer. Valley splittings in the range of 0.1 meV are too small to be clearly visible at this energy scale. The DFT model yields a valence band offset (VBO) of 200 meV.

Die approbierte gedruckte Originalversion dieser Dissertation ist an der TU Wien Bibliothek verfügbar.
The approved original version of this doctoral thesis is available in print at TU Wien Bibliothek.
TU WIEN Bibliothek Your knowledge hub

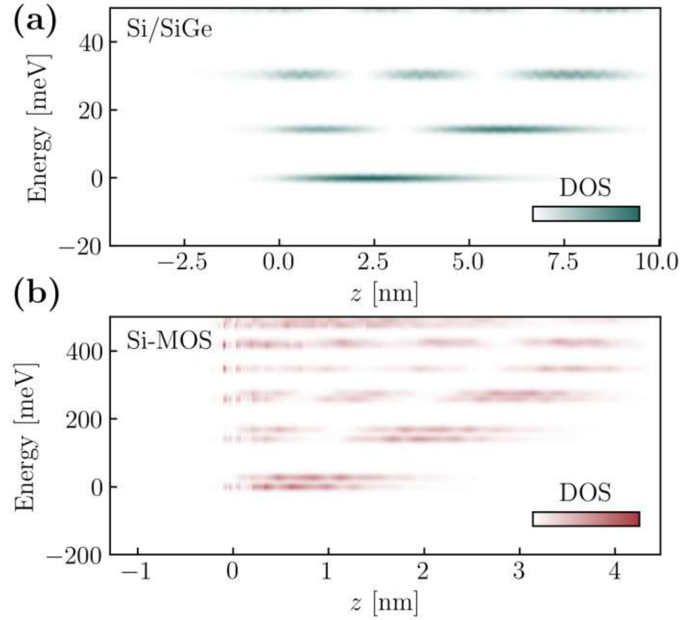


Figure 5.2: Local density of states in the energy range of the conduction band minimum as obtained from DFT for **(a)** Si-MOS and **(b)** Si/SiGe. The interface is at $z = 0$. The energy of the lowest state is set to zero. Each orbital state is comprised out of two valley states ($\pm z$) which are degenerate in bulk Si but couple here due to the presence of the interface. **(a)** For $F = 50\,\mathrm{mV/nm}$, the valley splitting in Si-MOS reaches values in the range between 1 and 10 meV, depending on details of the interface. **(b)** In Si/SiGe, the coupling is much weaker, with splitting below 300 µeV (see Chapter 5), which is not discernible given the figure energy-axis scale.

of the 2DEG. They arise as the eigenstates of the one-dimensional, approximately triangular, confinement of the interface: the wavefunction of the $n$-th excited state has $n$ nodes, if we count the ground state as the 0-th state. The subband energy splitting is determined by the electric field and is found to be 15 meV for Si/SiGe and 150 meV for Si-MOS. Each pair is further split by a much smaller energy (the valley splitting) and displays $k_0$ oscillations originating in the valley character of the state at the Si conduction band minimum. These oscillations are shifted by half a period in the two states of a pair.

### 5.1.2 Comparison to 2-band tight binding model

In the following, valley splittings obtained by DFT are compared to values from Boykin's TB model [54] with results summarized in Fig. 5.3. The method from [54] consists of a one-dimensional chain of (Si) atoms with one atom per unit cell, each with two orbitals ($s$ and $p$). The simple 1D two-band second-nearest neighbor Si TB model considers hard wall boundary conditions ($|\Psi_{\pm}(z)|^2$ vanishes at the interface – infinite well) or soft wall boundary conditions (the wavefunction extends in confining layers whose on-site energies are increased by 3.2 eV, which is the experimental band

Die approbierte gedruckte Originalversion dieser Dissertation ist an der TU Wien Bibliothek verfügbar.
The approved original version of this doctoral thesis is available in print at TU Wien Bibliothek.
TU WIEN Bibliothek Your knowledge hub

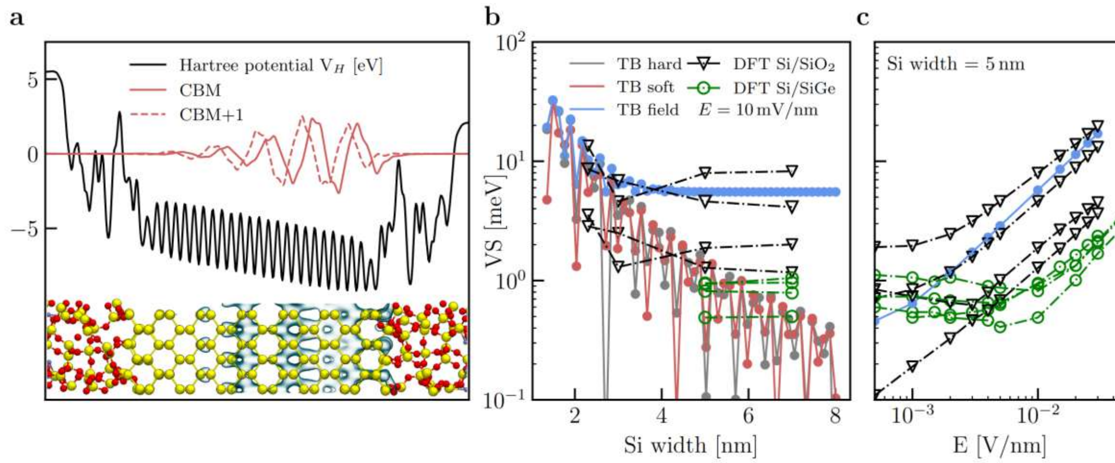


Figure 5.3: **(a)** The two valley wavefunctions averaged over the cross section confined in a 2D quantum well represented by the Hartree potential. The $z$ and $-z$ valley states are phase shifted in real space, which leads to different penetration depths into the confining barrier and introduces the valley splitting. The well is tilted due to the application of an electric field. **(b)** The valley splitting depends on the width of the Si layer. The electric field can push the wavefunction against one interface, so that the splitting stays constant even if the well size is further increased. The dot-dashed lines are DFT calculated values at $F = 10\,\mathrm{mV/nm}$ for qualitatively similar interfaces which are distributed over one order of magnitude. **(c)** Electric field dependence of the valley splitting. The onset of the single interface regime is indicated by a power-law increase (note the log-log scale). For comparison with experimental values of qubit devices, one needs to consider the strongly influential Si width.

offset of SiO2). Despite its simplicity, this model qualitatively captures the trends for the well width dependence as well as the influence of the electric field. In contrast to our DFT models, the basic TB approach does not take the disorder of the interface into account. Thus, there is no spread in the TB results. As can be seen in Fig. 5.3b, the valley splitting (VS) decreases substantially for certain numbers of Si layers in the well. This results from an interference between the two interfaces: without an electric field, the valley states couple with both interfaces. In order to probe single interfaces, we push the qubit wavefunction to one interface by applying an electric field in $z$ direction. Thus, for a given field, there is a Si width beyond which the valley splitting stays constant (blue line in Fig. 5.3b). Extending the Si width does not change the wavefunction anymore. The interference effect can also be observed in the electric field dependence (Fig. 5.3c) which results in a power-law increase above a certain value of the electric field, indicating the single-interface regime. As can be seen in Fig. 5.3b and Fig. 5.3c, the atomistic disorder yields a wide distribution of valley splittings by about one order of magnitude, in agreement with a wide range of experimentally observed valley splittings in Si-MOS and Si/SiGe [58, 56, 225].

Die approbierte gedruckte Originalversion dieser Dissertation ist an der TU Wien Bibliothek verfügbar.
The approved original version of this doctoral thesis is available in print at TU Wien Bibliothek.
TU Bibliothek WIEN Your knowledge hub

### 5.1.3 Comparison to $sp^3d^4s^*$ tight binding model

In order to validate the DFT model and to work out differences with another atomistic modeling technique that is capable of treating disorder, the valley splittings in Si/SiGe heterostructures are compared to a $sp^3d^4s^*$ TB model implemented in TB_Sim [226]. A big advantage of TB are the extremely reduced computational costs with respect to solving a full many-body Hamiltonian. Thereby, calculations in relatively large simulation cells containing millions of atoms become feasible. The results of larger simulation cells tend to show smaller variabilities because the effects of disorder average out. In some cases, the median value is a meaningful quantity when comparing different simulation cell sizes, as explained in App. D. However, here we aim to work out fundamental differences between DFT and TB, therefore the simulation cells used for both calculation methods are exactly the same including the atomic composition in the disordered SiGe layers. Only slight divergences in the atom positions appear after relaxing the cells using the hybrid functional in DFT and a valence force field [227, 226] in the case of TB.

Before discussing the results, other aspects of the modeling conditions shall be clarified. First, the application of an external electric field. As elaborated in App. B, a relatively complex external potential profile arises in DFT, see Fig. 5.4. Fulfilling the requirement of continuous and periodic potentials, the electric field in the Si and SiGe layers point in opposite directions. On the other hand, in TB, an external potential is simply included by adapting the on-site energies of the atoms [54]. As in DFT, discontinuous potentials should be avoided (see App. B). However, other than that, the potential profile can be chosen arbitrarily. Making the modeling conditions as similar as possible, we sample the DFT potential profile from Fig. 5.4 at the monolayer positions and add these values to the respective on-site energies in order to rebuild the external potential in the TB model as closely as possible.

There is another important difference that complicates the comparison, namely the valence band offset (VBO). The VBO in DFT (typically around 200 meV, see Fig. 5.1) overestimates the experimental value of 170 meV [258]. In TB, we find a VBO of 140 meV for the strained Si/SiGe heterostructures. The VBO (that is the energy barrier confining the 2DEG) controls the decay of the wavefunction in the barrier layers and therefore also the valley splitting. Thus, a comparison between TB and DFT is only meaningful if the band offsets match. At this point, we modify the standard TB parameters of [226] in order to match the band offset from DFT. The DFT band offset of 210 meV is reproduced by increasing the parameter for the unstrained valence-band offset between pure Si and Ge from 0.68 eV to 1.00 eV.

Having specified the modeling conditions, the TB and DFT models shall be compared in terms of resulting valley splittings as depicted in the scatter plot of Fig. 5.5. Various clean Si/SiGe quantum wells with interface widths ranging from 0 to 8 monolayers (ML) serve as the testbed for the comparison. Avoiding artifacts connected to the limited cell size of our model, the Ge profiles are chosen such, that an increase of the simulation cell size would not influence the median values, see App. D. The DFT potential profile for each of these structures is passed on to the TB model as explained above. In general, the trend towards increased valley splitting for sharp

Die approbierte gedruckte Originalversion dieser Dissertation ist an der TU Wien Bibliothek verfügbar.
The approved original version of this doctoral thesis is available in print at TU Wien Bibliothek.
TU WIEN Bibliothek Your knowledge hub

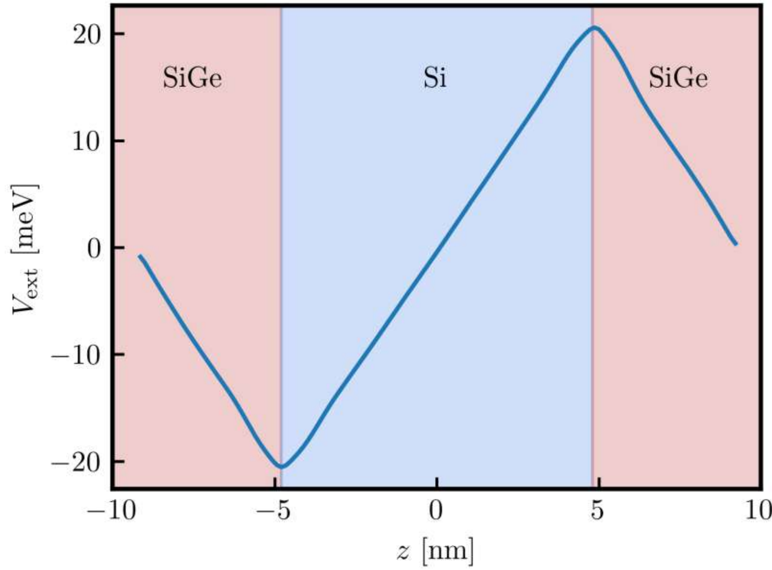


Figure 5.4: External potential profile $V_{\text{ext}}$ for the SiGe/Si/SiGe model structures. The bias corrected potential profile is continuous, periodic, and anti-symmetric. As a result, the electric fields in the material layers point in opposite directions. For comparison to TB calculations, this potential profile is included in the TB model.

interfaces along with a minimum for slightly smoothed interfaces is obtained by both methods and is also in line with experiments and previous studies [231, 67]. Indicated by larger spreads in the DFT results, the *ab-initio* calculations seem to be more sensitive to disorder at the interface. The TB results, on the other hand, imply that the valley splitting is mostly determined by the quantum well profile while the impact of the atomic details is less important. In Fig. 5.5, DFT and TB valley splitting values of each atomic configuration are connected by dashed lines. There is no clear correlation with respect to the disordered structures. Some configurations with large $E_{\text{VS}}$ in TB show low values in DFT and vice versa. However, on average, DFT gives slightly lower values (0.20 meV vs. 0.22 meV), as also depicted in Fig. 5.6. The averages align exactly if the unstrained valence-band offset between pure Si and Ge is further increased to 1.10 eV which corresponds to a band offset of 245 meV in the strained heterostructure. Tuning the VBO shifts the obtained valley splitting values but does not significantly impact the variability.

### 5.1.4 Well designs and comparison to "2$k_0$-theory"

Next to TB, material-related properties of spin qubits have been modeled by means of effective-mass (EM) approaches [63, 231, 67]. In this section we compare the outcomes of DFT to some fundamental results of EM.

Recalling Eq. (2.13), which assumes we are in the weak valley-orbit coupling regime, the inter-valley coupling matrix element can be expressed in a perturbative

Die approbierte gedruckte Originalversion dieser Dissertation ist an der TU Wien Bibliothek verfügbar.
The approved original version of this doctoral thesis is available in print at TU Wien Bibliothek.
TU Bibliothek WIEN Your knowledge hub

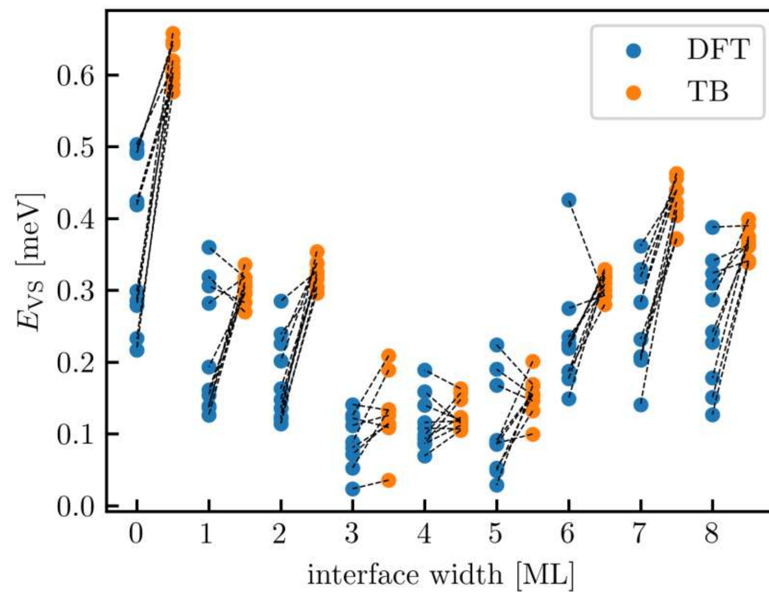


Figure 5.5: Comparison between DFT and TB. The valley splitting values obtained by methods are connected by dashed lines. The valley splitting $E_{\mathrm{VS}}$ strongly depends on the interface qualities. First, the interface width determines the overall trend with large $E_{\mathrm{VS}}$ for sharp interfaces and lower values for smooth interfaces. Although the configurations for each interface width show the same cross-section averaged Ge profile, the valley splitting varies strongly between these configurations. This spread is associated with atomic disorder, an effect that is much more pronounced in DFT.

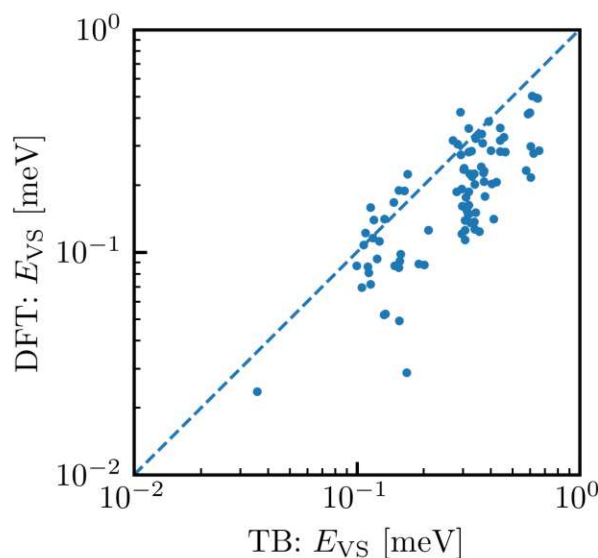


Figure 5.6: Correlation between valley splittings obtained from TB and DFT. The dashed line is a guide to the eye with slope 1. On average, the DFT results are slightly below TB with averages of 0.20 meV and 0.22 meV, respectively.

Die approbierte gedruckte Originalversion dieser Dissertation ist an der TU Wien Bibliothek verfügbar.
The approved original version of this doctoral thesis is available in print at TU Wien Bibliothek.
TU WIEN Bibliothek Your knowledge hub

picture as [63]

$$\Delta = \langle \Psi_+ | V_{\mathrm{qw}} | \Psi_- \rangle = \int \mathrm{d}z e^{-2ik_0 z} V_{\mathrm{qw}}(z) |\Phi(z)|^2, \tag{5.2}$$

which suggests that the valley splitting $E_{\mathrm{VS}} = 2|\Delta|$ is proportional to the Fourier transform of the envelope-weighted quantum-well potential

$$\tilde{V}^w_{\mathrm{qw}}(k) = \int \mathrm{d}z e^{-ikz} V_{\mathrm{qw}}(z) |\Phi(z)|^2, \tag{5.3}$$

evaluated at $k = 2k_0$. We refer to this model as " $2k_0$ theory" [67].

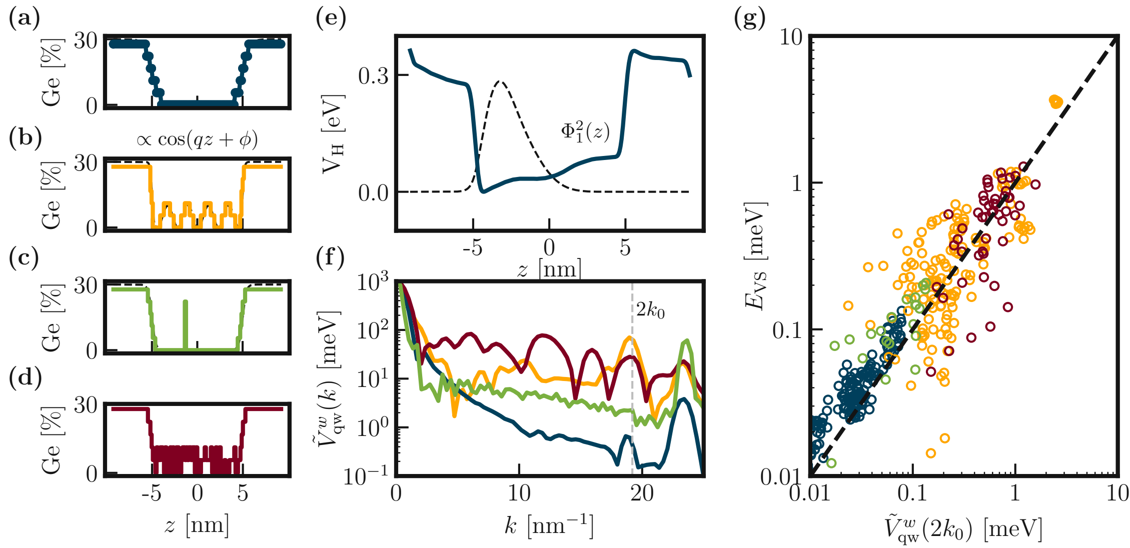


Figure 5.7: Schematics of studied quantum well geometries and associated DFT results. Disorder is introduced by distributing the Ge atoms randomly within the lateral layers so that the desired Ge profile is realized. **(a)** Clean Si wells with smooth interfaces. The number of monolayers used to transition between Si and $Si_{0.7}Ge_{0.3}$ determines the resulting width of the interface. **(b)** Wells with oscillating Ge concentration proportional to $\cos(qz + \phi)$ as proposed in [64]. **(c)** Wells with Ge spikes at different $z$ positions. **(d)** Randomly distributed Ge atoms with the same average Ge concentration as (b). **(e)** Comparison of the $2k_0$ theory from [67] against our DFT model. Procedure for the calculation of $\tilde{V}^w_{\mathrm{qw}}(k)$. The envelope $|\Phi_1(z)|^2$ and Hartree potential $V_{\mathrm{H}}(z)$ for each configuration are obtained from DFT. The lower panel shows the spectrum of the product $V^w_{\mathrm{qw}}(z) = V_{\mathrm{H}}(z)|\Phi_1(z)|^2$ which is evaluated at $k = 2k_0$. **(g)** Correlation between the valley splitting obtained from DFT and the Fourier component of the density weighted well potential $\tilde{V}^w_{\mathrm{qw}}(k)$ at $k = 2k_0$, characterized by a Pearson correlation coefficient of 0.91. The dashed line is a guide to the eye with slope 1.

In the following, four well designs are considered (Fig. 5.7a–d) for obtaining the valley splitting values from DFT, yielding results depicted in Fig. 5.7g. Verification of this approach for our comparatively small simulation cells can be found in App. D.

Die approbierte gedruckte Originalversion dieser Dissertation ist an der TU Wien Bibliothek verfügbar.
The approved original version of this doctoral thesis is available in print at TU Wien Bibliothek.
TU Bibliothek WIEN Your knowledge hub

The first type of well that we consider are Ge-free wells with smooth interfaces as shown in Fig. 5.7a. With respect to practical growth conditions, step-like interfaces are extremely difficult (if not impossible) to fabricate and smooth interfaces represent more realistic growth profiles. We model the monotonous increase of Ge by means of a step-like function (steps of 1/18, see App. D). The width of the interface is given in monolayers (ML).[13]

The main consequence of Eq. (5.2) is that $E_{\mathrm{VS}}$ is expected to reach a maximum if the quantum-well potential oscillates with a wavevector $q = 2k_0$ [63, 64]. This can be realized by introducing an oscillating Ge concentration in the well (wiggle wells), see Fig. 5.7b. Similarly, the valley splitting can be increased by introducing Ge peaks in the well [62], compare Fig. 5.7c.

Additionally, we compare the wiggle well results to randomly distributed Ge atoms considering that the average Ge concentration in the well stays the same, see Fig. 5.7d. The reduced valley splitting with respect to wiggle wells at $q = 19\,\mathrm{nm}^{-1}$ confirms the impact of periodically aligned Ge-enriched layers in the quantum well. The relatively large $E_{\mathrm{VS}}$ of up to 13 meV is attributed to strong local gradients in the Ge distribution that appear due to the random placement of Ge and effectively broaden $\tilde{V}^{w}_{\mathrm{qw}}(k)$. The same interpretation is valid for wells with Ge spikes in Fig. 5.7c.

The $2k_0$ theory has been verified against tight-binding calculations using a virtual crystal method in [67]. We refine this approach by using the envelope and quantum well potential obtained from first-principles to calculate $\tilde{V}^{w}_{\mathrm{qw}}$ for every structure as depicted in Fig. 5.7e and Fig. 5.7f. Good correlation with $E_{\mathrm{VS}}$ from DFT (Pearson correlation coefficient of 0.91) as shown in Fig. 5.7g justifies the implications of the $2k_0$ theory but also indicates limitations as discussed in the following section.

### 5.1.5 Valley-orbit coupling

A number of conceptual differences between DFT and EM have been outlined in Sec. 5.1.1. Another possible explanation for the deviation between the two methods could be the assumption leading to Eq. (5.2), namely, that both valley states share the same envelope $\Phi_+ = \Phi_-$ which is equivalent to considering an isolated two-valley system that does not coupling to excited orbital states. A pronounced valley-orbit coupling is indicated by our DFT calculations, a scenario in which the concept of pure valley splitting from Eq. (5.2) can not be applied [232].

Taking a closer look at the DFT envelopes of various well geometries reveals envelopes with the signature of the excited *orbital* states, namely the appearance of a second maximum in the quantum well. This indicates mixing of first and second orbital state, that are the envelopes with 0 and 1 node, respectively. In Fig. 5.8, three different scenarios are compared. First, the results for an entirely Ge-free well with an applied electric field $F = 7.5\,\mathrm{mV/nm}$ are shown in Fig. 5.8a. Such structures show typically low valley splitting with envelopes of the resulting states that are very

[13]The abbreviation ML has already been used to denote “Machine Learning”. However, it was decided to keep this standard abbreviation also for “monolayer” as it can be clearly distinguished in the respective context.

Die approbierte gedruckte Originalversion dieser Dissertation ist an der TU Wien Bibliothek verfügbar.
The approved original version of this doctoral thesis is available in print at TU Wien Bibliothek.
TU WIEN Bibliothek Your knowledge hub

similar but not exactly overlapping[14], compare Fig. 5.1. The electric field increases the splittings of both valleys and orbitals. Due to the large energy difference between ground and excited orbital states, mixing of these states is negligible and the envelopes overlap.

Next, a structure with an Ge oscillation of $q = 3\,\mathrm{nm}^{-1}$ is examined in Fig. 5.8b. The valley splitting is increased due to the wiggle well design. Here, no electric field is applied. Therefore, the obtained orbital splitting is only about 15 meV. The asymmetric envelopes occur due to an asymmetric distribution of Ge atoms in the well. The most important insight from this plot however is, that the appearance of a local minimum in the envelope of the excited valley state.

A structure with an Ge oscillation of $q = 20\,\mathrm{nm}^{-1}$, fulfilling the $2k_0$ condition from Eq. (2.12). The valley splitting is strongly increased to 5.12 meV due to the "resonant" Ge oscillation. Again, no electric field is applied and an orbital splitting of about 15 meV is found. In this example, valley-orbit mixing is especially important because the valley splitting is in the range of the orbital splitting. The excited valley state couples to the excited orbital state.

In conclusion, valley-orbit mixing is important in cases of large valley splitting and low orbital splitting. The assumptions of EM theories [67] are therefore valid under application of a strong electric field because this shifts the excited orbital state out of reach. However, the DFT results indicate that a comprehensive EM models should indeed contain valley-orbit mixing.

## 5.2 Spin splitting

So far, we did not consider spin in the simple band description above, thus each band is spin degenerate. This degeneracy is lifted by spin-orbit coupling (SOC). As described in Sec. 2.2.4, it can be shown that two types of spin Hamiltonians are allowed in a quantum well structure. We obtain Rashba- and Dresselhaus-type of spin-orbit couplings:

$$\begin{aligned} H_\mathrm{R} &= \alpha_\mathrm{R}(\sigma_x k_y - \sigma_y k_x) \\ H_\mathrm{D} &= \alpha_\mathrm{D}(\sigma_x k_x - \sigma_y k_y) \end{aligned} \tag{5.4}$$

Knowledge about the SOC in a spin qubit is essential for driving qubit state transitions by EDSR. Compared to holes (in hole spin qubits), the SOC is rather weak in the conduction band, which limits the electrical manipulation of electron spin qubits. For this reason, an enhancement of the SOC is highly desirable, and can be achieved either by placing micro-magnets in the vicinity of the qubit [14] or by engineering the shape of the quantum wells [233]. However, our results imply that SOC in electron spin qubit devices could also be enhanced by modifying the microscopic structure of the interface. We calculate the SOC for three Si-MOS heterostructures. As depicted in Fig. 5.9, we

[14] The states from DFT can not be assigned to $|+\rangle$ and $|-\rangle$, however we keep this notation for simplicity and use the convention that the ground and excited valley state are represented by $|+\rangle$ and $|-\rangle$, respectively.

Die approbierte gedruckte Originalversion dieser Dissertation ist an der TU Wien Bibliothek verfügbar.
The approved original version of this doctoral thesis is available in print at TU Wien Bibliothek.
TU Bibliothek WIEN Your knowledge hub

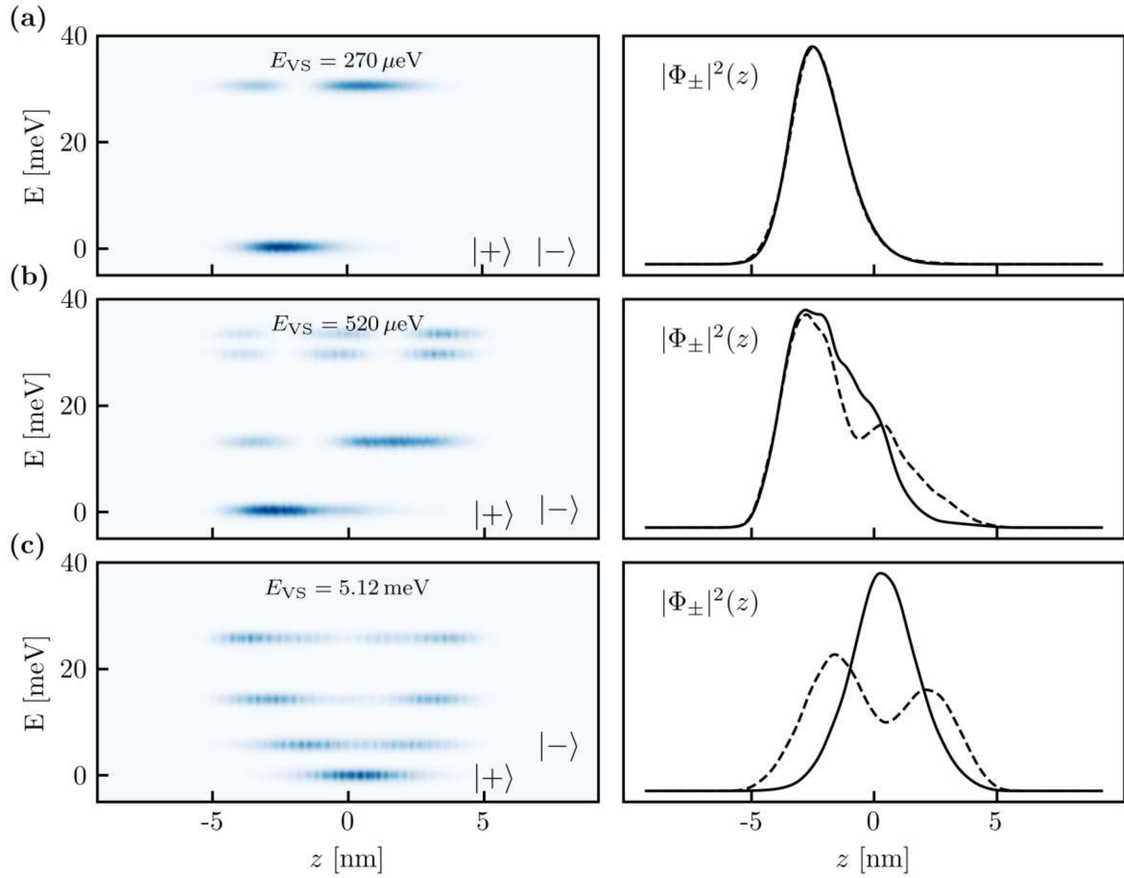


Figure 5.8: Local density of states for three different quantum wells an various electric fields (left) and associated envelopes $|\Phi_\pm(z)|^2$ of the valley-orbit states $|+\rangle$ and $|-\rangle$ (right). **(a)** Clean well with smooth interface (5 ML transition region) at $F = 7.5\,\mathrm{mV/nm}$. The excited orbital states are separated by about 30 meV. The DFT envelopes overlap almost perfectly. **(b)** Ge oscillation with $q = 3\mathrm{nm}^{-1}$ at zero electric field. The asymmetry comes from the asymmetric Ge distribution in the well. This configuration yields a moderate valley splitting of 520 µeV. The orbital splitting of 15 meV. is reduced because there is no electric field. While the envelope of $|+\rangle$ resembles a prototypical envelope of the lowest orbit, $|\Phi_2|^2$ develops a local minimum in the center of the well, that is the signature of valley-orbit mixing with the orbital state above. **(c)** Ge oscillation with $q = 20\mathrm{nm}^{-1}$ ($\approx 2k_0$) at zero electric field. The valley splitting of 5.6 meV is strongly enhanced by the Ge oscillations. Strong valley-orbit coupling with higher orbital states is indicated.

Die approbierte gedruckte Originalversion dieser Dissertation ist an der TU Wien Bibliothek verfügbar.
The approved original version of this doctoral thesis is available in print at TU Wien Bibliothek.
TU WIEN Bibliothek Your knowledge hub

find a linear-in-$k$ spin splitting for small $k$. For larger $k$, the splitting can be fitted to a cubic term as expected by the theory. This is depicted in the inset. The spin splitting was calculated for $k$ points along the [110] and [1$\bar{1}$0] directions, respectively. This allows for simple extraction of the Rashba and Dresselhaus coefficients $\alpha_R$ and $\alpha_D$ by symmetry arguments. With respect to the rotated $k$-axis, the Dresselhaus term gives the symmetric contributions while the Rashba term results in anti-symmetric contributions. The extracted values for $\alpha_R$ vary between 0.4 and 0.8 µeVnm and for $\alpha_D$ from 37 to 664 µeVnm. The dominating Dresselhaus contributions vary by more than one order of magnitude purely due to differences in the atomistic configuration at the interface. However, the average of 240 µeVnm agrees well with the experimental value of 178 µeVnm [234]. We interpret this result as a verification for our modeling approach.

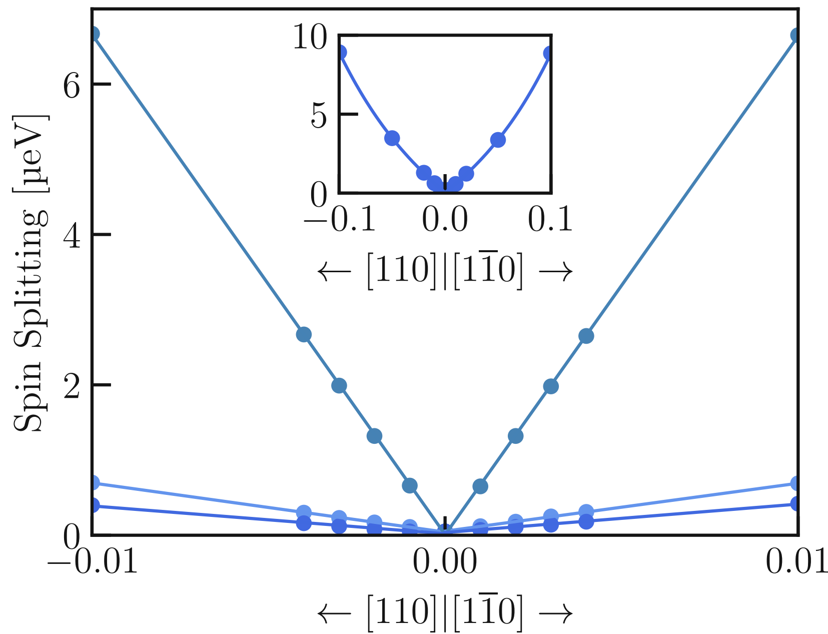


Figure 5.9: Spin splitting of the lowest valley state for $\mathbf{k} = [k_x, k_y]$ along the in-plane directions [110] and [1$\bar{1}$0] at E = 10 mV/nm for Si-MOS. The blue shadings distinguish three different interface structures. The splitting is linear in $k$ for small $k$ and cubic for larger $k$ as shown in the inset.

Because SOC is not implemented in CP2K, the Vienna Ab-initio Simulation Package (VASP) was employed for the purpose of extracting the SOC coefficients. Unfortunately, VASP demands more memory. Therefore, we could not conduct similar calculations for Si/SiGe (larger cells with more atoms compared to Si-MOS). This extension is left for future endeavors.

Die approbierte gedruckte Originalversion dieser Dissertation ist an der TU Wien Bibliothek verfügbar.
The approved original version of this doctoral thesis is available in print at TU Wien Bibliothek.
TU WIEN Bibliothek Your knowledge hub

Die approbierte gedruckte Originalversion dieser Dissertation ist an der TU Wien Bibliothek verfügbar.
The approved original version of this doctoral thesis is available in print at TU Wien Bibliothek.
TU WIEN Bibliothek Your knowledge hub

Die approbierte gedruckte Originalversion dieser Dissertation ist an der TU Wien Bibliothek verfügbar.
The approved original version of this doctoral thesis is available in print at TU Wien Bibliothek.
TU Bibliothek WIEN Your knowledge hub

# Chapter 6

# Coherence limit due to hyperfine interactions

*The results presented in this section have been published in [LC1]. Text and figures are adapted from there.*

On the quest to understand and reduce environmental noise in Si spin qubits, hyperfine interactions between electron and nuclear spins impose a major challenge. Silicon is a promising host material because one can enhance the spin coherence time by removing spinful $^{29}$Si isotopes. As more experiments rely on isotopic purification of Si, the role of other spinful atoms in the device should be clarified. This is not a straightforward task, as the hyperfine interactions with atoms in the barrier layers are poorly understood. We utilize density functional theory to determine the hyperfine tensors of both Si and Ge in a crystalline epitaxial Si/SiGe quantum well as well as Si and O atoms in an amorphous Si/$SiO_2$ (MOS) interface structure. Based on these results, as elaborated in Sec. 2.2.5, we estimate the dephasing time $T_2^*$ due to magnetic noise from the spin bath and show that the coherence is limited by interactions with non-Si barrier atoms to a few µs in Si/SiGe (for non-purified Ge) and about 100 µs in Si-MOS. Expressing these numbers alternatively, in Si/SiGe the interactions with Ge dominate below 1000 ppm of $^{29}$Si content, and, due to low natural concentration of the spinful oxygen isotopes, the interactions with oxygen in Si-MOS become significant only below 1 ppm of $^{29}$Si content.

## 6.1 Introduction

Although the relative importance of various decoherence mechanisms is still under debate [82, 83], a major source of decoherence is the hyperfine interaction with the nuclear spins of the host material [235, 103]. In this regard, silicon is an outstanding platform for implementing spin qubits due to the naturally low abundance of $^{29}$Si, its only stable spinful isotope. Removing $^{29}$Si by isotopic purification [236] improves several key spin-qubit metrics [35] including coherence, which can be pushed even up to a second for donor-bound electrons in bulk silicon [90]. The second reason for the auspicious status of silicon is the compatibility with classical semiconductor

device fabrication, the metal–oxide–semiconductor (MOS) technology [30]. Hence, the development of Si-MOS spin qubits is a direction currently pursued, with encouraging achievements such as high coherence [237, 238, 239], high-fidelity single and two-qubit gates [240], fast and high-fidelity single-shot readout [241, 242], high quality factors [243, 244], or the operation above 1 K [245]. As an alternative, Si/SiGe devices rely on a two-dimensional electron gas that is well separated from the heterostructure interface offering a clean system [246] and coherent [247, 83, 248, 249] and high-fidelity [20, 250, 251, 252] spin qubits.

We employ DFT to determine the hyperfine interactions between a conduction band electron in a Si quantum dot and a nuclear spin bath that is composed of atoms in the Si host lattice and the barrier layer. While previous *ab-initio* studies focused on donor-bound electrons [253] or delocalized electrons in bulk [93, 101], we consider realistic interfaces to which a conduction-band electron is confined by an external electric field. This model allows us not only to calculate the hyperfine interaction with $^{29}$Si, which is the dominant source of decoherence in natural Si, but also with spinful isotopes in the barrier, a weaker interaction with the evanescent tail of the electron that only becomes important for highly purified Si. Besides $^{29}$Si, spinful isotopes appearing in the barrier include $^{73}$Ge in SiGe and $^{17}$O in MOS structures. Based on the DFT results, we estimate dephasing times $T_2^*$ due to quasi-static noise from nuclei in the barrier.

For Si/SiGe, we come to the conclusion that $^{73}$Ge isotopes limit the coherence time to a few µs already at 3500 ppm of $^{29}$Si fraction. This value is less than 4.68%, the natural abundance of $^{29}$Si, but substantially more than 50 ppm, the lowest currently available fraction of $^{29}$Si in purified silicon. Considering isotopically purified Ge in addition to purified Si will suppress the nuclear noise further and, according to our model, allows to improve the decoherence time by another order of magnitude.

For Si-MOS, the hyperfine coupling to oxygen atoms in the barrier would overtake the spin-qubit dephasing if the isotopic purification of silicon would be increased by almost two orders of magnitude compared to the lowest currently used value of 50 ppm. While these conclusions depend on external parameters, especially the confining electric potential, we conclude that the spinful non-Si isotopes will not be a limiting factor of Si-MOS qubits unless the silicon is purified to levels much below 50 ppm.

## 6.2 Methodology

In addition to the information given in previous parts of this thesis, the employed methodology for the calculation of the hyperfine interactions is given in the following.

### 6.2.1 DFT setup

We employ density functional theory (DFT) implemented in the CP2K code [254] using the semi-local GGA functional PBE [116] for all calculations. We relax the geome-

Die approbierte gedruckte Originalversion dieser Dissertation ist an der TU Wien Bibliothek verfügbar.
The approved original version of this doctoral thesis is available in print at TU Wien Bibliothek.
TU Bibliothek WIEN Your knowledge hub

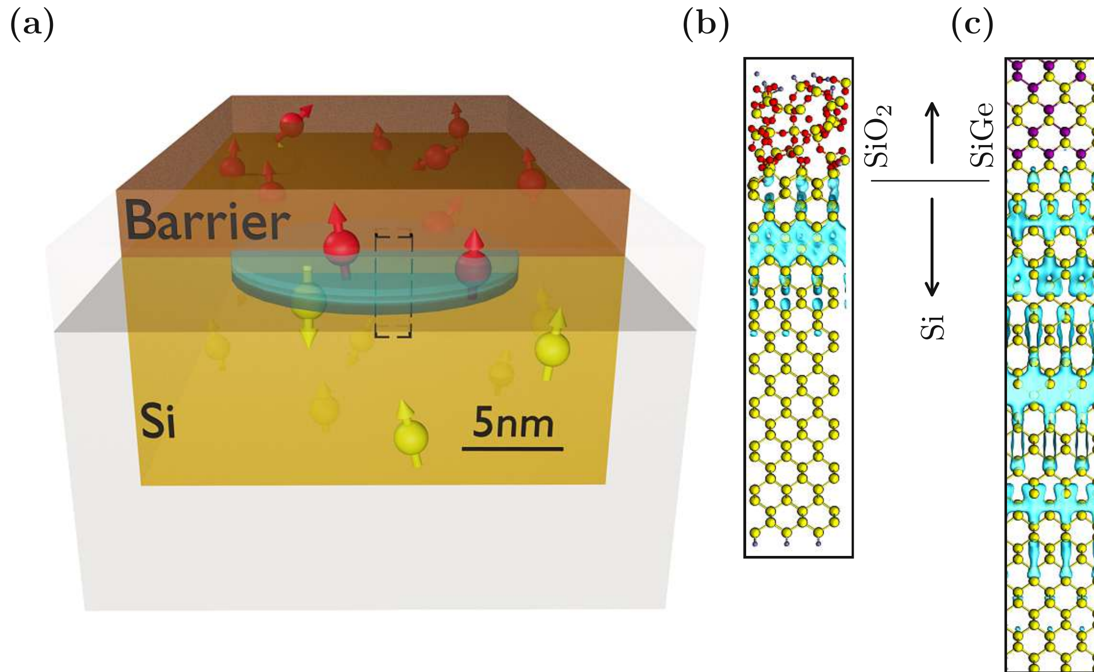


Figure 6.1: **(a)** Schematic device layout of a quantum dot (depicted as a blue ellipsoid) in a Si-based material stack. The dot is formed at the Si/barrier interface by top gates (not shown) which also confine the electron wavefunction in the lateral ($xy$) plane. Nuclear spins in both material layers (schematically represented as red and yellow arrows) act as a source of magnetic noise. This interaction and the resulting decoherence is mostly determined by the electron wavefunction amplitude at atomic nuclei. **(b)** Exemplary 3D model of an atomistic Si/$SiO_2$ interface structure (side view). We assume an external electric field 50 mV/nm in $z$-direction (perpendicular to the Si-barrier interface). The simulation cell measures $1.15\times1.15\times15\,\mathrm{nm}^3$ and contains 780 atoms (Si in yellow, O in red, H for the passivated dangling bonds in blue). The cyan surface displays the real part of the electron wavefunction as obtained from DFT. **(c)** A part (7.5 nm) of the Si/$Si_{0.7}Ge_{0.3}$ cell. The full cell of the model is $1.65\times1.65\times25\,\mathrm{nm}^3$ and contains 2500 atoms (Si in yellow, Ge in magenta). The plotted wavefunction corresponds to an electric field of 5.8 mV/nm. Because of the lower field, the wavefunction extends further into the Si layer.

Die approbierte gedruckte Originalversion dieser Dissertation ist an der TU Wien Bibliothek verfügbar.
The approved original version of this doctoral thesis is available in print at TU Wien Bibliothek.
TU WIEN Bibliothek Your knowledge hub

tries of the interface structures and calculate their electronic ground state imposing periodic boundary conditions in all directions. Since obtaining reliable hyperfine couplings within an *ab-initio* framework requires accurate modeling of the spin density in the vicinity of atomic nuclei [255], we use all-electron basis sets. Also, the orbitals are expanded in correlation-consistent polarized double-$\zeta$ basis sets for valence and core electrons [119, 120, 121]. Since the same basis sets are not available for Ge, we used the 6-31G double-$\zeta$ Pople basis sets [122], which were previously reported to provide accurate hyperfine couplings [123, 124]. The systems are self-consistently relaxed with a force convergence criterion of 0.02 eV/Å per atom. The calculation of the hyperfine tensors (including relativistic effects) is based on the CP2K implementation of Declerck [95].

We include a homogeneous electric field perpendicular to the heterostructure interface, using the Berry-phase formalism [229, 230] as presented in [228, 127]. This implementation corresponds to imposing closed-circuit boundary conditions with a constant applied bias across the simulation cell. The electric fields in the material layers adjust according to the layer thickness and relative permittivity, as discussed in Sec. 5.1.3. The values for the electric field $F$ quoted throughout this work refer to the field in the Si layer that is extracted from the Hartree potential. For the Si/SiGe heterostructure, we apply electric fields $F$ within the typical range of 1 to 10 mV/nm [64]. For the Si-MOS heterostructure, the electric field in the 2DEG depends on the doping density of the Si substrate [256]. Assuming a doping density of at most $10^{18}/\text{cm}^3$ in the substrate and a carrier density of at most $10^{12}/\text{cm}^2$ in the 2DEG, we estimate the field $F$ in the semiconductor [257] to be below 60 mV/nm.

### 6.2.2 Atomic structure and supercell

In contrast to the valley splitting calculations presented in Sec. 5, we do not use quantum wells with barrier layers on both sides of the Si layer for the calculation of the hyperfine interactions. Instead, a barrier material is only put at one side of the Si layers while the other side is passivated by H. An electric field is applied in the perpendicular direction to the Si/barrier interface, pushing the conduction-band electron (or better: the 2DEG) towards this interface, see Fig. 6.1. Because the 2DEG is strongly confined to one side of the Si crystal, the effects from the other interface are expected to be weak. Removing this second barrier allows to reduce the complexity of the DFT calculations that are quite challenging to converge numerically. The principle methodology for the generation of the interfaces as presented in Chapter 4 is unchanged. As before, we do not consider in-plane confinement and enforce periodic boundary conditions on simulation cells with lateral size of 1.15 or 1.6 nm along the interfaces. We extrapolate the calculated quantities to realistic in-plane quantum dot sizes by a straightforward rescaling of the electron wavefunction density, with the details given in Sec. 6.5.

Die approbierte gedruckte Originalversion dieser Dissertation ist an der TU Wien Bibliothek verfügbar.
The approved original version of this doctoral thesis is available in print at TU Wien Bibliothek.
TU WIEN Bibliothek Your knowledge hub

#### 6.2.2.1 Si/SiGe

Modeling typical experimental setups, we consider a SiGe layer with roughly 30% Ge content interfaced with a strained Si layer to get the correct band alignment to form a quantum well in the Si part of the simulation cell. By means of the PBE functional, we find a band offset of 200 meV, slightly overestimating the experimental value of 150 meV [258]. For the generation of the structure, we start from a pure [001] Si crystal with 120 monolayers in $z$ direction and $3 \times 3$ unit cells along $x$ and $y$, cf. Sec. 4.1. A 4.3 nm thick region (32 monolayers) on one end of the crystal is assigned to form the SiGe barrier. In this region, SiGe layers are produced by replacing random atoms of the Si lattice by Ge, such that the Ge proportion in each layer equals 27.7% (5 out of 18 atoms are Ge). The next 12 nm of pure Si represents the Si quantum well and the final 6 nm of vacuum serves as a boundary barrier in the model.[15] Dangling bonds at the material/vacuum interfaces are passivated with hydrogen. The whole cell is relaxed under 1 % of tensile in-plane strain in the Si layer. In total, we get a simulation cell of $1.65\times1.65\times25\,\mathrm{nm}^3$ with 2232 atoms.

#### 6.2.2.2 Si-MOS

We generate the amorphous interface structures by *ab-initio* molecular dynamics (AIMD) simulations, following our initial AIMD approach from Sec. 4.2 [LC4]. The thickness of the Si and $SiO_2$ layers were chosen such that the decay of the electron wavefunction into the semiconductor (along $z$) and into the oxide (along $-z$) makes the electron wavefunction negligible at the layer boundary (present in the model only) away from the interface. A Si thickness of 10 nm and an oxide thickness of 1 nm proved sufficient to suppress boundary effects as the wavefunction decays quickly as a result of the large conduction band offset ($|\Psi|^2$ decays by about a factor of $10^5$ per nm in $SiO_2$), in combination with the strong electric field. We observe that after a roughly 0.5 nm thick transition region at the crystalline Si, the amorphous $SiO_2$ shows geometric qualities (bond lengths and angles, densities) of bulk silicon dioxide [LC4].

To impose the periodicity in $z$-direction required by the DFT code, we adopt the repeated slab model: The top edge of the oxide layer and the bottom edge of the Si crystal are passivated with hydrogen and separated from their periodic image by a vacuum of 20 nm. Subsequently, the whole simulation cell is relaxed in $x$ and $y$ direction with respect to the lattice parameter of bulk Si (our DFT setup gives a relaxed Si lattice parameter $a_0 = 0.544\,\mathrm{nm}$ which is very close to the experimental value of $a_0 = 0.543\,\mathrm{nm}$).

## 6.3 The lowest subband of a Si heterostructure 2DEG

As described in Sec. 2.2.3, the six-fold degeneracy of the conduction band minimum of bulk silicon is lifted by the heterostructure confinement and, for Si/SiGe, by the

[15] Alternatively, one could consider sandwiched Si layers (barriers at both sides) as a way to confine the electron instead of using the electric field, and smooth transition between the Si and SiGe parts instead of an abrupt interface. We leave these extensions for the future.

Die approbierte gedruckte Originalversion dieser Dissertation ist an der TU Wien Bibliothek verfügbar.
The approved original version of this doctoral thesis is available in print at TU Wien Bibliothek.
TU Bibliothek WIEN Your knowledge hub

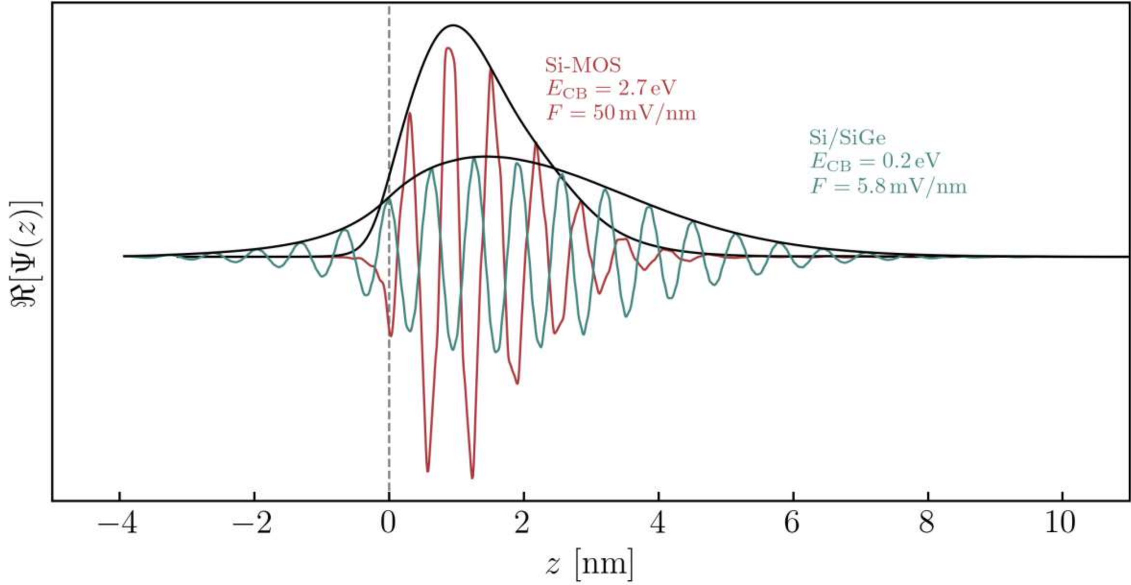


Figure 6.2: Real-part of the cross-section averaged wavefunction at the conduction band minimum as obtained from DFT for the Si-MOS and Si/SiGe interface model, respectively. The first atom in the barrier is at $z = 0$. When compared to Si-MOS, the Si/SiGe wavefunction extends further into the Si part of the simulation cell $(+z)$ due to the lower electric field $F$. In addition, due to the lower barrier $E_{\mathrm{CB}}$, it also extends further into the SiGe barrier $(-z)$. The associated envelopes $\Phi(z)$ (black lines) are obtained by low-pass filtering the wavefunction density with a Gaussian filter.

in-plane strain in the Si layer. [9, 10]. A four-dimensional subspace is raised in energy, leaving two so-called valley states at the conduction band minimum, at crystal momenta $k_0 \approx \pm\frac{2\pi}{a_0}0.83$ [9, 10].

These valley states are further split by the interface [54] [LC3], that is by the electric field pressing the electron onto the barrier.[16] Our DFT results are in line with this picture. We obtain a conduction band offset of about 0.2 eV and 2.7 eV for Si/SiGe and Si-MOS, respectively. The valley splitting is below 300 µeV in Si/SiGe and in the range of 1-3 meV for the oxide interface, cf. the results in Chapter 5.

The ground state wavefunctions are plotted in Fig. 6.2. One can identify the oscillations assigned to the expected valley wave vector $k_0$. The valley content of states at the conduction band minimum is also imprinted in the local density of states as already shown in Fig. 5.2 for an illustration.

## 6.4 The magnitudes of the hyperfine couplings

Having the conduction-band wavefunction, including a reliable description of its shape near the atomic cores, we can evaluate the hyperfine tensors. Building on the the-

[16] For zero electric field, they would be split by the Si/SiGe quantum well interfaces.

Die approbierte gedruckte Originalversion dieser Dissertation ist an der TU Wien Bibliothek verfügbar.
The approved original version of this doctoral thesis is available in print at TU Wien Bibliothek.
TU WIEN Bibliothek Your knowledge hub

oretical foundations and notation from Sec. 2.2.5, we denote the hyperfine tensor $\mathbf{A}$ and the direction of the magnetic field $\mathbf{m}$. The hyperfine tensor $\mathbf{A}$ are obtained for each atom in the system from DFT. We define – loosely speaking – the 'hyperfine strength', as the quantity entering the dephasing time formula[17],

$$A^{\perp} = |\mathbf{m} \cdot \mathbf{A}|, \tag{6.1}$$

where we again drop the indexes $i, n$. Figure 6.3 shows $A^{\perp}$ plotted against the atoms' distance from the interface. It shows large variations which are easily explained by the proportionality of the dominant (isotropic) part to the electron wavefunction density given in Eq. (2.19). Thus, the overall trend in Fig. 6.3 reflects the confinement in $z$-direction. We attribute variations on top of this trend to Bloch oscillations and, especially relevant for the Si-MOS case, details of the atomic configuration at the interface. Though probably of little practical importance, we have also confirmed that the tails of the hyperfine strengths at the left and right boundaries are due to the anisotropic contribution. Here, as the electron wavefunction drops exponentially, the anisotropic hyperfine terms take over. Thus, the saturation at the wavefunction tails seems to be physical rather than a numerical artifact and it is reassuring that our numerical calculations can uncover these small tails.

The most important observation in Fig. 6.3 is that the hyperfine coupling to non-Si nuclei in the barrier is comparable to the coupling to silicon (if located at a similar distance from the interface). While we refrain from any quantitative fitting of $\eta$,[18] the lack of an essential difference between germanium/oxygen and silicon is obvious from the figure. This is the crucial finding that decides the magnitude of the barrier-induced dephasing.

To quantify their contributions, we assign the following extensive quantity to each isotope, as a short-hand notation for its contribution in Eq. (2.22),

$$\langle \Delta_i \rangle \equiv \frac{I_i(I_i+1)}{3} \sum_{n \in \text{isotope}\, i} |\mathbf{m} \cdot \mathbf{A}_{i,n}|^2. \tag{6.2}$$

Even though our numerical calculations and plots include the anisotropic contributions, we find that they are small. It is then useful to neglect them in the preceding equation, upon which we obtain

$$\langle \Delta_i \rangle \approx \frac{I_i(I_i+1)}{3} \sum_{n \in \text{isotope}\, i} A_{i,n}^2 \tag{6.3a}$$

$$= c_i^2 \sum_{n \in \text{isotope}\, i} |\Psi(\mathbf{r}_n)|^4, \tag{6.3b}$$

[17] If one drops the anisotropic contributions, the 'hyperfine strength' equals the hyperfine coupling $A$ given in Eq. (2.19) and does not depend on the magnetic field direction $\mathbf{m}$.

[18] As already mentioned, $\eta$ is not well defined in the amorphous oxide. While well defined in crystalline semiconductors, fitting $\eta$ for both Ge and Si, is complicated by the interference of different valleys. We limit ourselves to a remark that we do not see any evidence of $\eta$ for Ge being much larger than for Si and, thus, our data give more support to the estimate for $\eta_{\mathrm{Ge}}/\eta_{\mathrm{Si}} \approx 3$ made in Ref. [99] compared to $\eta_{\mathrm{Ge}}/\eta_{\mathrm{Si}} \approx 10$ made in Ref. [98], see also the text below Eq. (2.21).

Die approbierte gedruckte Originalversion dieser Dissertation ist an der TU Wien Bibliothek verfügbar.
The approved original version of this doctoral thesis is available in print at TU Wien Bibliothek.
TU Bibliothek WIEN Your knowledge hub

where $c_i$ collects the constants from Eqs. (2.19) and (2.22),

$$c_i = \frac{4\mu_0}{9} I_i(I_i+1) g_e \mu_\mathrm{B} g_{N,i} \mu_N. \tag{6.3c}$$

The quantity $\langle \Delta_i \rangle$ gives the total sum of (squared) hyperfine couplings $A^\perp$ for a given isotope, and, through that, the isotope contribution to the electron spin energy variance.

With this notation, the dephasing time becomes,

$$T_2^* = \hbar \frac{\sqrt{2}}{\sqrt{\sum_i p_i \langle \Delta_i \rangle}}. \tag{6.4}$$

One point is worth discussing here. In the DFT code, we do not distinguish among different isotopes of the same element. Correspondingly, in Fig. 6.3 we plot the hyperfine strengths for all atoms in the simulation cell. In reality, out of these, only a few atoms will be the spinful isotopes for each of the considered elements (Si, O, Ge). The quantity $p_i \langle \Delta_i \rangle$ is thus the average contribution to the electron energy variance from a given isotope, the average being over all possible distributions of the spinful isotopes within the set of atoms of a given element. We hint at this fact by using the angular brackets. By excluding the factor $p_i$, we have made the average quantity $\langle \Delta_i \rangle$ independent of the isotopic concentration, and thus useful when judging the effects of purification. The total hyperfine coupling $\langle \Delta_i \rangle$ is set by the heterostructure: the 2DEG width, the confinement field, and the barrier chemical composition.

With this clarification, let us look at the composition of $\langle \Delta_i \rangle$ for our structures. For Si-MOS, the maximal hyperfine coupling to an oxygen atom is two orders of magnitude smaller than the one for silicon. Nevertheless, as we will see below, the coupling is large enough to contribute to the dephasing appreciably. Finally, due to the exponential decay of the wave function in the barrier, interactions with atoms deeper than 1 nm can be neglected.

For Si/SiGe, the difference between the maximum hyperfine coupling of Si and Ge is less than one order of magnitude. Therefore, a stronger dephasing is expected from the Ge atoms in the barrier. In addition, the exponential decay in the barrier is significantly weaker compared to Si-MOS (a factor of about 10 per nm SiGe vs. $10^5$ per nm oxide) because of the much lower conduction band offset of only 200 meV (vs. 2.7 eV in Si-MOS). This difference results in appreciable interactions with Ge atoms located up to several nm inside the barrier.

## 6.5 Rescaling the results for gated quantum dots

To estimate the dephasing time in a quantum dot spin qubit, we have to resolve one more issue. Namely, the size of a structure for which a DFT calculation is possible is limited. We focused on having a realistic description of the device along the $z$ direction, to faithfully describe the irregular interfaces. The lateral area of the modeled cell is thereby restricted to only about one or two square nanometers. However, gated quantum dot areas are hundred to thousand times larger. We overcome

Die approbierte gedruckte Originalversion dieser Dissertation ist an der TU Wien Bibliothek verfügbar.
The approved original version of this doctoral thesis is available in print at TU Wien Bibliothek.
TU WIEN Bibliothek Your knowledge hub

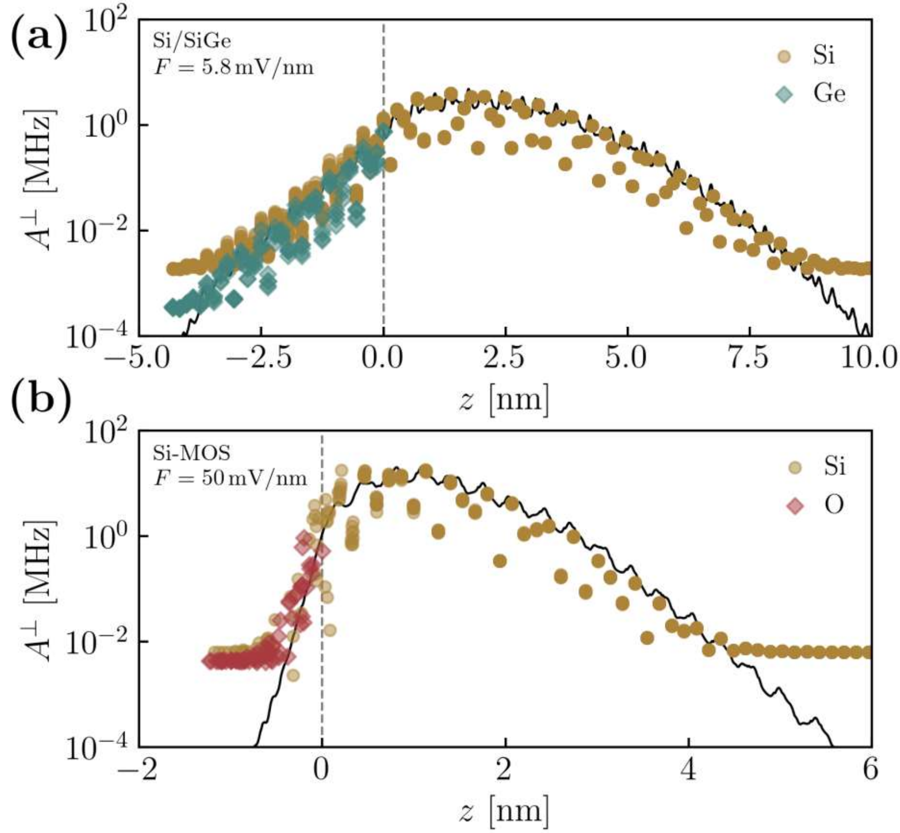


Figure 6.3: Effective hyperfine interaction $A^{\perp}/2\pi\hbar$, for **(a)** Si/SiGe and **(b)** Si-MOS, of all atoms plotted along the $z$-direction of the simulation cell. The distribution can be largely attributed to the shape of the wavefunction density (not smoothed, black line). The boundary of the barrier layer interfacing the Si at $z = 0$ is indicated by a dashed line. The interactions with barrier atoms further away from the interface subside quickly as a result of the exponential decay of the wavefunction in the barrier, while the saturation tail is due to anisotropic hyperfine interaction.

this limitation by relying on the scaling of the hyperfine strengths with the electron wavefunction given in Eq. (6.3b). As already stated, and in line with claims in literature [94], we have found that the isotropic contribution dominates the total hyperfine strength $\langle \Delta_i \rangle$. Equation (6.3b) predicts that upon enlarging the lateral area of the simulation cell by a factor $N$, the quantity $\langle \Delta_i \rangle$ gets $N$-times smaller: while there will be (on average) $N$-times more atoms of a given isotope, each individual hyperfine strength drops by a factor of $N^2$, since the electron probability density is reduced as $|\Psi(\mathbf{r})|^2 \to |\Psi(\mathbf{r})|^2/N$.

With these considerations, we define an effective density of the total hyperfine coupling $\langle \Delta^{1\mathrm{d}} \rangle$ by multiplying the value obtained from our DFT code according to Eq. (6.2) by the lateral area of the simulation cell. The isotope contribution to the quantum-dot electron energy variance is then

$$\langle \delta E_i^2 \rangle = p_i \times \langle \Delta_i^{1\mathrm{d}} \rangle / S, \tag{6.5}$$

Die approbierte gedruckte Originalversion dieser Dissertation ist an der TU Wien Bibliothek verfügbar.
The approved original version of this doctoral thesis is available in print at TU Wien Bibliothek.
TU WIEN Bibliothek Your knowledge hub

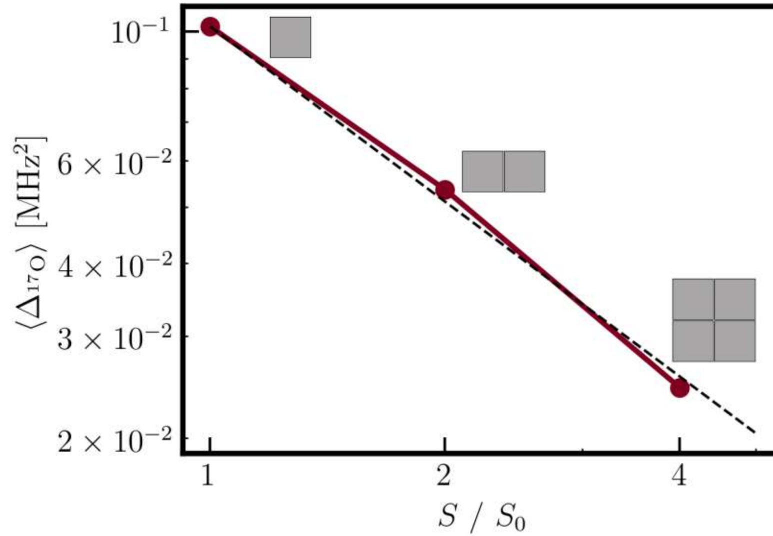


Figure 6.4: Scaling of the simulation cell size. The total hyperfine strength for oxygen $\langle \Delta_{^{17}\mathrm{O}} \rangle$ in three runs with, respectively, single, double, and quadruple repetition of a unit block of 1.15 nm×1.15 nm area. The dashed line is the expected scaling $\langle \Delta \rangle \propto 1/S$.

where $S$ is the actual area of the quantum dot in the lateral dimensions. This approximation assumes that the structure of the interface does not change drastically upon moving along the lateral coordinates and that the quantity $\langle \Delta_i \rangle$ in a quantum dot is self-averaging. We expect that this is the case, with supportive evidence and further comments given in the following.

## 6.6 Scaling of the total hyperfine coupling with the dot area

The scaling of the total hyperfine strength $\langle \Delta \rangle$ with the quantum-dot area $S$, is illustrated in Fig. 6.4. It shows the results of three runs in which the original cell is replicated two and four times laterally. We observe the scaling predicted by Eq. (6.3b) to good accuracy. Small deviations can be attributed to anisotropic contributions and numerical noise.

On the other hand, these results are not much more than a code sanity check since in those three runs we use the same configuration of atoms in each of the elementary squares depicted as the point labels in the figure. The inverse scaling with the quantum dot area (or volume) then follows from Eq. (6.3b) and from the fact that the isotropic hyperfine coupling dominates, which is obvious from Fig. 6.3. To check that the definition of $\langle \Delta^{1d} \rangle$ is of practical use, we need to estimate the variance of $\langle \Delta \rangle$ with respect to atomic configurations. To this end, we have repeated the full simulation, including the molecular dynamics, a few times. The configurations of the amorphous oxide vary, resulting in a spread of $\langle \Delta \rangle$. The obtained values, given in

Die approbierte gedruckte Originalversion dieser Dissertation ist an der TU Wien Bibliothek verfügbar.
The approved original version of this doctoral thesis is available in print at TU Wien Bibliothek.
TU WIEN Bibliothek Your knowledge hub

Table 6.1: Statistical uncertainty of $\langle\Delta\rangle$ for Si-MOS. The total hyperfine strength $\langle\Delta\rangle$ for $^{17}$O and $^{29}$Si as obtained in four full simulations at $F = 50\,\mathrm{mV/nm}$, including molecular dynamics building anew the semiconductor-oxide interface and the barrier oxide atomic structures.

| | | $\langle\Delta\rangle[\mathrm{MHz^2nm^2}]$ | |
|---|---|---|---|
| run number | H atom count | $^{17}$O | $^{29}$Si |
| 1 | 0 | 7.41 | 3766 |
| 2 | 1 | 3.43 | 3736 |
| 3 | 2 | 2.7 | 3912 |
| 4 | 2 | 2.8 | 3852 |
| mean ± std | | $4.1 \pm 2.2$ | $3817 \pm 80$ |

Tab. 6.1, can be considered independent samples of $\langle\Delta\rangle$ for our standard computation cell with 1.15 nm lateral size.

Apart from the variations in the atomic configurations in the oxide, the spread is further increased by varying hydrogen content at the interface. Paralleling their role in experiments, hydrogen atoms are used in DFT codes to passivate defects that occur as the structure is generated by *ab initio* molecular dynamics. Namely, imposing cell-size restrictions together with periodic boundary conditions generates simulated structures with defects at the interface with a large probability. Typically, these defects are Si dangling bonds, which are bonds at which oxygen would sit in a defect-free $SiO_2$. Due to the small cell area in our simulations, with less than five oxygen atoms at the interface on average, the structures with even a single defect show a significantly lower oxygen and an unrealistically high hydrogen concentration.[19] Despite all these limitations, we conjecture from the four runs for Si-MOS listed in Tab. 6.1 that, first, the presence of hydrogen-passivated defects has a strong influence, and, second, defect-free structures (more likely to be observed in experiments) will have a somewhat higher $\langle\Delta\rangle$ than the average calculated from also including structures with overestimated defects densities. The analogous data for Si/SiGe, given in Tab. 6.2, are in line with this guess. Here, the structure is crystalline and defect-free, and four runs gave values with a much smaller spread. The spread is due to variations in the placement of germanium atoms within the silicon matrix. Finally, the spread in the total effective hyperfine strength for silicon, in both Si/SiGe and Si-MOS, is well self-averaging even in our small simulation cell, as it is dominated by the contribution from the atoms in the defect-free crystalline silicon matrix of the 2DEG.

Die approbierte gedruckte Originalversion dieser Dissertation ist an der TU Wien Bibliothek verfügbar.
The approved original version of this doctoral thesis is available in print at TU Wien Bibliothek.
TU WIEN Bibliothek Your knowledge hub

Table 6.2: Statistical uncertainty of $\langle\Delta\rangle$ for Si/SiGe. The total hyperfine strength $\langle\Delta\rangle$ for $^{73}$Ge and $^{29}$Si as obtained in four full simulations at $F = 5.8\,\text{mV/nm}$.

| | $\langle\Delta\rangle[\text{MHz}^2\text{nm}^2]$ | |
|---|---|---|
| run number | $^{73}$Ge | $^{29}$Si |
| 1 | 64.9 | 1434 |
| 2 | 63.1 | 1422 |
| 3 | 65.5 | 1473 |
| 4 | 64.3 | 1461 |
| mean ± std | $64.5 \pm 1.0$ | $1448 \pm 24$ |

Table 6.3: As a function of the electric field (top row), the middle three rows give the isotope contributions $\langle\Delta_i^{1\text{d}}\rangle$ to the electron-spin energy variance in units of MHz$^2$nm$^2$. The bottom row gives the threshold isotopic concentration $p_{^{29}\text{Si}}$ at which the barrier element (germanium or oxygen) contributes as much as silicon. These thresholds are calculated using Eq. (6.6) and natural isotopic concentrations, $p_{^{73}\text{Ge}} = 7.76\%$ and $p_{^{17}\text{O}} = 377$ ppm.

| | Si/SiGe | | | Si-MOS | |
|---|---|---|---|---|---|
| | electric field $F$ [mV/nm] | | | | |
| | 4.5 | 5.8 | 7.5 | 43 | 50 |
| isotope | | | | | |
| $^{29}$Si | 1185 | 1450 | 1563 | 3592 | 3766 |
| $^{73}$Ge | 13.9 | 64.5 | 163.3 | | |
| $^{17}$O | | | | 5.86 | 7.41 |
| crossover [ppm] | 910 | 3453 | 5773 | 0.60 | 0.72 |

Die approbierte gedruckte Originalversion dieser Dissertation ist an der TU Wien Bibliothek verfügbar.
The approved original version of this doctoral thesis is available in print at TU Wien Bibliothek.
TU Bibliothek WIEN Your knowledge hub

## 6.7 Discussion

Equation (6.5) allows us to extrapolate our DFT results to quantum dots of experimentally relevant sizes. As an illustration, we consider a quantum dot with harmonic confinement with confinement lengths $l_x = l_y = 30\,\mathrm{nm}$, which corresponds to an effective QD area[20] of $S \approx 5500\,\mathrm{nm}^2$.

With this, we calculate the dephasing time $T_2^*$ according to Eqs. (6.4) and (6.5). We fix the isotopic concentration of Ge and O to their natural values, that is $p_{^{73}\mathrm{Ge}} = 7.76\%$ and $p_{^{17}\mathrm{O}} = 377\,\mathrm{ppm}$, and plot the electron spin dephasing time as a function of the $^{29}$Si content in Fig. 6.5. We find a strong increase of $T_2^*$, boosting the coherence time by a factor of 20 when reducing the amount of $^{29}$Si from its natural abundance of 4.7% down to the purest samples of nearly nuclear-spin-free Si with 50 ppm $^{29}$Si [240]. The obtained $T_2^*$ of 1 µs for natural Si and 20 µs for purified Si at 50 ppm are in line with earlier theoretical [94, 93] and experimental results [259, 36, 83, 240, 90, 14, 260, 261].

Further reduction of the $^{29}$Si content unveils the interactions with the barrier atoms. Identifiable as a crossover in Fig. 6.5, they (germanium in Si/SiGe and oxygen in Si-MOS, respectively) will eventually dominate and limit the dephasing time achievable by silicon purification. The location of the crossover can be obtained by equating the contributions from the barrier atom and silicon using Eq. (6.5),

$$p_\mathrm{X}\langle\Delta^{1\mathrm{d}}_\mathrm{X}\rangle = p_{^{29}\mathrm{Si}}\langle\Delta^{1\mathrm{d}}_{^{29}\mathrm{Si}}\rangle, \tag{6.6}$$

where X stands for $^{73}$Ge or $^{17}$O.

Solving for the silicon concentration using the DFT output gives results as listed in the last row of Tab. 6.3. In Si/SiO$_2$ we find $p_{^{29}\mathrm{Si}}$ around 1 ppm, while in Si/SiGe the threshold is much higher, and in many devices it will be above 3000 ppm.

As already mentioned, these numbers are particular to the structure details. As is clear from Eq. (6.6), the lateral size of the quantum dot is irrelevant for the crossover. However, the applied electric field is essential, especially for Si-MOS, as it determines how much the electron is pushed into the barrier. In our model the electric field has the same importance in the Si/SiGe variant even though for low electric fields, the penetration into the barrier will eventually be determined by the quantum well thickness. In both cases, increasing the electric field (or equivalently decreasing the quantum well thickness) enhances the barrier atoms' contribution, while the silicon contribution is affected less since the atoms inside the 2DEG dominate. As a result, the value of $p_{^{29}\mathrm{Si}}$ at the crossover increases. This behavior is on top of the expected dependence on the quantum dot area, which has been discussed around Eq. (6.5): With other factors fixed, in a twice larger dot the individual hyperfine couplings $A^\perp$ will be four times smaller, the total couplings $\langle\Delta\rangle$ twice smaller and the dephasing time twice longer. Such changes in quantum dot size would shift all curves plotted in Fig. 6.5 in the same way and do not change the horizontal position of the intersection.

[19] One defect, being one passivating hydrogen atom in our simulation cell area of about one nm$^2$, means a defect density about a hundred times more than what is expected from experiments [222].

[20] We use a standard definition of 'effective quantum dot volume' $V$ given by $V^{-1} = \int |\Psi(\mathbf{r})|^4\,\mathrm{d}\mathbf{r}$. Applying the definition within the $xy$ plane gives the effective area $S = \sqrt{2\pi}l_x \times \sqrt{2\pi}l_y$.

Die approbierte gedruckte Originalversion dieser Dissertation ist an der TU Wien Bibliothek verfügbar.
The approved original version of this doctoral thesis is available in print at TU Wien Bibliothek.
TU Bibliothek WIEN Your knowledge hub

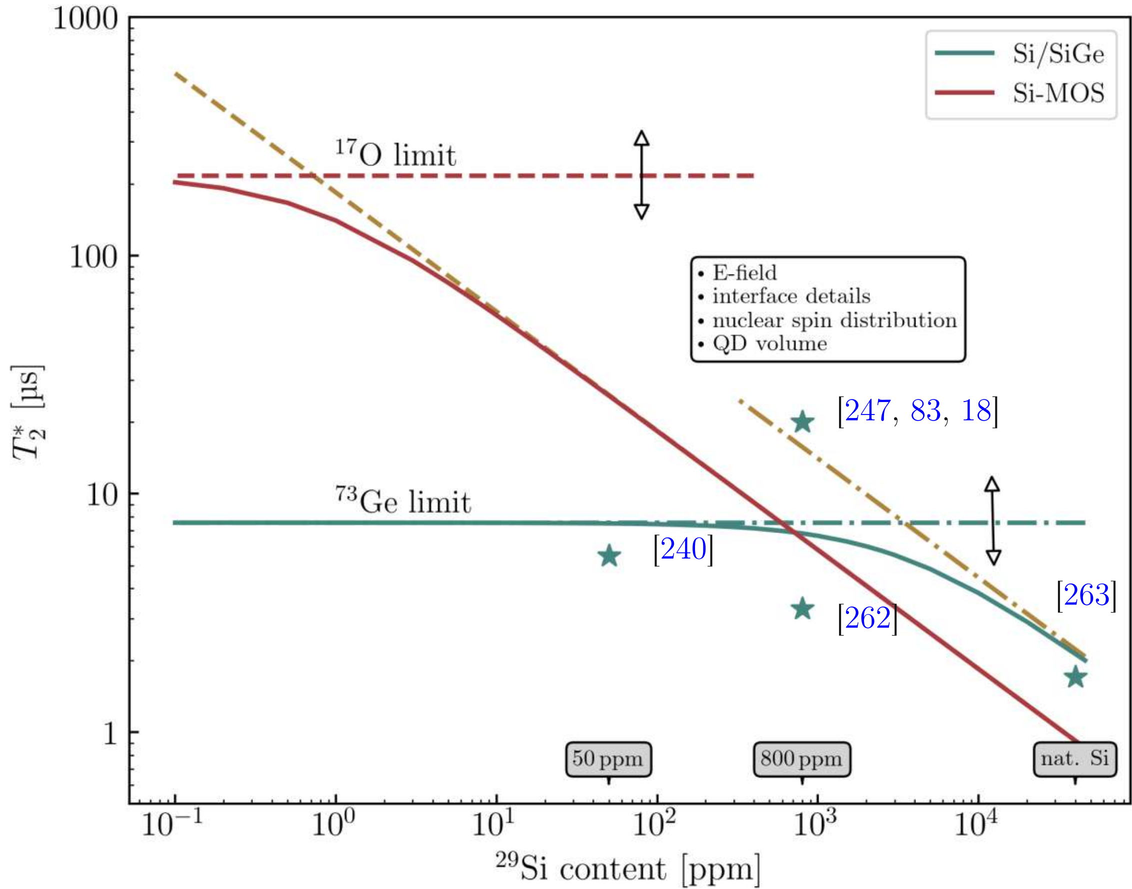


Figure 6.5: Dephasing times $T_2^*$ as a function of the amount of spinful $^{29}$Si nuclei. The field is $F = 5.8$ mV/nm for Si/SiGe and $F = 50$ mV/nm for Si-MOS. The increase of $T_2^*$ upon silicon purification is eventually limited by the germanium or oxygen atoms in the barrier. The uncertainty in the vertical position of the horizontal lines is pictorially represented by the double-headed arrows. The sources of this uncertainty are listed in the box and are explained and discussed in the main text below Eq. (11). The stars represent experimental values for Si/SiGe at 800 ppm from Ref. [247, 83, 18, 262], at 50 ppm from Ref. [240], and in natural Si from Ref. [263].

We represent the dependence of the barrier atoms' contribution on various factors pictorially in Fig. 6.5 with the double arrow and list the factors in the text box. As discussed, the electric field is crucial for the barrier atoms' contribution as it determines the strength of the wave function tails. The details of the atomic arrangement at the interface are of similar relevance in $Si/SiO_2$. Although not explicitly investigated, we suspect that analogous details might play a role in crystalline Si/SiGe, namely, how abruptly the Ge density changes (the interface width). We list this factor as 'interface details' in the box of Fig. 6.5. The next source of variations is the random location of the spinful isotopes, as we have already mentioned. This effect increases as the average number of spinful isotopes in the QD decreases and becomes

TU WIEN Bibliothek Your knowledge hub
Die approbierte gedruckte Originalversion dieser Dissertation ist an der TU Wien Bibliothek verfügbar.
The approved original version of this doctoral thesis is available in print at TU Wien Bibliothek.

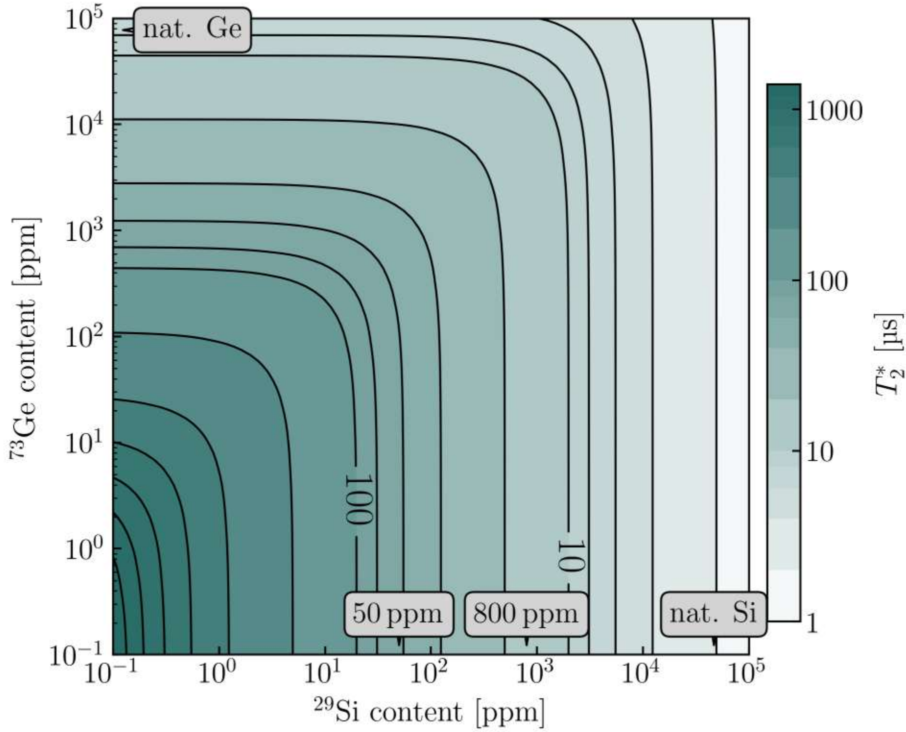


Figure 6.6: Coherence times for Si/SiGe as a function of isotopic purification of $^{29}$Si and $^{73}$Ge. We plot $T_2^*$ evaluated according to Eq. (6.4) using the parameters from Tab. 6.3 at $F = 5.8$ mV/nm.

pronounced when this number becomes of order one. Therefore, at the crossover, this effect will be strong in Si-MOS. [21]

Having all these error sources in mind, we anticipate a sizable spread of decoherence times in individual devices, even if they are dominated by nuclear noise. Comparison to experiments is further complicated by the fact that at low isotopic concentrations the coherence might be limited by other sources, for example charge noise [82, 264]. We have included a few experimentally measured dephasing times in Fig. 6.5 for illustration.

For Si purification above a few hundred ppm, Fig. 6.5 implies stronger dephasing in Si-MOS compared to Si/SiGe. The difference is not related to the barrier type but solely due to the stronger electric field. Pushing the QD against the interface generates a large spin density in the Si layers close to the interface, which translates into a stronger total hyperfine coupling.

[21] We define the average effective number $n_X$ of spinful atoms of isotope X contributing to the dephasing in a QD using the inverse participation ratio. Namely, we collect the values of individual atoms contributions $A_n^\perp$, normalize these numbers as a probability distribution, $A_n^\perp \to P_n$ so that $\sum_n P_n = 1$, and define $n_X = p_X / \sum_n P_n^2$. In this way, for an area $S = 5500$ nm$^2$ and at the crossover, we obtain $n_{^{29}\mathrm{Si}} \approx 3136$ and $n_{^{73}\mathrm{Ge}} \approx 3661$ in Si/SiGe and $n_{^{29}\mathrm{Si}} \approx 0.3$ and $n_{^{17}\mathrm{O}} \approx 14.2$ in Si-MOS.

Die approbierte gedruckte Originalversion dieser Dissertation ist an der TU Wien Bibliothek verfügbar.
The approved original version of this doctoral thesis is available in print at TU Wien Bibliothek.
TU Bibliothek Your knowledge hub WIEN

Finally, we discuss the isotopic purification of Ge, as its contribution to electron dephasing in Si/SiGe structures has been anticipated [100, 37, 83, 99]. Motivated by this prospect [265], in Fig. 6.6 we plot the dephasing as a function of both Si and Ge isotopic content. The figure visualizes the crossover map for various isotopic concentrations.

## 6.8 Summary

We calculate hyperfine interactions within a state-of-the-art *ab-initio* framework and estimate the resulting dephasing of a spin qubit in Si-MOS and Si/SiGe quantum dots. The simulations include planar heterostructures with disordered interfaces at which a 2DEG is induced by an external electric field. We extract the hyperfine tensors for the interaction between the conduction-band electron and nuclear spins of every atom in the structure and examine the impact of isotopic purification on the coherence. We find that the improvement of the electron spin coherence time by isotopic purification is limited by the presence of spinful atoms in the barrier layer of the heterostructure once the $^{29}$Si content drops below a threshold value. The threshold strongly depends on the interface electric field. For the Si-MOS case, this threshold is around 1 ppm at $F = 50$ mV/nm, below which the coherence-time is limited to 200 µs by oxygen atoms. In Si/SiGe with the natural abundance of 7.7% $^{73}$Ge, the threshold at $F = 5.8$ mV/nm is 3500 ppm of $^{29}$Si, below which the coherence time is limited to 10 µs by germanium atoms.

Die approbierte gedruckte Originalversion dieser Dissertation ist an der TU Wien Bibliothek verfügbar.
The approved original version of this doctoral thesis is available in print at TU Wien Bibliothek.
TU WIEN Bibliothek Your knowledge hub

Die approbierte gedruckte Originalversion dieser Dissertation ist an der TU Wien Bibliothek verfügbar.
The approved original version of this doctoral thesis is available in print at TU Wien Bibliothek.
TU WIEN Bibliothek Your knowledge hub

# Chapter 7

# Conclusions and outlook

The realization of a useful quantum computer requires the joint effort of physicists, material scientists, electronic engineers, computer scientists, and logicians. Expertises from all these fields need to be interwoven, rendering quantum computing one of the most interesting challenges of today's scientific endeavors. Of course, such a venture comes not without several pitfalls and it is still an open question if and how quantum computers can be made robust and noise resilient. The present work deals with the material aspect of one of the most promising platforms for quantum computing, quantum-dot based spin qubits, from a theoretical perspective. Focussing on electron spin qubits, the two most important material systems, Si/SiGe and Si-MOS, are investigated. Several material properties as well as their impact on qubit parameters are determined from elaborate DFT calculations.

DFT is a method to determine the electronic structure of a given atomic configuration. Therefore, the generation of credible atomistic interface models is an essential requirement for this study, and the first intermediate goal presented in this thesis. While the construction of Si/SiGe interfaces is trivial, Si/$SiO_2$ interfaces (as used in Si-MOS qubits) require sophisticated modeling. By means of dynamic AIMD calculations, we simulate the full thermal oxidation process of Si, leading to numerous insights in oxide growth and resulting interface properties. The simulations revealed an oxidation scheme which naturally integrates all previously reported experimental observations, from spontaneous surface reactions to molecular precursor mediated dissociation and $O_2$ diffusion through the oxide. This sequence of oxidation mechanisms leads to a decrease from the comparably fast oxidation rate in the initial regime (before the surface is saturated with O) to the linear oxidation regime described by the Deal-Grove model. The resulting interface structures show a 0.5 nm thick interfacial transition region characterized by increasing Si-O coordination and strained chemical bonds.

Running these AIMD simulations is a computationally highly expensive and time-consuming process (several months per structure). Because the $O_2$ molecules are introduced above the Si surface individually (and often repelled), constant supervision is required. This process becomes increasingly cumbersome, since the adsorption of $O_2$ molecules is inhibited with increasing oxygen surface coverage. Therefore, we introduced a Gaussian approximation potential (GAP)-based machine learning (ML)

interatomic potential tailored for generating ultra-thin oxide layers on a Si substrate. The training data is mostly taken from the AIMD calculations above. By means of this ML model, the thermal oxidation can be modeled even more realistically, in the sense that the Si surface is exposed to an oxygen atmosphere that is periodically "refilled" to maintain a constant pressure. In addition, given the highly reduced computational costs compared to AIMD, one oxidation cycle to generate a $Si/SiO_2$ interface structure with an oxide thickness of 1 nm requires about one week using a single core (compared to 384 cores used for AIMD).

In the next step, we establish an *ab-initio* based modeling approach to extract valley- and spin splittings from atomistic heterostructures. This first-principles based approach goes beyond modeling techniques that have been used so far, most importantly TB and $k \cdot p$, and allows to investigate the impact of atomistic disorder in considerable detail. Stress and strain, disorder at the interface, and atomistic fluctuations are inherently captured by our DFT model. We find wide distributions of valley and spin splittings by more than one order of magnitude, which can be attributed to the variability of atomic details at the interface to the confining materials. In a reliable quantum processor, millions of individually controllable qubits need to be integrated on one chip necessitating highly uniform devices. In this respect, our calculations underline the importance of reproducible interfaces as the qubit properties are strongly influenced by atomic disorder. On the other hand, our results imply that valley- and spin splittings could be tuned by engineering the interfaces to the confining materials.

Finally, we employ the DFT model for the determination of hyperfine tensors of all atoms in the simulation cell. Calculation of the expected decoherence time of a quantum-dot electron spin from these hyperfine tensors yields the following insights: In Si-MOS, oxygen is not relevant for electron spin coherence even at the highest current Si-purification levels. However, in Si/SiGe the $^{73}$Ge isotopes limit the coherence time to a few microseconds already at 3500 ppm of $^{29}$Si fraction. This value is less than 4.68 %, the natural abundance of $^{29}$Si, but substantially more than 50 ppm, the lowest currently available fraction of $^{29}$Si in purified silicon. This provides compelling evidence that the germanium must be purified in addition to silicon to suppress nuclear noise effectively. Our model indeed predicts a possible improvement of the coherence time by another order of magnitude. Our work therefore quantifies the effects of a new source of magnetic noise that must be dealt with to further improve the performance of Si spin qubits.

## 7.1 Future prospects

Semiconductor spin qubits are a highly pursued area of research and have evolved extremely quickly over the last decades. Given the fact that a broad range of material platforms fulfill the requirements to trap and manipulate electron or hole spins, many different approaches have attracted interest over the last years. In the course of this process, advantages and drawbacks of each material platform have been identified. Two prime examples are the strong hyperfine interaction in GaAs or the detrimentally

Die approbierte gedruckte Originalversion dieser Dissertation ist an der TU Wien Bibliothek verfügbar.
The approved original version of this doctoral thesis is available in print at TU Wien Bibliothek.
TU Bibliothek WIEN Your knowledge hub

low valley splitting in Si/SiGe. Some of these obstacles can be overcome in other materials (Si instead of GaAs to remove nuclear spins) or by structural engineering of the devices (wiggle wells in Si/SiGe to enhance the valley splitting). This thesis investigates some of these aspects. However, and possibly more importantly, it shows that DFT can be applied for modeling spin qubits. In this respect, the possibilities explored here have only scratched the surface. In the following, an incomplete list of possible extensions is given:

**Transferring the methodology to holes.** Recently, hole spin qubits in Ge have attracted a lot of attention. Reasons are fast and all-electrical driving (EDSR) and Ohmic contacts to superconductors. Applying DFT in this framework would be highly interesting.

**SOC in Si/SiGe.** The calculation of the SOC coefficients in Si/SiGe failed only due to technical issues (in combination with a limited amount of time to finish a PhD).

**Calculation of the $g$-factor.** A very important quantity for qubit application is the $g$-factor which can in principle be obtained from DFT.

**Larger simulation cells.** It is hard to say if DFT modeling of a full devices will be possible in the foreseeable future. However, taking larger simulation cells to have better averaging (especially in Si-MOS), less restrictions (e.g. arbitrary Ge profiles), and more long-range disorder would certainly improve the accuracy and predictive power of DFT models.

**Other device designs.** Next to planar heterostructures, qubits have also been fabricated in FinFETs or nanowires. In combination with larger simulation cells, modeling of such devices might become feasible.

**Hyperfine interaction in SiGe/Si/SiGe structures.** In order to reduce the system complexity for the calculation of the hyperfine interactions, only one interface to a barrier was considered. Since Si/SiGe qubits are typically realized in sandwiched Si layers, the second barrier would also impact the dephasing times.

Die approbierte gedruckte Originalversion dieser Dissertation ist an der TU Wien Bibliothek verfügbar.
The approved original version of this doctoral thesis is available in print at TU Wien Bibliothek.
TU WIEN Bibliothek Your knowledge hub

TU WIEN Bibliothek Your knowledge hub
Die approbierte gedruckte Originalversion dieser Dissertation ist an der TU Wien Bibliothek verfügbar.
The approved original version of this doctoral thesis is available in print at TU Wien Bibliothek.

# Appendix A

# Machine learning parameters and training dataset

## A.1 Descriptor parameters

The descriptors can be tuned by the user via a number of parameters as given in Tab. A.1. The weight of each descriptor is controlled by $\delta$, $r_{\text{cut}}$ is a cut-off radius which defines a sphere within which neighboring atoms are considered. $r_{\Delta}$ is the cutoff transition width, which defines the distance needed for the descriptor cut-off to smoothly go to zero. $n_{\max}$ and $l_{\max}$ are the number of angular and radial basis functions for the SOAP descriptor, respectively, and $\zeta$ is the power the kernel is raised to.

## A.2 Generation of the training dataset

One of the main challenges when developing an MLFF is finding suitable training data. Among the problems that can be encountered are overfitting [266], data quality issues (incomplete or biased data), as well as imbalanced data (some classes of structures in the training dataset appear more frequently than others, resulting in a bias or poor performance). A detailed overview of the data used for our MLFF is given in Tab. A.2. The dataset contains single atoms, dimers, periodic bulk structures (crystalline and amorphous), surfaces and nanowires, as well as gaseous $O_2$. In a first step, we tried several data compositions and chose the MLFF that gave the best results (based on evaluation of the properties from Fig. 4.16 and Tab. 4.1). This initial ML model was then used to generate new structures that were recalculated by DFT. This additional data was then implemented into the training dataset from Tab. A.2. With this data, we obtain the final MLFF.

Our efforts to further improve the MLFF by including more data into the training dataset gave the opposite result: the performance decreased. From this, we conclude that the model is prone to overfitting. One of the ways to avoid overfitting is the so-called "early-stopping strategy" [266]. Since the MLFF already gave satisfying results in its second iteration, we decided to stop at this point.



Die approbierte gedruckte Originalversion dieser Dissertation ist an der TU Wien Bibliothek verfügbar.
The approved original version of this doctoral thesis is available in print at TU Wien Bibliothek.
TU WIEN Bibliothek Your knowledge hub

Table A.1: Parameters of the employed SOAP, two-body and three-body descriptors, based on values from [210]. The meaning of the parameters is given in the text (with detailed description for SOAP in [138]).

| Parameter | SOAP | Two-body | Three-body |
|---|---|---|---|
| $\delta$ | 0.4 | 4 | 1 |
| $r_{\mathrm{cut}}$ | 5 | 4 | 3 |
| $r_{\Delta}$ | 1 | - | - |
| $n_{\mathrm{max}}$ | 8 | - | - |
| $l_{\mathrm{max}}$ | 4 | - | - |
| $\zeta$ | 4 | - | - |

Table A.2: Structures in the training dataset of the GAP force field. The type of structure is given along with the number of atoms in the structure as well as the number of individual structures. The associated parameters $\sigma_{\mathrm{E}}$ and $\sigma_{\mathrm{F}}$ represent the regularisation in the GAP corresponding to energies and forces, respectively [267].

| Structure type | Number of atoms | Number of structures | $\sigma_{\mathrm{E}}$ | $\sigma_{\mathrm{F}}$ |
|---|---|---|---|---|
| single atoms | 1 | 3 | 0.0001 | 0.001 |
| Si dimers | 2 | 97 | 0.01 | 0.1 |
| O dimers | 2 | 57 | 0.01 | 0.1 |
| Si–O dimers | 2 | 23 | 0.01 | 0.1 |
| Si–H dimers | 2 | 52 | 0.01 | 0.1 |
| Si bulk | 192 | 90 | 0.002 | 0.02 |
| $SiO_2$ bulk | 216 | 70 | 0.002 | 0.02 |
| clean Si surface | 224 | 50 | 0.002 | 0.02 |
| ox. Si surface | 232–5211 | 213 | 0.002 | 0.02 |
| Si nanowire | 576–1680 | 100 | 0.002 | 0.02 |
| ox. Si nanowire | 1682–2063 | 9 | 0.002 | 0.02 |
| $O_2$ gas | 3–200 | 143 | 0.002 | 0.02 |

Die approbierte gedruckte Originalversion dieser Dissertation ist an der TU Wien Bibliothek verfügbar.
The approved original version of this doctoral thesis is available in print at TU Wien Bibliothek.
TU WIEN Bibliothek Your knowledge hub

# Appendix B

# Electric field from first principles

Die approbierte gedruckte Originalversion dieser Dissertation ist an der TU Wien Bibliothek verfügbar.
The approved original version of this doctoral thesis is available in print at TU Wien Bibliothek.

The use of the Berry phase method [229, 230] allows to consider electric fields in periodic (supercell) structures. CP2K [114] employs the formalism presented in [228, 127]. This approach uses the Berry-phase formalism [229, 230] to enable application of a voltage bias across the whole simulation cell and circumvents problems arising from potential jumps in a periodic cell.[22] The implementation in CP2K is based on imposing closed-circuit boundary conditions with a constant bias. The electric fields in the material layers adjust according to the layer thickness and relative permittivity. However, the potential is ensured to be continuous, as illustrated by the Hartree potential $V_{\mathrm{H}}$ representing the DFT quantum well potential in Fig. B.1. Roughly speaking, the code works as follows. The applied bias polarizes the material layers and thereby leads to the formation of charge layers at the interfaces (see also Fig. C.1). Then, the initially applied bias is subtracted again in order to reinstall continuity of the potential at the cell border. With this, one arrives at the effective potential in the DFT calculation which strongly depends on the employed materials and the overall simulation setup. Considering simulation cells without vacuum (as employed for the valley splitting calculations of Chapter 5), one arrives at a scenario in which the electric fields in the material layers (Si and SiGe) point in opposite directions. This is not the case for slab models, as used for the calculations of hyperfine interactions in Chapter 6. In this case, the bias compensation changes the field direction in the vacuum.

Because $V_{\mathrm{H}}$ contains contributions from both the quantum well and the external bias, the pure external potential profile $V_{\mathrm{ext}}$ is obtained by removing the quantum well potential at zero electric field $V_{\mathrm{H},0}$ from the Hartree potential $V_{\mathrm{H}}$, see Fig. 5.4.

[22] A constant bias, i.e. a constant displacement field across the whole simulation cell is only consistent with periodic boundary conditions if discontinuities of the electrostatic potential appear. Such discontinuities lead to unphysical results.

TU WIEN Bibliothek Your knowledge hub

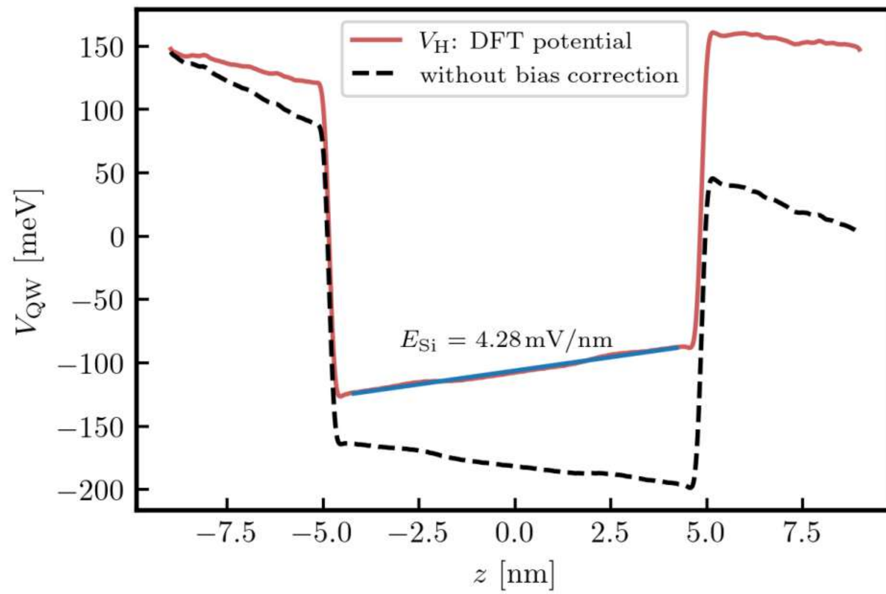


Figure B.1: Electrostatic potential profiles across the biased SiGe/Si/SiGe simulation cells with (red line) and without (black dashed line) bias correction. The latter represents an electric field distribution in the stacked materials according to their permittivity. Such a potential requires jumps at the cell border. The bias correction implemented in the DFT code maintains a continuous electrostatic potential across the cell border. Including the correction, a potential profile as represented by the Hartree potential $V_H$ emerges and defines the effective potential in DFT. Thus, the field in the Si layer is obtained by fitting to $V_H$ (blue line).

Die approbierte gedruckte Originalversion dieser Dissertation ist an der TU Wien Bibliothek verfügbar.
The approved original version of this doctoral thesis is available in print at TU Wien Bibliothek.
TU WIEN Bibliothek Your knowledge hub

# Appendix C

# Permittivity

Die approbierte gedruckte Originalversion dieser Dissertation ist an der TU Wien Bibliothek verfügbar.
The approved original version of this doctoral thesis is available in print at TU Wien Bibliothek.
TU Bibliothek WIEN Your knowledge hub

In order to validate the DFT approach, the relative permittivity $\epsilon_r$ is calculated as a sanity check for our calculations. Note that the structure is not relaxed under the influence of the applied bias. Thus, the ionic contributions to the displacement field are not taken into account as is the case for high-frequency (or optical) excitation. Experiments show that the high-frequency permittivity in Si is practically the same as in the electrostatic case ($\epsilon_r \approx 12$) [268]. However, the permittivity of $SiO_2$ reduces from 3.8 to around 2 in the high-frequency regime [269, 270]. The electric field is applied in growth direction, perpendicular to the interface.

For the calculation of $\epsilon_r$, the induced charge density (ICD) method is used [271, 272]. We start with Gauss' law

$$\nabla \cdot \mathbf{p}(\mathbf{r}) = -\rho_{\text{ind}}(\mathbf{r}) \tag{C.1}$$

using the microscopic polarization $\mathbf{p}(\mathbf{r})$ and the ICD $\rho_{\text{ind}}(\mathbf{r})$. The ICD $\rho_{\text{ind}}(\mathbf{r})$ is defined as the difference in charge density induced by application of an external electric field. In other words, $\rho_{\text{ind}}(\mathbf{r})$ is obtained when subtracting the charge density of two calculations with different electric fields (here $\pm 30\,\text{mV/nm}$). With the electric field aligned perpendicular to the interfaces (i.e. in $z$ direction), Eq. (C.1) simply writes

$$\frac{\mathrm{d}}{\mathrm{d}z}\bar{p}(z) = -\bar{\rho}_{\text{ind}}(z) \tag{C.2}$$

where $\bar{p}(z)$ and $\bar{\rho}_{\text{ind}}(z)$ are cross-section averages of polarization and induced charge density, respectively. Resulting from DFT calculations on a Si-MOS heterostructure, the averaged ICD $\bar{\rho}_{\text{ind}}(z)$ is plotted in Fig. C.1. The induced charge density is concentrated at interfaces and surfaces, where jumps of $\epsilon_r$ occur. Integration of Eq. (C.2) gives

$$\bar{p}(z) = \bar{p}_0 - \int_0^z \mathrm{d}z' \bar{\rho}_{\text{ind}}(z'). \tag{C.3}$$

Here, $\bar{p}_0$ is a constant resulting from integration and represents the polarization at one end of the simulation cell. The integration spans the entire simulation cell. When using slab models, i.e. structures passivated with H and surrounded by vacuum as in the present case, $\bar{p}_{-\infty}$ can be set to zero, because the charge density in the vacuum

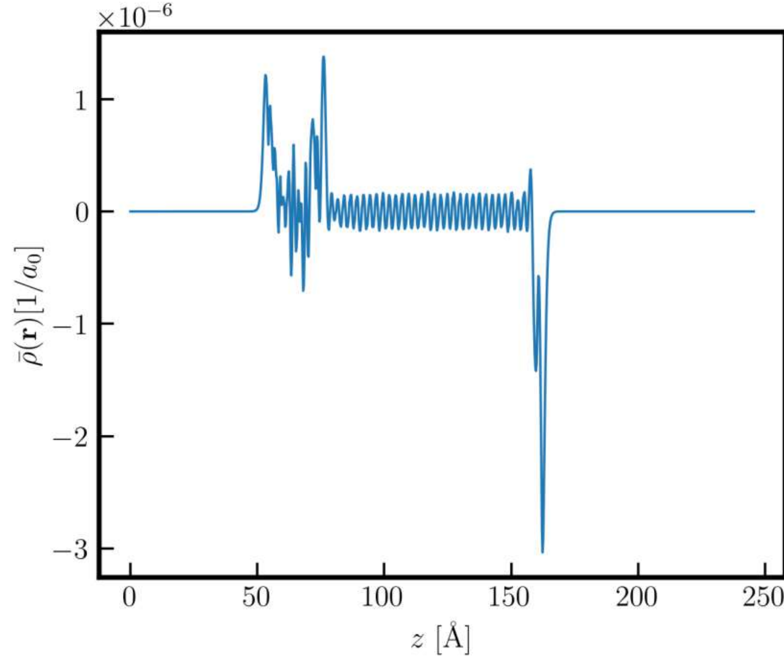


Figure C.1: Cross-section average of the induced charge density $\bar{\rho}_{\text{ind}}(z)$ plotted along the $z$ direction of a Si-MOS heterostructure.

is zero. From the polarization profile, one can determine the spatially resolved (high-frequency) permittivity $\epsilon_r(z)$ by means of the relation [271]

$$\epsilon_r(z) = \frac{\epsilon_0 F_{\text{ext}}}{\epsilon_0 F_{\text{ext}} - \bar{p}(z)} \tag{C.4}$$

with the vacuum permittivity $\epsilon_0$ and the external electric field $F_{\text{ext}}$. Because we applied $\pm 30\text{mV/nm}$, $F_{\text{ext}} = 60\,\text{mV/nm}$. As can be seen in Fig. C.2, the permittivity matches our expectations, going from 2 in the oxide layer to 12 in the Si crystal. Furthermore, one can identify the interfacial transition region (TR) in the plot. Similarly, we obtain $\epsilon_r \approx$14 for SiGe.

Die approbierte gedruckte Originalversion dieser Dissertation ist an der TU Wien Bibliothek verfügbar.
The approved original version of this doctoral thesis is available in print at TU Wien Bibliothek.
TU WIEN Bibliothek Your knowledge hub

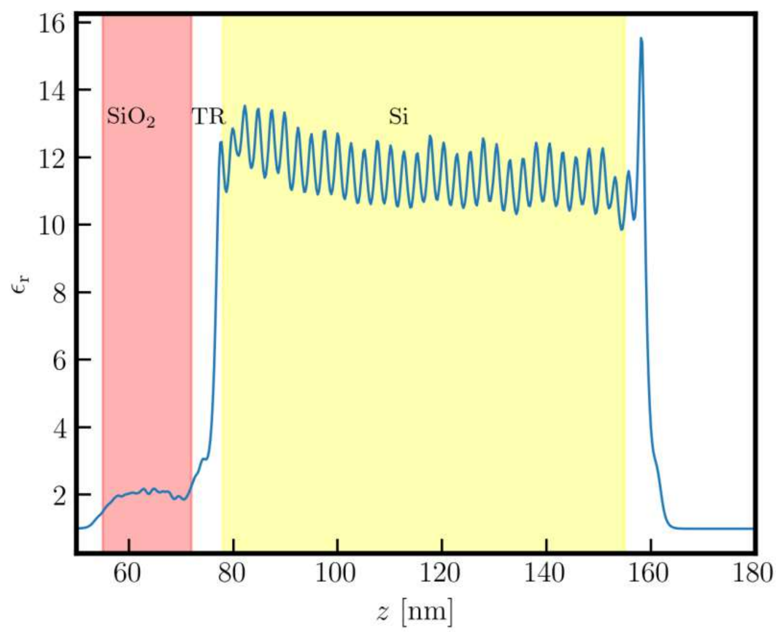


Figure C.2: Permittivity profile of a $SiO_2$/Si heterostructure. The materials are indicated by colored regions making the transition region (TR) visible.

Die approbierte gedruckte Originalversion dieser Dissertation ist an der TU Wien Bibliothek verfügbar.
The approved original version of this doctoral thesis is available in print at TU Wien Bibliothek.
TU Bibliothek Your knowledge hub WIEN

Die approbierte gedruckte Originalversion dieser Dissertation ist an der TU Wien Bibliothek verfügbar.
The approved original version of this doctoral thesis is available in print at TU Wien Bibliothek.
TU WIEN Bibliothek Your knowledge hub

# Appendix D

# Validation of the simulation cell setup

Die approbierte gedruckte Originalversion dieser Dissertation ist an der TU Wien Bibliothek verfügbar.
The approved original version of this doctoral thesis is available in print at TU Wien Bibliothek.
TU WIEN Bibliothek Your knowledge hub

The high computational costs of DFT calculation put restrictions on the size of the simulation cell. As a direct consequence, simulation cells with arbitrary Ge profiles can not be constructed. Because the simulation cell holds 18 atoms per atomic monolayer, the Ge content can only take discrete values with a step size of $1/18 \approx 5\,\%$. Since arbitrary Ge profiles can indeed be reconstructed in an infinitely large simulation cell, calculations in the small cell lead to artificially introduced errors. More specifically, the small cell introduces sharp step-like features in the Ge profile, broadening the Fourier transform of the confining quantum well potential and therefore increasing the valley coupling spectrum at all $k$, and specifically at $k \approx 2k_0$. As a result, the obtained valley splitting is overestimated with respect to a larger cell (large enough to correctly reconstruct the demanded Ge profile).

## D.1 Convergence of median $E_{\mathrm{VS}}$ with supercell size

In order to circumvent this problem, we narrow down the considered Ge profiles to target profiles with jumps of $1/18 \approx 5.5\,\%$. Such profiles can be rebuild in our simulation cell without deviations. The median valley splitting values is therefore directly obtained correctly. However, significant fluctuations around the median value originating from disorder at the interface can be expected. In larger simulation cells, the impact of disorder gets averaged out. In order to verify this idea, we performed tight-binding calculations on various cell sizes, see Fig. D.1. As can be seen, the results match our expectations of converged median values and fluctuations decreasing with increasing cell size.

## D.2 Spectra of wiggle wells

Wiggle wells with oscillating Ge content in the well do not fulfill our requirement of step-like Ge distributions with steps of $1/18\,\%$. Thus, the resulting profile in the small DFT cell can not represent the demanded oscillating profile exactly. Nevertheless, when calculating the Fourier spectrum of the Ge distributions in Fig. D.2, we find that peaks at the desired wave vectors. From this we conclude that the wiggle well

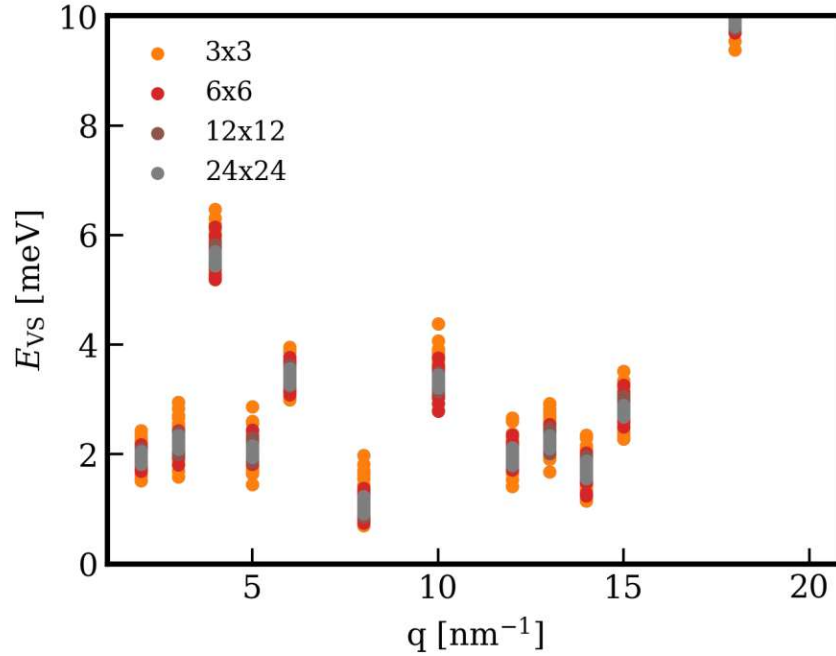


Figure D.1: Convergence of the median values of the valley splitting $E_{\mathrm{VS}}$ for Ge profiles in which the Ge amount varies in predefined steps of $1/18$. The underlying quantum wells show Ge oscillations with wavevector $q$, see also Fig. D.2. Because the steps of $1/18$ where chosen such that the profile is independent of the cell size, the median values obtained by a 3x3 supercell are directly converged. Averaging over the atomic fluctuations reduces the spread between the respective realizations with larger supercells.

oscillations are still captured correctly even in our small simulation cell, validating the calculations within the DFT framework.

TU Bibliothek Your knowledge hub WIEN
Die approbierte gedruckte Originalversion dieser Dissertation ist an der TU Wien Bibliothek verfügbar.
The approved original version of this doctoral thesis is available in print at TU Wien Bibliothek.

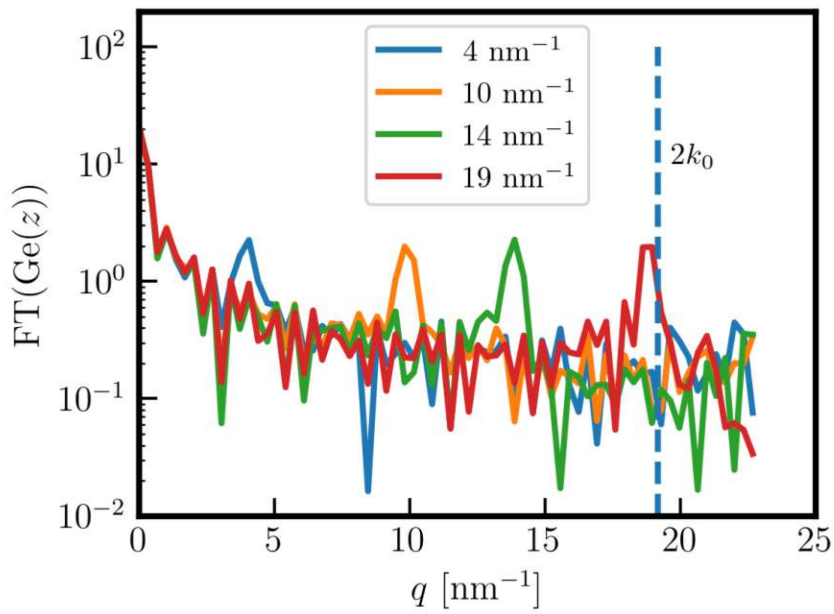


Figure D.2: Discrete Fourier transform of some representative Ge profiles that constitute wiggle wells with wave vector $q$. Despite the small cell size which allows only rough jumps of 5.5% in the Ge content, each structure shows a pronounced peak at the desired $q$.

Die approbierte gedruckte Originalversion dieser Dissertation ist an der TU Wien Bibliothek verfügbar.
The approved original version of this doctoral thesis is available in print at TU Wien Bibliothek.
TU WIEN Bibliothek Your knowledge hub

Die approbierte gedruckte Originalversion dieser Dissertation ist an der TU Wien Bibliothek verfügbar.
The approved original version of this doctoral thesis is available in print at TU Wien Bibliothek.

# Appendix E

# Estimation of the diffusion coefficient for $^{17}$O atoms

In the main text, we have estimated the effects of the oxygen and germanium nuclear spins on the quantum dot electron spin coherence assuming the so-called ergodic limit [102]. It applies if the total time over which data are collected (to evaluate the electron dephasing) is larger than the time scale over which the nuclear spin configuration changes due to its inherent dynamics. To make sure that the limit applies, the latter time scale must not be exceedingly long. One can understand this requirement also by pointing out that if the dynamics of the oxygen or germanium nuclear spins is very slow, the associated Overhauser field remains frozen during an experimental run probing the properties of the electron spin and does not contribute to its dephasing.

To estimate the internal dynamics time scale, we assume that the nuclear spins undergo diffusion induced by their dipole-dipole interaction. The diffusion constant can be estimated by the method of moments [273, 274]. To this end, we evaluate formulas derived in Ref. [275]. We aim at an order-of-magnitude estimate, and adopt approximations accordingly.



Die approbierte gedruckte Originalversion dieser Dissertation ist an der TU Wien Bibliothek verfügbar.
The approved original version of this doctoral thesis is available in print at TU Wien Bibliothek.
TU WIEN Bibliothek Your knowledge hub

## E.1 Expression for the diffusion constant derived by the method of moments

Previous work [275] considered an ensemble of alike nuclear spins in external magnetic field $B$ interacting pairwisely,[23]

$$H = -\hbar\gamma B \sum_i I_z^i + \frac{1}{2}\sum_{i\neq j}\left(A_{ij} I_+^i I_-^j + B_{ij} I_z^i I_z^j\right), \tag{E.1}$$

where for dipole-dipole interaction the couplings are

$$B_{ij} = \frac{\mu_0}{4\pi}\gamma^2\hbar^2 \frac{1-3\cos^2\theta_{ij}}{r_{ij}^3}, \tag{E.2a}$$

$$A_{ij} = -\frac{1}{2}B_{ij}, \tag{E.2b}$$

expressed through quantities

$$\mathbf{r}_i = \text{position of nucleus}\, i, \tag{E.3a}$$

$$\mathbf{r}_{ij} = \mathbf{r}_i - \mathbf{r}_j, \tag{E.3b}$$

$$\cos^2\theta_{ij} = \frac{|\mathbf{r}_{ij}\cdot\mathbf{z}|^2}{r_{ij}^2}, \tag{E.3c}$$

and with $\gamma = g\mu_N/\hbar$, $g$ being the nuclear $g$-factor, $\mu_N$ being the nuclear magneton, and $\mu_0$ being the vacuum magnetic permeability. We have also assumed that the magnetic field is applied along a unit vector $\mathbf{z}$ and define the nuclear spin operator in Cartesian components accordingly, with $I_z = \mathbf{I}\cdot\mathbf{z}$.

Starting from Eq. (E.1), Ref. [275] derives a simplified expression for the diagonal elements of the diffusion tensor,[24]

$$D_{\mu\mu} \simeq \frac{\sqrt{\pi I(I+1)}}{4\sqrt{12}\hbar}\frac{\sum_j |\mathbf{r}_{ij}\cdot\boldsymbol{\mu}|^2 B_{ij}^2}{\sqrt{\sum_k (B_{ik}-B_{jk})^2}}. \tag{E.4}$$

Here in the upper (lower) sum the term $j = i$ is excluded (the terms $k = i$ and $k = j$ are excluded) and the index $\mu$ denotes a Cartesian component along a unit vector $\boldsymbol{\mu}$. Following Ref. [275], we drop the cross term $B_{ik}B_{jk}$ from the sum in the denominator, which gives $\sum_k (B_{ik}-B_{jk})^2 \approx 2\sum_k B_{ik}^2$ upon renaming the summation index. With this change, we now further simplify the expression in Eq. (E.4).

[23]Our Eq. (E.1) is Eq. (19) of Ref. [275], except that we define the Zeeman term with the opposite sign. In addition, we note that in experiments, a micromagnet inducing spatially dependent magnetic field is often employed to enable electrical manipulation of the electron spin. A large gradient could suppress the nuclear spin diffusion by inducing a mismatch of Zeeman energies for a spin pair that could otherwise make an energy-conserving spin flip-flop. Large inhomogeneous electric field gradients, coupling to the nuclear spins $I > 1/2$ through the quadrupole interaction, or inhomogeneous Knight fields, could act similarly. Within our simple approach, we ignore these effects.

[24]It is given in Ref. [275] as Eq. (35), considering the relation $A_{ij} = -B_{ij}/2$.

Die approbierte gedruckte Originalversion dieser Dissertation ist an der TU Wien Bibliothek verfügbar.
The approved original version of this doctoral thesis is available in print at TU Wien Bibliothek.
TU Bibliothek WIEN Your knowledge hub

Die approbierte gedruckte Originalversion dieser Dissertation ist an der TU Wien Bibliothek verfügbar.
The approved original version of this doctoral thesis is available in print at TU Wien Bibliothek.
TU Wien Bibliothek Your knowledge hub



Table E.1: Estimated diffusion constants. The last column gives the diffusion constant calculated according to Eq. (E.13) for the isotope and material given in the first two columns. The table lists other quantities that enter the evaluated formula: the isotope nuclear spin $g$-factor $g$, spin magnitude $I$, (for crystalline materials) the number of atoms per unit cell with volume $a_0^3$, and the concentration (of the isotope among all isotopes of the given chemical element) $p$. The quantity $\rho_{\text{spin}}$ is the isotope volume density, given by $\rho_{\text{spin}} = p\rho_{\text{atom}}$, and it defines the effective radius $r_\rho$ by Eq. (E.12).

| system | | $g_N$ | $I$ | $\rho_{\text{atom}}$ | $p$ | $\rho_{\text{spin}}$ | $r_\rho$ | $D$ |
|---|---|---|---|---|---|---|---|---|
| isotope | lattice | dimensionless | dimensionless | $[\frac{1}{a_0^3}]$ | [ppm or %] | $[\frac{1}{\text{nm}^3}]$ | [Å] | $[\frac{\text{nm}^2}{\text{s}}]$ |
| $^{17}$O | $SiO_2$ | -1.89 | $5/2$ | – | 380 ppm | 0.017 | 24 | 8.5 |
| $^{29}$Si | $SiO_2$ | -0.555 | $1/2$ | – | 4.67 % | 1.02 | 6.2 | 0.85 |
| $^{29}$Si | diamond | -0.555 | $1/2$ | 8 | 4.67 % | 2.3 | 4.7 | 1.1 |
| $^{29}$Si | diamond | -0.555 | $1/2$ | 8 | 800 ppm | 0.04 | 18 | 0.29 |
| $^{29}$Si | diamond | -0.555 | $1/2$ | 8 | 50 ppm | 0.0025 | 46 | 0.11 |
| $^{29}$Si | SiGe | -0.555 | $1/2$ | 4 | 4.67 % | 1.1 | 6.1 | 0.86 |
| $^{73}$Ge | SiGe | -0.878 | $9/2$ | 4 | 7.76 % | 1.8 | 5.1 | 15 |
| $^{75}$As | GaAs | 1.44 | $3/2$ | 4 | 100 % | 22 | 2.2 | 36 |
| $^{71}$Ga | GaAs | 2.56 | $3/2$ | 4 | 40 % | 8.8 | 3.0 | 83 |
| $^{69}$Ga | GaAs | 2.02 | $3/2$ | 4 | 60 % | 13 | 2.6 | 59 |

First, we average over the direction of the diffusion, that is, the components of the diffusion tensor,

$$\langle \cdots \rangle_{\boldsymbol{\mu}} = \frac{1}{3} \sum_{\boldsymbol{\mu} \in \{\mathbf{x},\mathbf{y},\mathbf{z}\}} \cdots . \tag{E.5}$$

This averaging simplifies the expression in the numerator of Eq. (E.4),

$$\langle |\mathbf{r}_{ij} \cdot \boldsymbol{\mu}|^2 \rangle_{\boldsymbol{\mu}} = \frac{1}{3} r_{ij}^2. \tag{E.6}$$

Second, we average over the orientation of the magnetic field with respect to the crystal lattice,

$$\langle \cdots \rangle_{\boldsymbol{z}} = \frac{1}{4\pi} \int_0^{2\pi} \mathrm{d}\phi \int_0^{\pi} \sin\theta \, \mathrm{d}\theta \cdots . \tag{E.7}$$

The average of the angular factors present in Eq. (E.4) is

$$\langle (1 - 3\cos^2\theta)^2 \rangle_{\boldsymbol{z}} = \frac{4}{5}. \tag{E.8}$$

Applying Eq. (E.6) in the numerator, and Eq. (E.8) separately in the numerator and the square of the denominator, we simplify Eq. (E.4) into

$$D \simeq \frac{\sqrt{\pi I(I+1)}}{4\sqrt{24}\hbar} \frac{\mu_0}{4\pi} \gamma^2 \hbar^2 \frac{\sum_j (1/3) \times (4/5) r_{ij}^{-4}}{\sqrt{\sum_j (4/5) \times r_{ij}^{-6}}}. \tag{E.9}$$

Next, we replace the discrete sums with integrals, assuming that the spins $j$ are distributed approximately uniformly in space with density $\rho_{\mathrm{spin}}$,

$$\left\langle \sum_j r_{ij}^{-n} \right\rangle_{\rho} = \int_{r_{\mathrm{min}}}^{\infty} 4\pi r^2 \rho_{\mathrm{spin}} \times r^{-n} = 4\pi \rho_{\mathrm{spin}} \frac{r_{\mathrm{min}}^{3-n}}{n-3}, \tag{E.10}$$

for $n > 3$. Implementing the procedures defined in Eqs. (E.5), (E.7), (E.10), the average of Eq. (E.4) is

$$\langle D \rangle_{\boldsymbol{\mu},\mathbf{z},\rho} \simeq \frac{\pi}{3\sqrt{40}} \sqrt{I(I+1)} \frac{\mu_0}{4\pi} \gamma^2 \hbar \sqrt{\rho_{\mathrm{spin}} r_{\mathrm{min}}}. \tag{E.11}$$

We define the ‘nearest-neighbor distance’ as $2r_\rho$, twice the radius of a sphere that has a volume equal to the volume per single spinful isotope. The latter is defined by the relation

$$\rho_{\mathrm{spin}}^{-1} = \frac{4\pi}{3} r_\rho^3. \tag{E.12}$$

The density $\rho_{\mathrm{spin}}$ equals the density of a given atomic element in the lattice $\rho_{\mathrm{atom}}$ (for example, for Si it is 8 atoms per unit cell of the diamond lattice) times the isotopic ratio of a given isotope $p$ (for example, for $^{29}$Si with it would be 4.7% for Si with natural isotope composition).

As the final step, we choose the short-distance cutoff $r_{\mathrm{min}} = r_\rho$. This choice means that in the integral in Eq. (E.10) we implement the condition $j \neq i$ by excluding a sphere around spin $i$ with radius $r_\rho$, excluding a spherical volume corresponding to a single nuclear spin in the lattice. We obtain

$$\langle D \rangle_{\boldsymbol{\mu},\mathbf{z},\rho} \simeq \frac{\sqrt{\pi}}{4\sqrt{30}} \sqrt{I(I+1)} \frac{\mu_0}{4\pi} \gamma^2 \hbar \frac{1}{r_\rho}. \tag{E.13}$$

Die approbierte gedruckte Originalversion dieser Dissertation ist an der TU Wien Bibliothek verfügbar.
The approved original version of this doctoral thesis is available in print at TU Wien Bibliothek.
TU Bibliothek Your knowledge hub WIEN

## E.2 Numerical values for the diffusion coefficient in various materials

We evaluate Eq. (E.13) for several scenarios in Tab. E.1. While we are interested in the diffusion of nuclear spins of $^{17}$O and $^{73}$Ge, we include other standard spin-qubit materials and elements, namely Si, SiGe, and GaAs, to check the prediction of Eq. (E.13). The table lists the quantities that enter the formula, and gives the averaged diffusion constants in the last column. They are of order ten(s) of nm$^2$/s for GaAs isotopes and $^{73}$Ge in SiGe. The spins of silicon $^{29}$Si diffuse slower, about an order of magnitude, due to its lower spin magnitude, lower $g$-factor, and lower isotopic concentration. Surprisingly, the diffusion of $^{17}$O is not slow, despite its minuscule isotopic concentration. In $SiO_2$, it is an order of magnitude larger than that of Si. Again, the difference originates from the larger spin and $g$-factor of oxygen. We thus believe that concerning the expected time scales for the internal dynamics of Overhauser fields, there are no qualitative differences between oxygen in $SiO_2$ and isotopes of GaAs or SiGe. The latter fields have been observed to decorrelate on scales of seconds to minutes. We conclude that neither the oxygen- nor germanium-induced Overhauser field is frozen in a typical experiment and they both contribute to dephasing.

As an illustration, we further quantify the diffusion of oxygen nuclear spins by converting the diffusion constant value given in Tab. E.1 to a correlation time and a power spectral density. We do this conversion only for the Si-MOS case. The presented quantitative characteristics should be taken as ballpark estimates.

## E.3 Autocorrelation time of the Overhauser field

We start with the auto-correlator of the electron energy fluctuations due to the Overhauser field,

$$\langle \delta E(t) \delta E(t+\tau) \rangle \equiv C(\tau) = \frac{p\langle \Delta \rangle}{\prod_\mu (1+\gamma_\mu |\tau|)^{1/2}}. \tag{E.14}$$

We conjecture this equation from Eq. (A5) in Ref. [264]. We also amend it for our case and notation: The index $\mu \in \{x, y, z\}$ enumerates Cartesian coordinates, the quantity $\Delta$ is the oxygen-induced Overhauser field contribution defined in Eq. (6.2) and $\gamma_\mu = 2D_{\mu\mu}/l_\mu^2$. For $D_{\mu\mu}$ we take the value from Tab. E.1. In Ref. [264], the quantities $l_\mu$ denoted the quantum dot confinmenet lengths. Instead, here we take $l_\mu$ equal to the typical distance between spinful isotopes, $2r_\rho$.[25] We stipulate that, since there are very few spinful oxygen atoms in a given quantum dot, as soon as the nuclear spin diffuses to the next available position in the oxide, it will not be coupled to the electron anymore, with a high probability. These considerations result in the

[25]Since the value of $2r_\rho$ is about 5 nm, the difference to taking quantum dot size would not be radical.

Die approbierte gedruckte Originalversion dieser Dissertation ist an der TU Wien Bibliothek verfügbar.
The approved original version of this doctoral thesis is available in print at TU Wien Bibliothek.
TU WIEN Bibliothek Your knowledge hub

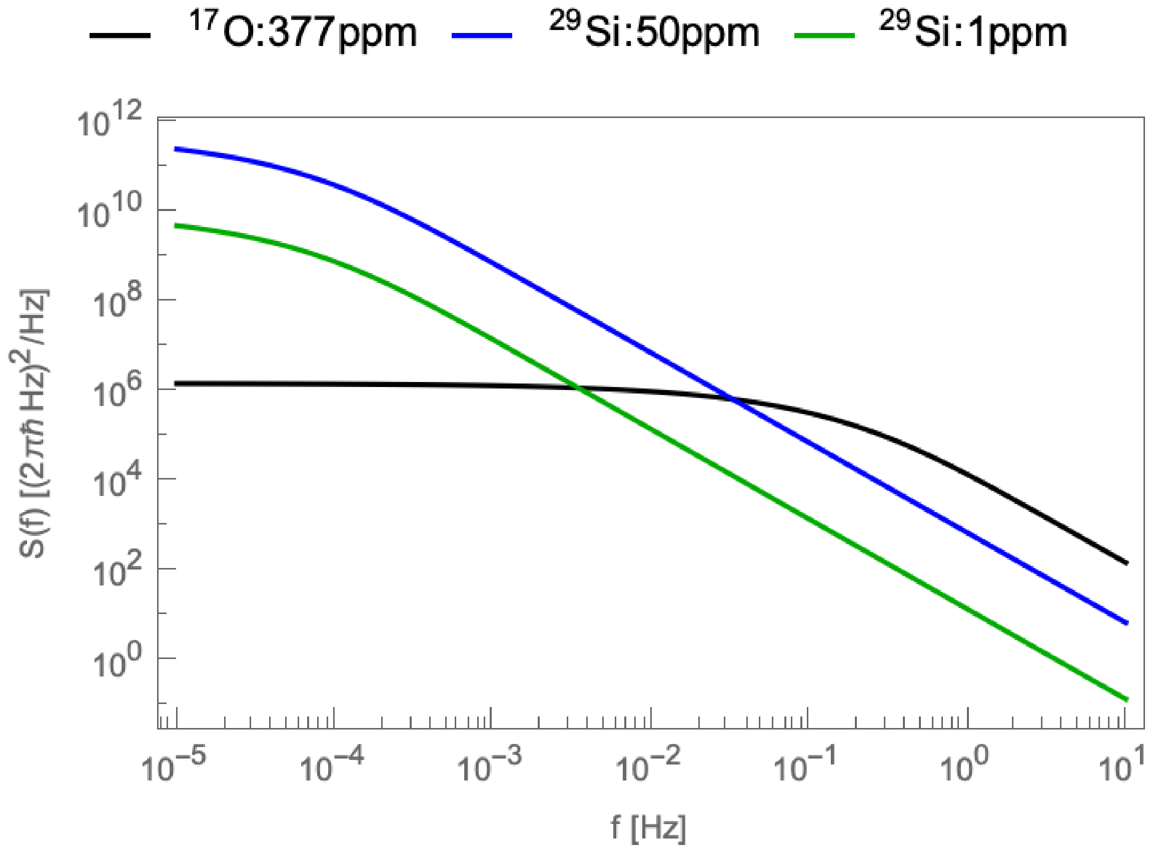


Figure E.1: Power spectral density. The curves show the integral in Eq. (E.17) evaluated analytically for $n = 3$, adopting the isotopic concentration $p$ as denoted in the curve labels, and the area $S = 2\pi \times (30\,\text{nm})^2$. Further, we took, for oxygen, $D = 8.5$ nm$^2$/s and $l_\mu = 4.8$ nm to evaluate $\tau_0$ and $\langle \Delta^{1\text{d}} \rangle = 4.1 \times (2\pi\hbar)^2$ MHz$^2$ nm$^2$ to evaluate $\langle \Delta \rangle$. For silicon, we took $D = 0.29$ or $0.11$ nm$^2$/s (depending on $p_{^{29}\text{Si}}$, as given in Tab. E.1), $l_\mu = (4 \times 2\pi \times 30^2)^{1/3}$ nm, and $\langle \Delta^{1\text{d}} \rangle = 3817 \times (2\pi\hbar)^2$ MHz$^2$ nm$^2$.

correlation time scale

$$\tau_0 \equiv \frac{1}{\gamma} = \frac{2r_\rho^2}{D}, \tag{E.15}$$

which evaluates to about 1 second for the parameters in the first line of Tab. E.1. This is the expected time scale over which the $^{17}$O nuclear spin configuration, as seen by the electron spin, changes.

## E.4 Power spectral density

A second quantity of immediate interest is the resulting noise spectral density. Defined by

$$P(\omega) \equiv \int_{-\infty}^{\infty} C(\tau) \exp(i\omega\tau)\, \mathrm{d}\tau, \tag{E.16}$$

Die approbierte gedruckte Originalversion dieser Dissertation ist an der TU Wien Bibliothek verfügbar.
The approved original version of this doctoral thesis is available in print at TU Wien Bibliothek.
TU Bibliothek WIEN Your knowledge hub

we get it in rescaled units $\tilde{\omega} = \omega\tau_0$ as

$$P(\tilde{\omega}) = P_0 \int_0^\infty \frac{2\cos(\tilde{\omega}x)}{(1+x)^{n/2}}\,\mathrm{d}x, \tag{E.17}$$

where the scale is

$$P_0 = p\langle\Delta\rangle\tau_0. \tag{E.18}$$

We have given the above equation for a variable number of dimensions $n$. The quantity $n$ is defined as the number of axes along which the diffusion can proceed, and enters our formula as the domain of the index $\mu$ in Eq. (E.14). For example, if for some reason the diffusion is only along $z$, the index $\mu \in \{z\}$ and $n = 1$. The case $n = 3$ being $\mu \in \{x, y, z\}$ corresponds to the three-dimensional diffusion considered in the above.

Taking $\langle\Delta^{1\text{d}}_{^{17}\text{O}}\rangle = (2\pi\hbar \times 4.1\,\text{Mhz})^2/\text{nm}^2$ from Tab. 6.1 and $S = 2\pi \times (30\,\text{nm})^2$, we get $P_0 = 3.7 \times 10^5 (2\pi\hbar \times \text{Hz})^2/\text{Hz}$. The corresponding PSD is plotted in Fig. E.1 using $n = 3$. We compare it with the PSD due to $^{29}$Si for two concentrations. The 1 ppm shows a PSD that, integrating over all frequencies, is approximately of the same strength as that of oxygen. Because of the difference in the characteristic times $\tau_0$, which is much larger for the diffusion of silicon nuclear spin, the shape of the curves is different. We also include the 50 ppm case. Interestingly, even though the total noise power is now much larger for silicon, the difference in the curve shapes still makes the oxygen contribution dominant at high enough frequencies. The reason is the same, the different characteristic times $\tau_0$.

Die approbierte gedruckte Originalversion dieser Dissertation ist an der TU Wien Bibliothek verfügbar.
The approved original version of this doctoral thesis is available in print at TU Wien Bibliothek.
TU WIEN Bibliothek Your knowledge hub

Die approbierte gedruckte Originalversion dieser Dissertation ist an der TU Wien Bibliothek verfügbar.
The approved original version of this doctoral thesis is available in print at TU Wien Bibliothek.
TU WIEN Bibliothek Your knowledge hub

# Own publications


[LC1] L. Cvitkovich, P. Stano, C. Wilhelmer, D. Waldhör, D. Loss, Y.-M. Niquet, and T. Grasser, "Coherence limit due to hyperfine interaction with nuclei in the barrier material of Si spin qubits." https://arxiv.org/abs/2405.10667, under review in *Physical Review Applied*.

[LC2] L. Cvitkovich, F. Fehringer, C. Wilhelmer, D. Milardovich, D. Waldhör, and T. Grasser, "Machine learning force field for thermal oxidation of silicon." https://arxiv.org/abs/2405.13635, under review in *Journal of Chemical Physics*.

[LC3] L. Cvitkovich, B. Sklénard, D. Waldhör, J. Li, C. Wilhelmer, G. Veste, Y.-M. Niquet, and T. Grasser, "Variability in Si/SiGe and Si/$SiO_2$ spin qubits due to interfacial disorder," in *2023 International Conference on Simulation of Semiconductor Processes and Devices (SISPAD)*, pp. 341–344, 2023.

[LC4] L. Cvitkovich, D. Waldhör, A.-M. El-Sayed, M. Jech, C. Wilhelmer, and T. Grasser, "Dynamic modeling of Si(100) thermal oxidation: Oxidation mechanisms and realistic amorphous interface generation," *Applied Surface Science*, vol. 610, p. 155378, 2023.

[LC5] L. Cvitkovich, M. Jech, D. Waldhör, A.-M. El-Sayed, C. Wilhelmer, and T. Grasser, "Multiscale modeling study of native oxide growth on a Si(100) surface," in *ESSDERC 2021 - IEEE 51st European Solid-State Device Research Conference (ESSDERC)*, pp. 235–238, 2021.




Die approbierte gedruckte Originalversion dieser Dissertation ist an der TU Wien Bibliothek verfügbar.
The approved original version of this doctoral thesis is available in print at TU Wien Bibliothek.
TU WIEN Bibliothek Your knowledge hub

Die approbierte gedruckte Originalversion dieser Dissertation ist an der TU Wien Bibliothek verfügbar.
The approved original version of this doctoral thesis is available in print at TU Wien Bibliothek.

# Bibliography


[1] A. Barenco, C. H. Bennett, R. Cleve, D. P. DiVincenzo, N. Margolus, P. Shor, T. Sleator, J. A. Smolin, and H. Weinfurter, "Elementary gates for quantum computation," *Phys. Rev. A*, vol. 52, pp. 3457–3467, Nov 1995.

[2] M. A. Nielsen and I. L. Chuang, *Quantum Computation and Quantum Information: 10th Anniversary Edition*. Cambridge University Press, 2010.

[3] D. Castelvecchi, "IBM releases first-ever 1,000-qubit quantum chip," 2023. https://www.nature.com/articles/d41586-023-03854-1 [Accessed: 13.02.2024].

[4] M. Kjaergaard, M. E. Schwartz, J. Braumüller, P. Krantz, J. I.-J. Wang, S. Gustavsson, and W. D. Oliver, "Superconducting qubits: Current state of play," *Annual Review of Condensed Matter Physics*, vol. 11, no. 1, pp. 369–395, 2020.

[5] C. D. Bruzewicz, J. Chiaverini, R. McConnell, and J. M. Sage, "Trapped-ion quantum computing: Progress and challenges," *Applied Physics Reviews*, vol. 6, p. 021314, 05 2019.

[6] M. Saffman, "Quantum computing with atomic qubits and rydberg interactions: progress and challenges," *Journal of Physics B: Atomic, Molecular and Optical Physics*, vol. 49, p. 202001, oct 2016.

[7] J. L. O'Brien, "Optical quantum computing," *Science*, vol. 318, no. 5856, pp. 1567–1570, 2007.

[8] D. Loss and D. P. DiVincenzo, "Quantum computation with quantum dots," *Phys. Rev. A*, vol. 57, pp. 120–126, Jan 1998.

[9] F. A. Zwanenburg, A. S. Dzurak, A. Morello, M. Y. Simmons, L. C. L. Hollenberg, G. Klimeck, S. Rogge, S. N. Coppersmith, and M. A. Eriksson, "Silicon quantum electronics," *Rev. Mod. Phys.*, vol. 85, pp. 961–1019, Jul 2013.

[10] G. Burkard, T. D. Ladd, A. Pan, J. M. Nichol, and J. R. Petta, "Semiconductor spin qubits," *Reviews of Modern Physics*, vol. 95, p. 025003, June 2023.

[11] B. Martinez Diaz, *Towards Scalable Si and Ge Spin Qubit Architectures : Highlights from Modelling*. PhD thesis, Université Grenoble Alpes, 2022.




TU WIEN Bibliothek Your knowledge hub
Die approbierte gedruckte Originalversion dieser Dissertation ist an der TU Wien Bibliothek verfügbar.
The approved original version of this doctoral thesis is available in print at TU Wien Bibliothek.

[12] C. H. Yang, A. Rossi, R. Ruskov, N. S. Lai, F. A. Mohiyaddin, S. Lee, C. Tahan, G. Klimeck, A. Morello, and A. S. Dzurak, "Spin-valley lifetimes in a silicon quantum dot with tunable valley splitting," *Nature Communications*, vol. 4, p. 2069, Jun 2013.

[13] A. M. J. Zwerver, T. Krähenmann, T. F. Watson, L. Lampert, H. C. George, R. Pillarisetty, S. A. Bojarski, P. Amin, S. V. Amitonov, J. M. Boter, R. Caudillo, D. Correas-Serrano, J. P. Dehollain, G. Droulers, E. M. Henry, R. Kotlyar, M. Lodari, F. Lüthi, D. J. Michalak, B. K. Mueller, S. Neyens, J. Roberts, N. Samkharadze, G. Zheng, O. K. Zietz, G. Scappucci, M. Veldhorst, L. M. K. Vandersypen, and J. S. Clarke, "Qubits made by advanced semiconductor manufacturing," *Nature Electronics*, vol. 5, pp. 184–190, Mar 2022.

[14] M. Veldhorst, J. C. C. Hwang, *et al.*, "An addressable quantum dot qubit with fault-tolerant control-fidelity," *Nature Nanotechnology*, vol. 9, no. 12, pp. 981–985, 2014.

[15] R. M. Jock, N. T. Jacobson, M. Rudolph, D. R. Ward, M. S. Carroll, and D. R. Luhman, "A silicon singlet–triplet qubit driven by spin-valley coupling," *Nature Communications*, vol. 13, no. 1, p. 641, 2022.

[16] T. Tanttu, W. H. Lim, J. Y. Huang, N. D. Stuyck, W. Gilbert, R. Y. Su, M. Feng, J. D. Cifuentes, A. E. Seedhouse, S. K. Seritan, C. I. Ostrove, K. M. Rudinger, R. C. C. Leon, W. Huang, C. C. Escott, K. M. Itoh, N. V. Abrosimov, H.-J. Pohl, M. L. W. Thewalt, F. E. Hudson, R. Blume-Kohout, S. D. Bartlett, A. Morello, A. Laucht, C. H. Yang, A. Saraiva, and A. S. Dzurak, "Consistency of high-fidelity two-qubit operations in silicon," 2023.

[17] F. Arute, K. Arya, R. Babbush, D. Bacon, J. C. Bardin, R. Barends, R. Biswas, S. Boixo, F. G. S. L. Brandao, D. A. Buell, B. Burkett, Y. Chen, Z. Chen, B. Chiaro, R. Collins, W. Courtney, A. Dunsworth, E. Farhi, B. Foxen, A. Fowler, C. Gidney, M. Giustina, R. Graff, K. Guerin, S. Habegger, M. P. Harrigan, M. J. Hartmann, A. Ho, M. Hoffmann, T. Huang, T. S. Humble, S. V. Isakov, E. Jeffrey, Z. Jiang, D. Kafri, K. Kechedzhi, J. Kelly, P. V. Klimov, S. Knysh, A. Korotkov, F. Kostritsa, D. Landhuis, M. Lindmark, E. Lucero, D. Lyakh, S. Mandrà, J. R. McClean, M. McEwen, A. Megrant, X. Mi, K. Michielsen, M. Mohseni, J. Mutus, O. Naaman, M. Neeley, C. Neill, M. Y. Niu, E. Ostby, A. Petukhov, J. C. Platt, C. Quintana, E. G. Rieffel, P. Roushan, N. C. Rubin, D. Sank, K. J. Satzinger, V. Smelyanskiy, K. J. Sung, M. D. Trevithick, A. Vainsencher, B. Villalonga, T. White, Z. J. Yao, P. Yeh, A. Zalcman, H. Neven, and J. M. Martinis, "Quantum supremacy using a programmable superconducting processor," *Nature*, vol. 574, pp. 505–510, Oct 2019.

[18] X. Xue, M. Russ, N. Samkharadze, B. Undseth, A. Sammak, G. Scappucci, and L. M. K. Vandersypen, "Quantum logic with spin qubits crossing the surface code threshold," *Nature*, vol. 601, pp. 343–347, Jan 2022.

Die approbierte gedruckte Originalversion dieser Dissertation ist an der TU Wien Bibliothek verfügbar.
The approved original version of this doctoral thesis is available in print at TU Wien Bibliothek.
TU WIEN Bibliothek Your knowledge hub

[19] F. Borsoi, N. W. Hendrickx, V. John, M. Meyer, S. Motz, F. van Riggelen, A. Sammak, S. L. de Snoo, G. Scappucci, and M. Veldhorst, "Shared control of a 16 semiconductor quantum dot crossbar array," *Nature Nanotechnology*, vol. 19, pp. 21–27, Jan 2024.

[20] K. Takeda, A. Noiri, J. Yoneda, T. Nakajima, and S. Tarucha, "Resonantly Driven Singlet-Triplet Spin Qubit in Silicon," *Physical Review Letters*, vol. 124, p. 117701, March 2020.

[21] D. Jirovec, A. Hofmann, A. Ballabio, P. M. Mutter, G. Tavani, M. Botifoll, A. Crippa, J. Kukucka, O. Sagi, F. Martins, J. Saez-Mollejo, I. Prieto, M. Borovkov, J. Arbiol, D. Chrastina, G. Isella, and G. Katsaros, "A singlet-triplet hole spin qubit in planar ge," *Nature Materials*, vol. 20, pp. 1106–1112, Aug 2021.

[22] L. Zhai, M. C. Löbl, G. N. Nguyen, J. Ritzmann, A. Javadi, C. Spinnler, A. D. Wieck, A. Ludwig, and R. J. Warburton, "Low-noise gaas quantum dots for quantum photonics," *Nature Communications*, vol. 11, p. 4745, Sep 2020.

[23] J. Yoneda, K. Takeda, T. Otsuka, T. Nakajima, M. R. Delbecq, G. Allison, T. Honda, T. Kodera, S. Oda, Y. Hoshi, N. Usami, K. M. Itoh, and S. Tarucha, "A quantum-dot spin qubit with coherence limited by charge noise and fidelity higher than 99.9%," *Nature Nanotechnology*, vol. 13, pp. 102–106, Feb 2018.

[24] F. Simmel, D. Abusch-Magder, D. A. Wharam, M. A. Kastner, and J. P. Kotthaus, "Statistics of the coulomb-blockade peak spacings of a silicon quantum dot," *Phys. Rev. B*, vol. 59, pp. R10441–R10444, Apr 1999.

[25] J. K. Gamble, P. Harvey-Collard, N. T. Jacobson, A. D. Baczewski, E. Nielsen, L. Maurer, I. Montaño, M. Rudolph, M. S. Carroll, C. H. Yang, A. Rossi, A. S. Dzurak, and R. P. Muller, "Valley splitting of single-electron Si MOS quantum dots," *Applied Physics Letters*, vol. 109, p. 253101, 12 2016.

[26] R. Hanson and D. D. Awschalom, "Coherent manipulation of single spins in semiconductors," *Nature*, vol. 453, pp. 1043–1049, Jun 2008.

[27] T. D. Ladd, F. Jelezko, R. Laflamme, Y. Nakamura, C. Monroe, and J. L. O'Brien, "Quantum computers," *Nature*, vol. 464, pp. 45–53, Mar 2010.

[28] M. Field, C. G. Smith, M. Pepper, D. A. Ritchie, J. E. F. Frost, G. A. C. Jones, and D. G. Hasko, "Measurements of coulomb blockade with a noninvasive voltage probe," *Phys. Rev. Lett.*, vol. 70, pp. 1311–1314, Mar 1993.

[29] J. M. Elzerman, R. Hanson, L. H. Willems van Beveren, B. Witkamp, L. M. K. Vandersypen, and L. P. Kouwenhoven, "Single-shot read-out of an individual electron spin in a quantum dot," *Nature*, vol. 430, pp. 431–435, Jul 2004.

[30] S. J. Angus, A. J. Ferguson, A. S. Dzurak, and R. G. Clark, "Gate-defined quantum dots in intrinsic silicon," *Nano Letters*, vol. 7, pp. 2051–2055, Jul 2007.

TU Bibliothek WIEN Your knowledge hub
Die approbierte gedruckte Originalversion dieser Dissertation ist an der TU Wien Bibliothek verfügbar.
The approved original version of this doctoral thesis is available in print at TU Wien Bibliothek.

[31] G. Scappucci, P. J. Taylor, J. R. Williams, T. Ginley, and S. Law, "Crystalline materials for quantum computing: Semiconductor heterostructures and topological insulators exemplars," *MRS Bulletin*, vol. 46, pp. 596–606, Jul 2021.

[32] B. Martinez and Y.-M. Niquet, "Variability of electron and hole spin qubits due to interface roughness and charge traps," *Phys. Rev. Appl.*, vol. 17, p. 024022, 2022.

[33] L. Cywiński, W. M. Witzel, and S. Das Sarma, "Electron spin dephasing due to hyperfine interactions with a nuclear spin bath," *Phys. Rev. Lett.*, vol. 102, p. 057601, Feb 2009.

[34] J. M. Taylor, J. R. Petta, A. C. Johnson, A. Yacoby, C. M. Marcus, and M. D. Lukin, "Relaxation, dephasing, and quantum control of electron spins in double quantum dots," *Phys. Rev. B*, vol. 76, p. 035315, Jul 2007.

[35] P. Stano and D. Loss, "Review of performance metrics of spin qubits in gated semiconducting nanostructures," *Nature Reviews Physics*, vol. 4, pp. 672–688, August 2022.

[36] R. Maurand *et al.*, "A CMOS Si spin qubit," *Nature Communications*, vol. 7, p. 13575, 2016.

[37] H. Watzinger, J. Kukučka, L. Vukušić, F. Gao, T. Wang, F. Schäffler, J.-J. Zhang, and G. Katsaros, "A germanium hole spin qubit," *Nature Communications*, vol. 9, p. 3902, Sep 2018.

[38] K. Wang, G. Xu, F. Gao, H. Liu, R.-L. Ma, X. Zhang, Z. Wang, G. Cao, T. Wang, J.-J. Zhang, D. Culcer, X. Hu, H.-W. Jiang, H.-O. Li, G.-C. Guo, and G.-P. Guo, "Ultrafast coherent control of a hole spin qubit in a germanium quantum dot," *Nature Communications*, vol. 13, p. 206, Jan 2022.

[39] N. Piot, B. Brun, *et al.*, "A single hole spin with enhanced coherence in natural silicon," *Nature Nanotechnology*, vol. 17, no. 10, pp. 1072–1077, 2022.

[40] O. Malkoc, P. Stano, and D. Loss, "Charge-noise-induced dephasing in silicon hole-spin qubits," *Phys. Rev. Lett.*, vol. 129, p. 247701, Dec 2022.

[41] D. Sabbagh, N. Thomas, J. Torres, R. Pillarisetty, P. Amin, H. George, K. Singh, A. Budrevich, M. Robinson, D. Merrill, L. Ross, J. Roberts, L. Lampert, L. Massa, S. Amitonov, J. Boter, G. Droulers, H. Eenink, M. van Hezel, D. Donelson, M. Veldhorst, L. Vandersypen, J. Clarke, and G. Scappucci, "Quantum transport properties of industrial $^{28}$Si/$^{28}$sio$_2$," *Phys. Rev. Appl.*, vol. 12, p. 014013, Jul 2019.

[42] D. M. Zajac, A. J. Sigillito, M. Russ, F. Borjans, J. M. Taylor, G. Burkard, and J. R. Petta, "Resonantly driven cnot gate for electron spins," *Science*, vol. 359, no. 6374, pp. 439–442, 2018.

Die approbierte gedruckte Originalversion dieser Dissertation ist an der TU Wien Bibliothek verfügbar.
The approved original version of this doctoral thesis is available in print at TU Wien Bibliothek.
TU WIEN Bibliothek Your knowledge hub

[43] M. Veldhorst, C. H. Yang, J. C. C. Hwang, W. Huang, J. P. Dehollain, J. T. Muhonen, S. Simmons, A. Laucht, F. E. Hudson, K. M. Itoh, A. Morello, and A. S. Dzurak, "A two-qubit logic gate in silicon," *Nature*, vol. 526, pp. 410–414, Oct 2015.

[44] L. C. Camenzind, L. Yu, P. Stano, J. D. Zimmerman, A. C. Gossard, D. Loss, and D. M. Zumbühl, "Hyperfine-phonon spin relaxation in a single-electron gaas quantum dot," *Nature Communications*, vol. 9, p. 3454, Aug 2018.

[45] S. Bosco and D. Loss, "Fully tunable hyperfine interactions of hole spin qubits in si and ge quantum dots," *Phys. Rev. Lett.*, vol. 127, p. 190501, Nov 2021.

[46] M. Vinet, "The path to scalable quantum computing with silicon spin qubits," *Nature Nanotechnology*, vol. 16, pp. 1296–1298, Dec 2021.

[47] A. Noiri, K. Takeda, T. Nakajima, T. Kobayashi, A. Sammak, G. Scappucci, and S. Tarucha, "Fast universal quantum gate above the fault-tolerance threshold in silicon," *Nature*, vol. 601, pp. 338–342, Jan 2022.

[48] B. Wuetz *et al.*, "Atomic fluctuations lifting the energy degeneracy in Si/SiGe quantum dots," *Nature Communications*, vol. 13, no. 1, p. 7730, 2022.

[49] C. Kittel, *Introduction to Solid State Physics*. Wiley, 8 ed., 2004.

[50] M. Lundstrom, *Fundamentals of Carrier Transport*. Cambridge University Press, 2 ed., 2000.

[51] V. Sverdlov, E. Ungersboeck, H. Kosina, and S. Selberherr, "Effects of shear strain on the conduction band in silicon: An efficient two-band k·p theory," in *ESSDERC 2007 - 37th European Solid State Device Research Conference*, pp. 386–389, 2007.

[52] V. Sverdlov, *Strain-Induced Effects in Advanced MOSFETs*. Springer Vienna, 1 ed., 2010.

[53] J. J. Welser, J. L. Hoyt, and J. F. Gibbons, "Nmos and pmos transistors fabricated in strained silicon/relaxed silicon-germanium structures," *1992 International Technical Digest on Electron Devices Meeting*, pp. 1000–1002, 1992.

[54] T. B. Boykin, G. Klimeck, M. Friesen, S. N. Coppersmith, P. von Allmen, F. Oyafuso, and S. Lee, "Valley splitting in low-density quantum-confined heterostructures studied using tight-binding models," *Phys. Rev. B*, vol. 70, p. 165325, 2004.

[55] M. Friesen, S. Chutia, C. Tahan, and S. N. Coppersmith, "Valley splitting theory of SiGe/Si/SiGe quantum wells," *Phys. Rev. B*, vol. 75, p. 115318, 2007.

[56] Z. Shi, C. B. Simmons, *et al.*, "Tunable singlet-triplet splitting in a few-electron Si/SiGe quantum dot," *Applied Physics Letters*, vol. 99, no. 23, 2011. 233108.

Die approbierte gedruckte Originalversion dieser Dissertation ist an der TU Wien Bibliothek verfügbar.
The approved original version of this doctoral thesis is available in print at TU Wien Bibliothek.
TU WIEN Bibliothek Your knowledge hub

[57] E. Kawakami, P. Scarlino, *et al.*, "Electrical control of a long-lived spin qubit in a Si/SiGe quantum dot," *Nature Nanotechnology*, vol. 9, no. 9, pp. 666–670, 2014.

[58] X. Mi, C. G. Péterfalvi, G. Burkard, and J. R. Petta, "High-resolution valley spectroscopy of Si quantum dots," *Phys. Rev. Lett.*, vol. 119, p. 176803, 2017.

[59] S. W. Oh, A. O. Denisov, P. Chen, and J. R. Petta, "Cryogen-free scanning gate microscope for the characterization of Si/Si0.7Ge0.3 quantum devices at milli-Kelvin temperatures," *AIP Advances*, vol. 11, p. 125122, 12 2021.

[60] S. F. Neyens, R. H. Foote, B. Thorgrimsson, T. J. Knapp, T. McJunkin, L. M. K. Vandersypen, P. Amin, N. K. Thomas, J. S. Clarke, D. E. Savage, M. G. Lagally, M. Friesen, S. N. Coppersmith, and M. A. Eriksson, "The critical role of substrate disorder in valley splitting in Si quantum wells," *Applied Physics Letters*, vol. 112, p. 243107, 06 2018.

[61] J. P. Dodson, H. E. Ercan, *et al.*, "How valley-orbit states in silicon quantum dots probe quantum well interfaces," *Phys. Rev. Lett.*, vol. 128, p. 146802, 2022.

[62] T. McJunkin, E. R. MacQuarrie, L. Tom, S. F. Neyens, J. P. Dodson, B. Thorgrimsson, J. Corrigan, H. E. Ercan, D. E. Savage, M. G. Lagally, R. Joynt, S. N. Coppersmith, M. Friesen, and M. A. Eriksson, "Valley splittings in si/sige quantum dots with a germanium spike in the silicon well," *Phys. Rev. B*, vol. 104, p. 085406, Aug 2021.

[63] Y. Feng and R. Joynt, "Enhanced valley splitting in si layers with oscillatory ge concentration," *Phys. Rev. B*, vol. 106, p. 085304, Aug 2022.

[64] T. McJunkin, B. Harpt, Y. Feng, M. P. Losert, R. Rahman, J. P. Dodson, M. A. Wolfe, D. E. Savage, M. G. Lagally, S. N. Coppersmith, M. Friesen, R. Joynt, and M. A. Eriksson, "Sige quantum wells with oscillating ge concentrations for quantum dot qubits," *Nature Communications*, vol. 13, p. 7777, Dec 2022.

[65] A. L. Saraiva, M. J. Calderón, R. B. Capaz, X. Hu, S. Das Sarma, and B. Koiller, "Intervalley coupling for interface-bound electrons in silicon: An effective mass study," *Phys. Rev. B*, vol. 84, p. 155320, Oct 2011.

[66] A. L. Saraiva, M. J. Calderón, X. Hu, S. Das Sarma, and B. Koiller, "Physical mechanisms of interface-mediated intervalley coupling in Si," *Phys. Rev. B*, vol. 80, p. 081305, Aug 2009.

[67] M. P. Losert, M. A. Eriksson, R. Joynt, R. Rahman, G. Scappucci, S. N. Coppersmith, and M. Friesen, "Practical strategies for enhancing the valley splitting in si/sige quantum wells," *Phys. Rev. B*, vol. 108, p. 125405, Sep 2023.

[68] T. B. Boykin, G. Klimeck, M. A. Eriksson, M. Friesen, S. N. Coppersmith, P. von Allmen, F. Oyafuso, and S. Lee, "Valley splitting in strained silicon quantum wells," *Applied Physics Letters*, vol. 84, pp. 115–117, 12 2003.

Die approbierte gedruckte Originalversion dieser Dissertation ist an der TU Wien Bibliothek verfügbar.
The approved original version of this doctoral thesis is available in print at TU Wien Bibliothek.
TU WIEN Bibliothek Your knowledge hub

[69] A. Manchon, "Chapter 2 - rashba spin–orbit coupling in two-dimensional systems," in *Spintronic 2D Materials* (W. Liu and Y. Xu, eds.), Materials Today, pp. 25–64, Elsevier, 2020.

[70] J. M. Luttinger and W. Kohn, "Motion of electrons and holes in perturbed periodic fields," *Phys. Rev.*, vol. 97, pp. 869–883, Feb 1955.

[71] R. Winkler, *Spin-orbit coupling effects in two-dimensional electron and hole systems.* Springer tracts in modern physics, Berlin: Springer, 2003.

[72] K. Takeda, J. Kamioka, T. Otsuka, J. Yoneda, T. Nakajima, M. R. Delbecq, S. Amaha, G. Allison, T. Kodera, S. Oda, and S. Tarucha, "A fault-tolerant addressable spin qubit in a natural silicon quantum dot," *Science Advances*, vol. 2, no. 8, p. e1600694, 2016.

[73] J. Yoneda, T. Otsuka, T. Nakajima, T. Takakura, T. Obata, M. Pioro-Ladrière, H. Lu, C. J. Palmstrøm, A. C. Gossard, and S. Tarucha, "Fast electrical control of single electron spins in quantum dots with vanishing influence from nuclear spins," *Phys. Rev. Lett.*, vol. 113, p. 267601, Dec 2014.

[74] Y. Tokura, W. G. van der Wiel, T. Obata, and S. Tarucha, "Coherent single electron spin control in a slanting zeeman field," *Phys. Rev. Lett.*, vol. 96, p. 047202, Jan 2006.

[75] U. Rössler and J. Kainz, "Microscopic interface asymmetry and spin-splitting of electron subbands in semiconductor quantum structures," *Solid State Communications*, vol. 121, no. 6, pp. 313–316, 2002.

[76] L. E. Golub and E. L. Ivchenko, "Spin splitting in symmetrical sige quantum wells," *Phys. Rev. B*, vol. 69, p. 115333, Mar 2004.

[77] M. O. Nestoklon, L. E. Golub, and E. L. Ivchenko, "Spin and valley-orbit splittings in SiGe/Si heterostructures," *Phys. Rev. B*, vol. 73, p. 235334, Jun 2006.

[78] M. Prada, G. Klimeck, and R. Joynt, "Spin–orbit splittings in Si/SiGe quantum wells: from ideal Si membranes to realistic heterostructures," *New Journal of Physics*, vol. 13, no. 1, p. 013009, 2011.

[79] G. Dresselhaus, "Spin-orbit coupling effects in zinc blende structures," *Phys. Rev.*, vol. 100, pp. 580–586, 1955.

[80] Y. A. Bychkov and E. I. Rashba, "Oscillatory effects and the magnetic susceptibility of carriers in inversion layers," *Journal of Physics C: Solid State Physics*, vol. 17, no. 33, p. 6039, 1984.

[81] M. Russ, D. M. Zajac, A. J. Sigillito, F. Borjans, J. M. Taylor, J. R. Petta, and G. Burkard, "High-fidelity quantum gates in Si/SiGe double quantum dots," *Phys. Rev. B*, vol. 97, p. 085421, Feb 2018.

Die approbierte gedruckte Originalversion dieser Dissertation ist an der TU Wien Bibliothek verfügbar.
The approved original version of this doctoral thesis is available in print at TU Wien Bibliothek.
TU WIEN Bibliothek Your knowledge hub

[82] J. Yoneda, J. S. Rojas-Arias, P. Stano, K. Takeda, A. Noiri, T. Nakajima, D. Loss, and S. Tarucha, "Noise-correlation spectrum for a pair of spin qubits in silicon," *Nature Physics*, vol. 19, pp. 1793–1798, Dec 2023.

[83] T. Struck, A. Hollmann, F. Schauer, O. Fedorets, A. Schmidbauer, K. Sawano, H. Riemann, N. V. Abrosimov, Ł. Cywiński, D. Bougeard, and L. R. Schreiber, "Low-frequency spin qubit energy splitting noise in highly purified $^{28}$Si/SiGe," *npj Quantum Information*, vol. 6, p. 40, May 2020.

[84] A. Abragam, *The principles of nuclear magnetism; Reprint with corrections.* International series of monographs on physics, Oxford: Clarendon Press, 1989.

[85] G. Burkard, D. Loss, and D. P. DiVincenzo, "Coupled quantum dots as quantum gates," *Phys. Rev. B*, vol. 59, pp. 2070–2078, Jan 1999.

[86] W. A. Coish and D. Loss, "Hyperfine interaction in a quantum dot: Non-markovian electron spin dynamics," *Phys. Rev. B*, vol. 70, p. 195340, Nov 2004.

[87] W. A. Coish and D. Loss, "Singlet-triplet decoherence due to nuclear spins in a double quantum dot," *Phys. Rev. B*, vol. 72, p. 125337, Sep 2005.

[88] I. A. Merkulov, A. L. Efros, and M. Rosen, "Electron spin relaxation by nuclei in semiconductor quantum dots," *Phys. Rev. B*, vol. 65, p. 205309, Apr 2002.

[89] A. V. Khaetskii, D. Loss, and L. Glazman, "Electron spin decoherence in quantum dots due to interaction with nuclei," *Phys. Rev. Lett.*, vol. 88, p. 186802, Apr 2002.

[90] A. M. Tyryshkin, S. Tojo, J. J. L. Morton, H. Riemann, N. V. Abrosimov, P. Becker, H.-J. Pohl, T. Schenkel, M. L. W. Thewalt, K. M. Itoh, and S. A. Lyon, "Electron spin coherence exceeding seconds in high-purity silicon," *Nature Materials*, vol. 11, pp. 143–147, Feb 2012.

[91] J. Schliemann, A. Khaetskii, and D. Loss, "Electron spin dynamics in quantum dots and related nanostructures due to hyperfine interaction with nuclei," *Journal of Physics: Condensed Matter*, vol. 15, pp. R1809–R1833, December 2003.

[92] E. Fermi, "Über die magnetischen momente der atomkerne," *Zeitschrift für Physik*, vol. 60, pp. 320–333, May 1930.

[93] C. G. Van de Walle and P. E. Blöchl, "First-principles calculations of hyperfine parameters," *Phys. Rev. B*, vol. 47, pp. 4244–4255, Feb 1993.

[94] L. V. C. Assali, H. M. Petrilli, R. B. Capaz, B. Koiller, X. Hu, and S. Das Sarma, "Hyperfine interactions in silicon quantum dots," *Phys. Rev. B*, vol. 83, p. 165301, Apr 2011.

TU Bibliothek WIEN Your knowledge hub
Die approbierte gedruckte Originalversion dieser Dissertation ist an der TU Wien Bibliothek verfügbar.
The approved original version of this doctoral thesis is available in print at TU Wien Bibliothek.

[95] R. Declerck, E. Pauwels, V. Van Speybroeck, and M. Waroquier, "First-principles calculations of hyperfine parameters with the gaussian and augmented-plane-wave method: Application to radicals embedded in a crystalline environment," *Phys. Rev. B*, vol. 74, p. 245103, Dec 2006.

[96] Declerck, Reinout, *Development and Implementation of Theoretical Methods for the Calculation of EPR Parameters in Periodic Simulations.* PhD thesis, Ghent University, 2008.

[97] Y. Fang, P. Philippopoulos, D. Culcer, W. A. Coish, and S. Chesi, "Recent advances in hole-spin qubits," *Materials for Quantum Technology*, vol. 3, p. 012003, March 2023.

[98] D. K. Wilson, "Electron Spin Resonance Experiments on Shallow Donors in Germanium," *Physical Review*, vol. 134, pp. A265–A286, April 1964.

[99] J. Kerckhoff, B. Sun, B. Fong, C. Jones, A. Kiselev, D. Barnes, R. Noah, E. Acuna, M. Akmal, S. Ha, J. Wright, B. Thomas, C. Jackson, L. Edge, K. Eng, R. Ross, and T. Ladd, "Magnetic Gradient Fluctuations from Quadrupolar 73 Ge in Si / Si Ge Exchange-Only Qubits," *PRX Quantum*, vol. 2, p. 010347, March 2021.

[100] W. M. Witzel, R. Rahman, and M. S. Carroll, "Nuclear spin induced decoherence of a quantum dot in Si confined at a SiGe interface: Decoherence dependence on 73 Ge," *Physical Review B*, vol. 85, p. 205312, May 2012.

[101] P. Philippopoulos, S. Chesi, and W. A. Coish, "First-principles hyperfine tensors for electrons and holes in GaAs and silicon," *Phys. Rev. B*, vol. 101, p. 115302, Mar 2020.

[102] M. R. Delbecq, T. Nakajima, P. Stano, T. Otsuka, S. Amaha, J. Yoneda, K. Takeda, G. Allison, A. Ludwig, A. D. Wieck, and S. Tarucha, "Quantum Dephasing in a Gated GaAs Triple Quantum Dot due to Nonergodic Noise," *Physical Review Letters*, vol. 116, p. 046802, January 2016.

[103] I. A. Merkulov, Al. L. Efros, and M. Rosen, "Electron spin relaxation by nuclei in semiconductor quantum dots," *Physical Review B*, vol. 65, p. 205309, April 2002.

[104] J. C. Slater and G. F. Koster, "Simplified lcao method for the periodic potential problem," *Phys. Rev.*, vol. 94, pp. 1498–1524, Jun 1954.

[105] R. O. Jones, "Density functional theory: Its origins, rise to prominence, and future," *Rev. Mod. Phys.*, vol. 87, pp. 897–923, Aug 2015.

[106] R. Parr and Y. Weitao, *Density-Functional Theory of Atoms and Molecules.* International Series of Monographs on Chemistry, Oxford University Press, 1994.

Die approbierte gedruckte Originalversion dieser Dissertation ist an der TU Wien Bibliothek verfügbar.
The approved original version of this doctoral thesis is available in print at TU Wien Bibliothek.
TU WIEN Bibliothek Your knowledge hub

[107] A. Szabo and N. Ostlund, *Modern Quantum Chemistry: Introduction to Advanced Electronic Structure Theory*. Dover Books on Chemistry, Dover Publications, 1996.

[108] R. M. Dreizler and E. K. U. Gross, *Density functional theory: an approach to the quantum many-body problem*. Berlin: Springer, 1990.

[109] D. R. Hartree, "The wave mechanics of an atom with a non-coulomb central field. part ii. some results and discussion," *Mathematical Proceedings of the Cambridge Philosophical Society*, vol. 24, no. 1, p. 111–132, 1928.

[110] P. Hohenberg and W. Kohn, "Inhomogeneous electron gas," *Phys. Rev.*, vol. 136, pp. B864–B871, Nov 1964.

[111] W. Kohn and L. J. Sham, "Self-consistent equations including exchange and correlation effects," *Phys. Rev.*, vol. 140, pp. A1133–A1138, Nov 1965.

[112] W. Cencek and K. Szalewicz, "On asymptotic behavior of density functional theory," *The Journal of Chemical Physics*, vol. 139, p. 024104, 07 2013.

[113] A. D. Becke, "A new mixing of Hartree–Fock and local density-functional theories," *The Journal of Chemical Physics*, vol. 98, pp. 1372–1377, 01 1993.

[114] T. D. Kühne, M. Iannuzzi, M. Del Ben, V. V. Rybkin, P. Seewald, F. Stein, T. Laino, R. Z. Khaliullin, O. Schütt, F. Schiffmann, D. Golze, J. Wilhelm, S. Chulkov, M. H. Bani-Hashemian, V. Weber, U. Borštnik, M. Taillefumier, A. S. Jakobovits, A. Lazzaro, H. Pabst, T. Müller, R. Schade, M. Guidon, S. Andermatt, N. Holmberg, G. K. Schenter, A. Hehn, A. Bussy, F. Belleflamme, G. Tabacchi, A. Glöß, M. Lass, I. Bethune, C. J. Mundy, C. Plessl, M. Watkins, J. VandeVondele, M. Krack, and J. Hutter, "CP2K: An electronic structure and molecular dynamics software package - Quickstep: Efficient and accurate electronic structure calculations," *The Journal of Chemical Physics*, vol. 152, p. 194103, 05 2020.

[115] G. Lippert, J. Hutter, and M. Parrinello, "The gaussian and augmented-plane-wave density functional method for ab initio molecular dynamics simulations," *Theoretical Chemistry Accounts*, vol. 103, pp. 124–140, Dec 1999.

[116] J. P. Perdew, K. Burke, and M. Ernzerhof, "Generalized gradient approximation made simple," *Phys. Rev. Lett.*, vol. 77, pp. 3865–3868, 1996.

[117] M. Guidon, J. Hutter, and J. VandeVondele, "Robust periodic hartree-fock exchange for large-scale simulations using gaussian basis sets," *Journal of Chemical Theory and Computation*, vol. 5, pp. 3010–3021, Nov 2009.

[118] Y.-i. Matsushita, K. Nakamura, and A. Oshiyama, "Comparative study of hybrid functionals applied to structural and electronic properties of semiconductors and insulators," *Phys. Rev. B*, vol. 84, p. 075205, Aug 2011.

Die approbierte gedruckte Originalversion dieser Dissertation ist an der TU Wien Bibliothek verfügbar.
The approved original version of this doctoral thesis is available in print at TU Wien Bibliothek.
TU WIEN Bibliothek Your knowledge hub

[119] J. Dunning, Thom H., "Gaussian basis sets for use in correlated molecular calculations. I. The atoms boron through neon and hydrogen," *The Journal of Chemical Physics*, vol. 90, pp. 1007–1023, 01 1989.

[120] K. A. Peterson and J. Dunning, Thom H., "Accurate correlation consistent basis sets for molecular core–valence correlation effects: The second row atoms Al–Ar, and the first row atoms B–Ne revisited," *The Journal of Chemical Physics*, vol. 117, pp. 10548–10560, 11 2002.

[121] D. E. Woon and J. Dunning, Thom H., "Gaussian basis sets for use in correlated molecular calculations. V. Core-valence basis sets for boron through neon," *The Journal of Chemical Physics*, vol. 103, pp. 4572–4585, 09 1995.

[122] V. A. Rassolov, M. A. Ratner, J. A. Pople, P. C. Redfern, and L. A. Curtiss, "6-31g* basis set for third-row atoms," *Journal of Computational Chemistry*, vol. 22, no. 9, pp. 976–984, 2001.

[123] P. Jakobsen and F. Jensen, "Probing basis set requirements for calculating hyperfine coupling constants," *The Journal of Chemical Physics*, vol. 151, p. 174107, 11 2019.

[124] L. Hermosilla, J. M. G. d. l. Vega, C. Sieiro, and P. Calle, "Dft calculations of isotropic hyperfine coupling constants of nitrogen aromatic radicals: The challenge of nitroxide radicals," *Journal of Chemical Theory and Computation*, vol. 7, pp. 169–179, Jan 2011.

[125] J. VandeVondele and J. Hutter, "Gaussian basis sets for accurate calculations on molecular systems in gas and condensed phases," *The Journal of Chemical Physics*, vol. 127, p. 114105, 09 2007.

[126] S. Goedecker, M. Teter, and J. Hutter, "Separable dual-space gaussian pseudopotentials," *Phys. Rev. B*, vol. 54, pp. 1703–1710, 1996.

[127] P. Umari and A. Pasquarello, "Ab initio molecular dynamics in a finite homogeneous electric field," *Phys. Rev. Lett.*, vol. 89, p. 157602, Sep 2002.

[128] G. Kresse and J. Furthmüller, "Efficiency of ab-initio total energy calculations for metals and semiconductors using a plane-wave basis set," *Computational Materials Science*, vol. 6, no. 1, pp. 15–50, 1996.

[129] P. E. Blöchl, "Projector augmented-wave method," *Phys. Rev. B*, vol. 50, pp. 17953–17979, Dec 1994.

[130] G. Kresse and D. Joubert, "From ultrasoft pseudopotentials to the projector augmented-wave method," *Phys. Rev. B*, vol. 59, pp. 1758–1775, Jan 1999.

[131] G. Seifert, "Tight-binding density functional theory: an approximate kohn-sham dft scheme," *The Journal of Physical Chemistry A*, vol. 111, pp. 5609–5613, Jul 2007.

TU WIEN Bibliothek Your knowledge hub
Die approbierte gedruckte Originalversion dieser Dissertation ist an der TU Wien Bibliothek verfügbar.
The approved original version of this doctoral thesis is available in print at TU Wien Bibliothek.

[132] M. Elstner, D. Porezag, G. Jungnickel, J. Elsner, M. Haugk, T. Frauenheim, S. Suhai, and G. Seifert, "Self-consistent-charge density-functional tight-binding method for simulations of complex materials properties," *Phys. Rev. B*, vol. 58, pp. 7260–7268, Sep 1998.

[133] F. Spiegelman, N. Tarrat, J. Cuny, D. L., E. Posenitskiy, C. Martí, A. Simon, and M. Rapacioli, "Density-functional tight-binding: basic concepts and applications to molecules and clusters," *Advances in Physics: X*, vol. 5, no. 1, p. 1710252, 2020. PMID: 33154977.

[134] M. Elstner, D. Porezag, G. Jungnickel, J. Elsner, M. Haugk, T. Frauenheim, S. Suhai, and G. Seifert, "Self-consistent-charge density-functional tight-binding method for simulations of complex materials properties," *Phys. Rev. B*, vol. 58, pp. 7260–7268, Sep 1998.

[135] B. Hourahine, B. Aradi, V. Blum, F. Bonafé, A. Buccheri, C. Camacho, C. Cevallos, M. Y. Deshaye, T. Dumitrică, A. Dominguez, S. Ehlert, M. Elstner, T. van der Heide, J. Hermann, S. Irle, J. J. Kranz, C. Köhler, T. Kowalczyk, T. Kubař, I. S. Lee, V. Lutsker, R. J. Maurer, S. K. Min, I. Mitchell, C. Negre, T. A. Niehaus, A. M. N. Niklasson, A. J. Page, A. Pecchia, G. Penazzi, M. P. Persson, J. Řezáč, C. G. Sánchez, M. Sternberg, M. Stöhr, F. Stuckenberg, A. Tkatchenko, V. W.-z. Yu, and T. Frauenheim, "DFTB+, a software package for efficient approximate density functional theory based atomistic simulations," *The Journal of Chemical Physics*, vol. 152, p. 124101, 03 2020.

[136] V. L. Deringer, M. A. Caro, and G. Csányi, "A general-purpose machine-learning force field for bulk and nanostructured phosphorus," *Nature Communications*, vol. 11, p. 5461, Oct 2020.

[137] O. T. Unke, S. Chmiela, H. E. Sauceda, M. Gastegger, I. Poltavsky, K. T. Schütt, A. Tkatchenko, and K.-R. Müller, "Machine learning force fields," *Chemical Reviews*, vol. 121, no. 16, pp. 10142–10186, 2021. PMID: 33705118.

[138] A. P. Bartók, R. Kondor, and G. Csányi, "On representing chemical environments," *Phys. Rev. B*, vol. 87, p. 184115, May 2013.

[139] A. P. Bartók, M. C. Payne, R. Kondor, and G. Csányi, "Gaussian approximation potentials: The accuracy of quantum mechanics, without the electrons," *Phys. Rev. Lett.*, vol. 104, p. 136403, Apr 2010.

[140] A. P. Bartók and G. Csányi, "Gaussian approximation potentials: a brief tutorial introduction," 2020.

[141] J. P. Dismukes, L. Ekstrom, and R. J. Paff, "Lattice parameter and density in germanium-silicon alloys1," *The Journal of Physical Chemistry*, vol. 68, pp. 3021–3027, Oct 1964.

Die approbierte gedruckte Originalversion dieser Dissertation ist an der TU Wien Bibliothek verfügbar.
The approved original version of this doctoral thesis is available in print at TU Wien Bibliothek.
TU WIEN Bibliothek Your knowledge hub

[142] Y. Wang, F. Zahid, J. Wang, and H. Guo, "Structure and dielectric properties of amorphous high-k oxides: Hfo2, zro2, and their alloys," *Phys. Rev. B*, vol. 85, p. 224110, Jun 2012.

[143] A. de Jamblinne de Meux, G. Pourtois, J. Genoe, and P. Heremans, "Comparison of the electronic structure of amorphous versus crystalline indium gallium zinc oxide semiconductor: structure, tail states and strain effects," *Journal of Physics D: Applied Physics*, vol. 48, p. 435104, sep 2015.

[144] L. Guo, E. Leobandung, and S. Y. Chou, "A silicon single-electron transistor memory operating at room temperature," *Science*, vol. 275, pp. 649–651, Jan 1997.

[145] R. Jansen, "Silicon spintronics," *Nature Materials*, vol. 11, pp. 400–408, May 2012.

[146] M. Razeghi, *Technology of Quantum Devices*, ch. 2, pp. 41–82. Springer US, 1 ed., 2010.

[147] S. T. Pantelides, S. Wang, A. Franceschetti, R. Buczko, M. Di Ventra, S. N. Rashkeev, L. Tsetseris, M. Evans, I. Batyrev, L. C. Feldman, S. Dhar, K. McDonald, R. A. Weller, R. Schrimpf, D. Fleetwood, X. Zhou, J. R. Williams, C. C. Tin, G. Chung, T. Isaacs-Smith, S. Wang, S. Pennycook, G. Duscher, K. Van Benthem, and L. Porter, "Si/sio2 and sic/sio2 interfaces for mosfets – challenges and advances," in *Silicon Carbide and Related Materials 2005*, vol. 527 of *Materials Science Forum*, pp. 935–948, Trans Tech Publications Ltd, 10 2006.

[148] M. M. Waldrop, "The chips are down for moore's law," *Nature*, vol. 530, pp. 144–147, 2016.

[149] Y. Illarionov, T. Knobloch, and T. Grasser, "Native High-k Oxides for 2D Transistors," *Nat. Electron.*, vol. 3, pp. 442–443, 2020.

[150] R. de Almeida and I. Baumvol, "Reaction–diffusion in high-k dielectrics on Si," *Surf. Sci. Rep.*, vol. 49, no. 1, pp. 1–114, 2003.

[151] C. Mahata, I.-K. Oh, C. M. Yoon, C. W. Lee, J. Seo, H. Algadi, M.-H. Sheen, Y.-W. Kim, H. Kim, and T. Lee, "The impact of atomic layer deposited sio2 passivation for high-k ta1-xzrxo on the inp substrate," *J. Mater. Chem. C*, vol. 3, pp. 10293–10301, 2015.

[152] A. Nakajima, Q. D. Khosru, T. Yoshimoto, and S. Yokoyama, "Atomic-layer-deposited silicon-nitride/sio2 stack—-a highly potential gate dielectrics for advanced cmos technology," *Microelectronics Reliability*, vol. 42, no. 12, pp. 1823–1835, 2002.

[153] O. Nur and M. Willander, *Chapter 4 - New emerging nanofabrication methods*, pp. 87–147. Micro and Nano Technologies, William Andrew Publishing, 2020.

Die approbierte gedruckte Originalversion dieser Dissertation ist an der TU Wien Bibliothek verfügbar.
The approved original version of this doctoral thesis is available in print at TU Wien Bibliothek.
TU WIEN Bibliothek Your knowledge hub

[154] Q. Yao, X. Ma, H. Wang, Y. Wang, G. Wang, J. Zhang, W. Liu, X. Wang, J. Yan, Y. Li, and W. Wang, “Investigate on the mechanism of hfo2/si0.7ge0.3 interface passivation based on low-temperature ozone oxidation and si-cap methods,” *Nanomater.*, vol. 11, no. 4, p. 955, 2021.

[155] C. Krzeminski, G. Larrieu, J. Penaud, E. Lampin, and E. Dubois, “Silicon dry oxidation kinetics at low temperature in the nanometric range: Modeling and experiment,” *J. Appl. Phys.*, vol. 101, no. 6, p. 064908, 2007.

[156] B. E. Deal and A. S. Grove, “General relationship for the thermal oxidation of silicon,” *J. Appl. Phys.*, vol. 36, no. 12, pp. 3770–3778, 1965.

[157] A. Bongiorno and A. Pasquarello, “O2 oxidation reaction at the si(100)-sio2 interface: A first-principles investigation,” *J. Mater. Sci.*, vol. 40, pp. 3047–3050, 06 2005.

[158] A. Bongiorno and A. Pasquarello, “Reaction of the oxygen molecule at the Si(100)$-$Sio$_2$ interface during silicon oxidation,” *Phys. Rev. Lett.*, vol. 93, p. 086102, Aug 2004.

[159] A. Bongiorno and A. Pasquarello, “Multiscale modeling of oxygen diffusion through the oxide during silicon oxidation,” *Phys. Rev. B*, vol. 70, p. 195312, Nov 2004.

[160] A. Pasquarello, M. S. Hybertsen, and R. Car, “Interface structure between silicon and its oxide by first-principles molecular dynamics,” *Nature*, vol. 396, no. 6706, pp. 58–60, 1998.

[161] F. J. Himpsel, F. R. McFeely, A. Taleb-Ibrahimi, J. A. Yarmoff, and G. Hollinger, “Microscopic structure of the sio$_2$/si interface,” *Phys. Rev. B*, vol. 38, pp. 6084–6096, Sep 1988.

[162] T. Akiyama and H. Kageshima, “Reaction mechanisms of oxygen at sio2/si(100) interface,” *Surf. Sci.*, vol. 576, no. 1, pp. L65–L70, 2005.

[163] E. P. Gusev, H. C. Lu, T. Gustafsson, and E. Garfunkel, “Growth mechanism of thin silicon oxide films on si(100) studied by medium-energy ion scattering,” *Phys. Rev. B*, vol. 52, pp. 1759–1775, Jul 1995.

[164] E. Rosencher, A. Straboni, S. Rigo, and G. Amsel, “An 18o study of the thermal oxidation of silicon in oxygen,” *Appl. Phys. Lett.*, vol. 34, no. 4, pp. 254–256, 1979.

[165] M. A. Hopper, R. A. Clarke, and L. Young, “Thermal oxidation of silicon: In situ measurement of the growth rate using ellipsometry,” *J. Electrochem. Soc.*, vol. 122, pp. 1216–1222, sep 1975.

[166] K. Ohsawa, Y. Hayashi, R. Hasunuma, and K. Yamabe, “Roughness increase on surface and interface of sio$_2$ grown on atomically flat si (111) terrace,” *J. Phys. Conf. Ser.*, vol. 191, p. 012031, 11 2009.

TU WIEN Bibliothek Your knowledge hub
Die approbierte gedruckte Originalversion dieser Dissertation ist an der TU Wien Bibliothek verfügbar.
The approved original version of this doctoral thesis is available in print at TU Wien Bibliothek.

[167] L. C. Ciacchi and M. C. Payne, "First-principles molecular-dynamics study of native oxide growth on si(001)," *Phys. Rev. Lett.*, vol. 95, p. 196101, Nov 2005.

[168] K. Kato and T. Uda, "Chemisorption of a single oxygen molecule on the si(100) surface: Initial oxidation mechanisms," *Phys. Rev. B*, vol. 62, pp. 15978–15988, Dec 2000.

[169] C.-Y. Niu and J.-T. Wang, "Adsorption and dissociation of oxygen molecules on si(111)-(7×7) surface," *J. Chem. Phys.*, vol. 139, p. 194709, 11 2013.

[170] Y.-C. Liao, A. M. Nienow, and J. T. Roberts, "Surface chemistry of aerosolized nanoparticles: Thermal oxidation of silicon," *J. Phys. Chem. B*, vol. 110, no. 12, pp. 6190–6197, 2006.

[171] A. Yoshigoe, Y. Yamada, R. Taga, S. Ogawa, and Y. Takakuwa, "Detection of molecular oxygen adsorbate during room-temperature oxidation of si(100)2 × 1 surface: In situ synchrotron radiation photoemission study," *Jpn. J. Appl. Phys.*, vol. 55, p. 100307, sep 2016.

[172] D. Kaya, R. J. Cobley, and R. E. Palmer, "Combining scanning tunneling microscope (stm) imaging and local manipulation to probe the high dose oxidation structure of the si(111)-7×7 surface," *Nano Res*, vol. 13, pp. 145–150, 2020.

[173] E. Hwang, Y. H. Chang, Y.-S. Kim, J.-Y. Koo, and H. Kim, "Precursor state of oxygen molecules on the Si(001) surface during the initial room-temperature adsorption," *J. Korean Phys. Soc.*, vol. 61, pp. 1046–1050, October 2012.

[174] U. Höfer, P. Morgen, W. Wurth, and E. Umbach, "Initial stages of oxygen adsorption on Si(111). ii. the molecular precursor," *Phys. Rev. B*, vol. 40, pp. 1130–1145, Jul 1989.

[175] B. A. Ferguson, C. T. Reeves, and C. B. Mullins, "Oxygen adsorption on si(100)-2×1 via trapping-mediated and direct mechanisms," *J. Chem. Phys.*, vol. 110, no. 23, pp. 11574–11584, 1999.

[176] P. Morgen, U. Höfer, W. Wurth, and E. Umbach, "Initial stages of oxygen adsorption on si(111): The stable state," *Phys. Rev. B*, vol. 39, pp. 3720–3734, Feb 1989.

[177] B. A. Ferguson, C. T. Reeves, and C. B. Mullins, "Oxygen adsorption on si(100)-2×1 via trapping-mediated and direct mechanisms," *J. Chem. Phys.*, vol. 110, no. 23, pp. 11574–11584, 1999.

[178] T. K. Whidden, P. Thanikasalam, M. J. Rack, and D. K. Ferry, "Initial oxidation of silicon (100): A unified chemical model for thin and thick oxide growth rates and interfacial structure," *J. Vac. Sci. Technol. B*, vol. 13, no. 4, pp. 1618–1625, 1995.

Die approbierte gedruckte Originalversion dieser Dissertation ist an der TU Wien Bibliothek verfügbar.
The approved original version of this doctoral thesis is available in print at TU Wien Bibliothek.
TU WIEN Bibliothek Your knowledge hub

[179] Y. Hoshino, T. Nishimura, T. Nakada, H. Namba, and Y. Kido, "Initial oxidation of si(001)-2×1 surface studied by photoelectron spectroscopy coupled with medium energy ion scattering," *Surf. Sci.*, vol. 488, no. 3, pp. 249–255, 2001.

[180] F. Fuchs, W. G. Schmidt, and F. Bechstedt, "Understanding the optical anisotropy of oxidized si(001) surfaces," *Phys. Rev. B*, vol. 72, p. 075353, Aug 2005.

[181] N. Salles, N. Richard, N. Mousseau, and A. Hemeryck, "Strain-driven diffusion process during silicon oxidation investigated by coupling density functional theory and activation relaxation technique," *J. Chem. Phys.*, vol. 147, no. 5, p. 054701, 2017.

[182] P. Mur, M. Semeria, M. Olivier, A. Papon, C. Leroux, G. Reimbold, P. Gentile, N. Magnea, T. Baron, R. Clerc, and G. Ghibaudo, "Ultra-thin oxides grown on silicon (1 0 0) by rapid thermal oxidation for cmos and advanced devices," *Appl. Surf. Sci.*, vol. 175-176, pp. 726–733, 2001. 10th International Conference on Solid Films and Surfaces.

[183] B. Aradi, B. Hourahine, and T. Frauenheim, "Dftb+, a sparse matrix-based implementation of the dftb method," *J. Phys. Chem. A*, vol. 111, no. 26, pp. 5678–5684, 2007. PMID: 17567110.

[184] C. Köhler, Z. Hajnal, P. Deák, T. Frauenheim, and S. Suhai, "Theoretical investigation of carbon defects and diffusion in $\alpha$-quartz," *Phys. Rev. B*, vol. 64, p. 085333, Aug 2001.

[185] A. Ramstad, G. Brocks, and P. J. Kelly, "Theoretical study of the si(100) surface reconstruction," *Phys. Rev. B*, vol. 51, pp. 14504–14523, May 1995.

[186] A. C. Diebold, D. Venables, Y. Chabal, D. Muller, M. Weldon, and E. Garfunkel, "Characterization and production metrology of thin transistor gate oxide films," *Mater. Sci. Semicond. Process.*, vol. 2, no. 2, pp. 103–147, 1999.

[187] R. L. Mozzi and B. E. Warren, "The structure of vitreous silica," *J. Appl. Crystallogr.*, vol. 2, pp. 164–172, Oct 1969.

[188] K. Hirose, H. Nohira, T. Koike, K. Sakano, and T. Hattori, "Structural transition layer at $sio_2$/Si interfaces," *Phys. Rev. B*, vol. 59, pp. 5617–5621, Feb 1999.

[189] E. P. EerNisse, "Stress in thermal $SiO_2$ during growth," *Appl. Phys. Lett.*, vol. 35, no. 1, pp. 8–10, 1979.

[190] E. Kobeda and E. A. Irene, "Intrinsic $SiO_2$ film stress measurements on thermally oxidized si," *J. Vac. Sci. Technol.*, vol. 5, no. 1, pp. 15–19, 1987.

[191] S. Ling, A.-M. El-Sayed, F. Lopez-Gejo, M. B. Watkins, V. Afanas'ev, and A. L. Shluger, "A computational study of si–h bonds as precursors for neutral e' centres in amorphous silica and at the si/sio2 interface," *Microelectron. Eng.*, vol. 109, pp. 310–313, 2013.

Die approbierte gedruckte Originalversion dieser Dissertation ist an der TU Wien Bibliothek verfügbar.
The approved original version of this doctoral thesis is available in print at TU Wien Bibliothek.
TU Bibliothek WIEN Your knowledge hub

[192] U. Khalilov, E. C. Neyts, G. Pourtois, and A. C. T. van Duin, “Can we control the thickness of ultrathin silica layers by hyperthermal silicon oxidation at room temperature?,” *J. Phys. Chem. C*, vol. 115, no. 50, pp. 24839–24848, 2011.

[193] M. Jech, A.-M. El-Sayed, S. Tyaginov, A. L. Shluger, and T. Grasser, “*ab initio* treatment of silicon-hydrogen bond rupture at si/$sio_2$ interfaces,” *Phys. Rev. B*, vol. 100, p. 195302, Nov 2019.

[194] A.-M. El-Sayed, M. B. Watkins, V. V. Afanas’ev, and A. L. Shluger, “Nature of intrinsic and extrinsic electron trapping in $sio_2$,” *Phys. Rev. B*, vol. 89, p. 125201, Mar 2014.

[195] D. A. Muller, T. Sorsch, S. Moccio, F. H. Baumann, K. Evans-Lutterodt, and G. Timp, “The electronic structure at the atomic scale of ultrathin gate oxides,” *Nature*, vol. 399, pp. 758–761, June 1999.

[196] W. Bond and W. Kaiser, “Interstitial versus substitutional oxygen in silicon,” *J. Phys. Chem. Solids*, vol. 16, no. 1, pp. 44–45, 1960.

[197] M. Needels, J. Joannopoulos, Y. BAR-YAM, S. Pantelides, and R. WOLFE, “The enchanting properties of oxygen atoms in silicon,” *MRS Proceedings*, vol. 209, p. 103, 1990.

[198] M. Saito and A. Oshiyama, “Stable atomic geometries of oxygen microclusters in silicon,” *Phys. Rev. B*, vol. 38, pp. 10711–10717, Nov 1988.

[199] P. J. Kelly and R. Car, “Green’s-matrix calculation of total energies of point defects in silicon,” *Phys. Rev. B*, vol. 45, pp. 6543–6563, Mar 1992.

[200] S. Lee and D. Nichols, “Outdiffusion and diffusion mechanism of oxygen in silicon,” *Appl. Phys. Lett.*, vol. 47, no. 9, pp. 1001–1003, 1985.

[201] M. Ramamoorthy and S. T. Pantelides, “Coupled-barrier diffusion: The case of oxygen in silicon,” *Phys. Rev. Lett.*, vol. 76, pp. 267–270, Jan 1996.

[202] J. Koettgen, T. Zacherle, S. Grieshammer, and M. Martin, “Ab initio calculation of the attempt frequency of oxygen diffusion in pure and samarium doped ceria,” *Phys. Chem. Chem. Phys.*, vol. 19, pp. 9957–9973, 2017.

[203] T. Hoshino and Y. Nishioka, “Inward diffusion of oxygen on a silicon surface,” *Phys. Rev. Lett.*, vol. 84, pp. 4633–4636, May 2000.

[204] T. Bakos, S. N. Rashkeev, and S. T. Pantelides, “Reactions and diffusion of water and oxygen molecules in amorphous sio2,” *Phys. Rev. Lett.*, vol. 88 5, p. 055508, 2002.

[205] T. Hoshino, M. Hata, S. Neya, Y. Nishioka, T. Watanabe, K. Tatsumura, and I. Ohdomari, “Diffusion of molecular and atomic oxygen in silicon oxide,” *Jpn. J. Appl. Phys.*, vol. 42, pp. 3560–3565, jun 2003.

Die approbierte gedruckte Originalversion dieser Dissertation ist an der TU Wien Bibliothek verfügbar.
The approved original version of this doctoral thesis is available in print at TU Wien Bibliothek.
TU WIEN Bibliothek Your knowledge hub

[206] J. Perez-Bueno, R. Ramirez-Bon, Y. Vorobiev, F. Espinoza-Beltran, and J. Gonzalez-Hernandez, "Oxygen diffusion in silicon oxide films produced by different methods," *Thin Solid Films*, vol. 379, no. 1, pp. 57–63, 2000.

[207] S. Pantelides, S. Wang, A. Franceschetti, B. R., M. Vetra, S. Rashkeev, L. Tsetseris, M. Evans, and B. I. G., "Sisio2 and sic/sio2 interfaces for mosfets - challenges and advances," *Mater. Sci. Forum*, vol. 527–529, pp. 935–948, 2006.

[208] A. M. Stoneham, M. A. Szymanski, and A. L. Shluger, "Atomic and ionic processes of silicon oxidation," *Phys. Rev. B*, vol. 63, p. 241304, Jun 2001.

[209] H. Kageshima and K. Shiraishi, "First-principles study of oxide growth on si(100) surfaces and at $sio_2$/si(100) interfaces," *Phys. Rev. Lett.*, vol. 81, pp. 5936–5939, Dec 1998.

[210] D. Milardovich, C. Wilhelmer, D. Waldhoer, L. Cvitkovich, G. Sivaraman, and T. Grasser, "Machine learning interatomic potential for silicon-nitride (Si3N4) by active learning," *The Journal of Chemical Physics*, vol. 158, p. 194802, 05 2023.

[211] J. VandeVondele, M. Krack, F. Mohamed, M. Parrinello, T. Chassaing, and J. Hutter, "Quickstep: Fast and accurate density functional calculations using a mixed gaussian and plane waves approach," *Comput. Phys. Commun.*, vol. 167, no. 2, pp. 103–128, 2005.

[212] J. VandeVondele and J. Hutter, "Gaussian basis sets for accurate calculations on molecular systems in gas and condensed phases," *J. Chem. Phys.*, vol. 127, no. 11, p. 114105, 2007.

[213] S. Goedecker, M. Teter, and J. Hutter, "Separable dual-space gaussian pseudopotentials," *Phys. Rev. B*, vol. 54, pp. 1703–1710, Jul 1996.

[214] N. Miyata, H. Watanabe, and M. Ichikawa, "Atomic-scale structure of $sio_2$/Si interface formed by furnace oxidation," *Phys. Rev. B*, vol. 58, pp. 13670–13676, Nov 1998.

[215] D. A. Muller and G. D. Wilk, "Atomic scale measurements of the interfacial electronic structure and chemistry of zirconium silicate gate dielectrics," *Applied Physics Letters*, vol. 79, pp. 4195–4197, 12 2001.

[216] J. H. Oh, H. W. Yeom, Y. Hagimoto, K. Ono, M. Oshima, N. Hirashita, M. Nywa, A. Toriumi, and A. Kakizaki, "Chemical structure of the ultrathin $sio_2$/Si(100) interface: An angle-resolved si $2p$ photoemission study," *Phys. Rev. B*, vol. 63, p. 205310, Apr 2001.

[217] Y. Tsuda, A. Yoshigoe, S. Ogawa, T. Sakamoto, and Y. Takakuwa, "Observation of chemisorbed $O_2$ molecule at $SiO_2$/Si(001) interface during si dry oxidation," *e-Journal of Surface Science and Nanotechnology*, vol. 21, no. 1, pp. 30–39, 2023.

Die approbierte gedruckte Originalversion dieser Dissertation ist an der TU Wien Bibliothek verfügbar.
The approved original version of this doctoral thesis is available in print at TU Wien Bibliothek.
TU Wien Bibliothek Your knowledge hub

[218] B. Schubert, P. Avouris, and R. Hoffmann, “A theoretical study of the initial stages of Si(111)–7×7 oxidation. I. The molecular precursor,” *The Journal of Chemical Physics*, vol. 98, pp. 7593–7605, 05 1993.

[219] A. H. Carim and R. Sinclair, “The Evolution of Si/$SiO_2$ Interface Roughness,” *Journal of The Electrochemical Society*, vol. 134, p. 741, mar 1987.

[220] K. Ohsawa, Y. Hayashi, R. Hasunuma, and K. Yamabe, “Roughness increase on surface and interface of $SiO_2$ grown on atomically flat Si(111) terrace,” *Japanese Journal of Applied Physics*, vol. 48, p. 05DB02, may 2009.

[221] N. Nayir, A. C. T. van Duin, and S. Erkoc, “Development of the reaxff reactive force field for inherent point defects in the Si/silica system,” *The Journal of Physical Chemistry A*, vol. 123, pp. 4303–4313, May 2019.

[222] A. Stesmans and V. V. Afanas’ev, “Electrical activity of interfacial paramagnetic defects in thermal (100) si/$sio_2$,” *Phys. Rev. B*, vol. 57, pp. 10030–10034, Apr 1998.

[223] J. L. Benton, C. J. Doherty, S. D. Ferris, D. L. Flamm, L. C. Kimerling, and H. J. Leamy, “Hydrogen passivation of point defects in silicon,” *Applied Physics Letters*, vol. 36, pp. 670–671, 04 1980.

[224] C. Wilhelmer, D. Waldhoer, M. Jech, A.-M. B. El-Sayed, L. Cvitkovich, M. Waltl, and T. Grasser, “Ab initio investigations in amorphous silicon dioxide: Proposing a multi-state defect model for electron and hole capture,” *Microelectronics Reliability*, vol. 139, p. 114801, 2022.

[225] C. B. Simmons, T. S. Koh, *et al.*, “Pauli spin blockade and lifetime-enhanced transport in a Si/SiGe double quantum dot,” *Phys. Rev. B*, vol. 82, p. 245312, 2010.

[226] Y. M. Niquet, D. Rideau, C. Tavernier, H. Jaouen, and X. Blase, “Onsite matrix elements of the tight-binding hamiltonian of a strained crystal: Application to silicon, germanium, and their alloys,” *Phys. Rev. B*, vol. 79, p. 245201, Jun 2009.

[227] P. N. Keating, “Effect of invariance requirements on the elastic strain energy of crystals with application to the diamond structure,” *Phys. Rev.*, vol. 145, pp. 637–645, May 1966.

[228] I. Souza, J. Íñiguez, and D. Vanderbilt, “First-principles approach to insulators in finite electric fields,” *Phys. Rev. Lett.*, vol. 89, p. 117602, Aug 2002.

[229] R. D. King-Smith and D. Vanderbilt, “Theory of polarization of crystalline solids,” *Phys. Rev. B*, vol. 47, pp. 1651–1654, Jan 1993.

[230] D. Vanderbilt and R. D. King-Smith, “Electric polarization as a bulk quantity and its relation to surface charge,” *Phys. Rev. B*, vol. 48, pp. 4442–4455, Aug 1993.

TU WIEN Bibliothek Your knowledge hub
Die approbierte gedruckte Originalversion dieser Dissertation ist an der TU Wien Bibliothek verfügbar.
The approved original version of this doctoral thesis is available in print at TU Wien Bibliothek.

[231] J. R. F. Lima and G. Burkard, "Interface and electromagnetic effects in the valley splitting of si quantum dots," *Materials for Quantum Technology*, vol. 3, p. 025004, may 2023.

[232] M. Friesen and S. N. Coppersmith, "Theory of valley-orbit coupling in a si/sige quantum dot," *Phys. Rev. B*, vol. 81, p. 115324, Mar 2010.

[233] B. D. Woods, M. A. Eriksson, R. Joynt, and M. Friesen, "Spin-orbit enhancement in Si/SiGe heterostructures with oscillating Ge concentration," *Phys. Rev. B*, vol. 107, p. 035418, 2023.

[234] T. Tanttu, B. Hensen, K. W. Chan, C. H. Yang, W. W. Huang, M. Fogarty, F. Hudson, K. Itoh, D. Culcer, A. Laucht, A. Morello, and A. Dzurak, "Controlling spin-orbit interactions in silicon quantum dots using magnetic field direction," *Phys. Rev. X*, vol. 9, p. 021028, May 2019.

[235] A. V. Khaetskii, D. Loss, and L. Glazman, "Electron Spin Decoherence in Quantum Dots due to Interaction with Nuclei," *Physical Review Letters*, vol. 88, p. 186802, April 2002.

[236] K. M. Itoh and H. Watanabe, "Isotope engineering of silicon and diamond for quantum computing and sensing applications," *MRS Communications*, vol. 4, pp. 143–157, December 2014.

[237] M. Veldhorst, J. C. C. Hwang, C. H. Yang, A. W. Leenstra, B. de Ronde, J. P. Dehollain, J. T. Muhonen, F. E. Hudson, K. M. Itoh, A. Morello, and A. S. Dzurak, "An addressable quantum dot qubit with fault-tolerant control-fidelity," *Nature Nanotechnology*, vol. 9, pp. 981–985, October 2014.

[238] I. Hansen, A. E. Seedhouse, K. W. Chan, F. E. Hudson, K. M. Itoh, A. Laucht, A. Saraiva, C. H. Yang, and A. S. Dzurak, "Implementation of an advanced dressing protocol for global qubit control in silicon," *Applied Physics Reviews*, vol. 9, p. 031409, September 2022.

[239] A. Elsayed, M. Shehata, C. Godfrin, S. Kubicek, S. Massar, Y. Canvel, J. Jussot, G. Simion, M. Mongillo, D. Wan, B. Govoreanu, I. P. Radu, R. Li, P. V. Dorpe, and K. D. Greve, "Low charge noise quantum dots with industrial cmos manufacturing," 2022.

[240] T. Tanttu, W. H. Lim, J. Y. Huang, N. D. Stuyck, W. Gilbert, R. Y. Su, M. Feng, J. D. Cifuentes, A. E. Seedhouse, S. K. Seritan, C. I. Ostrove, K. M. Rudinger, R. C. C. Leon, W. Huang, C. C. Escott, K. M. Itoh, N. V. Abrosimov, H.-J. Pohl, M. L. W. Thewalt, F. E. Hudson, R. Blume-Kohout, S. D. Bartlett, A. Morello, A. Laucht, C. H. Yang, A. Saraiva, and A. S. Dzurak, "Consistency of high-fidelity two-qubit operations in silicon," September 2023.

[241] D. J. Niegemann, V. El-Homsy, B. Jadot, M. Nurizzo, B. Cardoso-Paz, E. Chanrion, M. Dartiailh, B. Klemt, V. Thiney, C. Bäuerle, P.-A. Mortemousque,

TU WIEN Bibliothek Your knowledge hub
Die approbierte gedruckte Originalversion dieser Dissertation ist an der TU Wien Bibliothek verfügbar.
The approved original version of this doctoral thesis is available in print at TU Wien Bibliothek.

B. Bertrand, H. Niebojewski, M. Vinet, F. Balestro, T. Meunier, and M. Urdampilleta, "Parity and Singlet-Triplet High-Fidelity Readout in a Silicon Double Quantum Dot at 0.5 K," *PRX Quantum*, vol. 3, p. 040335, December 2022.

[242] G. A. Oakes, V. N. Ciriano-Tejel, D. F. Wise, M. A. Fogarty, T. Lundberg, C. Lainé, S. Schaal, F. Martins, D. J. Ibberson, L. Hutin, B. Bertrand, N. Stelmashenko, J. W. A. Robinson, L. Ibberson, A. Hashim, I. Siddiqi, A. Lee, M. Vinet, C. G. Smith, J. J. L. Morton, and M. F. Gonzalez-Zalba, "Fast High-Fidelity Single-Shot Readout of Spins in Silicon Using a Single-Electron Box," *Physical Review X*, vol. 13, p. 011023, February 2023.

[243] R. C. C. Leon, C. H. Yang, J. C. C. Hwang, J. Camirand Lemyre, T. Tanttu, W. Huang, J. Y. Huang, F. E. Hudson, K. M. Itoh, A. Laucht, M. Pioro-Ladrière, A. Saraiva, and A. S. Dzurak, "Bell-state tomography in a silicon many-electron artificial molecule," *Nature Communications*, vol. 12, p. 3228, May 2021.

[244] L. C. Camenzind, S. Geyer, A. Fuhrer, R. J. Warburton, D. M. Zumbühl, and A. V. Kuhlmann, "A spin qubit in a fin field-effect transistor," *Nature Electronics*, vol. 5, pp. 178–183, March 2022.

[245] J. Y. Huang, R. Y. Su, W. H. Lim, M. Feng, B. van Straaten, B. Severin, W. Gilbert, N. D. Stuyck, T. Tanttu, S. Serrano, J. D. Cifuentes, I. Hansen, A. E. Seedhouse, E. Vahapoglu, N. V. Abrosimov, H.-J. Pohl, M. L. W. Thewalt, F. E. Hudson, C. C. Escott, N. Ares, S. D. Bartlett, A. Morello, A. Saraiva, A. Laucht, A. S. Dzurak, and C. H. Yang, "High-fidelity operation and algorithmic initialisation of spin qubits above one kelvin," August 2023.

[246] D. D. Esposti, L. E. A. Stehouwer, Ö. Gül, N. Samkharadze, C. Déprez, M. Meyer, I. N. Meijer, L. Tryputen, S. Karwal, M. Botifoll, J. Arbiol, S. V. Amitonov, L. M. K. Vandersypen, A. Sammak, M. Veldhorst, and G. Scappucci, "Low disorder and high valley splitting in silicon," September 2023.

[247] J. Yoneda, K. Takeda, T. Otsuka, T. Nakajima, M. R. Delbecq, G. Allison, T. Honda, T. Kodera, S. Oda, Y. Hoshi, N. Usami, K. M. Itoh, and S. Tarucha, "A quantum-dot spin qubit with coherence limited by charge noise and fidelity higher than 99.9%," *Nature Nanotechnology*, vol. 13, pp. 102–106, December 2017.

[248] A. R. Mills, C. R. Guinn, M. J. Gullans, A. J. Sigillito, M. M. Feldman, E. Nielsen, and J. R. Petta, "Two-qubit silicon quantum processor with operation fidelity exceeding 99%," *Science Advances*, vol. 8, p. eabn5130, April 2022.

[249] A. J. Weinstein, M. D. Reed, A. M. Jones, R. W. Andrews, D. Barnes, J. Z. Blumoff, L. E. Euliss, K. Eng, B. H. Fong, S. D. Ha, D. R. Hulbert, C. A. C. Jackson, M. Jura, T. E. Keating, J. Kerckhoff, A. A. Kiselev, J. Matten, G. Sabbir, A. Smith, J. Wright, M. T. Rakher, T. D. Ladd, and M. G. Borselli, "Universal logic with encoded spin qubits in silicon," *Nature*, vol. 615, pp. 817–822, March 2023.

Die approbierte gedruckte Originalversion dieser Dissertation ist an der TU Wien Bibliothek verfügbar.
The approved original version of this doctoral thesis is available in print at TU Wien Bibliothek.
TU WIEN Bibliothek Your knowledge hub

[250] J. Z. Blumoff, A. S. Pan, T. E. Keating, R. W. Andrews, D. W. Barnes, T. L. Brecht, E. T. Croke, L. E. Euliss, J. A. Fast, C. A. Jackson, A. M. Jones, J. Kerckhoff, R. K. Lanza, K. Raach, B. J. Thomas, R. Velunta, A. J. Weinstein, T. D. Ladd, K. Eng, M. G. Borselli, A. T. Hunter, and M. T. Rakher, "Fast and High-Fidelity State Preparation and Measurement in Triple-Quantum-Dot Spin Qubits," *PRX Quantum*, vol. 3, p. 010352, March 2022.

[251] S. G. J. Philips, M. T. Mądzik, S. V. Amitonov, S. L. de Snoo, M. Russ, N. Kalhor, C. Volk, W. I. L. Lawrie, D. Brousse, L. Tryputen, B. P. Wuetz, A. Sammak, M. Veldhorst, G. Scappucci, and L. M. K. Vandersypen, "Universal control of a six-qubit quantum processor in silicon," *Nature*, vol. 609, pp. 919–924, September 2022.

[252] A. Mills, C. Guinn, M. Feldman, A. Sigillito, M. Gullans, M. Rakher, J. Kerckhoff, C. Jackson, and J. Petta, "High-Fidelity State Preparation, Quantum Control, and Readout of an Isotopically Enriched Silicon Spin Qubit," *Physical Review Applied*, vol. 18, p. 064028, December 2022.

[253] M. W. Swift, H. Peelaers, S. Mu, J. J. L. Morton, and C. G. Van de Walle, "First-principles calculations of hyperfine interaction, binding energy, and quadrupole coupling for shallow donors in silicon," *npj Computational Materials*, vol. 6, p. 181, Nov 2020.

[254] T. D. Kühne, M. Iannuzzi, M. Del Ben, V. V. Rybkin, P. Seewald, F. Stein, T. Laino, R. Z. Khaliullin, O. Schütt, F. Schiffmann, D. Golze, J. Wilhelm, S. Chulkov, M. H. Bani-Hashemian, V. Weber, U. Borštnik, M. Taillefumier, A. S. Jakobovits, A. Lazzaro, H. Pabst, T. Müller, R. Schade, M. Guidon, S. Andermatt, N. Holmberg, G. K. Schenter, A. Hehn, A. Bussy, F. Belleflamme, G. Tabacchi, A. Glöß, M. Lass, I. Bethune, C. J. Mundy, C. Plessl, M. Watkins, J. VandeVondele, M. Krack, and J. Hutter, "Cp2k: An electronic structure and molecular dynamics software package - quickstep: Efficient and accurate electronic structure calculations," *J. Chem. Phys.*, vol. 152, pp. 580–586, 2020.

[255] K. Ghosh, H. Ma, V. Gavini, and G. Galli, "All-electron density functional calculations for electron and nuclear spin interactions in molecules and solids," *Phys. Rev. Mater.*, vol. 3, p. 043801, Apr 2019.

[256] A. G. Sabnis and J. T. Clemens, "Characterization of the electron mobility in the inverted [100]Si surface," *1979 International Electron Devices Meeting*, pp. 18–21, 1979.

[257] S. Dhar, *Analytical Mobility Modeling for Strained Silicon-Based Devices*. PhD thesis, TU Vienna, 2007.

[258] C. K. Maiti, L. K. Bera, and S. Chattopadhyay, "Strained-si heterostructure field effect transistors," *Semiconductor Science and Technology*, vol. 13, p. 1225, nov 1998.

Die approbierte gedruckte Originalversion dieser Dissertation ist an der TU Wien Bibliothek verfügbar.
The approved original version of this doctoral thesis is available in print at TU Wien Bibliothek.
TU WIEN Bibliothek Your knowledge hub

[259] J. T. Muhonen, J. P. Dehollain, A. Laucht, F. E. Hudson, R. Kalra, T. Sekiguchi, K. M. Itoh, D. N. Jamieson, J. C. McCallum, A. S. Dzurak, and A. Morello, “Storing quantum information for 30 seconds in a nanoelectronic device,” *Nature Nanotechnology*, vol. 9, pp. 986–991, Dec 2014.

[260] R. M. Jock, N. T. Jacobson, P. Harvey-Collard, A. M. Mounce, V. Srinivasa, D. R. Ward, J. Anderson, R. Manginell, J. R. Wendt, M. Rudolph, T. Pluym, J. K. Gamble, A. D. Baczewski, W. M. Witzel, and M. S. Carroll, “A silicon metal-oxide-semiconductor electron spin-orbit qubit,” *Nature Communications*, vol. 9, p. 1768, May 2018.

[261] J. K. Gamble, P. Harvey-Collard, N. T. Jacobson, A. D. Baczewski, E. Nielsen, L. Maurer, I. Montaño, M. Rudolph, M. S. Carroll, C. H. Yang, A. Rossi, A. S. Dzurak, and R. P. Muller, “Valley splitting of single-electron Si MOS quantum dots,” *Applied Physics Letters*, vol. 109, p. 253101, 12 2016.

[262] R. Zhao, T. Tanttu, K. Y. Tan, B. Hensen, K. W. Chan, J. C. C. Hwang, R. C. C. Leon, C. H. Yang, W. Gilbert, F. E. Hudson, K. M. Itoh, A. A. Kiselev, T. D. Ladd, A. Morello, A. Laucht, and A. S. Dzurak, “Single-spin qubits in isotopically enriched silicon at low magnetic field,” *Nature Communications*, vol. 10, p. 5500, Dec 2019.

[263] K. Takeda, A. Noiri, T. Nakajima, J. Yoneda, T. Kobayashi, and S. Tarucha, “Quantum tomography of an entangled three-qubit state in silicon,” *Nature Nanotechnology*, vol. 16, pp. 965–969, Sep 2021.

[264] J. S. Rojas-Arias, A. Noiri, P. Stano, T. Nakajima, J. Yoneda, K. Takeda, T. Kobayashi, A. Sammak, G. Scappucci, D. Loss, and S. Tarucha, “Spatial noise correlations beyond nearest-neighbor in 28Si/SiGe spin qubits,” February 2023.

[265] A. J. Sigillito, R. M. Jock, A. M. Tyryshkin, J. W. Beeman, E. E. Haller, K. M. Itoh, and S. A. Lyon, “Electron Spin Coherence of Shallow Donors in Natural and Isotopically Enriched Germanium,” *Physical Review Letters*, vol. 115, p. 247601, December 2015.

[266] X. Ying, “An overview of overfitting and its solutions,” *Journal of Physics: Conference Series*, vol. 1168, p. 022022, feb 2019.

[267] S. Klawohn, J. P. Darby, J. R. Kermode, G. Csányi, M. A. Caro, and A. P. Bartók, “Gaussian approximation potentials: Theory, software implementation and application examples,” *The Journal of Chemical Physics*, vol. 159, p. 174108, 11 2023.

[268] “Silicon (Si) high-frequency dielectric constant: Datasheet from landolt-börnstein - group iii condensed matter · volume 41a1$\alpha$: “group iv elements, iv-iv and iii-v compounds. part a - lattice properties” in springermaterials (https://doi.org/10.1007/10551045_218).” accessed 2024-05-23.

Die approbierte gedruckte Originalversion dieser Dissertation ist an der TU Wien Bibliothek verfügbar.
The approved original version of this doctoral thesis is available in print at TU Wien Bibliothek.
TU Bibliothek WIEN Your knowledge hub

[269] W. A. Pliskin and R. P. Esch, “Refractive Index of $SiO_2$ Films Grown on Silicon,” *Journal of Applied Physics*, vol. 36, pp. 2011–2013, 06 1965.

[270] J. Matsuoka, N. Kitamura, S. Fujinaga, T. Kitaoka, and H. Yamashita, “Temperature dependence of refractive index of sio2 glass,” *Journal of Non-Crystalline Solids*, vol. 135, no. 1, pp. 86–89, 1991.

[271] N. Shi and R. Ramprasad, “Atomic-scale dielectric permittivity profiles in slabs and multilayers,” *Phys. Rev. B*, vol. 74, p. 045318, Jul 2006.

[272] Y. Park, K. jeong Kong, H. Chang, and M. Shin, “First-principles studies of the electronic and dielectric properties of $Si/SiO_2/HfO_2$ interfaces,” *Japanese Journal of Applied Physics*, vol. 52, p. 041803, mar 2013.

[273] A. G. Redfield, “Spatial diffusion of spin energy,” *Physical Review*, vol. 116, no. 2, p. 315, 1959.

[274] C. P. Slichter, *Principles of Magnetic Resonance*. No. 1 in Springer Series in Solid-State Sciences, Berlin ; New York: Springer, 3rd enl. and updated ed., 1996.

[275] A. G. Redfield and W. N. Yu, “Moment-Method Calculation of Magnetization and Interspin-Energy Diffusion,” *Physical Review*, vol. 169, pp. 443–450, May 1968.

TU WIEN Bibliothek Your knowledge hub
Die approbierte gedruckte Originalversion dieser Dissertation ist an der TU Wien Bibliothek verfügbar.
The approved original version of this doctoral thesis is available in print at TU Wien Bibliothek.

# Curriculum Vitae

05/2020 – present

Doctoral Candidate and Research Assistant
Institute for Microelectronics, TU Wien
Vienna, Austria

09/2023 – 11/2023

Research Stay
RIKEN Center for Emergent Matter Science (CEMS)
Tokio, Japan

07/2023 – 09/2023 and 09/2022 – 01/2023

Research Stay
CEA Grenoble
Grenoble, France

10/2016 – 07/2019

Master's degree, Material Science
Thesis titled "Physical properties of $CeCuAs_2$"
Institute of Solid State Physics,, TU Wien
Vienna, Austria

10/2012 – 07/2016

Bachelor's degree, Electronic Engineering

10/2014 – 07/2016

Research Assistant
Institute of Sensor and Actuator Systems
TU Wien, Vienna, Austria

Die approbierte gedruckte Originalversion dieser Dissertation ist an der TU Wien Bibliothek verfügbar.
The approved original version of this doctoral thesis is available in print at TU Wien Bibliothek.
TU WIEN Bibliothek Your knowledge hub

Die approbierte gedruckte Originalversion dieser Dissertation ist an der TU Wien Bibliothek verfügbar.
The approved original version of this doctoral thesis is available in print at TU Wien Bibliothek.
TU WIEN Bibliothek Your knowledge hub

# List of publications

## Journal Articles

1. L. Cvitkovich, F. Fehringer, C. Wilhelmer, D. Milardovich, D. Waldhör, and T. Grasser. "Machine Learning Force Field for Thermal Oxidation of Silicon", under review in *Journal of Chemical Physics*, arXiv: https://arxiv.org/abs/2405.13635.

2. L. Cvitkovich, P. Stano, C. Wilhelmer, D. Waldhör, D. Loss, Y.-M. Niquet, and T. Grasser. "Coherence limit due to hyperfine interaction with nuclei in the barrier material of Si spin qubits", under review in *Physical Review Applied*, arXiv: https://arxiv.org/abs/2405.10667.

3. L. Cvitkovich, D. Waldhör, A.-M. El-Sayed, M. Jech, C. Wilhelmer, and T. Grasser. "Dynamic modeling of Si(100) thermal oxidation: Oxidation mechanisms and realistic amorphous interface generation", *Applied Surface Science*, vol. 610, 155378, 2023, doi: 10.1016/j.apsusc.2022.155378.

4. C. Wilhelmer, D. Waldhoer, L. Cvitkovich, D. Milardovich, M. Waltl, and T. Grasser. "Polaron formation in the hydrogenated amorphous silicon nitride $Si_3N_4$:H" *Phys. Rev. B* (in print), 2024

5. C. Wilhelmer, D. Waldhoer, M. Jech, A.-M. B. El-Sayed, L. Cvitkovich, M. Waltl, and T. Grasser. "Ab initio investigations in amorphous silicon dioxide: Proposing a multi-state defect model for electron and hole capture", *Microelectronics Reliability*, vol. 139, 114801, 2022, doi: 10.1016/j.microrel.2022.114801.

6. D. Milardovich, C. Wilhelmer, D. Waldhör, L. Cvitkovich, G. Sivaraman, and T. Grasser. "Machine learning interatomic potential for silicon-nitride ($Si_3N_4$) by active learning", *Journal of Chemical Physics*, vol. 158, 194802, 2023, doi: 10.1063/5.0146753.

7. C. Wilhelmer, D. Waldhör, L. Cvitkovich, D. Milardovich, M. Waltl, and T. Grasser. "Over- and Undercoordinated Atoms as a Source of Electron and Hole Traps in Amorphous Silicon Nitride (a-$Si_3N_4$)", *Nanomaterials*, vol. 13, 2286, 2023, doi: 10.3390/nano13162286.

8. B. Sklenard, L. Cvitkovich, D. Waldhoer, and J. Li. "Oxygen vacancy and hydrogen in amorphous $HfO_2$", *Journal of Physics D: Applied Physics*, vol. 56, 245301, 2023, doi: 10.1088/1361-6463/acc878.



Die approbierte gedruckte Originalversion dieser Dissertation ist an der TU Wien Bibliothek verfügbar.
The approved original version of this doctoral thesis is available in print at TU Wien Bibliothek.
TU Bibliothek WIEN Your knowledge hub

9. P. Stampfer, F. Roger, L. Cvitkovich, T. Grasser, and M. Waltl. "A DLTS study on deep trench processing induced trap states in silicon photodiodes", *IEEE Transactions on Device and Materials Reliability.*, 2024, doi: 10.1109/TDMR.2024.3382396.

## Conference proceedings

1. L. Cvitkovich, B. Sklénard, D. Waldhör, J. Li, C. Wilhelmer, G. Veste, Y.-M. Niquet, and T. Grasser. "Variability in Si/SiGe and Si/$SiO_2$ spin qubits due to interfacial disorder", in *2023 International Conference on Simulation of Semiconductor Processes and Devices (SISPAD)*, pp. 341–344, 2023, doi: 10.23919/SISPAD57422.2023.10319618.

2. L. Cvitkovich, D. Waldhör, A.-M. El-Sayed, M. Jech, C. Wilhelmer, and T. Grasser. "Multiscale modeling study of native oide growth on a Si(100) surface", in *ESSDERC 2021 – IEEE European Solid-State Device Research Conference*, pp. 235–238, 2021, doi: 10.1109/ESSDERC53440.2021.9631790.

3. L. Cvitkovich, D. Zocco, G. Eguchi, M. Waas, R. Svagera, B. Stöger, R. Mondal, A. Thamizhavel, S. Paschen. "Anisotropic physical properties of the Kondo Semimetal $CeCuAs_2$", in *Proceedings of the International Conference on Strongly Correlated Electron Systems (SCES2019)*, Okayama, Japan, doi: 10.7566/jpscp.30.011020.

## Talks

1. L. Cvitkovich, P. Stano, Y.-M. Niquet, and T. Grasser. "Ab-initio study of valley-orbit states in Si/SiGe and Si/$SiO_2$ heterostructures", *Silicon Quantum Computing Workshop*, 2023, Kyoto, Japan

2. L. Cvitkovich, B. Sklénard, D. Waldhör, J. Li, C. Wilhelmer, G. Veste, Y.-M. Niquet, and T. Grasser. "Variability in Si/SiGe and Si/$SiO_2$ spin qubits due to interfacial disorder", *International Conference on Simulation of Semiconductor Processes and Devices (SISPAD)*, 2023, Kobe, Japan

3. L. Cvitkovich, D. Waldhör, A.-M. El-Sayed, M. Jech, C. Wilhelmer, and T. Grasser. "Multi-scale modeling of thermal oxidation of Si", *$SiO_2$ Conference*, 2023, Palermo, Italy

4. L. Cvitkovich, B. Sklénard, D. Waldhör, J. Li, C. Wilhelmer, Y.M. Niquet, and T. Grasser. "Variability in Si spin qubits due to disordered Si/$SiO_2$ interfaces", *European Materials Research Society Spring Meeting*, 2023, Strasbourg, Belgium

Die approbierte gedruckte Originalversion dieser Dissertation ist an der TU Wien Bibliothek verfügbar.
The approved original version of this doctoral thesis is available in print at TU Wien Bibliothek.
TU WIEN Bibliothek Your knowledge hub

5. L. Cvitkovich, D. Waldhör, A.-M. El-Sayed, M. Jech, C. Wilhelmer, and T. Grasser. "Multiscale modeling study of native oide growth on a Si(100) surface", *IEEE European Solid-State Device Research Conference (ESSDERC)*, 2022, online

## Poster presentations

1. L. Cvitkovich, Y.-M. Niquet, and T. Grasser. "Variability in Si/$SiO_2$ and Si/SiGe Spin Qubits due to Interfacial Disorder", *Hybrid Quantum Technologies Workshop*, 2023, Klosterneuburg, Austria

2. L. Cvitkovich, D. Waldhör, A.-M. El-Sayed, M. Jech, C. Wilhelmer, and T. Grasser. "Ab-Initio Modeling of the Initial Stages of Si(100) Thermal Oxidation", *Psi-K*, 2022, Lausanne, Switzerland

## Public outreach

1. L. Cvitkovich "Keeping quantum information safe and sound", *Pint of Science*, May 2024, Vienna, Austria

Die approbierte gedruckte Originalversion dieser Dissertation ist an der TU Wien Bibliothek verfügbar.
The approved original version of this doctoral thesis is available in print at TU Wien Bibliothek.
TU WIEN Bibliothek Your knowledge hub

Die approbierte gedruckte Originalversion dieser Dissertation ist an der TU Wien Bibliothek verfügbar.
The approved original version of this doctoral thesis is available in print at TU Wien Bibliothek.
TU WIEN Bibliothek Your knowledge hub